

## Theory and Modeling of Transport for Simple Fluids in Nanoporous Materials: From Microscopic to Coarse-Grained Descriptions

Alexander Schlaich, Jean-Louis Barrat, and Benoit Coasne\*

Cite This: <https://doi.org/10.1021/acs.chemrev.4c00406>

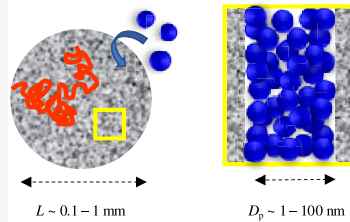
Read Online

ACCESS |

Metrics &amp; More

Article Recommendations

**ABSTRACT:** We present the state-of-the-art of theoretical modeling, molecular simulation, and coarse-graining strategies for the transport of gases and liquids in nanoporous materials (pore size 1–100 nm). Special emphasis is placed on the transport of small molecules in zeolites, active carbons, metal–organic frameworks, but also in nanoporous materials with larger pores such as ordered and disordered mesoporous oxides. We present different atomistic and mesoscopic methods as well as available theoretical formalisms to describe such a complex problem. Attention is given to the investigation of different molecular transport coefficients—including the self, collective and transport diffusivities—but also to the determination of free energy barriers and their role in overall adsorption/separation process rates. We further introduce other available approaches such as hierarchical simulations and upscaling strategies. This review focuses on simple fluids in prototypical nanoporous materials. While the phenomena covered here capture the main physical mechanisms in such systems, complex molecules will exhibit additional specific features. For the sake of clarity and brevity, we also omit multicomponent systems (e.g., fluid mixtures, electrolytes, etc.) and electrokinetic effects arising when charged systems are considered (ionic species, charged surfaces, etc.), both of which add to the complexity.



### CONTENTS

1. Introduction	
2. General Principles of Diffusion and Transport	
2.1. Different Frameworks	
2.1.1. Fluid Dynamics	
2.1.2. Diffusion, Advection, Convection, Reaction	
2.2. Onsager Theory of Transport	
2.2.1. Transport Coefficients	
2.2.2. Self, Collective, and Transport Diffusivities	
3. Self-Diffusion and Tracer Diffusion at the Pore Scale	
3.1. Diffusion Mechanisms	
3.1.1. Molecular Sieving	
3.1.2. Knudsen Diffusion	
3.1.3. Molecular Diffusion	
3.1.4. Surface Diffusion	
3.2. Diffusion in Nanopores	
3.2.1. Combined Knudsen/Molecular Diffusion	
3.2.2. Surface versus Volume Diffusion	
3.2.3. Intermittent Brownian Motion	
3.2.4. Density-Dependent Diffusion	
4. Self-Diffusion and Tracer Diffusion in Porous Networks	
4.1. Effective Diffusion	
4.1.1. Tortuosity	
4.1.2. Serial/Parallel Models	

B	4.1.3. Maxwell Model	AB
D	4.1.4. Effective Medium Theories	AB
D	4.2. Hierarchical and Mesoscopic Approaches	AC
D	4.2.1. General Considerations	AC
D	4.2.2. Diffusion in Heterogeneous Media	AC
D	4.2.3. Random Walk	AE
E	5. Gradient-Driven Transport in Nanoporous Materials	AI
F	5.1. Flow Mechanisms	AI
F	5.1.1. Convection, Advection, and Diffusion	AI
F	5.1.2. Gas and Liquid Flows	AJ
H	5.2. Viscous Flow	AL
M	5.2.1. Poiseuille Law	AL
M	5.2.2. Darcy's Law and Its Extensions	AN
M	5.2.3. Beyond Viscous Flows	AO
N	5.3. Adsorption/Desorption Kinetics	AR
O	5.3.1. Liquid Imbibition	AR
O	5.3.2. Mass Uptake: Surface, Internal, and External Resistances	AR
Q	5.3.3. Transport Barriers	AU
R	6. Gradient-Driven Transport in Porous Networks	AX
S		
T		
V		
W		

Received: May 31, 2024

Revised: January 20, 2025

Accepted: January 27, 2025

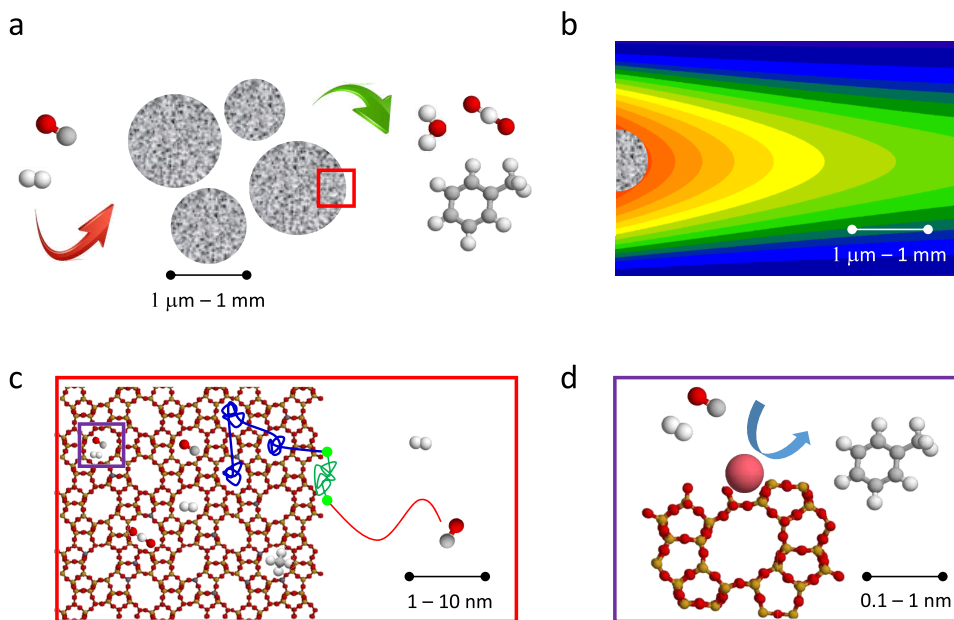


**Figure 1. Multiscale theoretical approach to an engineering process in porous materials.** (a) Schematic view of the use of nanoporous materials for heterogeneous adsorption, separation or catalysis. Here, a zeolite is considered as an example but the scheme presented is valid for any type of nanoporous materials including mesoporous alumina, silica, active carbons, etc. The competitive adsorption and/or reaction between different molecules occur at active sites on the material internal surface. Typically, the nanoporous material is shaped into pellets which form a granular material with dimensions that should optimize the transport of molecules within the material but also to optimize access to the porosity. The description of adsorption, separation or catalysis requires to develop a multiscale approach which includes at least the three characteristic time and length scales schematically depicted in b, c, and d. (b) Transport at the macroscopic scale ( $\sim 1 \mu\text{m} - 1 \text{ mm}$ ) is usually described using hydrodynamics with methods from computational fluid dynamics. (c) At the mesoscopic scale ( $\sim 1 - 100 \text{ nm}$ ), molecular dynamics and other molecular or mesoscopic simulation tools such as Monte Carlo techniques, dissipative particle dynamics, free energy calculations, etc. are used to describe adsorption and dynamics of molecules at the surface of the porous material and within its porosity. (d) At the microscopic/molecular scale ( $\sim 0.1 - 1 \text{ nm}$ ), quantum mechanical approaches, which include *ab initio* techniques and density functional theory calculations, allow describing at the atomic scale the molecular reactions that correspond to the elementary adsorption, separation and/or catalytic steps.

## 6.1. Coarse-Grained Models

- 6.1.1. Lattice Boltzmann Method
- 6.1.2. Dynamic Monte Carlo
- 6.1.3. Dynamic Mean-Field DFT

## 6.2. Network Models

- 6.2.1. Pore Network Models
- 6.2.2. Other Lattice Models

## 7. Discussion and Perspectives

- 7.1. Chemomechanical Effects
- 7.2. Separation and Phase Transition at the Nanoscale
- 7.3. Solid/Fluid Coupling at Interfaces
- 7.4. Upscaling Transport under Reactive or Phase-Transition Conditions

## Author Information

### Corresponding Author

### Authors

### Author Contributions

### Notes

### Biographies

### Acknowledgments

### References

## 1. INTRODUCTION

Transport in nanoporous environments (pore size in the range  $1 - 100 \text{ nm}^1$ ) are ubiquitous in chemistry, biology and physics.<sup>2–6</sup> In particular, such dynamical phenomena are key aspects to rationalize the role of nanoconfinement and surface

forces on the behavior of fluids adsorbed in nanoporous solids.<sup>7–18</sup> Such situations are also relevant to important applications related to the energy and environment fields:<sup>2–4</sup> chemistry and chemical engineering (zeolites and mesoporous materials are used for phase separation and catalysis), energy (supercapacitors and fuel cells), environment (water remediation, nuclear waste storage, and desalination), etc. From a fundamental viewpoint, the dynamics of fluids in the vicinity of surfaces or confined in nanoporous materials remain mysterious in many aspects. Indeed, the subtlety of the surface molecular interactions in such environments has not been fully embraced yet, and new phenomena still get uncovered experimentally—therefore making this topic more active than ever.<sup>8,19,20</sup> In particular, beyond known adsorption and confinement effects that affect the chemistry and physics of fluid transport, there is a large amount of experimental and theoretical works highlighting the role of morphological/topological pore disorder<sup>6,12,14,21</sup> and specific surface interactions (hydrophilic/hydrophobic, insulating/metalllic,<sup>24,25</sup> etc.). Moreover, there is also an increasing number of reports providing evidence for the complex multiscale behavior of fluid transport in nanoporous media (pore scale versus material network scale).<sup>7,26–28</sup> Such behavior, which challenges existing theoretical frameworks, points to the needs for fundamental developments in the theoretical description of multiscale transport in nanoporous materials.

As a generic feature, nanoporous materials possess a large intrinsic specific surface which scales as the surface to volume ratio  $S_{\text{sp}} \sim S/\rho V$ , where  $S$ ,  $V$ , and  $\rho$  are the surface area, volume and density.<sup>1,4</sup> Typically, regardless of its geometry, the specific

surface area of a pore of a size  $D_p$  scales as  $S_{sp} \sim 1/D_p$ ; using the density of silica,  $\rho \sim 2.65 \text{ g/cm}^3$ , the specific surface area is of the order of  $100 \text{ m}^2/\text{g}$  for  $D_p \sim 1 \text{ nm}$ ,  $10 \text{ m}^2/\text{g}$  for  $D_p \sim 10 \text{ nm}$ ,  $1 \text{ m}^2/\text{g}$  for  $D_p \sim 1 \mu\text{m}$ , and so on. The realm of nanoporous solids includes different classes of materials such as zeolites, metal-organic frameworks, oxides (e.g., alumina, titania, and silica), active porous carbons, etc.<sup>3,29,30</sup> Optimizing processes involving nanoporous materials requires better understanding adsorption and transport in the vicinity of surfaces and in confining environments.<sup>31–33</sup> The specific surface area and surface chemistry are obviously key parameters that control the efficiency of a given chemical engineering process involving nanoconfined fluids. However, other important ingredients have to be considered to unravel and characterize the role of nanoconfinement in nanoporous materials. These additional ingredients include the pore size  $D_p$  which, in addition to being a property that controls the specific surface area developed by the nanoporous material (see above), also governs the thermodynamics and dynamics of the molecules within their porosity.<sup>7–9,34</sup> Typically, depending on pore size and thermodynamic conditions (such as temperature, pressure, etc.), the nanoporous material can be either completely filled by a liquid containing the fluid or incompletely filled with an adsorbed film at the pore surface while the pore center remains filled by a gas phase. Correspondingly, as will be discussed in the present review, different transport types can be observed depending on pore size  $D_p$ , kinetic diameter of the molecule  $\sigma$ , fluid/solid interactions and thermodynamic conditions such as temperature  $T$  and pressure  $P$ . These transport mechanisms include but are not limited to molecular sieving, surface diffusion, molecular diffusion, Knudsen diffusion, etc.<sup>6,15</sup> Other properties such as pore morphology (pore shape, geometrical defects, etc.) and network topology (pore connectivity and accessibility) strongly affect the efficiency of an adsorption, separation or catalytic process by modifying the transport properties of the different interacting/reacting species.<sup>8,31,35</sup>

In order to set the frame of the present review, let us consider the transport of a fluid in a multiscale porous material as depicted in Figure 1. While we consider here the adsorption, separation and/or catalysis of fluid molecules in such systems as an illustrative example, we stress that the depicted situation pertains to all fields where the transport of a fluid in a porous material containing nanoporosity is considered. This includes situations such as transport in geological porous media and porous membranes (where many phenomena couple to lead to complex nonreactive or reactive transport). As a result, while the following introductory discussion is focused on a specific class of systems, we believe that the concepts described and phenomena covered are ubiquitous in all the fields listed above. The complexity of describing and predicting transport in a multiscale porous material stems from two main difficulties (Figure 1).<sup>36</sup> First, such processes involve a variety of complex phenomena that pertain to chemistry (chemical reaction or adsorption at active sites), chemical physics (local thermodynamic equilibria and molecular separation in the vicinity of the active sites), physics (diffusion and possible coupling between transport and adsorption properties), and chemical engineering (transport properties and heat transfer at the scale of the adsorption device/catalytic reactor). Second, while these phenomena occur at different scales—typically, from the molecular to the engineering scales—they are coupled so that describing the overall process requires the development of robust upscaling strategies. From a theoretical viewpoint, available approaches to

adsorption and reaction in a nanoporous material rely on the decomposition of the problem into the three following steps. (1) *adsorption or chemical reaction at the surface of the nanoporous material*. These processes are usually investigated using the so-called *ab initio* methods, which solve the electronic structure problem based on the underlying principles of quantum mechanics. Such approaches—which in principle can be employed to provide an accurate prediction of the system—are not discussed within this work as they fall out of its scope and have been thoroughly reviewed recently.<sup>37–39</sup> (2) *Thermodynamic equilibrium and transport properties in the nanoporous material*. These phenomena can be investigated using the large panel of numerical methods that are coined as molecular simulation. Such molecular modeling strategies, which are at the heart this review, allow simulating both adsorption equilibrium and transport of pure molecular components and their mixtures in a porous material. (3) *Process efficiency at the macroscopic scale*. The process yield under given thermodynamic and hydrodynamic conditions can be estimated using mesoscopic, coarse-grained or continuum models such as computational fluid dynamics, as we will discuss in this review both for equilibrium and nonequilibrium transport conditions.

From a modeling point of view, significant efforts are usually devoted to understanding chemical processes (reactive or nonreactive) at the molecular scale and the process efficiency at the macroscopic scale.<sup>40–42</sup> On the other hand, in practice, the thermodynamics and dynamics of the molecular species in the nanoporous solids are often treated only in an empirical manner despite the availability of fairly simple molecular simulation approaches. This is in part due to the lack of simple robust strategies to upscale the parameters obtained at a smaller scale into coarse-grained calculations at a larger scale. Yet, molecular simulation techniques are very efficient at providing, for a reasonable computational cost, adsorption equilibrium and transport coefficients in nanoporous materials.<sup>9,15</sup> Such methods, which include but are not limited to Molecular Dynamics and Monte Carlo techniques,<sup>43,44</sup> are much less fraught with theoretical difficulties than quantum mechanics<sup>37,45</sup> since electron-level details are not considered and the set of atoms or molecules are treated as classical objects obeying classical statistical physics.<sup>46–49</sup> Thanks to this simplification, molecular simulations involving thousands or even hundreds of thousands of atoms are possible and time scales of up to hundreds of nanoseconds and even beyond can be reached. Molecular simulation methods also include mesoscopic coarse-grained methods such as Brownian Dynamics and Dissipative Particle Dynamics as well as simple random walk models which allow probing even larger systems and on much larger time scales. Finally, other strategies that will be also discussed in this review include free energy techniques, lattice gas models, and upscaling strategies.

This review aims to be a comprehensive, critical, and accessible document of general interest to the chemistry, physical chemistry, chemical physics, and geologists communities. In particular, researchers working in domains including but not limited to adsorption, separation, catalysis, batteries, micro/nanofluidics are among the targeted audience. We also believe that engineering communities (e.g., chemical engineering, soil engineering, petrochemical engineering) would benefit from such an up-to-date review on transport in nanoporous materials. The specificities of this review can be listed as follows. (1) We present the state of the art on the fundamentals of self-diffusion and transport in nanoporous materials. As an important feature,

the present review adopts a multiscale view of the problem under consideration: both fundamental aspects and effective strategies are considered. (2) Considering the time/length scales involved in diffusion and transport in porous materials (from in pore dynamics to dynamics within the pore network), we treat all relevant approaches from molecular simulation (e.g., molecular dynamics, free energy calculations) to mesoscopic approaches (e.g., effective theories, random walk techniques, pore network models) but also upscaling strategies. (3) We discuss the determination of transport barriers, including surface/geometrical barriers and free energy barriers as encountered when phase transitions occur. Their role in overall transfer and process rates is also discussed. Finally, we also cover available approaches to include these aspects in a mesoscopic fashion such as hierarchical simulations. (4) For each approach, we provide the basic underlying concepts in a way that helps the reader to get familiar with such fundamental aspects without being an expert. While the different strategies considered in this review all rely on similar physical formalisms (statistical mechanics ground), we feel that no review encompassing these methods in a multiscale picture is available to date. (5) This contribution covers both self-diffusion and transport aspects and is not restricted to a given type of materials but deals with the broad class of nanoporous materials including—but not limited to—zeolites, active carbons, metalorganic frameworks, ordered and disordered nanoporous oxides. In this context, the present review considers both small and large nanoporous materials with pore sizes ranging from the subnanometer scale to tens of nanometers. (6) Last but not least, by considering both ordered and disordered materials, we feel that this review connects two important parts of the literature on fluids in nanoporous solids: (*i*) dynamics at the pore scale, which is mostly investigated using simple pore geometries (e.g., cages, channels, slits, etc.) and (*ii*) transfer through porous structures where morphological and topological features of the host network are known to impact the overall, macroscopic dynamics.

The present review covers important insights as well as methodological developments in the very broad field of transport of simple fluids in the vicinity or confined within nanoporous materials. It is thus complementary to the existing literature as it covers additional aspects compared to available reviews.<sup>7,9,11–16,50</sup> First, we cover all transport modes (diffusion, advection, and convection). In particular, we wish to connect the molecular mechanisms observed in nanoporous media to classical approaches such as Poiseuille law, Darcy law, Darcy–Forchheimer law, etc. Second, we include additional aspects connected to transport in nanoporous media such as liquid imbibition and activated transport across interfaces. Third, while the impact of disorder at the pore scale and of pore network morphology/topology are discussed in available reviews, we here cover additional aspects by discussing coarse-grained descriptions such as Lattice–Boltzmann calculations and dynamic mean-field DFT for instance. Finally, we also treat physical models such as free volume theories, Intermittent Brownian Motion, De Gennes narrowing, etc., which so far have not been discussed in available reviews on similar topics. As a final remark on this review and its content, to allow interested readers to deepen their understanding of the underlying scientific and practical aspects, we decided to provide a limited set of references only for every covered concept. However, while we omit many relevant works in our reference list for the sake of clarity and readability, we acknowledge that a large number of

references on each given effect/phenomenon are available (such missing references can be found in other available reviews cited in this introduction).

To provide a comprehensive overview, the remainder of this work is organized as follows. First, we consider the self-diffusion and tracer diffusion of molecules in systems at equilibrium, where transport is driven by local density/concentration gradients as induced by thermal fluctuations. While the two concepts are often invoked in different contexts, they refer to the same phenomenon corresponding to the diffusion of a tagged, i.e., identified, molecule in a given medium. Second, we consider all transport mechanisms as observed when applying a thermodynamic gradient to the system. In general, to avoid any confusion, transport will be used as a generic term to encompass all transport mechanisms (diffusion, advection, etc.). In **Section 2**, we discuss the fundamentals of transport in porous media. We introduce the different transport coefficients relevant to the dynamics of simple fluids confined in nanoporous materials but also important concepts such as tortuosity, diffusion factor, surface energy barriers, etc. In **Section 3** we review the state of the art of molecular simulation and other statistical mechanics approaches applied to the problem of self-diffusion and tracer diffusion in nanoporous materials. In this section, we only consider diffusion at the pore scale. In contrast, **Section 4** treats the problem of diffusion at the porous network scale. In both **Sections 3** and **4**, in addition to molecular simulation approaches, we also discuss other available methods such as hierarchical simulations (in which one probes the dynamics in a precalculated free energy landscape), random walk approaches, etc., but also theoretical formalisms based on statistical mechanics, such as Intermittent Brownian Dynamics, to tackle the problem of dynamics in heterogeneous media. In **Sections 5** and **6**, we review the application of molecular simulation and theoretical approaches to the problem of transport in porous media as induced by a thermodynamic gradient. After reviewing the different mechanisms that pertain to transport in porous media, we consider both stationary transport under a constant driving force and transient transport such as in situations dealing with mass uptakes, adsorption/desorption kinetics, etc. **Section 5** first deals with gradient-driven transport at the pore scale while **Section 6** considers the problem of gradient-driven transport at a much larger scale with techniques such as lattice and pore network models but also Lattice Boltzmann calculations. In **Section 7**, we provide some concluding remarks and perspectives for future work.

## 2. GENERAL PRINCIPLES OF DIFFUSION AND TRANSPORT

### 2.1. Different Frameworks

**2.1.1. Fluid Dynamics.** Fluid transport in general as well as in porous media can be described using the Navier–Stokes equation for momentum transfer, which reads for an incompressible fluid (constant density  $\rho$ ):<sup>51</sup>

$$\rho \left( \frac{\partial \mathbf{u}}{\partial t} + \mathbf{u} \cdot \nabla \mathbf{u} \right) = -\nabla P + \eta \nabla^2 \mathbf{u} + \mathbf{f} \quad (1)$$

This equation, which is valid when the system can be described as a continuous medium, corresponds to Newton's second law. It relies on key assumptions that define its applicability. In particular, in its form given in **eq 1**, it assumes that the fluid is incompressible (i.e., its density is constant) and Newtonian (i.e., its viscosity is independent of the applied shear

rate) and that the fluid can be treated as homogeneous fluid particles (therefore omitting strong structuring of the fluid especially near interfaces). Moreover, as will be discussed later in this review, the use of eq 1 assumes that the momentum relaxation time scale is much larger than the molecular relaxation time scale. The left-hand side term in the equation above is the fluid particle acceleration  $a = du/dt$  at a given time  $t$  multiplied by the fluid mass density  $\rho$ , while the right-hand side term corresponds to the sum of the forces per unit volume applied to the fluid particle ( $\mathbf{u}$  is the fluid particle velocity). In more detail, the left-hand side term is the total time derivative of the fluid particle momentum which gives rise to a linear and a nonlinear term:

$$\rho \frac{d\mathbf{u}}{dt} = \rho \left( \frac{\partial \mathbf{u}}{\partial t} + \mathbf{u} \cdot \nabla \mathbf{u} \right) \quad (2)$$

While the linear term is a time-dependent acceleration describing the change in the fluid velocity with time, the second term is a spatial contribution which describes the effect of flow field spatial heterogeneity on the fluid velocity. The forces applied to the fluid particle include the viscous forces that arise because of velocity heterogeneity in the fluid ( $\eta$  is the dynamic viscosity), any pressure gradient  $\nabla P$ , and any other body forces  $\mathbf{f}$ , such as e.g. gravity. In the context of fluid transport in nanoporous materials, the gravity term is usually omitted as the corresponding force is negligible compared to the force induced by the pressure gradient and the intermolecular forces between the fluid molecules and those with the porous material. The Navier–Stokes equation is very general so that it can be used to describe a broad range of phenomena including laminar, convective and turbulent flows for both compressible and incompressible flows. In particular, as will be discussed in Section 2.2.2, an incompressible fluid at a small Reynolds numbers obeys Poiseuille's law<sup>52</sup> (equivalent to Darcy's law<sup>53</sup>), where the flow is purely viscous.

There are several dimensionless numbers that characterize fluid transport in general and in porous materials in particular.<sup>52,54</sup> The Reynolds number  $Re$  is a dimensionless quantity that describes the ratio of the inertial (convective) contribution to the viscous force term in the Navier–Stokes equation given in eq 1:  $Re = \rho u L / \eta = u L / \nu$  where  $L$  is the characteristic length in the system and  $\nu = \eta / \rho$  is the kinematic viscosity of the fluid (with  $\rho$  the fluid density). For small Reynolds numbers, the flow is laminar which means that liquids flow in parallel layers with no strong mixing between adjacent layers having different velocities. On the other hand, for large Reynolds numbers, the flow is turbulent as a result of the strong inertia contributions which arise when the viscous force is not sufficient to overcome the convection flow between adjacent fluid particles. For intermediate  $Re$ , the system is in the laminar-turbulent transition regime where convection makes the laminar flow rough and then unstable (and eventually turbulent). The critical Reynolds numbers describing the boundaries between the different regimes depend on the geometry in which the fluid flows. Typically, as examples, the flow is laminar for  $Re < 20$  and fully turbulent for  $Re > 1500$  for a falling fluid film<sup>52</sup> and laminar for  $Re < 10$  and fully turbulent for  $Re < 2000$  for a fluid flowing in a packed bed.<sup>55</sup> In porous media, depending on the typical pore size  $D_p$ , the flow can be laminar or turbulent as predicted using the Reynolds number expression with the characteristic length  $L$  taken equal to  $D_p$ . However, in practice, for nanoporous materials typically used in adsorption, separation and catalysis, it is easy to show that  $Re \ll 1$ . For instance, in the case of water

involved in processes at room temperature,  $\rho \sim 1 \text{ g/cm}^3$  and  $\eta = 1 \text{ cP} = 1 \text{ mPa s}$ , confined in pores of a size  $D_p$  in the range 1–100 nm, we find  $Re < 10^{-4}$ .<sup>56</sup> As a result, for all examples considered in this review, we will always assume that the flow in nanoporous materials is laminar unless stated otherwise.

There are other dimensionless numbers that are of utmost importance when investigating transport in porous materials. Of particular relevance for the present review, the Mach number describes the ratio of the flow velocity  $u$  and sound velocity  $c$ , i.e.,  $Ma = u/c$  (typically, the sound velocity is  $c \sim 350 \text{ m/s}$  in air and  $3500 \text{ m/s}$  in water at room temperature). This dimensionless number indicates whether the fluid flow can be treated as incompressible or compressible (even when a compressible fluid such as a gas is considered). For small  $Ma$ , typically  $Ma < 1$ , the flow velocity is smaller than the sound velocity, i.e., the velocity of a compression wave, so that a fluid element can be treated as incompressible because it is not affected by the compression wave that its displacement generates. In contrast, for large  $Ma$ , typically  $Ma \gg 1$ , the compression wave generated by the fluid particle motion affects its own motion so that the fluid must be treated as compressible. In practice, even when transport of a compressible fluid (gas or vapor for instance) in nanoporous materials is considered, the fluid flow is usually slow compared to the velocity of sound such that  $Ma \ll 1$ . This is an important result as this implies that the Navier–Stokes equation given in eq 1—which was written for an incompressible fluid—remains valid in many cases. For instance, taking  $N_2$  flow at room temperature, the sound velocity is  $c \sim 350 \text{ m/s}$ ,<sup>57</sup> which leads to  $Ma \sim 10^{-3}$ . Finally, another important dimensionless number that should be considered when dealing with fluid transport in nanoporous media is the capillary number  $Ca$ . The latter describes the ratio of the viscous forces with respect to the force corresponding to the Laplace pressure across a gas/liquid interface (or any fluid/fluid interface in general such as when fluid mixtures are considered). In more detail,  $Ca \sim \eta u / \gamma$  where we recall that  $\eta$  is the fluid dynamic viscosity,  $u$  its velocity, and  $\gamma$  the fluid surface tension. While the flow is dominated by capillary forces for small  $Ca$ , the flow is dominated by viscous forces for large  $Ca$ .

**2.1.2. Diffusion, Advection, Convection, Reaction.** Let us consider the transport of tracers (molecules) in any porous material—by tracers, we refer either to solute molecules in a liquid or to a single tagged molecule that is of the same nature as the liquid but we distinguish this single molecule to probe its motion. Here, we restrict ourselves to the case of passive tracers in a prescribed velocity flow field  $\mathbf{u}(\mathbf{r})$ . In a very general way, the transport of such tracers can be described using the reaction-diffusion-advection equation which describes the change in the tracer density over time<sup>52</sup>

$$\frac{\partial c}{\partial t} = \nabla \cdot (D_s \nabla c) - \nabla \cdot (\mathbf{u}c) + R \quad (3)$$

where  $c$  is the tracer concentration at a time  $t$ ,  $D_s$  is the self-diffusion coefficient,  $\mathbf{u}$  is the fluid velocity and  $R$  is a source/sink term that adds or removes tracers from the system ( $R$  can be either positive or negative). In more detail, this expression is a mass balance equation where the change in the concentration  $c$  over an infinitesimal time step is the sum of (1) the diffusion contribution,  $\nabla \cdot (D_s \nabla c)$ , which disperses the tracers in the fluid, (2) the change because of the fluid motion carrying away the concentration with a velocity  $u$ ,  $\nabla \cdot (\mathbf{u}c)$ , and (3) a sink/source term,  $R$ , such as a chemical reaction in the case of catalysis which increases or decreases locally the concentration of tracers.

Here, it must be made clear that the various dispersion contributions to eq 3 arise from very different mechanisms. Acknowledging that conventions and definitions vary from one scientific field to another, we introduce the following concepts that will be used and discussed in detail in this review. The reaction term in the above equation describes either a chemical reaction that would consume or create tracer molecules or a physical adsorption/desorption contribution which can be seen as a nonchemical reaction that changes locally the concentration of molecules. The diffusion term—as will be discussed in Section 2.2—is due to diffusion which occurs both under uniform chemical potential (such as the self-diffusion or tracer diffusion probed using pulsed field gradient nuclear magnetic resonance or quasi-elastic neutron scattering) and nonuniform chemical potential (such as transport diffusion measured when the system is subjected to a thermodynamic gradient). Advection refers to the different mechanisms where the fluid is set in motion by thermodynamic gradients (temperature, pressure, concentration, etc.), whereas convection here refers to the transport induced by the nonlinear acceleration term (inertial effects), which was introduced when discussing the Navier–Stokes equation above. In this context, we note that the term convection often also refers to the collective motion of fluid regardless of the flow mechanism or nature.

Assuming for now that the Fickian diffusion term is known (see Section 2.2.2), the derivation of the advection-diffusion-reaction equation given in eq 3 is straightforward. A simple mass balance equation at any spatial position implies that the change over time in the local concentration is related to the sum of the incoming/outgoing tracer fluxes  $J$  and the sink/source term:

$$\frac{\partial c}{\partial t} = -\nabla \cdot J + R \quad (4)$$

$J$  is the sum of the diffusive flux, i.e.,  $J_d = -D_s \nabla c$ , and the advective flux, i.e.,  $J_a = uc$  and  $R$  is the rate of creation/removal of tracers ( $\nabla \cdot$  is the divergence operator). Equation 4 as presented here is identical to eq 3, but written in a more compact form to gather the diffusion and advection term together. In another common case of self-diffusion coefficient being homogeneous in space, the advection-diffusion equation given in eq 3 can be recast in a simpler form:

$$\frac{\partial c}{\partial t} = D_s \nabla^2 c - \nabla \cdot (uc) + R \quad (5)$$

However, in general, the self-diffusion coefficient depends on the local environment (for instance the local pore size in a disordered porous medium, the crowding by other constituents or the “self-crowding” by other, non tagged molecules of the same nature as the tracer) so that the most general form of the advection-diffusion equation given in eq 3 must be kept. It is interesting to note the analogy between the advection-diffusion equation in eq 5 and the Navier–Stokes equation for the momentum transfer in eq 1. While the former corresponds to a mass balance condition for the tracer diffusion, the latter describes the momentum conservation condition within the flowing fluid. In principle, the reaction-advection-diffusion equation could be used to model reaction and transport in porous media. However, in practice, the resolution of such equations remains only at the qualitative level with input parameters that cannot be derived from molecular thermodynamic and dynamical coefficients. This is due to the fact that the different terms, i.e., reactive, diffusive, and advective contributions, in this equation are strongly coupled at the molecular scale

so that any set of effective parameters will fail to describe the complexity and richness of the phenomena occurring in the nanoscale porosity (even when simple nonreactive transport is considered).

The advection-diffusion equation emphasizes the competition/combination of diffusive and advective transport in porous media. This competition is also characterized by the Peclét number. This dimensionless number,  $Pe$ , describes the ratio of the advective fluxes,  $J_a$  to the diffusive fluxes,  $J_d$ ,  $Pe = J_a/J_d = uD_p/D_s$  where  $u$  is the fluid velocity,  $D_s$  is the self-diffusion coefficient, and  $D_p$  is the characteristic length scale taken equal to the pore size.  $Pe$  therefore describes the relative efficiency of diffusion and advection to disperse tracers within the porous medium. For very small  $Pe$ , i.e., when the advection contribution can be neglected (such as when no thermodynamic gradient is applied to induce transport or when the flow induced by the thermodynamic gradient is negligible compared to the diffusive flow), the advection-diffusion equation is equivalent to the well-known “equation of porous media” for a purely diffusive regime and without any chemical reaction ( $R = 0$ )<sup>54</sup>

$$\frac{\partial c}{\partial t} = \nabla \cdot [D_s(\vec{r}) \nabla c] \quad (6)$$

where  $D_s(\vec{r})$  is the local, environment-dependent self-diffusion coefficient. In the context of nanopores, owing to the very small pore size considered, transport mostly occurs through diffusion, i.e.,  $Pe \ll 1$ —typically, both the advective flow rate  $u \sim \nabla P$  and the self-diffusion coefficient  $D_s$  decrease with the pore size  $D_p$  but there is always a critical pressure gradient  $\nabla P_c$  below which  $D_p u \ll D_s$  (i.e.,  $Pe \ll 1$ ).

## 2.2. Onsager Theory of Transport

**2.2.1. Transport Coefficients.** We now briefly discuss Onsager’s phenomenological theory of transport as it allows introducing key concepts for the transport of molecules in nanoporous media—namely the self, collective and transport diffusivities.<sup>47,58</sup> Let us consider a system which is characterized at the macroscopic scale by a set of thermodynamic extensive quantities  $X_i$  (energy, volume, number of molecules). The thermodynamics of the system is governed by the entropy-state function of these extensive variables which is maximum at equilibrium:  $S = S(X_i)$ .<sup>59,60</sup> The differential of the entropy, known as the Gibbs relation, introduces the conjugated intensive variable  $F_i$ , the so-called affinity, of each extensive quantity  $X_i$

$$dS = \sum_i \left. \frac{\partial S(X_i, X_j, \dots)}{\partial X_i} \right|_{j \neq i} dX_i = \sum_i F_i dX_i \quad (7)$$

where the bar “ $\bar{}$ ” in the partial derivative indicates that all other quantities  $j \neq i$  are kept constant. For most practical situations, the extensive quantities  $X_i$  are the internal energy  $E$ , the volume  $V$  and the number of molecules  $N_k$  for each chemical component  $k$  in the system, which leads to  $S = S(E, V, N_1, \dots, N_k)$  and the following Gibbs relation

$$dS = \frac{1}{T} dE + \frac{P}{T} dV - \sum_{i=1}^k \frac{\mu_i}{T} dN_i \quad (8)$$

where we used that  $\partial S/\partial E = 1/T$ ,  $\partial S/\partial V = P/T$ , and  $\partial S/\partial N_i = -\mu_i/T$  for  $i = \{1, \dots, k\}$  to define the different affinities  $F_i$ .

Transport phenomena induced by thermodynamic gradients such as  $\nabla T$ ,  $\nabla P$ ,  $\nabla \mu$ , etc. in a given thermodynamic system can

be described using the second law of thermodynamics under the local thermodynamic equilibrium approximation. The latter assumption states that, even under nonequilibrium conditions, the system can be subdivided into mesoscopic volume elements which are (1) small enough to assume that local thermodynamic properties do not vary within these elements but (2) large enough to be treated like thermodynamic subsystems. Typically, the size  $\lambda$  of these mesoscopic elements should be such that the change  $\Delta\chi$  in a given thermodynamic property  $\chi$  due to the gradient  $\nabla\chi = \Delta\chi/\lambda$  is smaller than the thermodynamic fluctuations at equilibrium  $\delta\chi$ , i.e.,  $\Delta\chi/\chi < \delta\chi/\chi \ll 1$  (the last part of the inequality states that the equilibrium fluctuations must be small enough to assume that the system can be treated using macroscopic thermodynamics).<sup>60</sup> Under such local thermodynamic equilibrium, the change in any thermodynamic quantity  $\chi$  can be described using a variable that depends on spatial coordinates  $\mathbf{r}$  and time  $t$ , i.e.,  $\chi(\mathbf{r}, t)$  (typically,  $\chi$  is the temperature, fluid density, pressure, etc.). As discussed in ref 46, the local thermodynamic equilibrium condition requires a time scale separation with a much shorter molecular relaxation time (typically,  $\tau_m \sim 1$  ps) compared to the macroscopic evolution time governed by the local thermodynamic gradient (typically,  $\tau_M \gg 1$  ps). Under thermodynamic equilibrium, the maximization of the entropy implies that the affinities are homogeneous throughout the system, i.e.,  $\nabla F_i = 0 \forall i$ .<sup>61</sup> We recall that the different affinities  $F_i$ , which were introduced right after eq 8, correspond to partial derivatives of the entropy with respect to the extensive variables  $N, V, E$ , etc. We also indicate here that  $i$  simply corresponds to an index that lists the different affinity gradients that can be applied to the system. In contrast to the situation without any affinity gradients, a nonzero affinity gradient  $\nabla F_i$  will induce a flux in the conjugated extensive variable  $X_i$ ,  $J_i = dX_i/dt$ . For small affinity gradients  $\nabla F_i$ , the flux  $J_i$  in the extensive quantities  $X_i$  varies linearly with  $\nabla F_i$ . Note that an affinity gradient  $\nabla F_i$  involves a direct flux of its conjugated extensive variable  $X_i$  but also an indirect flux of all other conjugated variables  $X_j$  with  $j \neq i$ , cf. eq 7 and refs 46 and 60)

$$J_i = \sum_j L_{ij} \nabla F_j \quad (9)$$

where the coefficients  $L_{ij}$  are called Onsager transport coefficients. An important property of these coefficients—arising from the time reversibility of the equations governing the motion of atoms and molecules at the microscopic scale—is known as Onsager reciprocal relations:  $L_{ij} = L_{ji} \forall i, j$ . For the system defined above (internal energy  $E$ , volume  $V$  and number of molecules  $N_k$  for each chemical component  $k$ ), eq 9 leads to the following equations:

$$J_E = L_{EE} \nabla F_E + L_{EV} \nabla F_V + \sum_{j=1}^k L_{EN_j} \nabla F_{N_j} \quad (10)$$

$$J_{N_i} = L_{NE} \nabla F_E + L_{NV} \nabla F_V + \sum_{j=1}^k L_{NN_j} \nabla F_{N_j} \quad (11)$$

Under specific conditions (i.e., when the system is subjected to a single thermodynamic/affinity gradient), the general linear equations given in eqs 10 and 11 simplify to a number of well-known equations. They include Fourier law when the chemical potential/pressure are uniform:  $J_E = -\lambda_T \nabla T$  with  $\lambda_T = L_{EE}/T^2$ . Another important example, particularly relevant in the context of the present review, is the case of isothermal/isobaric system

which leads to the following linear relationship for the molecule flux:

$$J_N = -L_{NN} \nabla \left( \frac{\mu}{T} \right) = -\frac{L_{NN}}{T} \nabla \mu \quad (12)$$

This equation, which governs diffusion under static pressure/temperature conditions in local thermodynamic equilibrium, is a cornerstone of diffusion in porous media as it allows defining the different diffusivities that can be measured in typical transport experiments: the self-diffusivity  $D_s$ , the collective diffusivity  $D_0$ , and the transport diffusivity  $D_T$ . Before discussing in details below each diffusion mechanism, a few comments are in order (see also refs 6, 11, 14). On the one hand, the self-diffusion  $D_s$  pertains to the diffusion of a single molecule so that it corresponds either to a very diluted solute molecule in a liquid or to a single molecule (tracer) in a liquid that would be tagged to follow its trajectory. On the other hand, the collective diffusivity  $D_0$  refers to the collective displacement of the fluid in response to a chemical potential gradient. As will be shown below, the collective diffusivity is a very important parameter as it is formally linked to the so-called permeability. Finally, the transport diffusivity  $D_T$  is similar to the collective diffusivity  $D_0$ , but with the induced transport written as a response to a concentration/density gradient instead of a chemical potential gradient.

While these three diffusion coefficients are identical in the limit of very dilute systems such as in gas transport or for ultraconfined molecules, they strongly depart from each other when the molecular density becomes non-negligible. In particular, as far as the difference between  $D_s$  and  $D_0$  is concerned, both direct molecular interactions between molecules and the so-called hydrodynamic interactions, i.e., when the velocity field created by a moving molecule affects the trajectory of the others, are responsible for the marked differences seen between these two diffusion coefficients and their dependence on density, temperature, etc. From a practical viewpoint, the three diffusion coefficients  $D_s$ ,  $D_0$  and  $D_T$  are probed using different experimental techniques; see ref 6. Typically, the self-diffusivity  $D_s$  can be determined using Pulsed Field Gradient Nuclear Magnetic Resonance (PFG-NMR) and Quasi Elastic Neutron Scattering (QENS). PFG-NMR probes the dynamics corresponding to displacements over microns, while QENS probes dynamics at the nm scale. As a result, in a real material with defects (pore collapse/amorphization, impurities, vacancies, etc.), PFG-NMR is sensitive to these defects since it probes displacements over lengths that are comparable to the typical distance between them—therefore, PFG-NMR leads to transport coefficients that can be more than an order of magnitude lower than those measured using QENS. Yet, other NMR methods can be used to probe dynamics over much shorter distances and times. Finally, while QENS techniques typically probe the self-diffusivity because hydrogen is a strongly incoherent scatterer (large incoherent scattering length), deuteration allows probing with the same technique the collective diffusivity because deuterium atoms are strong coherent scatterers. As for the transport diffusivity  $D_T$ , macroscopic transport experiments are needed to probe this effective transport coefficient. Similarly, as will be illustrated in the rest of this section, different theoretical and numerical methods can be used to probe  $D_s$ ,  $D_0$  and  $D_T$ . Typically, both equilibrium and nonequilibrium molecular dynamics can be used to determine  $D_s$  and  $D_0$ . Assessing  $D_T$  is more complex as it usually requires to determine  $D_0$  and the correction factor to

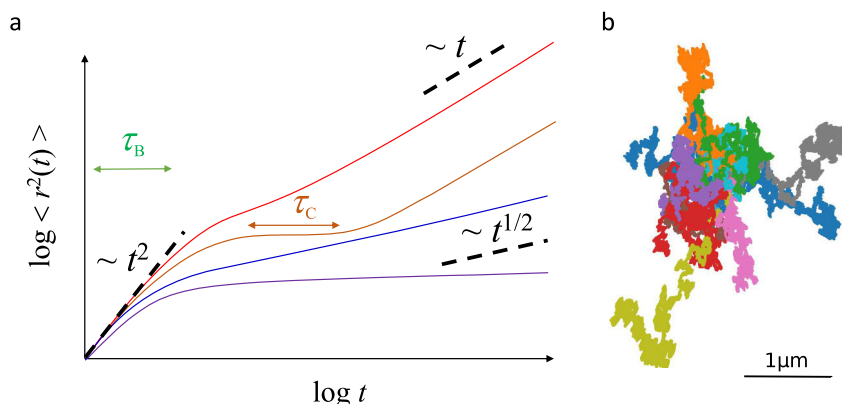


**Figure 2. Mean square displacements  $\langle r(t)^2 \rangle$  observed as a function of time  $t$  on a log–log scale.** (a) In the short time limit, the regime is said to be ballistic with  $\langle r(t)^2 \rangle \sim t^2$ . This regime is observed until an average time  $\tau_B$ , which corresponds to the characteristic time before the molecule collides with other molecules. At longer times, in general, the molecule follows the normal diffusion regime also known as Fickian regime where  $\langle r(t)^2 \rangle \sim t$ . This general behavior is shown with the red line. In complex systems such as glasses,  $\langle r(t)^2 \rangle$  can display cage effects where the molecule remains trapped for a time  $\tau_C$  inside cages formed by other molecules before escaping and entering the Fickian regime (brown line). In case of diffusion in extremely confining porous materials, i.e., when molecules are trapped for times much larger than the observation time  $\tau_{obs}$ , the cage effect appears over time scales such as  $\tau_C \gg \tau_{obs}$ . As a result, in this regime,  $\langle r(t)^2 \rangle \sim \text{constant}$  (purple line). In unidimensional confining channels, diffusion can obey a non-Fickian regime known as single-file diffusion with  $\langle r(t)^2 \rangle \sim t^{1/2}$  (blue line). (b) Typical trajectories observed over 100 ns for a set of 10 molecules in bulk liquid nitrogen at 77 K. (Each molecule trajectory is shown with a different color code.)

account for the change when replacing the chemical potential gradient by a concentration/density gradient (see discussion below).

**2.2.2. Self, Collective, and Transport Diffusivities.** In the framework of the Onsager phenomenological theory of transport introduced above, transport coefficients relevant to very different experimental situations can be described. In the spirit of eqs 10 and 11, several Onsager transport coefficients can be defined from the corresponding thermodynamic driving forces directly related to their entropy derivatives. By extension, any other transport coefficients can be defined in the context of linear response theory by considering different driving forces. This includes important examples such as Ohm's law for electrical conductivity, Fourier's law for thermal conductivity, etc. As far as transport in nanoporous materials is concerned, the following important transport coefficients, which characterize the mass flow  $\mathbf{J} = \rho\mathbf{u}$  – defined as the fluid density  $\rho$  multiplied by the flow velocity  $\mathbf{u}$ , can be introduced. They describe experimental situations corresponding to (1) the tracer or self-diffusion of particles governed by concentration gradients  $\nabla c$ , (2) the flow induced by a pressure gradient  $\nabla P$ , (3) the flow induced by a density gradient  $\nabla \rho$ , and (4) the flow induced by a chemical potential gradient  $\nabla \mu$ :<sup>9</sup>

$$\mathbf{J} = -D_s \nabla c, \mathbf{J} = -\rho K \nabla P, \mathbf{J} = -D_T \nabla \rho, \text{ and } \mathbf{J} = -\rho \frac{D_0}{k_B T} \nabla \mu \quad (13)$$

In these equations,  $D_s$  is the self-diffusivity,  $K$  the permeability,  $D_T$  the transport diffusivity, and  $D_0$  the collective diffusivity. As will be seen below and in the rest of this document, these coefficients correspond to different physical situations as encountered in applications but they are linked through simple thermodynamic quantities obtained from simple experiments. For instance,  $D_T \sim D_0 (\partial \mu / \partial \rho)_T$  where the proportionality factor can be inferred from the adsorption isotherm  $\rho(\mu, T)$  at constant temperature  $T$  as measured under static conditions.<sup>9</sup> In what follows, we discuss in detail the different transport coefficients above with special emphasis on their connections through

thermodynamic factors. While the notations above will be used throughout this review, we acknowledge that the conventions for the different diffusion coefficients differ from one field to another. In this context, we wish to highlight the forthcoming Technical Report on "Diffusion in Nanoporous Materials with special Consideration of the Measurement of Determining Parameters" in the framework of the IUPAC project "Diffusion in nanoporous solids".<sup>62</sup>

**2.2.2.1. Self-Diffusivity  $D_s$ .** For a very dilute system, the chemical potential  $\mu$  can be expressed by making use of the ideal-gas law as  $\mu \sim k_B T \ln c$ , where  $k_B$  is the Boltzmann constant,  $T$  is the temperature, and  $c$  is the concentration. Upon inserting this expression in the isothermal/isobaric version of the Onsager linear relationship given in eq 12, one obtains Fick's first law

$$J_N = -D_s(c) \nabla c \quad (14)$$

with  $D_s(c) = L_{NN}(c)/k_B c$ . Generally,  $L_{NN}$  is concentration-dependent with the dilute limit  $L_{NN}(c) \propto D_s c$  where  $D_s$  is a molecular property independent of  $c$  ( $D_s$  depends on the molecular mass, i.e., the thermal velocity). It is important to reckon that, as already mentioned above, diffusion occurs even under equilibrium conditions, i.e., when there is no net molecule flux that would be induced by a thermodynamic gradient applied to the system. In many textbooks, the concentration  $c$  is replaced by the density  $\rho$  as it allows encompassing the situation where the self-diffusivity refers to the diffusion of a single molecule in a pure fluid at equilibrium under static conditions.

Inserting Fick's first law into the mass conservation equation, i.e.,  $\partial c / \partial t + \nabla \cdot \mathbf{J} = 0$ , leads to Fick's second law:

$$\frac{\partial c}{\partial t} = \nabla \cdot [D_s \nabla c] \quad (15)$$

For uniform (or weakly position dependent) self-diffusivities, i.e.,  $D_s \sim \text{constant}$ , the latter equation can be recast in a simpler form:

$$\frac{\partial c}{\partial t} = D_s \Delta c \quad (16)$$

As expected, this equation is strictly equivalent to the advection-diffusion-reaction equation derived in Section 2.1.2 if no reaction and advection contributions are considered. Starting from an initial configuration at  $t = 0$  where all particles are located at  $\mathbf{r} = 0$ , the spatial and time dependent solution of Fick's second law is known as the Gaussian propagator  $P(\mathbf{r}, t)$ <sup>63,64</sup>

$$c(\mathbf{r}, t) = NP(\mathbf{r}, t) = \frac{N \exp(-\mathbf{r}^2/4D_s t)}{(4\pi D_s t)^{3/2}} \quad (17)$$

where  $N$  is the total number of diffusing species (this constant is needed here since the propagator is a quantity defined for a single molecule while the concentration is for the  $N$  molecules). The Gaussian propagator is the probability density that a molecule moves by a vector  $\mathbf{r}$  over a time  $t$ . The equation above states that, starting from the initial configuration, the concentration in a position  $\mathbf{r}$  at a time  $t$  is simply given by the probability that molecules move by a vector  $\mathbf{r}$ . The average mean-square displacement  $\langle r(t)^2 \rangle$  of the  $N$  molecules over a time  $t$  can be estimated from the Gaussian propagator:

$$\langle r^2(t) \rangle = |\mathbf{r}(t) - \mathbf{r}(0)|^2 = \int r^2 P(\mathbf{r}, t) d\mathbf{r} = 6D_s t \quad (18)$$

The last equation is an important cornerstone of diffusion as it allows one, using the Gaussian propagator formalism, to recover Einstein's formula which relates the mean square displacement to the self-diffusivity in Brownian motion, i.e.,  $\langle r^2(t) \rangle = 2dD_s t$  where  $d$  is the space dimensionality of the system ( $d = 3$  in the example treated above).

In practice, eq 18 is routinely used in molecular dynamics studies to determine the self-diffusivity  $D_s$  from the mean square displacement  $\langle r(t)^2 \rangle$  as a function of time  $t$ . Figure 2 shows schematic yet characteristic examples of mean square displacements in different physical situations.<sup>63</sup>  $\langle r(t)^2 \rangle$  scales quadratically with time  $t$ , i.e.,  $\langle r(t)^2 \rangle \sim t^2$  in the short time limit  $t < \tau_B$ ; this regime corresponds to the ballistic regime where the molecule obeys Newton's equation of motion until it collides with other molecules at a typical time  $\tau_B$ . At longer times, the molecule follows the normal diffusion regime, also known as Fickian regime, where  $\langle r(t)^2 \rangle \sim t$  as expected from eq 18. These two asymptotic regimes are very general but, as discussed in ref 63, other regimes can be observed. From a very general standpoint, the time dependence of the mean square displacement can be described as a power law,  $\langle r(t)^2 \rangle \sim t^\alpha$ , where  $\alpha$  is a real number smaller or larger than 1. While  $\alpha = 1$  corresponds to normal or Fickian diffusion, other regimes are coined as anomalous diffusion (note that only the normal regime has an underlying Gaussian propagator as defined in eq 17). In more detail,  $\alpha = 0$  corresponds to a localized state,  $\alpha < 1$  to a subdiffusive regime,  $\alpha > 1$  to a superdiffusive regime,  $\alpha = 2$  to the ballistic regime, and  $\alpha = 3$  to a fully developed turbulent regime. Two typical examples of subdiffusive regimes, i.e., single-file diffusion  $\alpha = 1/2$  and confined diffusion  $\alpha = 0$ , are shown in Figure 2.

As a specific example of the subdiffusive regime, we consider single-file diffusion which can apply to ultraconfining materials where the porosity consists of narrow cylindrical pores.<sup>65,66</sup> Single-file diffusion is just given as an example here so that we provide the main ingredients/results without further explanation (also, we note that the typical time-dependence of the corresponding mean-square displacement cannot be described

in the framework of Fickian diffusion). In this regime, owing to the very small pore size, molecules cannot pass each other so that their dynamics is severely hindered. The typical scaling for this regime is  $\langle r(t)^2 \rangle \sim t^{1/2}$ , which indeed falls in the category of subdiffusion. As shown by Kärger and co-workers, except when the repulsive fluid/fluid potential is infinite (hard core potential), there is always a time beyond which molecules eventually pass each other and the Fickian regime is recovered. The typical time for this crossover is given by  $\tau_c \sim 1/D_s^2$ .<sup>65</sup> However, for practical use, in the framework of molecular dynamics simulations, considering reasonable time scales that can be reached, it is likely that the crossover time cannot be accessed so that only single-file diffusion is reached (in contrast to experiments where much longer times are often probed).<sup>65</sup>

It should be emphasized that diffusion in complex, i.e., heterogeneous, materials can also lead to different Fickian diffusion regimes. For instance, depending on pore size and temperature, the mean square displacement as a function of time in materials made of different domains can show different regimes where  $\langle r(t)^2 \rangle \sim t$ . While the diffusivity at short times corresponds to diffusion within a given domain, the diffusivity at long times corresponds to a diffusion time for molecules that explore the entire material with significant exchanges between the different porosity domains (see the discussion by Roosen-Runge et al. in ref 67). When diffusion is probed on short time scales, the Gaussian propagator is characteristic for different subpopulations that do not exchange and rather explore the domain they belong to. On the other hand, as the typical time scale becomes much larger than the exchange time between domains, the diffusion coefficient being probed is a single effective diffusivity which depends on the diffusivity in the different domains. From an experimental viewpoint, this can also be used in PFG-NMR for instance to probe interconnectivity in multiscale porous media such as hierarchical zeolites (see ref 26 for instance); while diffusion corresponds to the superimposition of diffusion in microporous and mesoporous domains when short time scales are considered (i.e., both slow and fast diffusions are observed), a single intermediate effective diffusivity is obtained when long time scales are considered.

Determining the self-diffusion coefficient using molecular dynamics from the average mean square displacements can fail as the typical time scale attainable using computers might be insufficient to reach the Fickian regime. This is particularly true for ultraconfined nanoporous materials or when low temperatures or strong fluid/solid interactions are considered. Another strategy consists of calculating the self-diffusivity  $D_s$  from the velocity autocorrelation function using the Green–Kubo formalism.<sup>48</sup> The velocity autocorrelation function  $\langle \mathbf{v}(0) \cdot \mathbf{v}(t) \rangle$  is a time autocorrelation function which describes the correlation between the velocity  $\mathbf{v}(0)$  of an atom at a time  $t = 0$  and the velocity  $\mathbf{v}(t)$  of the same atom at a time  $t$  later

$$\langle \mathbf{v}(0) \cdot \mathbf{v}(t) \rangle = \frac{1}{N} \sum_{i=1}^N \mathbf{v}_i(0) \cdot \mathbf{v}_i(t) \quad (19)$$

where the brackets denote a statistical average over the  $N$  atoms forming the system. Once  $\langle \mathbf{v}(0) \cdot \mathbf{v}(t) \rangle$  has been determined using a molecular dynamics simulation under static equilibrium conditions, the self-diffusivity can be obtained readily as<sup>68</sup>

$$D_s = \frac{1}{d} \int_0^\infty \langle \mathbf{v}(0) \cdot \mathbf{v}(t) \rangle dt \quad (20)$$

where we recall that  $d$  is the dimensionality of the system. The latter expression reveals the equivalence between the self-diffusion coefficients obtained from the mean square displacement,  $D_s^{\text{MSD}} = \lim_{t \rightarrow \infty} \langle |\mathbf{r}(t) - \mathbf{r}(0)|^2 \rangle / 2dt$ , and from the velocity autocorrelation function,  $D_s^{\text{VACF}} = 1/d \times \int \langle \mathbf{v}(t) \cdot \mathbf{v}(0) \rangle dt$ , i.e.,  $D_s^{\text{MSD}} = D_s^{\text{VACF}} = D_s$ . Note that the computational cost of evaluating the correlation in eq 20 can be significantly reduced using the convolution theorem.<sup>69,70</sup> From a practical standpoint, the comparison between these two techniques constitutes an important consistency check to validate the robustness of a given molecular dynamics study. Figure 3 compares the self-diffusivity

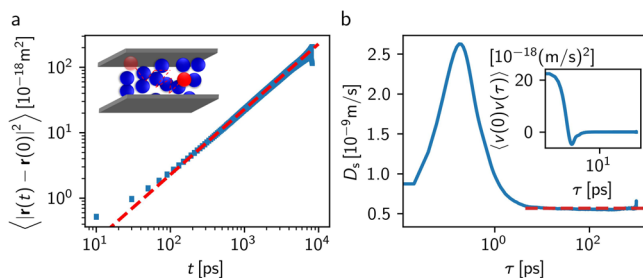


**Figure 3.** Self-diffusivity  $D_s$  of liquid  $N_2$  at  $T = 77$  K in a silica mesopore of width  $D_p = 2$  nm. (a) Mean square displacement (symbols) and fit according to eq 18. Note that the uncertainty increases with  $t$  as fewer initial positions  $\mathbf{r}(0)$  are averaged over. (b) Self-diffusivity obtained from the velocity autocorrelation according to eq 20 (solid line). Dashed line shows the fitting results from (a). The inset shows the velocity autocorrelation before integration. Note that for a slit pore, the dimensionality is  $d = 2$  and only the components parallel to the pore surface for displacement and velocity vectors are considered. Data shown are obtained from a total simulation time of 100 ns.

$D_s$  obtained using these two techniques for  $N_2$  at 77 K in mesoporous silica. As can be seen, provided long enough simulations are carried out, the two techniques give the same value within statistical accuracy.

**2.2.2.2. Collective Diffusivity  $D_0$ .** In the previous section, Fick's first law was derived from the isothermal/isobaric linear response law given in eq 12 by considering a very dilute system. As discussed earlier, this assumption is fully justified for a solute molecule dispersed in a liquid at very low concentration or for a tracer diffusion (since a tagged particle can indeed be considered as infinitely diluted in the liquid formed by all other molecules). However, in most general situations, this assumption breaks down and the general form given in eq 12 must be kept

$$J_N = -\frac{L'_{NN}}{k_B T} \nabla \mu \quad (21)$$

where we replaced  $L_{NN}$  by  $L'_{NN} = k_B L_{NN}$  in order to be consistent with the units of energy given in the following derivation. In the framework of the linear response theory, the transport coefficient  $L'_{NN}$  can be determined from the Green-Kubo formula involving the time correlation function of the fluid velocity.<sup>71</sup> In what follows, we present the standard derivation based on the linear response theory in which the Hamiltonian  $\mathcal{H}_0$  of the system at thermodynamic equilibrium is perturbed using a time-dependent perturbation  $\Delta\mathcal{H}(t)$ <sup>48,72</sup>

$$\mathcal{H} = \mathcal{H}_0 + \Delta\mathcal{H}(t) \quad (22)$$

with  $\Delta\mathcal{H}(t)$  taken to be a simple time-oscillating function:

$$\Delta\mathcal{H}(t) = -\mathcal{A}(\mathbf{r}^N) \mathcal{F}_0 \exp(-i\omega t) \quad (23)$$

$\omega$  is the frequency of the perturbation field while  $\mathcal{A}(\mathbf{r}^N)$  is the conjugated quantity of the perturbation field (the product of the field with its conjugated variable must be homogeneous to an energy). In practice, to derive a microscopic expression for  $L'_{NN}$ , we choose  $F_0 = -\nabla \mu_x$ , i.e., a homogeneous force field corresponding to a chemical potential gradient  $\nabla \mu_x$  along  $x$  which applies to all particles in the fluid. The corresponding conjugated variable then is  $\mathcal{A}(\mathbf{r}^N) = \sum_{i=1}^N x_i$ . In the linear response theory, the change  $\langle \Delta\mathcal{B} \rangle$  induced by the perturbation  $\Delta\mathcal{H}(t)$  in an observable  $\mathcal{B}$  is given by<sup>73</sup>

$$\langle \Delta\mathcal{B} \rangle = M_{BA}(\omega) \mathcal{F}_0 \exp(-i\omega t) \quad (24)$$

with

$$M_{BA}(\omega) = \frac{1}{k_B T} \int_0^\infty \left\langle \mathcal{B}(t) \dot{\mathcal{A}} \right\rangle \exp(i\omega t) dt \quad (25)$$

where  $\dot{\mathcal{A}} = d\mathcal{A}/dt$  is the time derivative of the observed quantity  $\mathcal{A}$ . On the one hand, the observed quantity is the molecule flux defined in eq 11:  $\langle \Delta\mathcal{B} \rangle = J_N = \rho \nu_x = 1/V \sum_{i=1}^N v_{x,i}$  ( $\rho$  is the fluid density of the  $N$  molecules while  $\nu_x$  and  $v_{x,i}$  are the average flow velocity and velocity of molecule  $i$  along  $x$ , respectively). On the other hand, we recall that  $\mathcal{A} = \sum_{i=1}^N x_i$  so that  $\dot{\mathcal{A}} = \sum_{i=1}^N v_{x,i}$ . With these definitions, eqs 24 and 25 lead to

$$M_{BA}(\omega) = \frac{1}{V k_B T} \int_0^\infty \left\langle \sum_{i,j} v_{x,i}(t) v_{x,j}(0) \right\rangle \exp(-i\omega t) dt \quad (26)$$

For an isotropic medium,  $\sum_{i,j} v_{x,i}(t) v_{x,j}(0) = 1/3 \sum_{i,j} \mathbf{v}_i(t) \cdot \mathbf{v}_j(0)$  which allows recasting eq 26 as

$$M_{BA}(\omega) = \frac{1}{3V k_B T} \int_0^\infty \left\langle \sum_{i,j} \mathbf{v}_i(t) \cdot \mathbf{v}_j(0) \right\rangle \exp(-i\omega t) dt \quad (27)$$

For an anisotropic medium, eq 26 has to be used but, in that case, transport coefficients  $L_{\alpha\beta}$  are also anisotropic and must be replaced by a vector  $L_{\alpha\beta}^k$  with  $k = x, y, z$ .

In conventional transport experiments, one is often interested in the static response to a stationary perturbation, i.e., a thermodynamic gradient, which is obtained by considering the limit  $\omega \rightarrow 0$  in eq 24, i.e.,  $J_N = -M_{BA}(0) \nabla \mu$  with

$$M_{BA}(0) = \frac{1}{3V k_B T} \int_0^\infty \left\langle \sum_{i,j} \mathbf{v}_i(t) \cdot \mathbf{v}_j(0) \right\rangle dt \quad (28)$$

Comparison between eq 21 and  $J_N = -M_{BA}(0) \nabla \mu$  leads to

$$L'_{NN} = k_B T M_{BA}(0) = \frac{1}{3V} \int_0^\infty \left\langle \sum_{i,j} \mathbf{v}_i(t) \cdot \mathbf{v}_j(0) \right\rangle dt \quad (29)$$

Note that these definitions and formalism are only applicable to a fluid that can exchange momentum with a reservoir—in our case the porous solid. If the total momentum was conserved,

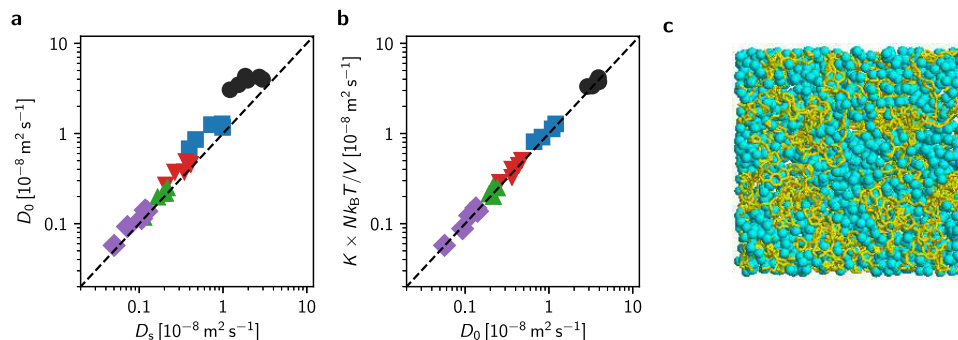


**Figure 4. Self/collective diffusivities and permeance.** (a) Collective diffusivity  $D_0$  as a function of the self-diffusivity  $D_s$  for different hydrocarbons confined at  $T = 450$  K in a disordered porous carbon with subnanometric pores. The black, blue, green, orange, and red circles are for methane, propane, hexane, nonane and dodecane, respectively. The dashed line indicates the bisector  $D_0 = D_s$ . (b) Equivalence between the permeance  $K$  and the collective diffusivity  $D_0 = KNk_B T/V$  for different hydrocarbons confined at  $T = 450$  K in a disordered porous carbon with subnanometric pores. The color code is the same as in (a). (c) Typical molecular configuration corresponding to the data shown in (a) and (b) with methane molecules diffusing in a disordered porous carbon. The cyan spheres are the methane molecules while the yellow segments are the chemical bonds between carbon atoms in the host porous material. Adapted with permission from ref 74. Copyright 2015 Macmillan Publishers Limited under Creative Commons Attribution 4.0 International License (<http://creativecommons.org/licenses/by/4.0/>).

$L'_{NN}$  would vanish identically in the frame of the center of mass—and in fact application of a force would lead to a constant acceleration, rather than a finite velocity and current.

Let us now introduce the collective—sometimes referred to as corrected—diffusivity,  $D_0$ :

$$D_0 = \frac{1}{3N} \int_0^\infty \left\langle \sum_{i,j} \mathbf{v}_i(t) \cdot \mathbf{v}_j(0) \right\rangle dt \quad (30)$$

Comparison between eqs 21, 28, and 29 leads to

$$J_N = -\frac{\rho D_0}{k_B T} \nabla \mu \quad (31)$$

with  $D_0 = L'_{NN}/\rho$ .

The microscopic expression given in eq 30 for the collective diffusivity  $D_0$  can be separated into velocity time correlations for the same molecule  $i = j$  and cross-correlations between different molecules  $i \neq j$

$$D_0 = \frac{1}{3N} \int_0^\infty \left\langle \sum_{i=1}^N \mathbf{v}_i(t) \cdot \mathbf{v}_i(0) \right\rangle dt + \frac{1}{3N} \int_0^\infty \left\langle \sum_{i=1}^N \sum_{j \neq i}^N \mathbf{v}_i(t) \cdot \mathbf{v}_j(0) \right\rangle dt \quad (32)$$

where the first term is identical to the microscopic expression for the self-diffusivity  $D_s$  given in eq 20. This important result shows that the collective diffusivity, which describes the fluid response to any chemical potential gradient applied to the system, is the sum of an individual response characterized by the self-diffusivity  $D_s$  and a collective contribution that arises from the direct collective interactions between fluid molecules. There is a number of situations where the velocities between different molecules are uncorrelated so that  $D_s \sim D_0$ . This includes very dilute systems for which velocity cross-correlations are negligible. Other situations include adsorbed fluids in the limit of very small adsorbed amounts or in ultraconfined environments where the velocity cross-correlations are negligible compared to the individual (i.e., self) velocity correlations induced by the interactions with the pore walls. As an illustration, Figure 4 (a) shows the self and collective diffusivities

for different alkanes (methane, propane, hexane, nonane and dodecane) confined in the porosity of a host porous carbon mimicking kerogen in gas shales.<sup>74</sup> For a given molecule type, while  $D_s \sim D_0$  at low densities,  $D_0 > D_s$  at larger densities as the velocity cross-correlations become non-negligible. The fact that  $D_0 > D_s$  indicates that collective molecular interactions, i.e., the fact that a given molecule motion creates a velocity field affecting its neighbors, make overall diffusion faster. Comparison between different fluid molecules in Figure 4(a) shows that differences between  $D_s$  and  $D_0$  are more pronounced upon decreasing the molecule size. This result can be explained by crowding effects; for a given cavity size, a larger number of small molecules can be confined compared to large molecules so that the role of velocity cross-correlations is more pronounced for small molecules.

Like eq 20 for the self-diffusivity  $D_s$ , the microscopic expression given in eq 30 for the collective diffusivity  $D_0$  belongs to the family of Green–Kubo relations which relate a transport coefficient to microscopic fluctuations.<sup>75</sup> The latter can serve as the basis of a theoretical model of transport based on the analysis of the fluctuations of microscopic variables. Such microscopic relations are particular cases of the general fluctuation dissipation theorem (FDT).<sup>46,60,76,77</sup> The latter considers the response of an observable (e.g., position) to a driving force at finite frequency. In particular, its imaginary part that describes the out-of-phase response and therefore dissipation relates to the power spectrum of the time correlations in a system at equilibrium. The physical significance of this theorem, sometimes described as Onsager’s regression principle, is that the fluctuations that exist in a system at equilibrium (without driving force) follow a dynamics that is identical to the time evolution of a perturbation induced by an external driving.

In the spirit of the connection between the Green–Kubo framework and Einstein formula for the self-diffusivity  $D_s$  discussed above,<sup>68</sup> a direct relationship can be established between the microscopic fluctuation-based formula given in eq 30 and the mean-square displacements of the fluid particles (more exactly, the mean square displacement of the center of mass of the fluid)

$$D_0 = \lim_{t \rightarrow \infty} \frac{1}{2Ndt} \left\langle \sum_{i,j} [\mathbf{r}_i(t) - \mathbf{r}_i(0)] \cdot [\mathbf{r}_j(t) - \mathbf{r}_j(0)] \right\rangle \quad (33)$$

where we recall that  $d$  is the dimensionality of the system. For the sake of brevity, the formal derivation of this equation will not be provided here as it follows very closely the step-by-step derivation provided for the self-diffusivity to arrive at eq 20.<sup>68</sup> As already mentioned, when considering a non isolated system (such as a system in equilibrium with a reservoir or a nanoconfined fluid in contact with a solid surface), momentum exchange between the system and its surrounding allows defining a collective diffusion coefficient from the position of the center of mass (mean squared displacements) or its velocity fluctuations (Green–Kubo formula). In contrast, for a perfectly isolated system (such as a bulk fluid), the total momentum conservation makes that the molecule current is zero at all times so that it is not possible to assess the collective diffusivity of the system. In that case, as exemplified in ref 78, it is possible to measure the collective diffusivity from the coherent scattering functions  $F_{\text{coh}}(q, t)$  taken for different nonzero wave vectors  $q$ . In practice, by taking the characteristic relaxation times  $\tau(q)$  as a function of  $q$ , one can estimate the collective diffusivity from  $\tau(q) \sim 1/[D_0(q)q^2]$  in the limit of  $q$  approaching zero. As another solution, it was recently proposed to use a “countoscope” in which one explores number/density fluctuations in real space using virtual boxes of variable size  $L$ .<sup>79</sup> Using this approach, one defines a scale-dependent transport coefficient whose limit in  $L \rightarrow \infty$  provides the macroscopic collective diffusion. In spirit, this “countoscope” technique is similar to deriving the collective diffusivity  $D_0(q)$  by taking the limit when  $q \sim 1/L \rightarrow 0$ .

The different expressions for  $D_s$  and  $D_0$  show that the latter is a collective property that depends on the total motion of all molecules while the former only depends on individual motions. This trivial statement has important practical implications when undertaking a molecular simulation study. Independently of the formalism used (i.e., Green–Kubo versus mean square displacement calculations), all molecule velocities contribute to calculating  $D_s$  therefore leading to improved statistics. In contrast,  $D_0$  is a collective property where all molecule motions are combined into a single quantity which results in much poorer statistics. Finally, for both  $D_s$  and  $D_0$ , the Green–Kubo or mean square displacement formulas allow one to evaluate their value from equilibrium molecular dynamics simulations, i.e., when no thermodynamic gradient is applied to induce transport. However, while this approach should always be successful in principle, long time tails are difficult to assess using typical molecular dynamics simulations and can thus lead to erroneous estimates for the different transport coefficients. As a result, nonequilibrium molecular dynamics simulations in the linear response limit, where transport is induced using an applied thermodynamic gradient, are sometimes preferred as they provide a direct measurement of the fluxes induced by a chemical potential, pressure and/or temperature gradient (see e.g. ref 80 for a comparison between equilibrium and nonequilibrium molecular dynamics applied to electrokinetic effects in nanopores).

As mentioned earlier, the collective diffusivity is formally linked to the so-called permeance or permeability through the fluctuation–dissipation theorem. Let us consider experiments on liquid transport where the fluid can be assumed to be incompressible such as water at room temperature. In that case, fluid transport is usually induced through a pressure drop which triggers a viscous flow described using Darcy equation.<sup>53</sup> In more detail, as will be shown below, the molecular flow  $J_N = \rho v$  induced by a pressure gradient  $\nabla P$  corresponds to a flow rate

(velocity)  $v = -k/\eta \nabla P = -K \nabla P$  where  $\eta$  is the fluid viscosity,  $k$  the permeability and  $K = k/\eta$  the permeance. Exact definitions for the permeability and permeance vary from a document to another in the literature. In the context of membranes and membrane processes, we note that IUPAC has established strict recommendations regarding the definitions of permeance, permeability, etc.<sup>81</sup> For an incompressible liquid, using the Gibbs–Duhem equation  $\rho d\mu = dP$ , we have  $J_N = \rho v = -K\rho^2 \nabla \mu$ . Comparison between this expression and eq 31 for the collective diffusivity leads to  $K = D_0/\rho k_B T$ . This is a very important result of the fluctuation–dissipation theorem which can be easily verified using molecular simulation for incompressible fluids if the fluid response  $v$  is linear in the driving force  $\nabla P$ , i.e., for properly chosen values  $\nabla P$ . Figure 4(b) compares the permeance  $K$  and collective diffusivity  $D_0$  for alkanes confined in the same nanoporous carbon as that considered in Figure 4(a). In agreement with the prediction of the fluctuation–dissipation theorem,  $K = D_0/\rho k_B T$  for all fluids and densities considered.<sup>74</sup>

**2.2.2.3. Transport Diffusivity  $D_T$ .** As introduced in Section 2.2, because the number of molecules  $N$  and the chemical potential  $\mu$  are conjugated variables, the direct driving force for molecular fluxes  $J_N$  is a chemical potential gradient  $\nabla \mu$ . This is also clear from eq 31, where the molecular flux  $J_N$  is expressed as a linear response to  $\nabla \mu$  with a transport coefficient directly proportional to the collective diffusivity  $D_0$ . Yet, in most practical experiments, transport is induced using a concentration, density or pressure gradient which raises the question of the comparison between the different transport coefficients.<sup>6,9,11</sup> While the concentration/density gradient  $\nabla \rho$  is not *stricto sensu* an affinity as defined in Onsager’s theory of transport, it is always possible to assume a linear response between a molecular flux  $J_N$  and  $\nabla \rho$ :

$$J_N = -D_T \nabla \rho \quad (34)$$

$D_T$  is the so-called transport diffusivity that can be measured using experiments where transport is induced by applying a concentration gradient across the sample. As discussed earlier, in many textbook notations, the number density  $\rho$  (in molecule per unit volume) is replaced by the concentration  $c$  as they are strictly equivalent (except for the fact that the concentration explicitly refers to mixtures). Comparison between eqs 31 and 34 provides a straightforward link between  $D_T$  and  $D_0$

$$D_T = \frac{\rho D_0}{k_B T} \left. \frac{\partial \mu}{\partial \rho} \right|_T \quad (35)$$

where  $\nabla \mu / \nabla \rho \sim \partial \mu / \partial \rho$  was used and “ $|_T$ ” recalls that the derivation only applies to a system at constant temperature  $T$ . For any fluid, the chemical potential  $\mu$  is related to the fugacity  $f$  which corresponds to the pressure that the fluid would have if it were an ideal gas (i.e.,  $f = P$  for an ideal gas):  $\mu = k_B T \ln(f \Lambda^3 / k_B T)$  where  $\Lambda$  is the de Broglie thermal wavelength. Using  $\partial \mu = k_B T \partial \ln f$  at constant temperature  $T$  and  $\partial \rho / \rho = \partial \ln \rho$ , eq 35 can be recast as

$$D_T = D_0 \left. \frac{\partial \ln f}{\partial \ln \rho} \right|_T \quad (36)$$

The term  $\partial \ln f / \partial \ln \rho |_T$  is known as the Darken or thermodynamic factor in the literature. Physically, it describes how a change in the local concentration converts into a chemical potential (recalling that, in the context of Onsager’s theory of

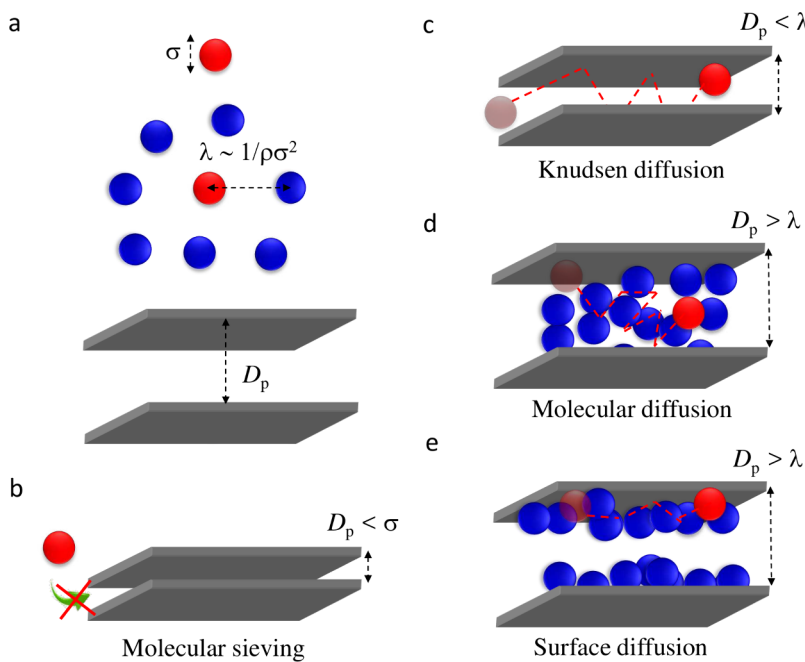


**Figure 5. Diffusion mechanisms in porous materials.** (a) Illustration of a fluid composed of molecules with a molecular size  $\sigma$ . The mean free path  $\lambda$  in the gas or liquid scales as  $1/\rho\sigma^2$  where  $\rho$  is the number density. (b) For very small pore sizes  $D_p \lesssim \sigma$ , molecular sieving is observed as only molecules smaller than the pore size can enter and diffuse through the porosity. (c) For  $D_p < \lambda$ , diffusion occurs through Knudsen diffusion which results from the fluid mean free path affected by collisions with the pore surface. (d) For  $D_p > \lambda$ , diffusion in the porosity is coined as molecular diffusion which resembles molecular diffusion in the bulk fluid. (e) For strong wall fluid interactions and pores large enough, the confined fluid forms an adsorbed film at the pore surface which coexists with the gas phase in the pore center. If the density difference between the adsorbed and gas phases is large, diffusion in the porosity predominantly occurs through surface diffusion within the adsorbed film.

transport, the chemical potential is the driving force for molecular diffusion). In the limit of small gas chemical potentials/densities, the gas fugacity is equal to the gas pressure and the density scales linearly with pressure, i.e.,  $\rho \sim P$ . This is known as Henry's law which introduces the Henry constant  $K_H$  as a proportionality factor, i.e.,  $\rho = K_H P$ —this relation is valid both for gas solubility in liquids and in porous solids (i.e., adsorption).<sup>82,83</sup> In such an asymptotic regime where  $\rho \rightarrow 0$ , the thermodynamic factor goes to  $\partial \ln \mu / \partial \ln \rho \rightarrow 1$ , which leads to  $D_T = D_0$ . Moreover, since  $D_s = D_0$  at very low fluid densities, we have  $D_T = D_0 = D_s$  in the Henry regime. In contrast, as the density increases,  $D_T \neq D_0 \neq D_s$ . Equation 36 is an important result as it shows that the effective transport diffusivity  $D_T$  can be easily determined by assessing independently the collective diffusivity  $D_0$  and the thermodynamic factor  $\partial \ln \mu / \partial \ln \rho$ . In practice, using molecular simulation tools, the former is usually determined from either at equilibrium or nonequilibrium molecular dynamics simulations while the latter can be evaluated using Monte Carlo simulation in the Grand Canonical ensemble to estimate the adsorption isotherm  $\rho(\mu)$ . In Section 3, simple yet representative examples will be provided to illustrate how  $D_T$  can be assessed using such a two-step strategy.

### 3. SELF-DIFFUSION AND TRACER DIFFUSION AT THE PORE SCALE

#### 3.1. Diffusion Mechanisms

Fluid transport in porous media occurs through diffusion and advection whenever a thermodynamic gradient such as a pressure or concentration gradient is applied to the system. Diffusion occurs both in systems at equilibrium, i.e., in the absence of any thermodynamic gradient, and in nonequilibrium situations, i.e., in the presence of a thermodynamic gradient. In

the latter case, an important question arises regarding the transport resulting from the combination of advection and diffusion in nanopores. In this section, in a first step, the different diffusion mechanisms that pertain to fluid transport in nanoporous media are presented with special attention to their dependence on pore size  $D_p$ , fluid molecule size  $\sigma$  and thermodynamic variables such as fluid density  $\rho$ , pressure  $P$ , temperature  $T$ , etc. Then, in a second step, combination rules which allow one to describe the transport resulting from different diffusion mechanisms are introduced. Advection mechanisms will be discussed in Sections 5 and 6 together with underlying theoretical models such as Poiseuille's flow and Darcy's law.

Let us consider a fluid made up of molecules having a molecular size  $\sigma$  which diffuses in a pore of size  $D_p$ . The fluid is taken at thermodynamic conditions  $T, P$  such that its density is  $\rho$  and the corresponding mean free path  $\lambda \sim 1/\rho\sigma^2$  as shown in Figure 5(a). The main diffusion mechanisms that can be encountered in a nanoporous material are presented in Figure 5(b)-(e) for increasing pore diameters  $D_p$ . In the following, we discuss diffusion in nanopores not as a function of the absolute pore size  $D_p$  but its ratio to the molecular size  $\sigma$  and mean free path  $\lambda$  (see also ref 84 for a discussion on the relation between fluid size, entropy, and diffusivity).

**3.1.1. Molecular Sieving.** For  $D_p < \sigma$ , molecular sieving is observed as the typical pore size is not large enough to accommodate any fluid molecule [Figure 5(b)]. Obviously, for this regime, no transport—either through diffusion or advection—can be observed. While molecular sieving for a pure fluid is trivial, separation processes in the case of mixtures can rely on such effects when fluid components with different molecular sizes are considered.

**3.1.2. Knudsen Diffusion.** **3.1.2.1. Principles.** Knudsen diffusion occurs in rarefied gases, i.e., for gases at very low pressures and, hence, very low densities.<sup>85</sup> In practice, in this regime, collisions between gas molecules can be neglected and molecular displacements can be assumed to occur only through collisions with the surface of the host nanoporous material [Figure 5(c)]. The dimensionless Knudsen number  $\text{Kn}$  is the quantity that characterizes the importance of Knudsen diffusion in transport mechanisms as a function of pore size  $D_p$  and fluid mean free path  $\lambda$ :

$$\text{Kn} = \frac{\lambda}{D_p} \quad (37)$$

The mean free path  $\lambda \sim 1/\rho\sigma^2$  follows from the pressure  $P$ , temperature  $T$  and molecular size  $\sigma$ :<sup>86</sup>

$$\lambda = \frac{k_B T}{\sqrt{2} P \pi \sigma^2} \quad (38)$$

$\sigma$  can be obtained from the covolume  $b$  in the van der Waals equation describing the gas, or using for example the Lennard-Jones parameter  $\sigma_{\text{LJ}}$  from typical force-fields when the gas molecule is treated as a single-sphere particle.  $\sigma$  can also be taken as the kinetic diameter estimated from bulk self-diffusivity/viscosity data using Stokes-Einstein relation. Equivalently, using the kinetic theory of gases to estimate the viscosity  $\eta = m/3\sqrt{2}\pi\sigma^2 \times \sqrt{8k_B T/\pi m}$ , eq 38 can be recast as

$$\lambda = \frac{3\eta}{2P} \sqrt{\frac{\pi k_B T}{2m}} \quad (39)$$

For  $\text{Kn} > 10$ , collisions between gas molecules and the surface of the host porous material prevail and molecular diffusion can be neglected. For  $\text{Kn} \ll 0.1$ , interactions between gas molecules prevail and Knudsen diffusion can be neglected. As will be discussed below, for values in the range  $0.1 < \text{Kn} < 10$ , the different mechanisms must be considered.

To derive the expression for the Knudsen diffusivity, we consider a cylindrical pore of diameter  $D_p$  and length  $L_p$ . This pore is set in contact with an ideal gas at pressure  $P$  and temperature  $T$  so that its density is  $\rho = P/k_B T$ . Let  $J_K$  be the flux, i.e., the number of molecules per unit of time and surface area that pass through the cylindrical pore. In the Knudsen regime,  $\text{Kn} \gg 1$ , this flux can be written as  $J_K = -\omega v_T \rho$ , where  $\omega$  is the probability that a molecule entering one pore cross section area crosses another pore cross section area and  $v_T = \sqrt{8k_B T/\pi m}$  is the mean thermal velocity (the latter expression is directly obtained from the Maxwell-Boltzmann distribution function) and  $\omega = D_p/3L_p$  for a cylindrical pore with  $D_p \ll L_p$ . On average, for a pore or a porous material in contact with the same gas density downstream and upstream, the total flow  $J_K$  passing through Knudsen diffusion is equal to 0 since there are as many molecules traveling in one direction than in the other. On the other hand, if a gas density gradient  $\Delta\rho$  is applied along the pore, the net flow is  $J_K = -\omega v_T \Delta\rho$ . This relationship allows one to estimate the Knudsen permeability  $\Pi_K$  and the Knudsen diffusivity  $D_K$  which are defined as  $J_K = -\Pi_K \Delta P = -D_K \nabla \rho$ . Invoking the ideal gas law,  $\Delta\rho = \Delta P/k_B T$  and  $\nabla \rho = \Delta\rho/L_p$ , one obtains  $\Pi_K = D_p/3L_p \times \sqrt{8/\pi m k_B T}$  and  $D_K = D_p/3 \times \sqrt{8k_B T/\pi m}$ . These expressions are valid for a cylindrical pore but they can be generalized to any porous material by introducing its porosity  $\Phi$  and tortuosity  $\tau$  to correct the

permeability and diffusivity.<sup>87</sup> This yields the corresponding quantities  $X_K = \Phi/\tau X_{K,0}$  where  $X_{K,0}$  is the permeability or diffusivity for a cylindrical pore having the same pore size  $D_p$ . This leads to the following general expressions:

$$\Pi_K = \frac{D_p \Phi}{3L_p \tau} \times \sqrt{\frac{8}{\pi m k_B T}} \quad (40)$$

$$D_K = \frac{D_p \Phi}{3\tau} \times \sqrt{\frac{8k_B T}{\pi m}} \quad (41)$$

In practice,  $\tau$  is often treated as a fitting parameter. It is interesting to note that the Knudsen diffusivity has a temperature dependence  $D_K \sim \sqrt{T}$  which drastically differs from the dependence for other regimes. This allows in principle to quantify the Knudsen contribution with respect to molecular diffusion since the latter is expected to follow an Arrhenius-type temperature dependence,  $D_s \sim \exp[-\Delta E/k_B T]$  (where  $\Delta E$  is the activation energy). Similarly, according to the kinetic theory of gases, the viscous gas flow—as will be seen below—follows a temperature dependence  $\sim 1/\eta$  where  $\eta \sim \sqrt{T}$  which differs from the temperature dependence expected for the Knudsen diffusivity. Finally, it can be noted that the Knudsen diffusivity is sensitive to the mass of the gas molecules diffusing within the porous material,  $D_K \sim \sqrt{m}$ .

**3.1.2.2. Corrections to the Knudsen Regime.** In the derivation above, we implicitly assumed that in the Knudsen regime molecules colliding with the surface of the porous solid undergo diffuse scattering. This corresponds to an important approximation as rigorously only a fraction  $f$  of the colliding molecules undergoes this mechanism while the complementary fraction  $1-f$  undergoes specular reflections (elastic collisions).  $f$  is known as the tangential momentum accommodation coefficient. In this context, diffuse scattering indicates that, upon colliding with the surface of the host porous medium, some molecules become adsorbed at the surface, get thermalized and are then released into the porous volume with a velocity that is independent of their initial velocity at the collision time. Equation 41 can be generalized to any value of  $f$ :

$$D_K = \frac{D_p \Phi}{3\tau} \times \frac{2-f}{f} \sqrt{\frac{8k_B T}{\pi m}} \quad (42)$$

Specular reflections of the fraction  $1-f$  of the molecules colliding with the surface lead to a surface slippage phenomenon, where the term  $(2-f)/f$  in eq 42 must be seen as a slippage coefficient. In Section 5, it will be shown that this correction is inversely proportional to the pressure of the gas. Due to this effect, the Knudsen permeability defined in eq 40 underestimates Knudsen permeabilities measured in experimental set-ups. Thus, the permeability must be corrected to obtain a permeability  $\Pi_K^*$  accounting for this slippage effect which adds up to the Knudsen permeability  $\Pi_K$ . This correction is known in the literature as the Klinkenberg effect<sup>88,89</sup>

$$\Pi_K^* = \Pi_K(1 + a/P) \quad (43)$$

where  $a$  is the correction term in pressure units. In practice, this correction is negligible for  $\text{Kn} < 0.1$ , very small for  $\text{Kn} \sim 1$  and important or even very important for  $\text{Kn} > 10$ .

**3.1.2.3. Molecular Simulation.** In spite of the abundant literature on Knudsen diffusion in porous media, only a few studies have examined the role of molecular parameters such as the size of the diffusing gas molecule or the strength of the

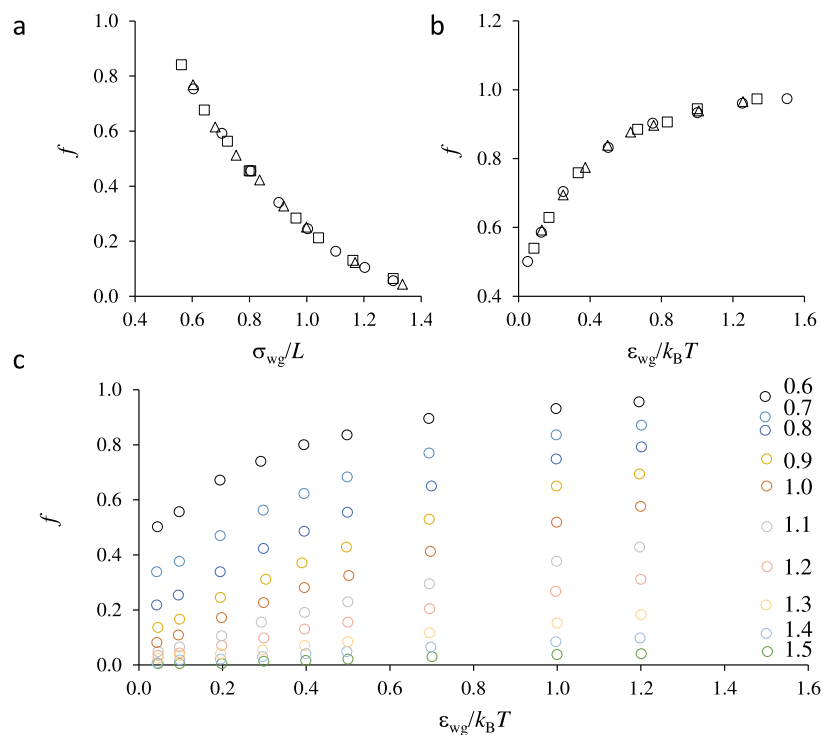


**Figure 6. Knudsen diffusion.** Effect of the different molecular parameters on the tangential momentum accommodation coefficient  $f$ . (a) Effect of the wall/gas interaction parameter  $\sigma_{wg}$  normalized to the characteristic distance  $L$  between substrate atoms. In this case, all calculations are taken at constant  $\epsilon_{wg}/k_B T = 100$  with  $T = 300$  K. The circles, squares and triangles correspond to  $L = 0.4$ ,  $0.5$ , and  $0.6$  nm, respectively. (b) Effect of the solid/fluid interaction  $\epsilon_{wg}$  normalized to the thermal energy  $k_B T$ . In this case, all calculations are for  $\sigma_{wg} = 0.24$  nm and  $L = 0.4$  nm. The circles, squares and triangles correspond to  $T = 200$ ,  $300$ , and  $400$  K, respectively. (c) Effect of the solid/fluid interaction  $\epsilon_{wg}$  normalized to the thermal energy  $k_B T$  for different ratios  $\sigma_{wg}/L$  indicated in the figure. Data adapted with permission from Arya et al.<sup>90</sup> Copyright 2003 Taylor & Francis.

molecular interactions between the gas and the solid surface. In this context, the molecular simulation work carried out by Maginn and co-workers is particularly relevant.<sup>90</sup> These authors have investigated the role of different parameters such as the temperature  $T$ , the size  $\sigma$  of the gas molecule and the solid/fluid molecular interaction energy  $\epsilon_{wg}$ . Let us consider a Lennard–Jones fluid whose parameters are  $\sigma_g$  and  $\epsilon_g$  (i.e., interaction parameters between fluid molecules). These parameters can be estimated for any gas. Indeed, the phase diagram of the Lennard–Jones fluid is universal; this means that for any pair of parameters  $\sigma_g$  and  $\epsilon_g$ , certain thermodynamic points such as the temperature of the triple point  $T_{tr}$ , the temperature of the critical point  $T_c$ , the pressure of the critical point  $P_c$ , the melting temperature  $T_m$  are uniquely defined. For example, the critical point of Lennard–Jones fluids in reduced units is given by  $T_c \sim 1.32\epsilon_g$ .<sup>91</sup> Other thermodynamic properties such as the critical point density  $\rho_c$  also take unique values when expressed in Lennard–Jones reduced units. For a given gas, the corresponding parameters  $\sigma_g$  and  $\epsilon_g$  can also be estimated from the second coefficient of the virial  $B(T)$ . These values as well as the parameters  $\sigma_g$  and  $\epsilon_g$  can be found in the book by Hirschfelder et al.<sup>92</sup>

The parameters describing the interactions within the solid phase  $\sigma_{ww}$  and  $\epsilon_{ww}$  can be defined in a similar way. Typical parameters are as follows:  $\epsilon_{ww}/k_B = 230$  K and  $\sigma_{ww} = 0.27$  nm for oxygen atoms in oxide materials and  $\epsilon_{ww}/k_B = 28$  K and  $\sigma_{ww} = 0.34$  nm for carbon atoms in carbonaceous materials. From these parameter sets, using the Lorentz–Berthelot combination rules,<sup>44,48</sup> we can estimate the cross-terms governing the solid/gas interactions,  $\sigma_{wg} = (\sigma_{ww} + \sigma_{gg})/2$  and  $\epsilon_{wg} = \sqrt{\epsilon_{ww}\epsilon_{gg}}$ .

In what follows, all quantities are normalized; energies are normalized to the thermal energy  $k_B T$ , while the different  $\sigma$  and lengths are normalized to the solid lattice parameter  $L$  ( $L \sim 0.25$  nm for graphite/carbon and  $L \sim 0.28$  nm for siliceous materials). The use of normalized data is very convenient because it allows one to extend the results of Maginn and co-workers to any gas/solid systems. These authors have studied for a large number of parameters  $T$ ,  $\sigma_{wg}$  and  $\epsilon_{wg}$  the values reached for  $f$  in the Knudsen regime (Figure 6). Figure 6(a) shows that, for a given interaction energy  $\epsilon_{wg}$ ,  $f$  does not depend on  $L$  when plotted as a function of  $\sigma_{wg}/L$ . Similarly, in Figure 6(b), for a ratio  $\sigma_{wg}/L$ , if  $f$  is plotted as a function of  $\epsilon_{wg}/k_B T$ , we obtain a master curve. The set of results obtained by means of molecular dynamics simulation are shown in Figure 6(c) where  $f$  is plotted as a function of  $\epsilon_{wg}/k_B T$  for different  $\sigma_{wg}/L$  ratios. Indeed, eq 42 suggests a diverging transport coefficient for  $f \rightarrow 0$ , i.e., in the limit of purely specular reflections. This unphysical behavior would correspond to perfectly smooth and athermal surfaces, which does not correspond to a real system (therefore a finite  $f$  should always be considered).

**3.1.3. Molecular Diffusion.** In contrast to Knudsen diffusion, which relies on a clear underlying mechanism (gas transport driven by a mean free path affected by collisions with the pore surface), there is no general prediction for molecular diffusion in nanopores ( $\lambda < D_p$ ) as it might correspond to different mechanisms. Yet, several robust theoretical predictions for the self-diffusivity in pores can be established, which remain valid in most physical situations encountered when dealing with diffusion in porous media. Self-diffusion can be discussed by introducing the random walk model where a molecule, the walker, jumps from a site to a random neighboring site on a

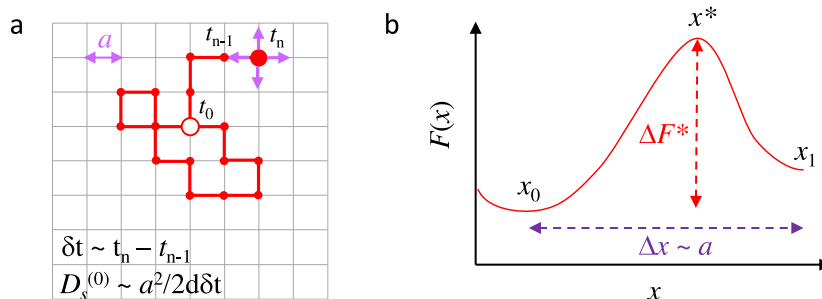


**Figure 7. Random walk and transition state theory.** (a) In the random walk model, the molecule moves by a quantity  $a$  in a random direction over a characteristic time  $\delta t$ . Starting from an initial position at  $t = t_0$ , the mean square displacement at a time  $t_n$ , i.e., after  $n$  time steps, is  $r^2(t) \sim 2dD_s^{(0)}n\delta t$  where  $D_s^{(0)}$  is the self-diffusivity and  $d$  the dimensionality of the system. (b) The random walk model assumes that there is no free energy barrier involved in the displacement from one site to another. In contrast, at the molecular scale, displacements are stochastic processes with an acceptance rate that depends on the free energy barrier  $\Delta F^*$  to move from a position  $x_0$  to a position  $x_1$ . In such cases, the hopping rate  $k \sim \exp(-\Delta F^*/k_B T)$  as described in detail in the text.

lattice within a time  $\delta t$  [Figure 7(a)]. This leads to an average mean-square displacement of the particle at a time  $t$  given by  $\langle r^2(t) \rangle \sim 2dD_s t$  where  $a$  is the lattice spacing and  $d$  is the dimensionality of the lattice (1D, 2D, etc.). Comparison between this expression and the mean-square displacement predicted using the Gaussian propagator expected in the Fickian regime leads to  $D_s^{(0)} = a^2/6\delta t = k_0 a^2/6$  where  $k_0 = 1/\delta t$  is the hopping rate on the lattice model. In practice,  $k_0 \sim v_0/a$  is related to the mean thermal velocity in one direction  $v_0 = \sqrt{2k_B T/\pi m}$  and the lattice parameter  $a$  (the latter is of the order of the intermolecular distance in the liquid).

In the derivation above, by relying on the random walk model, we implicitly assumed that there is no free energy barrier involved in the displacement from one site to another. This assumption holds in a coarse-grained picture when considering displacement over a supramolecular size (in which case, any free energy barrier is encompassed in the value of the self-diffusivity  $D_s$ ). However, at the molecular scale, it is clear that displacements from one site to another site are stochastic processes with an acceptance rate that depends on the local free energy barrier  $\Delta F^*$  (the sign \* is used to indicate that we refer to a free energy barrier and not a free energy difference between two stable states). When such free energy barriers exist, the hopping rate  $k$  is not simply  $k_0 = 1/\delta t$  but  $k \sim k_0 \exp(-\Delta F^*/k_B T)$ . If we assume that the free energy barrier  $\Delta F^*$  is temperature independent in the temperature range considered, the above ingredients lead to the following expression:

$$D_s = D_s^{(0)} \exp\left(-\frac{\Delta F^*}{k_B T}\right) \quad (44)$$

The latter equation, which has a characteristic temperature dependence  $\ln D_s \sim 1/T$ , is known as Arrhenius law.<sup>93,94</sup>

The transition state theory provides a more rigorous basis for eq 44.<sup>95,96</sup> Let us consider a molecule in a bulk or confined liquid where the typical free energy profile as a function of the molecule position is shown in Figure 7(b). The molecule, initially located at a position  $x_0$ , will move to an available site  $x_1$  by crossing the free energy barrier  $\Delta F^*$ . Typically, mapping this free energy approach to the random walk model shown in Figure 7(a) implies that  $a \sim x_1 - x_0$ . In the transition state theory, the rate  $k_{\text{TST}}$ , which is defined as the number of molecules located in  $x_0$  that cross the free energy barrier per unit of time, is given by the probability that a molecule is located at the free energy barrier

multiplied by the frequency at which it crosses the barrier. By virtue of the definition of the free energy profile  $F(x)$  in the region  $[0, x^*]$ , the probability  $p(x^*)dx$  to have a molecule located in a region  $dx$  at the free energy barrier  $\Delta F^*$  located in  $x^*$  is

$$\int_0^{x^*} \exp[-\beta\Delta F(x)]dx \quad (45)$$

where we used the reciprocal temperature  $\beta = 1/k_B T$ . The frequency with which a molecule crosses the barrier once reaching the top of the barrier can be defined as  $1/dt \sim v_0/dx$ , where the average velocity  $v_0$  of the molecule at the top of the barrier is taken equal to the mean thermal velocity  $v_0 = \sqrt{2k_B T/\pi m}$ . From these estimates, one predicts the rate  $k_{\text{TST}} \sim 1/2 p(x^*) dx/dt$  according to

$$k_{\text{TST}} = \sqrt{\frac{k_B T}{2\pi m}} \times \frac{\exp(-\beta\Delta F^*)}{\int_0^{x^*} \exp[-\beta\Delta F(x)]dx} \quad (46)$$

where the factor  $1/2$  accounts for the fact that only molecules going in the direction from  $x_0$  to  $x_1$  will cross the barrier (hence not those going in the direction from  $x_1$  to  $x_0$ ). In practice, the last expression overestimates the crossing rate as a non-negligible number of molecules recross the energy barrier in the other direction. In order to correct eq 46 for this effect, one needs to compute the transmission coefficient,  $\kappa \in [0, 1]$ , known as the Bennett–Chandler dynamic correction factor.<sup>97</sup> Such computations require to run independent molecular dynamics simulations in which molecules are initially positioned at the top of the energy barrier with a velocity selected randomly from a Maxwell–Boltzmann distribution at a temperature  $T$ . With these simulations,  $\kappa$  is readily obtained by counting the number of molecules that do cross the free energy barrier and the corrected transition state expression reads

$$k_{\text{TST}} = \kappa \sqrt{\frac{k_B T}{2\pi m}} \times \frac{\exp(-\beta\Delta F^*)}{\int_0^{x^*} \exp[-\beta\Delta F(x)]dx} \quad (47)$$

By using the latter expression for the hopping rate  $k_{\text{TST}}$ , we can establish a simple equation for the self-diffusivity as  $D_s = z_0 k_{\text{TST}} a^2 / 2d$  where  $z_0$  is the number of sites accessible by a single jump (e.g.,  $z_0 = 6$  for a cubic lattice). In practice,  $z_0 = 2d$  so that  $D_s = k_{\text{TST}} a^2$ .

**3.1.4. Surface Diffusion.** Let us come back to the situation described in the previous paragraph where intermediate adsorbed amounts  $\Gamma$  are considered (i.e., incomplete pore fillings). While surface diffusion within an adsorbed film is always possible, it often becomes very small or even negligible when strongly adsorbed molecules are considered. In fact, when the adsorption energy is just above or a few times the thermal energy  $k_B T$ , jump diffusion through the adsorbed film necessarily occurs. Let us consider an adsorbed layer coexisting with a gas phase having a very low density (this system is typically obtained at low temperatures where the gas density can be very low). In that case, diffusion only occurs through surface diffusion within the adsorbed film since diffusion in the gas phase is negligible—not because the gas diffusivity is low but because the very low fraction of molecules within the gas phase makes their contribution to overall diffusion very small or negligible. Another illustrative example of surface diffusion corresponds to transport in an adsorbed layer where the free energy landscape near the solid surface is smooth. In that case, the molecules can be strongly adsorbed because of a large binding energy but the absence of significant surface corrugation leads to significant diffusivity within the adsorbed film.

Provided that the temperature is low enough, the pore surface is covered with an adsorbed film while the pore center is filled by the gas. If the density ratio between the adsorbed and gas phases sufficiently differs from 1, molecular diffusion mostly occurs through diffusion within the surface phase (situations where self-diffusion occurs through a combination of diffusion within the surface and through the gas phase will be treated in Section 3.2). Such diffusion restricted to the adsorbed phase, which is referred to as surface diffusion in the literature, is illustrated in Figure 5(e). Like molecular diffusion in pores, the underlying mechanisms that lead to surface diffusion can be complex and of different nature. Yet, the Reed–Ehrlich model<sup>98</sup> described in the rest of this subsection provides a robust and simple theoretical framework to describe such surface diffusion. As discussed below, in its asymptotic limit of negligible lateral interactions between adsorbed molecules, this model leads to a very simple expression for the adsorbed amount dependence of the collective diffusivity  $D_0$  known as the surface diffusion model where  $D_0 \sim 1 - \theta$  ( $0 \leq \theta \leq 1$  is the site occupancy in the adsorbed phase).

As discussed in Section 2, upon fluid transport in a porous material with a flow  $J$ , the transport diffusivity  $D_T$  defined as  $J = -D_T \nabla c$  and the collective diffusivity  $D_0$  defined as  $J = -c D_0 / k_B T \times \nabla \mu$  are related through the so-called Darken or thermodynamic factor

$$D_T(\theta) = D_0(\theta) \frac{\partial(\mu/k_B T)}{\partial \ln c} \Big|_T \quad (48)$$

where  $c$  is the fluid concentration in the porous material. Formally, this equation is strictly equivalent to eq 36 since the fugacity is  $f = k_B T / \Lambda^3 \exp[\mu/k_B T]$ , where  $\Lambda$  is de Broglie's thermal wavelength. Let us describe the adsorbed phase as a 2D lattice gas where the occupancy  $\theta$  is defined from the number of adsorbed molecules  $N$  normalized to the number of available sites for adsorption  $N_0$ , i.e.,  $\theta = N/N_0$ . The jump rate  $k(\theta)$  at a given occupancy  $\theta$  defines the local diffusivity  $D_0(\theta) \sim k(\theta)a^2$  where  $a$  is the lattice parameter which scales with the molecular size of the fluid (more precisely, if  $c_s$  is the maximum density at the pore surface,  $a \sim c_s^{-1/2}$ ). Equation 48 allows one to write

$$D_T(\theta) = k(\theta)a^2 \frac{\partial(\mu/k_B T)}{\partial \ln \theta} \Big|_T \quad (49)$$

where we used that  $\partial \ln c = \partial \ln \theta$  since  $\theta = c/c_s$ .

The last equation shows that  $D_T$  is the product of the jump rate  $k(\theta)$  and the thermodynamic factor  $\partial(\mu/k_B T)/\partial \ln \theta$  which can be evaluated independently of each other. The jump rate  $k(\theta)$  is proportional to the probability  $P^{(z)}$  that  $z$  of the  $z_0$  neighboring sites of an adsorbed molecule are occupied by other molecules—typically, in a 2D square lattice,  $z_0 = 4$ —multiplied by the jump rate in such a configurational environment  $k^{(z)}$

$$k(\theta) = \sum_{z=0}^{z_0} \frac{z_0 - z}{z_0} \times P^{(z)} k^{(z)} \quad (50)$$

where the contribution  $(z_0 - z)/z_0$  simply accounts for the number of sites in which the molecule can jump. Assuming additive lateral interactions between the adsorbed molecules and its neighbors, i.e.,  $E \sim wz$  with  $w$  the interaction with a single neighbor,  $P(z)$  can be estimated in the quasi-chemical approximation—an extension of the Bragg–Williams approximation proposed by Fowler and Guggenheim<sup>99,100</sup>

$$P^{(z)} = \frac{z_0!}{z!(z_0 - z)!} \frac{(\eta\epsilon)^z}{(1 + \eta\epsilon)^{z_0}} \quad (51)$$

with  $\eta = \exp(-w/k_B T)$  and  $\epsilon = (\beta - 1 + 2\theta)/[2\theta(1 - \theta)]$  with  $\beta = [1 - 4\theta(1 - \theta)(1 - \eta)]^{1/2}$ . As for the jump rate  $k^{(z)}$ , Reed and Ehrlich assumed that it scales as a power law with an exponent corresponding to the number of nearest neighbors:  $k^{(z)} = k^{(0)}\eta^{-z}$ .<sup>98</sup> Gathering all these results into eq 50 leads to

$$k^{(z)} = k^{(0)} \frac{(1 + \epsilon)^{z_0 - 1}}{(1 + \eta\epsilon)^{z_0}} \quad (52)$$

In the quasi-chemical approximation, the chemical potential of the adsorbed phase reads

$$\mu = \mu_0 + k_B T \ln \left[ \frac{\theta}{1 - \theta} \right] + \frac{z_0}{2} k_B T \ln \left[ \frac{(\beta - 1 + 2\theta)(1 - \theta)}{(\beta + 1 - 2\theta)\theta} \right] \quad (53)$$

where the first, second, and third terms on the right-hand side correspond respectively to (1) the chemical potential at the bulk saturating vapor pressure where  $\theta \rightarrow 1$ , (2) the occupancy term for the lattice gas model in the absence of lateral interactions between adsorbed molecules and (3) a correction term that accounts for the lateral interactions between adsorbed molecules. By using eq 53 to derive the thermodynamic factor from eq 48, we obtain

$$\frac{\partial(\mu/k_B T)}{\partial \ln \theta} \Big|_T = \frac{1}{1 - \theta} \left[ 1 + \frac{z_0(1 - \beta)}{2\beta} \right] \quad (54)$$

By inserting eqs 52 and 54 into eq 49, we can establish a simple expression for the transport diffusivity:

$$D_T(\theta) = \frac{k(0)a^2(1 + \epsilon)^3}{(1 - \theta)(1 + \eta\epsilon)^4} \left[ 1 + \frac{2(1 - \beta)}{\beta} \right] \quad (55)$$

As an important remark, note that the model by Reed–Ehrlich in the limit of negligible adsorbate/adsorbate interactions ( $w \sim 0$ ) allows one to recover the well-known asymptotic limit of the Langmuir model. Briefly, for  $w \sim 0$ , we have  $\eta \sim 1$ ,  $\beta \sim 1$  and  $\epsilon \sim \theta/(1 - \theta)$  which leads to

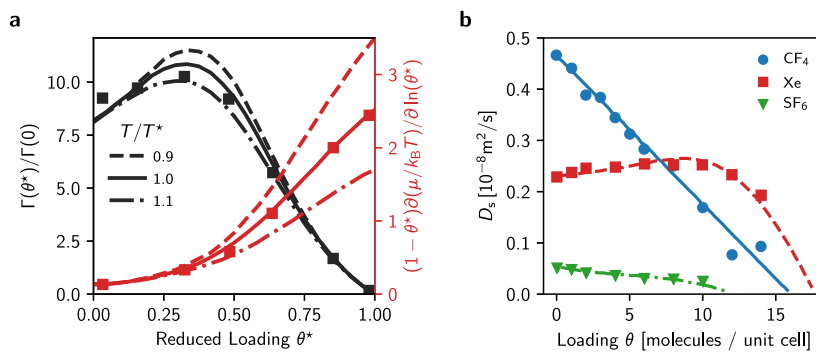


**Figure 8. Surface diffusion model.** (a) Effect of loading at different temperatures on the jump rate  $\Gamma(\theta)$  and the thermodynamic factor  $\partial(\mu/k_B T)/\partial \ln \theta_T$  as derived within the quasi-chemical approximation for repulsive interactions ( $w = k_B T^* > 0$ ). Note that the jump rate is normalized to  $\Gamma(0)$ , i.e., the jump rate in the zero loading limit, and the thermodynamic factor is multiplied by  $(1 - \theta^*)$  for clarity. The lines are the predictions of the theoretical model while the symbols are the results from Monte Carlo simulations for  $T = T^*$ . Adapted with permission from ref 98. Copyright 1982 North-Holland Publishing Company. (b) Effect of loading  $\theta$  on the diffusivity of  $\text{CF}_4$ ,  $\text{Xe}$ , and  $\text{SF}_6$  in silicalite zeolite (MFI). The lines are the results from the surface diffusion model by Reed and Ehrlich. The open symbols are Molecular Dynamics simulation data from Skouidas and Sholl<sup>103,104</sup> and Chempath et al.<sup>105</sup> Adapted with permission from ref 106. Copyright 2004 Elsevier Inc.

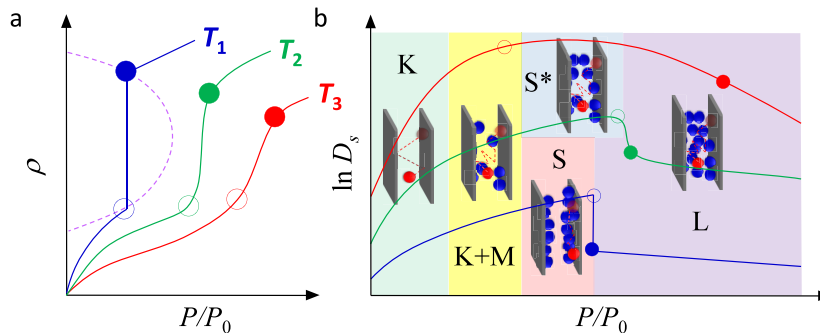


**Figure 9. Diffusion at the pore scale.** (a) Typical adsorption isotherms for a fluid in a single nanopore of a size  $D_p$  at different temperatures  $T_1 < T_2 < T_3$ . The y-axis shows the fluid density  $\rho$  as a function of the reduced gas pressure  $P/P_0$  shown in the x-axis (where  $P_0$  is the saturating vapor pressure for fluids below their critical point  $T_c$  and its extrapolated value for  $T > T_c$ ). At low temperature, the fluid is below its capillary critical point  $T_1 < T_{cc}(D_p)$  and pore filling proceeds through the formation of an adsorbed film coexisting with the bulk gas phase in the pore center followed by discontinuous capillary condensation at a pressure  $P < P_0$ .<sup>34</sup> At higher temperatures  $T_3 > T_2 > T_{cc}$ , the fluid is in a pseudocritical state and capillary condensation is replaced by a continuous and reversible pore filling.<sup>117</sup> (b) Typical self-diffusivities for a fluid in a single nanopore of a size  $D_p$  at different temperatures  $T_1 < T_2 < T_3$  as a function of the fluid pressure  $P/P_0$ . Independently of temperature, the diffusivity first increases upon increasing the pressure (and therefore the confined fluid density) as fluid molecules first occupy strongly adsorbing sites (large negative adsorption energies) before filling weaker adsorbing sites (less negative adsorption energies). In all cases, in the very low density/pressure range, molecules first obey the Knudsen diffusion regime (K) before entering a hybrid regime combining Knudsen and molecular diffusion (K + M). Upon further increasing the pressure or confined fluid density, surface diffusion (S) is observed with two possible scenarios depending on the density difference  $\Delta\rho = \rho_s - \rho_b$  between the adsorbed fluid phase at the pore surface and the bulk-like fluid phase in the pore center. At high temperature,  $|\Delta\rho| \sim \rho_s$  so that significant exchange is observed between these two phases (S\*). At low temperature,  $|\Delta\rho| \sim \rho_b$  so that exchange between the two phases is limited (S). Upon further increasing the pressure the pore gets filled with a single liquid phase (L).

$$\mu = \mu_0 + k_B T \ln \left[ \frac{\theta}{1 - \theta} \right] \quad (56)$$

and

$$D_T(\theta) = k(0)a^2 \text{ and } D_0(\theta) = k(0)a^2(1 - \theta) \quad (57)$$

as expected in the Langmuir regime. In particular, by using the chemical potential/pressure for an ideal gas,  $\mu \sim k_B T \ln P$ , eq 56 can be recast into the Langmuir adsorption isotherm:  $\theta = \alpha P/(1 + \alpha P)$  where  $\alpha$  is an affinity parameter that depends on the fluid/solid interaction strength.<sup>101</sup>

In their seminal paper,<sup>98</sup> Reed and Ehrlich discussed the effect of surface coverage  $\theta$  on the jump rate  $k(\theta)$  as well as on the thermodynamic factor  $\partial(\mu/k_B T)/\partial \ln \theta_T$ . In more detail, these authors showed that the predictions of their model based on the quasi-chemical approximation are in good agreement with results from Monte Carlo simulations (Figure 8). Upon

considering repulsive lateral interactions between adsorbed molecules,  $w = k_B T^* > 0$ , the jump rate was found to be strongly affected by the loading  $\theta$  with important deviations observed with respect to the prediction for the Langmuir regime. It was also recently shown that upon increasing the coverage  $\theta$  there is a continuous transition to classical hydrodynamics for adsorbed water films.<sup>102</sup>

### 3.2. Diffusion in Nanopores

In Section 3.1, the different diffusion mechanisms that can occur in a pore have been discussed and identified as a function of simple parameters—namely, the pore size  $D_p$ , fluid molecule size  $\sigma$ , and mean free path  $\lambda$ . Despite the rather exhaustive description given of these phenomena, the emerging picture often remains insufficient to describe transport in a nanoporous medium. Even when a single pore of a simple geometry is considered, the description provided in the previous section is

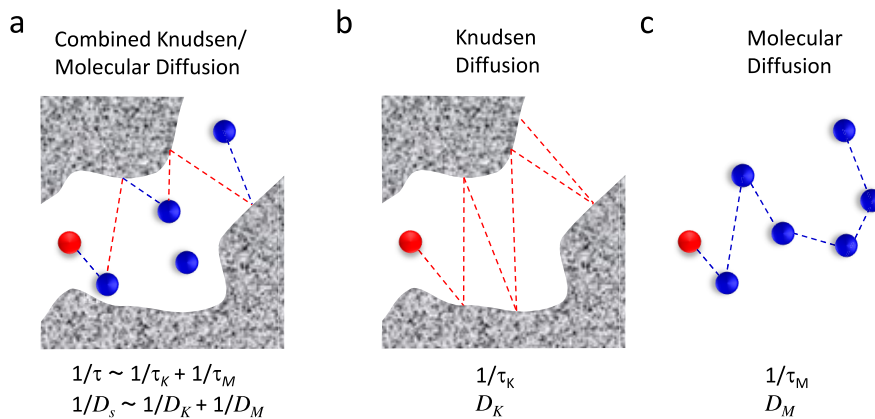


**Figure 10. Combined Knudsen/molecular diffusion.** (a) Schematic illustration of the diffusion of a tagged molecule (red sphere) in a porous material delimited by pore walls represented as gray areas. In the combined Knudsen/molecular diffusion regimes, the tagged molecule undergoes collisions with both the pore surface (dashed red segments) and with other fluid molecules (dashed blue segments with other fluid molecules shown as blue spheres). This transition regime between the Knudsen and molecular diffusion regimes can be described using an effective model where the two mechanisms—Knudsen diffusion as shown in (b) and molecular diffusion as shown in (c)—are assumed to be independent of each other.

incomplete for the two following reasons. First, except in well-defined asymptotic regimes (vanishing confined fluid density, incompressible confined liquid, etc.), the physical diffusion mechanism in a given pore can show a non trivial dependence on fluid pressure and/or density. As will be discussed below, even though some hints at the effect of pore loading on diffusivity have been already provided in Section 3.1, the theoretical description of such density and/or pressure dependence often varies from one example to another. Second, even for a single pore, in most situations, diffusion arises from a combination of different mechanisms rather than a single mechanism. Such intrinsic complexity raises the question of the formalism required to describe such combined mechanisms and, more practically, of the existence of simple combining rules. In what follows, these different points are examined in detail. In particular, we will see under what specific conditions the usual approximations consisting of assuming that Knudsen and molecular diffusions occur in series while surface diffusion occurs in parallel are valid.

Figure 9 shows the self-diffusivity  $D_s$  as a function of fluid pressure  $P$  at different temperatures for a simple fluid confined in a slit pore of a width  $D_p$  of about a few  $\sigma$ . At all temperatures, the self-diffusivity shows a nonmonotonic behavior with  $D_s$  that first increases with pressure  $P$  and then decreases upon further increasing  $P$ . At low temperature, i.e., below the so-called critical capillary temperature  $T_{cc}$ ,<sup>107–115</sup> the self-diffusivity exhibits a marked discontinuous change in  $D_s$  as capillary condensation occurs. In contrast, at higher temperature, i.e., above  $T_{cc}$ , the self-diffusivity decreases in a continuous and reversible fashion as pore filling becomes also continuous and reversible (for a detailed discussion on the effect of confinement on the fluid critical temperature and the so-called critical capillary temperature, the reader is invited to read refs 34 and 116). There is a number of physical situations encountered in the self-diffusivity data shown in Figure 9 that were already examined in the previous section: namely, the Knudsen regime, the surface diffusion regime and the molecular diffusion regime. In contrast, intermediate regimes obtained for fluid densities or pressures where these different regimes coexist remain to be addressed. Such transition regimes, which are discussed in the rest of this section, include the combination of Knudsen and molecular diffusion through the pore center, the combination of surface

diffusion and molecular diffusion through the pore center but also the change in the molecular diffusion upon increasing the fluid density within the pore.

**3.2.1. Combined Knudsen/Molecular Diffusion.** In the limit of very low confined fluid density, the diffusion of gases within a porous material occurs through Knudsen diffusion characterized by a Knudsen diffusivity  $D_K$  and a corresponding permeance  $\Pi_K$  given in eqs 40 and 41 in Section 3.1. However, in practice, even for very low densities, depending on temperature, diffusion in a porous material can show non negligible departures from such equations because diffusion through collisions between fluid molecules cannot be completely ignored. Such molecular diffusion needs to be accounted for to derive a simple expression for the effective self-diffusivity arising from the combination of Knudsen and molecular diffusion. This problem is analogous to the treatment of electron diffusion in solids which occurs through the combination of two different diffusion mechanisms:<sup>119,120</sup> (1) diffusion through interactions with lattice vibrations, i.e., phonons, and (2) diffusion through collisions with impurities. Such a derivation leads to the so-called Matthiessen's rule which is useful to describe electrical conductivity and resistivity in real metals and semiconductors. In what follows, the Matthiessen's rule in the context of diffusion of fluid molecules in the combined Knudsen/molecular diffusion regime is derived.

Let us consider an ensemble of  $N(0)$  fluid molecules diffusing in a porous material at a density such that the mean free path is  $\lambda$ . The number of molecules that have not undergone a collision with another molecule or with the pore surface at a time  $t$  is  $N(t)$ . Let us now define the characteristic time  $\tau_M$  such that  $dt/\tau_M$  is the probability that a particle undergoes a collision with another fluid molecule over the time  $dt$ . Similarly, we define the characteristic time  $\tau_K$  such that  $dt/\tau_K$  is the probability that a particle undergoes a collision with the pore surface over the time  $dt$ . These definitions imply that the number of molecules  $N(t+dt)$  that have not undergone a collision at a time  $t+dt$  is given by

$$N(t+dt) = N(t) - N(t) \frac{dt}{\tau_M} - N(t) \frac{dt}{\tau_K} = N(t)[1 - dt/\tau] \quad (58)$$

where we have introduced  $1/\tau = 1/\tau_K + 1/\tau_M$ . Note that the additivity of the different processes (collisions with the wall or

with another fluid molecule) is equivalent to assuming that they are independent of each other while diffusion in real porous media might show departure from this simple condition. Upon integrating the latter equation, one arrives at the distribution  $N(t) = N(0) \exp(-t/\tau)$ . Let us now consider the 3D average velocity autocorrelation function  $C_{vv}(t) = \langle \mathbf{v}(0) \cdot \mathbf{v}(t) \rangle$  for the  $N(t)$  molecules that have not undergone a collision at a time  $t$  (where  $\langle \mathbf{v}(0) \cdot \mathbf{v}(t) \rangle = 1/N \times \sum_{i=1}^{N(t)} \langle \mathbf{v}_i(0) \cdot \mathbf{v}_i(t) \rangle$  is averaged over each fluid molecule  $i = \{1, N(t)\}$ ). In the spirit of eq 58, at time  $t + dt$ , the average velocity autocorrelation function is given by

$$C_{vv}(t + dt) = C_{vv}(t)[1 - dt/\tau] \quad (59)$$

which leads to  $C_{vv}(t) = v_T^2 \exp(-t/\tau)$  (where  $v_T$  is the average constant velocity of the fluid). This expression relies on the assumption that the contribution  $C_{vv}(t)$  from molecules colliding between  $t$  and  $t + dt$  averages to zero (uncorrelated velocities before and after collision). The self-diffusivity  $D_s$  is then readily obtained from the Green–Kubo expression based on the velocity time autocorrelation function  $C_{vv}(t)$  of the fluid molecules:

$$D_s = \frac{1}{3} \int_0^\infty \langle \mathbf{v}(0) \cdot \mathbf{v}(t) \rangle dt = \frac{1}{3} \int_0^\infty C_{vv}(t) dt = v_T^2 \tau / 3 \quad (60)$$

With such an effective approach, the reciprocal of the characteristic diffusion time,  $1/\tau$ , is the sum of the inverse of the two characteristic times, i.e.,  $1/\tau \sim 1/\tau_K + 1/\tau_M$ . This result, known as Matthiessen's rule, and the underlying derivation above show that the self-diffusivity for a confined fluid under thermodynamic conditions of combined Knudsen/molecular diffusion regime should display an effective diffusivity  $D_s$  such that  $1/D_s = 1/D_K + 1/D_M$  where  $D_K$  is the Knudsen diffusivity and  $D_s$  is the molecular diffusion (defined in conditions where only one mechanism, i.e., Knudsen versus molecular diffusion, pertains, cf. Figure 10). It is important to keep in mind that the derivation above relies on the assumption that the two mechanisms are independent of each other (while, in practice, the probability for a given fluid molecule of colliding with the pore surface or with another fluid molecule can be linked as conditional properties).

**3.2.2. Surface versus Volume Diffusion.** Knudsen diffusion and combined Knudsen/molecular diffusion are limited to very low gas densities where gas collisions with the pore surface are dominant (mean free path  $\lambda$  larger or comparable with the pore size  $D_p$ ). However, in most practical situations, the gas density is such that this limit is not relevant as the porosity gets filled with a gas or liquid phase whose mean free path  $\lambda$  is smaller than the pore size  $D_p$ . In this case, as depicted in Figure 9, there are typically two situations that can be encountered. Depending on the gas pressure/temperature, either the pore is completely filled with the liquid/fluid phase or the pore surface is covered by an adsorbed phase having a density close to that of the liquid phase while the pore center is occupied by a gas phase having a much lower density. In both cases, the dynamics of the confined fluid is heterogeneous with strong differences between diffusion of the molecules at the pore surface and molecules in the pore center. This raises the question of the ratio of the surface and volume diffusion contributions and how they should be combined to predict the overall (effective) diffusivity.

Like in a homogeneous medium, the heterogeneous dynamics in a pore either completely or partially filled with a fluid phase is described through the self-correlation function  $G_s(\mathbf{r}, t)$ . This function corresponds to the probability that a molecule moves of a distance  $\mathbf{r}$  over a time  $t$

$$G_s(\mathbf{r}, t) = \langle \delta(\mathbf{R}(t) - \mathbf{R}(0) - \mathbf{r}(t)) \rangle \quad (61)$$

where  $\mathbf{R}(t)$  and  $\mathbf{R}(0)$  are the molecule position at times  $t$  and 0, respectively. The symbols  $\langle \dots \rangle$  denote average over all molecules and times.  $G_s(r, t)$  is related to the mean propagator which was introduced in Section 2 when discussing the solution of the diffusion equation (Fick's second law). In the Fickian regime, the propagator is a Gaussian function as given in eq 17. At this stage, it is convenient to introduce the spatial Fourier transform  $I_s(\mathbf{q}, t)$  of the self-correlation function  $G_s(\mathbf{r}, t)$ ,  $I_s(\mathbf{q}, t) = \int G_s(\mathbf{r}, t) e^{i\mathbf{q} \cdot \mathbf{r}} d\mathbf{r}$ . The functions  $G_s(\mathbf{r}, t)$  and  $I_s(\mathbf{q}, t)$ , which can be probed experimentally through techniques such as PFG-NMR or neutron scattering experiments, contain all the information on the self-diffusion dynamics. However, in general, for a heterogeneous medium such as a fluid diffusing in a nanoporous material, these functions are complex to interpret as they include the detailed dynamics such as the crossing dynamics between different domains for which there is no simple general model.<sup>67</sup> In particular, as discussed in more detail in Section 4 on diffusion at the porous network scale, these functions include the effects of possible surface barriers at the border between different domain types. Even at the pore scale, such crossing dynamics between the adsorbed phase and the fluid phase manifests itself in the functions  $G_s(\mathbf{r}, t)$  and  $I_s(\mathbf{q}, t)$  in a fashion that is difficult to capture and is system-dependent. However, there are two asymptotic limits that can be considered for heterogeneous systems depending on the ratio of the diffusion times within each domain type and the crossing time between different domains. Typically, for diffusion at the pore scale, one has to consider two domains  $\alpha = [1, 2]$ : (1) the region in the vicinity of the pore surface where the molecules experience the interaction potential generated by the host porous solid and (2) the pore center where the molecules behave in a bulk-like fashion as they do not feel the interaction potential generated by the host porous solid. On the one hand, for a typical displacement on a distance  $r \sim 2\pi/q$ , the diffusion time is  $\tau_D^\alpha \sim (D_s^\alpha q^2)^{-1}$  where  $D_s^\alpha$  is the self-diffusion coefficient for molecules located in domains  $\alpha$ . On the other hand, the typical crossing time  $\tau_C^\alpha$  can be estimated as the mean first-passage time which corresponds to the time for a molecule in a domain  $\alpha$  to reach the boundary domain. In the limit  $\tau_C^\alpha \gg \tau_D^\alpha \forall \alpha$ , known as the slow-switching regime, molecule exchange between the different domains is limited and the correlation function  $I_s(\mathbf{q}, t)$  is dominated by diffusion in each of the domains. In this slow-switching limit, the correlation function  $I_s(\mathbf{q}, t)$  is given by the sum of all intradomain diffusion contributions  $D_s^\alpha$  pondered by the average fraction  $x^\alpha$  of molecules in these domains

$$I_s(\mathbf{q}, t) = \sum_\alpha x_\alpha \exp(-D_s^\alpha q^2 t) \quad (62)$$

where  $q = |\mathbf{q}|$ . In contrast, in the limit  $\tau_C^\alpha \ll \tau_D^\alpha \forall \alpha$ , known as the fast-switching regime, molecule exchange between the different domains is significant over the typical time scale needed to diffuse through the different domains. In other words, in this limit, for displacements over a length scale  $r \sim 2\pi/q$ , each molecule explores the different domains so that the observed diffusivity is an effective diffusivity that reflects the diffusivities in

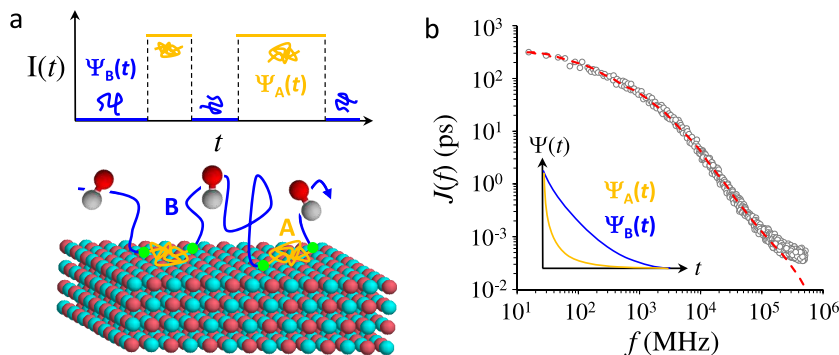


**Figure 11. Intermittent Brownian Motion.** (a) Principle of the Intermittent Brownian Motion formalism applied to fluid adsorption and diffusion in a porous material. Each molecule trajectory subdivides into segments during which the molecule diffuses at the pore surface—orange subtrajectories—and segments during which the molecule is relocated/diffuses through the bulk part of the porosity—blue subtrajectories. Each type of segments is characterized by a time distribution  $\Psi_\alpha(t)$  with  $\alpha = A, B$  which is related to the mean first passage time within each domain. For a given molecule, the function  $I(t)$  is defined as  $I(t) \neq 0$  if the molecule is adsorbed at the surface and  $I(t) = 0$  when it relocates through the nonadsorbed fluid phase in the pore center. (b) From the statistical distributions,  $\Psi_\alpha(t)$  ( $\alpha = A, B$ ), the spectral density  $J(f)$  of the function  $I(t)$  can be predicted. The example shown here corresponds to the specific situation of water adsorbed in a hydrophilic silica slit pore of width  $D_p$ . The symbols are data obtained using molecular dynamics simulations while the line is the prediction from the Intermittent Brownian Motion formalism (note that the statistical distributions shown in the inset are schematic examples). Data adapted with permission from ref 123. Copyright 2013 Royal Society of Chemistry.

all the different domains. In this fast-switching limit, the correlation function  $I_s(\mathbf{q}, t)$  is given by a single contribution with a characteristic diffusion coefficient  $\overline{D}_s$ :

$$I_s(\mathbf{q}, t) = \exp\left(-\sum_\alpha x_\alpha D_s^\alpha q^2 t\right) = \exp(-\overline{D}_s q^2 t) \quad (63)$$

The two asymptotic situations considered above are limiting cases which can show strong departure with experimental measurements. Before addressing in more detail this problem using the formalism of Intermittent Brownian Motion, it is instructive to consider the following reasoning which illustrates the breakdown of the fast and slow switching limits. Let us consider the average displacement  $\langle \Delta r^2(\tau) \rangle$  of molecules in a single pore over a typical time  $\tau$ . As introduced above, the fluid molecules will diffuse through two domains  $\alpha = [1, 2]$  (vicinity of the pore surface and pore center) as depicted in Figure 11(a). Each molecule trajectory  $\mathbf{r}(\tau) - \mathbf{r}(0)$  from its initial position at time  $t = 0$  to its position at time  $\tau$  can be split into the different displacements  $\Delta \mathbf{r}_\alpha^k$  which correspond to the  $k^{\text{th}}$  trajectory segment in the domain  $\alpha$ . With such notations, the mean square displacement over a time  $\tau$  reads

$$\Delta r^2(\tau) = \langle (\mathbf{r}(\tau) - \mathbf{r}(0))^2 \rangle = \left\langle \left( \sum_{\alpha=1}^M \sum_k \Delta \mathbf{r}_\alpha^k \right)^2 \right\rangle \quad (64)$$

where  $M = 2$  is the number of domain types (adsorbed region and pore center). It can reasonably be assumed that displacements in the same domain type  $\alpha$  are uncorrelated, i.e.,  $\langle \Delta \mathbf{r}_\alpha^k \Delta \mathbf{r}_\alpha^{k'} \rangle = 0$  when  $k \neq k'$  (because these two trajectory segments are separated by a trajectory segment in the other domain type  $\alpha' \neq \alpha$ ). Similarly, when considering trajectory segments in different domains  $\alpha' \neq \alpha$ , it can be assumed that only two consecutive segments are correlated so that  $\langle \Delta \mathbf{r}_\alpha^k \Delta \mathbf{r}_{\alpha'}^{k'} \rangle = 0$  when  $k \neq k'$ . With these assumptions, the mean square displacement in eq 64 can be rewritten as

$$\Delta r^2(\tau) \approx \sum_{\alpha=1}^M \sum_k \langle (\Delta \mathbf{r}_\alpha^k)^2 \rangle + \sum_{\alpha, \alpha'=1}^M \sum_{k \neq k'} \langle \Delta \mathbf{r}_\alpha^k \Delta \mathbf{r}_{\alpha'}^{k'} \rangle \quad (65)$$

Assuming each trajectory segment  $\Delta \mathbf{r}_\alpha^k$  obeys Fickian diffusion, it can be written that  $\sum_k (\Delta \mathbf{r}_\alpha^k)^2 \sim 6 D_s^\alpha \tau_\alpha$  where  $D_s^\alpha$  is the self-diffusion coefficient of the fluid molecules in domain  $\alpha$  while  $\tau_\alpha$  is the time spent by the molecules in domains  $\alpha$  in the course of the trajectory of a duration  $\tau$ . Equation 65 can be used to estimate the effective diffusivity  $\overline{D}_s$  defined as  $\overline{D}_s = \Delta r^2(\tau)/6\tau$ :

$$\begin{aligned} \overline{D}_s &= \sum_{\alpha=1}^M \frac{\tau_\alpha D^\alpha}{\tau} + \frac{1}{6\tau} \langle \Delta \mathbf{r}_\alpha^k \Delta \mathbf{r}_{\alpha'}^{k'} \rangle \\ &= \sum_{\alpha=1}^M x_\alpha D^\alpha + \frac{1}{6\tau} \langle \Delta \mathbf{r}_\alpha^k \Delta \mathbf{r}_{\alpha'}^{k'} \rangle \end{aligned} \quad (66)$$

The principle of ergodicity—which implies that the average time fraction spent by a molecule in domains  $\alpha$ ,  $\tau_\alpha/\tau$ , is equal to the fraction of molecules located in these domains,  $x_\alpha$ —was used to obtain the second equality. Upon further assuming that consecutive trajectory segments are uncorrelated,  $\langle \Delta \mathbf{r}_\alpha^k \Delta \mathbf{r}_{\alpha'}^{k'} \rangle = 0$ , we arrive at the simple combination rule for the effective diffusivity:  $\overline{D}_s = \sum_\alpha x_\alpha D_s^\alpha$ . The latter condition is known as the fast-exchange model where, independently of the geometrical distribution of domains in the porous solid, the effective diffusivity is given by a combination rule where the domains are assumed to be visited in parallel. In the case of partially filled pores, the conditions under which the fast-exchange model is expected to be valid was discussed by Kaerger, Valiullin, and co-workers.<sup>21,121</sup> In practice, this approximated expression should be considered with caution as eq 66 shows that correlations between two consecutive trajectory segments in different domains  $\alpha \neq \alpha'$  strongly affect the effective diffusivity in heterogeneous media. In particular, when significant recrossing between domains is expected, cross correlations  $\langle \Delta \mathbf{r}_\alpha^k \Delta \mathbf{r}_{\alpha'}^{k'} \rangle$  are expected to be negative on average so

that they should significantly decrease the effective diffusivity  $\overline{D}_s$ . Moreover, as will be established in [Section 4](#) on diffusion at the porous network scale, from simple arguments based on the analogy with electrical transport in resistance networks, intermittent adsorption/relocation should be considered as a model of domains visited in series so that the effective diffusivity should be given by a combination rule:  $1/\overline{D}_s = \sum_\alpha x_\alpha/D_s^\alpha$ .

From a very general viewpoint, there is no simple model to predict the cross-correlation terms in [eq 66](#) as they are system-dependent. However, theoretical frameworks such as Langevin and Fokker–Planck equations are invaluable to describe such correlations and the dynamics of molecules in heterogeneous environments. In particular, using either a path integral approach or a transition matrix approach, Roose-Runge et al. derived simple expressions which allow one to probe the dynamics in complex heterogeneous media from data available using PFG-NMR, neutron scattering, or dynamic light scattering.<sup>67</sup> This powerful formalism will be introduced in [Section 4](#) where diffusion at the porous network scale will be considered (we will also consider the different simple combination rules such as model in series, in parallel and the effective medium theory). As far as dynamics at the pore scale is concerned, another formalism, known as “Intermittent Brownian Motion”, is presented in the following subsection as it provides a simple framework to describe adsorption and diffusion in a pore partially or completely filled with a fluid phase.

**3.2.3. Intermittent Brownian Motion.** In order to introduce the framework of Intermittent Brownian Motion, we follow the approach proposed by Levitz as derived in [ref 122](#). Let us consider a fluid confined in a porous medium with pores large enough to assume that molecules are located either in the vicinity of the pore surface or in the bulk-like region of the pore center. In practice, a molecule can be considered located in the pore surface region if its interaction energy with the solid atoms forming the porous medium is larger than the thermal energy  $k_B T$ . Every molecular trajectory can be described as an alternating series of adsorption steps at the pore surface, followed by relocation steps within the pore center [[Figure 11\(a\)](#)]. Let us define the function  $I(t)$  which is equal to 1 if the molecule is adsorbed at time  $t$  and 0 if the molecule is in the pore center [[Figure 11\(a\)](#)]. The formalism of Intermittent Brownian Motion allows one to describe the long-time dynamics of such a confined fluid from the time autocorrelation  $C(t) = \langle I(t)I(0) \rangle / \eta_A$  where  $\eta_A = \tau_A / (\tau_A + \tau_B)$  is the time fraction spent in adsorption steps ( $\tau_A$  and  $\tau_B$  are the average adsorption and relocation times). At this stage, let us also introduce the spectral density of the time correlation function  $C(t)$ :  $J(\omega) = \int_{-\infty}^{\infty} C(t) \exp(i\omega t) dt$ .  $C(t)$  is defined as a time average over the variable  $\tau$ :

$$C(t) = \frac{\langle I(t)I(0) \rangle}{\eta_A} = \frac{1}{\eta_A T} \int_0^T I(\tau)I(t+\tau)d\tau \quad (67)$$

Microscopic information on the residence time within the adsorbed phase, bulk relocation time, and time exchange between these different domains is all encoded in the function  $L(t) = 1/T \times \int_0^T I(\tau)I(t+\tau)d\tau$ —and equivalently its Fourier transform  $\tilde{L}(\omega)$ . While there is no direct measurement of such time correlation functions or their spectral density, experimental techniques such as NMR relaxometry provide

data from which they can be inferred. In this technique, the characteristic relaxation time for the different populations is used as it is a direct signature of the molecule environment. Typically, by performing such relaxation measurements separated by a time lapse  $\Delta$ , it is possible to probe molecules that move from one environment to another or that remain within the same environment over this specific time  $\Delta$ .

For reasons that will become clearer below, let us introduce the second time derivative of the function  $L(t)$ :<sup>124</sup>

$$L''(t) = -\frac{1}{T} \times \int_0^T I'(\tau)I'(t+\tau)d\tau \quad (68)$$

Typically, as shown in [Figure 11\(a\)](#),  $I(t)$  can be described as a series of Heaviside functions  $H(t-t_i)$ :  $I(t) = \sum_i (-1)^i H(t-t_i)$ . Inserting this expression into [eq 68](#) and using  $H'(t-t_i) = \delta(t-t_i)$  lead to

$$\begin{aligned} L''(t) &= -\frac{1}{T} \times \sum_{i,j} (-1)^{i+j} \int_0^T \delta(\tau-t_j)\delta(t+\tau-t_i)d\tau \\ &= -\frac{1}{T} \times \sum_{i,j} (-1)^{i+j} \delta(t-[t_i-t_j]) \end{aligned} \quad (69)$$

In the Intermittent Brownian Motion, each molecular trajectory is a succession of adsorption steps ( $2n \rightarrow 2n+1$ ) and relocation steps through the porosity in the pore center ( $2n+1 \rightarrow 2n+2$ ). The last equality in [eq 69](#) shows that  $L''(t)$  is the sum of Dirac functions with (1) terms  $i=j$ , (2) terms  $j=i+1$  and  $i=2n$  which correspond to an adsorption step, (3) terms  $j=i+1$  and  $i=2n+1$  which correspond to a relocation step, (4) terms  $j=i+2$  and  $i=2n$  which correspond to an adsorption step followed by a relocation step, (5) terms  $j=i+3$  and  $i=2n+1$  which correspond to an adsorption step followed by a relocation step followed by an adsorption step, (6) terms  $j=i+3$  and  $i=2n$  which correspond to a relocation step followed by an adsorption step followed by a relocation step, and so on. Such a hierarchy can be described using the following averages

$$\langle \delta(t-(t_{2n+1}-t_{2n})) \rangle = \psi_A(t) \quad (70)$$

$$\langle \delta(t-(t_{2n+2}-t_{2n+1})) \rangle = \psi_B(t) \quad (71)$$

$$\langle \delta(t-(t_{2n+2}-t_{2n})) \rangle = \psi_A(t) * \psi_B(t) \quad (72)$$

$$\langle \delta(t-(t_{2n+3}-t_{2n+1})) \rangle = \psi_B(t) * \psi_A(t) \quad (73)$$

$$\langle \delta(t-(t_{2n+4}-t_{2n})) \rangle = \psi_A(t) * \psi_B(t) * \psi_A(t) \quad (74)$$

$$\langle \delta(t-(t_{2n+5}-t_{2n+1})) \rangle = \psi_B(t) * \psi_A(t) * \psi_B(t) \quad (75)$$

...

where the symbol  $*$  denotes convolution, i.e.,  $f(t) * g(t) = \int_{-\infty}^{\infty} f(\tau)g(t+\tau)d\tau$ . Based on these definitions,  $\psi_A(t)$  [or  $\psi_B(t)$ , respectively] is the probability that an adsorption step [or relocation step, respectively] lasts a time  $t$ . These two functions, which are schematically illustrated in [Figure 11\(b\)](#), contain the fingerprint of the adsorption properties of the confined fluid as well as of the porous medium (specific surface area, mean pore size, tortuosity, etc.). Using the statistical distributions above and considering that  $L''(t)$  is an even function,  $L''(t)$  in [eq 69](#) can be expressed as

$$\begin{aligned}
L''(t) &= \frac{N}{T}[-2\delta(t) + \psi_A(t) + \psi_B(t) - 2\psi_A(t)^*\psi_B(t) \\
&\quad + \psi_A(t)^*\psi_B(t)^*\psi_A(t) + \psi_B(t)^*\psi_A(t)^*\psi_B(t) - ...](t \geq 0) \\
L''(t) &= \frac{N}{T}[-2\delta(t) + \psi_A(-t) + \psi_B(-t) - 2\psi_A(-t)^*\psi_B \\
&\quad (-t) \\
&\quad + \psi_A(-t)^*\psi_B(-t)^*\psi_A(-t) + \psi_B(-t)^*\psi_A(-t)^*\psi_B(-t) - \\
&\quad ...](t \leq 0)
\end{aligned} \tag{76}$$

where  $N$  is the number of adsorption/relocation steps over the total duration  $T$ . From eq 76, the Fourier transform  $\tilde{L}''(\omega) = \int_{-\infty}^{\infty} L''(t)\exp(i\omega t)dt$  of the function  $L''(t)$  reads<sup>125</sup>

$$\begin{aligned}
\tilde{L}''(\omega) &= \frac{N}{T}\text{Re}[-2 + 2 \times (\tilde{\psi}_A(\omega) + \tilde{\psi}_B(\omega) - 2\tilde{\psi}_A(\omega)\tilde{\psi}_B(\omega)) \\
&\quad + \tilde{\psi}_A(\omega)\tilde{\psi}_B(\omega)\tilde{\psi}_A(\omega) + \tilde{\psi}_B(\omega)\tilde{\psi}_A(\omega)\tilde{\psi}_B(\omega) - ...]
\end{aligned} \tag{77}$$

The latter equation can be rearranged as

$$\begin{aligned}
\tilde{L}''(\omega) \times \tilde{\psi}_A(\omega)\tilde{\psi}_B(\omega) &= \\
\frac{N}{T}\text{Re}[-2\tilde{\psi}_A(\omega)\tilde{\psi}_B(\omega) + 2\tilde{\psi}_A^2(\omega)\tilde{\psi}_B(\omega) + 2\tilde{\psi}_A(\omega)\tilde{\psi}_B^2(\omega) \\
- 4\tilde{\psi}_A^2(\omega)\tilde{\psi}_B^2(\omega) + 2\tilde{\psi}_A^3(\omega)\tilde{\psi}_B(\omega) + 2\tilde{\psi}_A(\omega)\tilde{\psi}_B^3(\omega) - ...]
\end{aligned} \tag{78}$$

By subtracting eqs 77 and 78, we obtain  $\tilde{L}''(\omega) \times (1 - \tilde{\psi}_A(\omega)\tilde{\psi}_B(\omega)) = N/T \times \text{Re}[-2 + 2\tilde{\psi}_A(\omega) + 2\tilde{\psi}_B(\omega) - 2\tilde{\psi}_A(\omega)\tilde{\psi}_B(\omega)]$ , which can be recast as

$$\tilde{L}''(\omega) = -\frac{2N}{T} \times \text{Re} \left[ \frac{(1 - \tilde{\psi}_A(\omega))(1 - \tilde{\psi}_B(\omega))}{1 - \tilde{\psi}_A(\omega)\tilde{\psi}_B(\omega)} \right] \tag{79}$$

Finally, by virtue of the Fourier transform properties,  $\tilde{L}''(\omega) = -\omega^2\tilde{L}(\omega)$ , we obtain

$$\tilde{L}(\omega) = \frac{2N}{T\omega^2} \text{Re} \left[ \frac{(1 - \tilde{\psi}_A(\omega))(1 - \tilde{\psi}_B(\omega))}{1 - \tilde{\psi}_A(\omega)\tilde{\psi}_B(\omega)} \right] \tag{80}$$

Equivalently, recalling that  $C(t) = L(t)/\eta_A$  with  $\eta = \tau_A/[\tau_A + \tau_B]$  and noting that  $N/T = 1/[\tau_A + \tau_B]$  (i.e., the number of adsorption/relocation segments per time unit), we obtain  $J(\omega) = 2/\tau_A\omega^2 \times \text{Re}[(1 - \tilde{\psi}_A(\omega))(1 - \tilde{\psi}_B(\omega))]/[1 - \tilde{\psi}_A(\omega)\tilde{\psi}_B(\omega)]$ . This equation is a very important expression as it shows that multiscale diffusion in a porous medium can be described from two simple statistical distributions: the adsorption time distribution  $\psi_A(t)$  and relocation time distribution  $\psi_B(t)$ . Such functions can be estimated from molecular simulation and fitted against simple mathematical functions. In a second step, by inserting these molecular time distributions into eq 80, the long-time dynamics of the confined fluid can be described up to time and length scales that go well beyond those accessible using molecular simulation. Figure 11(b) illustrates the application of the Intermittent Brownian Motion model to molecular simulation data for water in a hydrophilic silica pore having a width  $D_p = 2$  nm.<sup>123</sup> At high frequencies  $f = \omega/2\pi$ , some expected discrepancy is observed between the molecular simulation data and the predictions based on the Intermittent Brownian Motion model. This is due to the coarse-grained, i.e., mesoscopic, level employed in the theory which does not capture the details of the molecular dynamics explicitly treated in molecular simulation. On the other hand, for frequencies smaller than  $10^5$  MHz, the Intermittent Brownian Motion model

is found to capture very accurately the molecular simulation data. In particular, while molecular simulations typically cannot probe time scales much longer than 10–100 ns ( $f < 10$ –100 MHz), the data in Figure 11(b) suggests that the Intermittent Brownian Motion framework allows accurately upscaling molecular dynamics to the long time, i.e., macroscopic, limit. In practice, while being a robust and efficient theory, in order to calculate the time distributions  $\psi_A(t)$  and  $\psi_B(t)$ , the Intermittent Brownian Motion requires to subdivide a given confined fluid into an adsorbed phase in the vicinity of the surface and a bulk-like phase in the pore center. For disordered porous materials, this task can be complex even if descriptors such as the minimum distance to the pore surface and/or the value of the fluid/wall energy at a given position  $\mathbf{r}$  can be used. Even for a simple pore geometry, such as cylindrical and slit pores considered in ref 123,  $\psi_A(t)$  and  $\psi_B(t)$  must be calculated by using a minimum distance criterion to the pore surface (typically,  $r < R - r_c$  where  $r$  is the distance to the pore surface,  $R$  the pore radius or half-width, and  $r_c$  the cutoff). While this appears as an arbitrary choice at first, it was shown in ref 123 that using  $r_c \sim 2\sigma$ , where  $\sigma$  is the fluid molecule size, leads to accurate predictions such as those illustrated in Figure 11. Such a choice  $r_c \sim 2\sigma$  can be rationalized by the fact that, at temperatures under which adsorption occurs, the range of fluid–wall intermolecular forces is about  $2\sigma$  (as can be inferred from typical density profiles which show that the adsorbate displays important positional ordering—with marked density oscillations—that extends up to two layers from the pore surface). Recently, the intermittent Brownian formalism was extended to disordered nanoporous materials by obtaining residence and relocation distributions and associated characteristic times through a mapping with molecular dynamics simulations.<sup>126</sup>

**3.2.4. Density-Dependent Diffusion.** Until now, we have focused on the different diffusion mechanisms that can occur in a single pore (Knudsen diffusion, surface diffusion, molecular diffusion, etc.). For each mechanism, the theoretical foundations were provided together with a description of transition regimes between them. In the present subsection, we turn to a different aspect which is the description of density, i.e., loading, effects on the self-diffusivity in a single pore. The schematic behavior summarized in Figure 9 can be considered representative of any fluid confined below or above their capillary critical point  $T_{cc}$ . The exact shape of the adsorption isotherms and self-diffusivity as a function of pressure plots will depend on pore size, temperature, strength of the fluid/wall interaction, etc. However, irrespective of the adsorbate/adsorbent couple considered, the self-diffusivity usually varies in a nonmonotonic fashion with pressure (and, therefore, with density since the density increases monotonically with pressure). Such a typical diffusivity/density dependence with the existence of a maximum is seen in many experiments on fluids, e.g. in activated carbons<sup>127</sup> or in zeolites.<sup>128</sup> However, in other experiments, this maximum diffusivity regime might not be observable because it is located in the very low pressure/density range. Before going into more details, the nonmonotonic behavior observed when plotting the self-diffusivity as a function of fluid pressure or density can be understood as follows.<sup>129</sup> At low densities, the self-diffusivity  $D_s$  increases with density as the fluid molecules get adsorbed in adsorption sites of decreasing energies. In other words, while the first adsorbed molecules are located in strongly adsorbing sites leading to a very slow self-diffusivity, further adsorption takes place in less energetic sites so that the average diffusivity increases. As the pore gets filled, the

self-diffusivity of the fluid molecules decreases upon increasing the density as steric repulsion/crowding becomes dominant. In what follows, we first discuss the regime corresponding to the range where the self-diffusivity increases with density—as will be shown below, this regime can be simply described using a spatially averaged diffusivity. We then discuss the second regime where the decrease in the self-diffusivity upon increasing the density is governed by steric repulsion. This second regime can be accounted for by considering the change in the volume accessible to the diffusing molecules through a simple free volume theory.

**3.2.4.1. Spatially Averaged Diffusivity.** Before addressing the increase in the diffusivity upon increasing the fluid loading, it is instructive to consider the following simple model. Consider a pore of any arbitrary geometry filled with a fluid phase of  $N$  molecules at a given temperature  $T$  and chemical potential  $\mu$ . If the pore is completely filled by the fluid phase, it can reasonably be assumed that fluid molecules explore on a reasonable time scale the whole porosity so that the problem can be treated in the fast switching limit. As was done in the previous section, within this approximation, we can assume that the mean square displacements of each fluid molecule is a succession of mean square displacements in different pore regions so that the effective diffusivity reads

$$\overline{D}_s = \frac{1}{N} \int D_s(\mathbf{r}) \rho(\mathbf{r}) d^3\mathbf{r} = \frac{1}{\pi R_p^2 \bar{\rho}} \int_0^{R_p} D_s(r) \rho(r) \times 2\pi r dr \quad (81)$$

where  $D_s(\mathbf{r})$  and  $\rho(\mathbf{r})$  are the self-diffusivity and density of the fluid at the position  $\mathbf{r}$  in the pore. In the second equality, the specific case of an infinite cylindrical pore of radius  $R_p$  is considered and the average density  $\bar{\rho}$  is introduced so that  $N = \pi R_p^2 \bar{\rho}$ . In the framework of the transition state theory, it was shown in Section 3.1.3 that self-diffusion can be described as an activated process involving an activation free energy  $\Delta F^0$ , i.e.,  $D_s \sim \exp[-\Delta F^0/k_B T]$ . For a confined fluid, a simple physical assumption is that the activation energy for diffusion is that of the bulk augmented by the fluid/wall potential  $\phi(\mathbf{r})$ , i.e.,  $\Delta F = \Delta F^0 + \phi(\mathbf{r})$ . In other words, it can be assumed that the attractive interaction potential generated by the pore surface slows down the confined/adsorbed molecules which therefore display a slower self-diffusivity with respect to their bulk counterpart. With these arguments, one simply obtains that  $D_s(r) = D_s^0 \exp[-\phi(r)/k_B T]$  where  $D_s^0$  is the bulk self-diffusivity.<sup>130</sup> If we further assume that the density is constant within the pore  $\rho(r) \sim \bar{\rho}$  and that the fluid/wall potential can be described as a square well interaction potential such that  $\phi(r) = -\epsilon$  for  $R_p - r < 2\sigma$  where  $\sigma$  is the size of the fluid molecule (such a fluid/wall interaction range is consistent with the fact that most adsorbed fluids show properties that depart from their bulk counterpart when located at a distance smaller than  $2\sigma$  from the pore surface while the bulk fluid properties are recovered beyond this value). Upon inserting these different approximations in eq 81, one arrives at

$$\begin{aligned} \overline{D}_s &= \frac{D_s^0}{R_p^2} \left[ (R_p - 2\sigma)^2 + \frac{D_s^0}{D_s^0} (R_p^2 - (R_p - 2\sigma)^2) \right] \\ &\approx D_s^0 \left[ 1 - \frac{4\sigma}{R_p} \left( 1 - \frac{D_s^0}{D_s^0} \right) \right] \end{aligned} \quad (82)$$

where the second equality was obtained by expanding each term while keeping only leading order terms in  $\sigma$  (i.e., assuming

$\sigma^2 \ll R_p^2$ ) and  $D_s^0$  is the self-diffusivity in the surface layer of width  $2\sigma$ .

Equation 82 is a general expression that applies to cylindrical pores filled by a liquid with a homogeneous density profile. Using simple yet realistic approximations, more specific situations including partially filled pores can be described as follows. We write that the self-diffusivity  $D_s$  is a function of the distance  $r$  to the pore surface that decays exponentially with a characteristic molecular length  $r_0$  ( $r_0 < R_p$ ):  $D_s(r) = D_s^0 + (D_s^s - D_s^0) \exp[-(R_p - r)/r_0]$ . The latter function ensures that the local self-diffusivity  $D_s(r)$  varies from the surface self-diffusivity  $D_s^s$  to the bulk diffusivity  $D_s^0$  as the distance to the surface increases.

- For a totally filled pore, upon inserting the expression for the local self-diffusivity in eq 81, the effective diffusivity  $\overline{D}_s$  reads

$$\begin{aligned} \overline{D}_s &= D_s^0 + \frac{2}{R_p^2} \int_0^{R_p} (D_s^s - D_s^0) \times r \exp\left[-\frac{(R_p - r)}{r_0}\right] dr \\ &= D_s^0 + 2(D_s^s - D_s^0) \left[ \frac{r_0}{R_p} - \frac{r_0^2}{R_p^2} + \frac{r_0^2}{R_p^2} \exp(-R_p/r_0) \right] \\ &\approx D_s^0 + \frac{2r_0}{R_p} (D_s^s - D_s^0) \end{aligned} \quad (83)$$

In the third equality, only the leading order terms  $r_0/R_p$  were kept (i.e.,  $r_0^2/R_p^2$  and  $r_0^2/R_p^2 \times \exp(-R_p/r_0) \sim 0$ ).<sup>131</sup> Interestingly, the second expression in eq 83 is strictly equivalent to that in eq 82 if  $r_0$  is taken equal to  $2\sigma$ ,

- For a partially filled pore at low temperature, the density profile can be assumed to be a step function with  $\rho(r) = \bar{\rho}$  for  $R_p - R' = t$  where  $t$  is the film thickness and  $\rho = \rho_g \sim 0$  otherwise ( $\rho_g$ , which is the gas density under the considered temperature and pressure, is taken equal to zero as the system is at low temperature). With such a profile, eq 81 leads to

$$\begin{aligned} \overline{D}_s &= \frac{2}{R_p^2} \int_{R'_p}^{R_p} D_s(r) r dr \\ &= \frac{(R_p - R')^2}{R_p^2} D_s^0 + 2(D_s^s - D_s^0) \times \\ &\quad \left[ \frac{r_0}{R_p} - \frac{r_0^2}{R_p^2} - \left( \frac{R'_p}{R_p^2} - \frac{r_0^2}{R_p^2} \right) \exp(-(R_p - R')/r_0) \right] \end{aligned} \quad (84)$$

For  $R_p > r_0$ , the terms in  $r_0/R_p$  in eq 84 can be neglected so that the dependence over the film thickness  $t = R_p - R'$  is given by the first term only. This predicts that  $\overline{D}_s$  increases with  $t$  and, therefore, with pore loading/pressure.<sup>133</sup>

- For a partially filled pore at high temperature, diffusion through the pore center becomes an important contribution as the gas density is not negligible. In such a regime,  $\rho(r)$  can be taken as a decaying function  $\rho(r) = \rho_0 \exp[-(R_p - r)/r_1]$  with a characteristic length  $r_1$  while the function  $D_s = D_s^0 + (D_s^s - D_s^0) \exp[-(R_p - r)/r_0]$  is kept (in practice,  $r_0$  and  $r_1$  do not have to be identical but are similar since they are both affected by the same surface molecular interactions). Direct integration of the density  $\rho(r)$  allows estimating the average density as  $\bar{\rho} = (\pi R_p^2)^{-1} \int_0^{R_p} 2\pi r \rho_0 \exp[-(R_p - r)/r_1] dr$

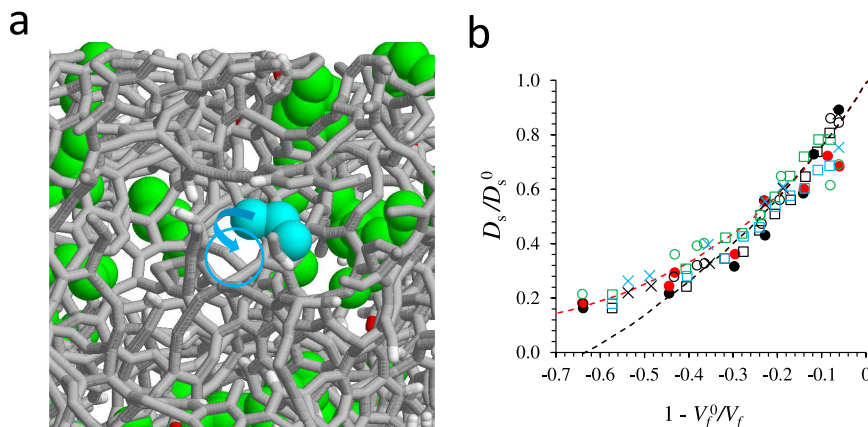


**Figure 12.** Free volume theory. (a) Principle of the free volume theory applied to diffusion in a porous material. A tagged molecule, here a propane molecule depicted in blue, will diffuse provided a cavity (denoted by the blue circle) is available around it. In the context of diffusion in a porous material, the free volume refers here to all cavities—irrespective of their size—available to the diffusing molecules, i.e., regions that do not intersect with a host matrix atom, another fluid molecule, or their covolume. (b) Self-diffusivities  $D_s$  normalized to the bulk self-diffusivity  $D_s^0$  as a function of the free volume fraction  $V_f^0/V_f$  for alkane mixtures in the disordered porous carbon shown in (a).  $V_f^0$  and  $V_f$  are the free volume of the empty and filled porous matrix, respectively. The symbols denote different mixtures: methane/dodecane (filled circles), methane/hexane (empty circles), methane/propane (crosses), and methane/propane/hexane (squares). The color code is methane (black), propane (blue), hexane (green), and dodecane (red). The red line is the prediction of the free volume theory  $D_s \propto \exp[1 - V_f^0/V_f]$  obtained from the single-component fluids. The black dashed line corresponds to the prediction of the surface diffusion model. Figure adapted with permission from ref 134. Copyright 2016 American Chemical Society.

$= 2r_1^2\rho_0/R_p^2 \times [R/r_1 - 1 + \exp(-R_p/r)]$ . Finally, using the position-dependent density  $\rho(r)$  and self-diffusivity  $D_s(r)$  in eq 83 leads to (with  $\tilde{r}^{-1} = r_0^{-1} + r_1^{-1}$ ):

$$\begin{aligned} \overline{D_s} &= \frac{1}{\bar{\rho}\pi R_p^2} \int_0^{R_p} 2\pi r D_s(r) \rho(r) dr \\ &= \frac{2}{\bar{\rho}R_p^2} \int_0^{R_p} r D_s^0 \rho(r) dr + \frac{2}{\bar{\rho}R_p^2} \int_0^{R_p} r (D_s^0 - D_s^0) \\ &\quad \rho(r) dr \\ &= D_s^0 + \frac{2\rho_0}{\bar{\rho}R_p^2} (D_s^0 - D_s^0) \int_0^{R_p} \exp[-(R_p - r)/\tilde{r}] dr \\ &= D_s^0 + (D_s^0 - D_s^0) \frac{\tilde{r}^2}{r_1 R_p} \left[ \frac{R_p}{\tilde{r}} - 1 + \exp[-R_p/\tilde{r}] \right] \end{aligned} \quad (85)$$

**3.2.4.2. Free Volume Theory.** In the previous subsection, we considered a spatially averaged diffusivity which captures the different regimes observed upon varying the average confined fluid density  $\bar{\rho}$ . However, as schematically shown in Figure 9, upon further increasing  $\bar{\rho}$  or, equivalently, the pressure  $P$ , most experimental and simulation data show that the effective self-diffusivity  $\overline{D_s}$  decreases. Such a pressure or density-driven behavior is accurately described using a simple free volume theory (see for instance refs 74 and 134). In this model, density effects are accounted for by writing that a fluid molecule diffuses provided a free cavity is available around it as illustrated in Figure 12. In what follows, we first derive the free volume theory initially proposed by Cohen and Turnbull<sup>135</sup> before illustrating its quantitative application to self-diffusion in porous media. Let us define the free volume  $v$  of a cavity available in the confined fluid as the volume of the cavity minus the volume occupied by a fluid molecule. If we define the diameter  $a(v)$  of this cavity having a free volume  $v$ , the contribution from this cavity to the average fluid self-diffusivity is assumed to be  $D_s(v) = ga(v)$

where  $u$  is the average fluid velocity (taken equal to the thermal velocity,  $u = \sqrt{3k_B T/m}$ ), and  $g$  is an effective geometry factor. The average diffusivity  $D_s$  is simply defined as an integral over every possible cavity sizes

$$D_s = \int_{v^*}^{\infty} p(v) D_s(v) dv \quad (86)$$

where  $p(v)$  is the probability to find a cavity having a free volume  $v$  and  $v^*$  is the minimum cavity volume in which the molecule can diffuse. There are two important properties that must be verified by the probability distribution  $p(v)$ :

$$\int_0^{\infty} p(v) dv = 1 \text{ and } \int_0^{\infty} \gamma v p(v) dv = V_f \quad (87)$$

While the first condition simply ensures normalization, the second condition ensures that the total cavity volume corresponds to the free volume  $V_f$ . The numerical factor  $\gamma$  is a factor which accounts for the fact that several molecules can share part of the same free volume. If one assumes that the distribution  $p(v)$  is exponential,  $p(v) = \gamma N/V_f \exp(-\gamma Nv/V_f)$ , inserting this expression into eq 86 together with the assumption  $D_s(v) = D_s(v^*)$  for all  $v$  leads to

$$D_s = D_s(v^*) \exp\left[-\frac{\gamma v^* N}{V_f}\right] = g a(v^*) u \exp\left[-\frac{\gamma v^* N}{V_f}\right] \quad (88)$$

As shown in refs 74 and 134, the latter equation is a robust framework to describe diffusion in nanoporous media. In particular, it was shown to be more general than the surface diffusion model (as discussed in what follows, the surface diffusion model can be seen as an asymptotic limit of the free volume theory). In this context, we note that the use of the free volume theory to rationalize experimental measurements of the self-diffusion for fluids in zeolites was reported in a seminal paper by Kärger et al.<sup>136</sup> In the free volume theory, the effect of the confined fluid density, i.e., the adsorbed amount, is included in the exponential term through the change in the free volume  $V_f$

as adsorption occurs ( $V_f^0$  is the porous volume which corresponds to the free volume when no molecule is adsorbed in the porosity). As shown in eq 88,  $D_s(v^*)$  is the self-diffusivity at infinite dilution, i.e.,  $N \rightarrow 0$ , which can be estimated from molecular dynamics simulations for an isolated molecule.  $D_s(v^*)$  is linked to the so-called mobility  $\mu k_B T$  at infinite dilution. For a single molecule at equilibrium in the nanoporosity of a host porous material, the drag force responsible for diffusion  $F_u = u/\mu$ , balances the friction force  $F_f = -\xi u$  (where  $u$  is the molecule velocity and  $\xi$  is the friction coefficient). In molecular dynamics simulations, it can be easily checked that this important force balance condition is verified as the confined fluid is at rest (i.e., no flow condition). In order to illustrate the applicability of the free volume theory to diffusion in nanoporous materials, Figure 12 compares its predictions with molecular simulation data for different alkane mixtures in a disordered nanoporous carbon. Even for binary and ternary mixtures confined in such a heterogeneous material, the free volume model accurately predicts the self-diffusivity  $D_s$  of each mixture component. The change in the accessible volume  $V_f$  as adsorption occurs scales with the adsorbed amount  $\Gamma$ ,  $V_f/V_f^0 = 1 - \beta\Gamma$  where  $\beta = 0.37$  is the packing fraction of the confined molecules. Inserting this expression into eq 88, the self-diffusivity can be rewritten as a function of  $\Gamma$ :

$$D_s = D_s(v^*) \exp\left[-\frac{\gamma\beta\Gamma}{1 - \beta\Gamma}\right] \quad (89)$$

In agreement with experimental and molecular simulation data at large confined fluid loadings, eq 89 shows that the self-diffusivity decreases upon increasing the adsorbed amount  $\Gamma$ . By taking the limit of the model at very low densities,  $\beta\Gamma \ll 1$  (i.e.,  $V_f \ll V_f^0$ ),  $D_s/D_s(v^*) \sim 1 - \gamma\beta\Gamma$ . In ref 134,  $\gamma = 2.76$  and  $\beta = 0.37$  was found for alkanes in a disordered nanoporous material. Because  $\gamma\beta \sim 1$  with these numbers, this leads to  $D_s/D_s(v^*) \sim 1 - \Gamma$  which is identical to the surface diffusion model introduced previously. This suggests that the free volume theory is very general and robust as its asymptotic limit encompasses the surface diffusion model. Figure 12 compares the free volume theory, the surface diffusion model, and the molecular simulation data. It is found that the free volume theory describes more accurately the self-diffusivity while the two models merge at low fluid densities ( $\Gamma \ll 1$ ).

## 4. SELF-DIFFUSION AND TRACER DIFFUSION IN POROUS NETWORKS

### 4.1. Effective Diffusion

**4.1.1. Tortuosity.** The tortuosity, usually denoted by  $\tau$ , is an important concept related to both diffusion and transport in porous materials.<sup>137,138</sup> It characterizes the way in which the porous medium slows down transport processes due to its geometrical complexity. While there have been attempts to define  $\tau$  based on a geometrical analysis,<sup>53,137</sup> it remains unclear how these geometrical characterizations can be applied to the prediction of transport properties. Therefore, in this review, we take the pragmatic point of view that consists in defining  $\tau$  as the ratio of a transport coefficient for the bulk fluid,  $L_{\alpha\beta}^0$ , and for the confined fluid,  $L_{\alpha\beta}$ , i.e.,  $\tau = L_{\alpha\beta}^0/L_{\alpha\beta}$ . As will be seen in Section 5, any transport coefficient such as electrical conductivity  $\sigma$ , permeance  $K$  or collective diffusivity  $D_0 \sim K$ , heat conductivity  $\lambda_T$ , etc. can be considered for  $L_{\alpha\beta}$ . In the context of the present,

which is devoted to self-diffusivity in porous media, the self-diffusivity can be also used to define the tortuosity  $\tau = D_s^0/D_s$ . Usually, because of confinement and adsorption within a porous material, the tortuosity  $\tau > 1$  since  $D_s^0 > D_s$ . This definition is valid for a single pore but can be easily extended to porous materials made of different pores by introducing the porosity  $\phi$  as

$$\tau = \frac{\phi D_s^0}{D_s} \quad (90)$$

As an important remark related to experiments on self-diffusion in nanoporous media, we note that the porosity in eq 90 is needed when tracer-permeation measurements are performed (to correct for the difference in the space explored upon transport). In contrast, such porosity correction is not needed when probing diffusion using PFG NMR. Confined transport coefficients must be normalized to the volume fraction in which transport occurs, i.e., the porosity  $\phi$ . The latter definition ensures that  $\tau \rightarrow 1$  for  $\phi \rightarrow 1$  (since  $D_s = D_s^0$  when the porosity  $\phi = 1$ ).<sup>137</sup> As an extension of eq 90, the tortuosity can be defined as any transport coefficient normalized to its bulk value under the same thermodynamic conditions (self-diffusivity, collective diffusivity, electrical conductivity, thermal conductivity, etc.). While these different definitions are acceptable, they tend to assume a very unlikely situation where all transport coefficients are defined by a unique tortuosity. Of course, this description ignores that underlying physical phenomena can drastically differ from one transport coefficient to another. In fact, we know that the mechanisms behind individual dynamical processes (self- or tracer diffusion) and collective dynamical processes (e.g., permeability, electrical conductivity) involve very different mechanisms so that using a single tortuosity for all transport types is necessarily restrictive.

Several models have been proposed in the literature to describe the tortuosity of fluids confined in porous materials. While some of the tortuosity expressions are empirical relationships that possess the right asymptotic behavior, other expressions are more grounded on robust physical concepts. The Weissberg expression belongs to the former category as it corresponds to an empirical expression between  $\tau$  and  $\phi$ <sup>139</sup>

$$\tau = 1 - p \ln \phi \quad (91)$$

where  $p$  is a geometrical factor that depends on the morphology (pore shape) and topology (pore connectivity) of the host porous material.<sup>140</sup> Typically,  $p$  takes well-defined values for materials with simple geometry such as overlapping spheres, cylinders, etc. but in practice it is used as an empirical parameter fitted against available experimental data. Another empirical relationship between tortuosity  $\tau$  and porosity  $\phi$  is Archie's law that was initially observed for electrolyte transport in porous rocks<sup>141</sup>

$$\tau = \frac{1}{\phi^m} \quad (92)$$

where  $m$  is an exponent that usually falls between 1.8 and 2.<sup>142</sup>

Besides empirical equations, different models have been proposed to describe the tortuosity in porous materials.<sup>138</sup> Using Maxwell's effective medium theory for the conductivity of very diluted spherical particles in an electrolyte,<sup>143</sup> it is possible to obtain an approximate analytical expression for the tortuosity (defined from the ratio of the bulk and confined electrical

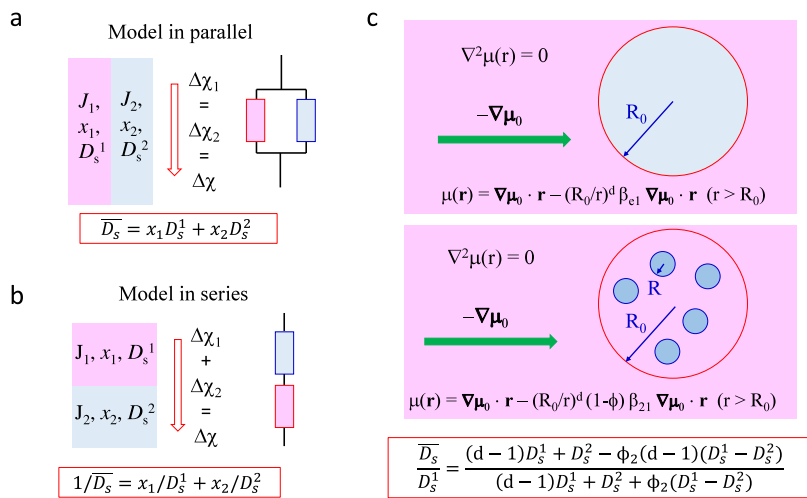


**Figure 13. Effective medium models.** (a) For a porous medium made of domains aligned parallel to the thermodynamic gradient inducing transport, the total flux is proportional to the fluxes in each domain  $J = J_1 + J_2$ . In this case, the effective diffusivity  $\overline{D}_s$  is the sum of the self-diffusivity  $D_s^\alpha$  in each domain type  $\alpha$  weighted by the fraction  $x_\alpha$  of molecules located in this domain type. (b) For a porous medium made of domains aligned in series with respect to the direction of the thermodynamic gradient inducing transport, the total flux is equal to the flux in each domain  $J = J_1 = J_2$ . In this case, the reciprocal of the effective diffusivity  $\overline{D}_s$  is the sum of the reciprocal of the self-diffusivity  $D_s^\alpha$  in each domain type  $\alpha$  weighted by the fraction  $x_\alpha$  of molecules located in this domain type. (c) In general, when a porous medium cannot be assumed to be made of domains aligned in parallel or in series with respect to the direction of the thermodynamic gradient inducing transport, the flow can be predicted using Maxwell's effective model. The physical solution is obtained by writing that the chemical potential field verifies Laplace equation, i.e.,  $\nabla^2\mu = 0 \forall r$ , since there is no source or sink term that modifies the local chemical potential  $\mu(r)$ .

conductivity but the derivation can be extended to any transport coefficient). While a formal derivation will be given in the next subsection on effective models (combination rules and effective medium approximation), in the Maxwell–Garnett model, also known as Maxwell model, the tortuosity  $\tau$  is defined from the effective conductivity  $\bar{\sigma}$  of an electrolyte having an intrinsic conductivity  $\sigma_0$  and containing spherical particles with conductivity  $\sigma_p$

$$\tau = \frac{\phi\bar{\sigma}}{\sigma_0} = \phi \frac{2\sigma_0 + \sigma_p - 2(1 - \phi_{\text{ext}})(\sigma_0 - \sigma_p)}{2\sigma_0 + \sigma_p + (1 - \phi_{\text{ext}})(\sigma_0 - \sigma_p)} \quad (93)$$

where  $\phi_{\text{ext}}$  is the interparticle porosity ( $1 - \phi_{\text{ext}}$  is therefore the volume fraction of the spherical particles) and  $\phi$  is the total porosity, i.e., the sum of the interparticle porosity and of the particle porosity  $\phi_p$  (again, a formal derivation of this expression will be given in the next subsection). As shown by Barrande et al.,<sup>144</sup> for non porous, i.e., non conducting particles ( $\sigma_p = 0$  and  $\phi_{\text{ext}} = \phi$ ), eq 93 leads to  $\tau = 1 + 0.5(1 - \phi) = (3 - \phi)/2$ . Note that Weissberg equation given in eq 91 in the asymptotic limit of large porosities  $\phi \rightarrow 1$  is compatible with Maxwell's expression:  $\tau = 1 - p \ln \phi \sim 1 + p(1 - \phi)$ . Maxwell's effective model for spherical objects corresponds to the choice  $p = 0.5$ . Extensions of Maxwell's effective medium theory have been proposed by Torquato<sup>35</sup> or Landauer.<sup>145</sup> For further reading on the different models available to describe tortuosity in porous materials, the reader is invited to consult refs 138, 140, 144, and 146 and the review paper by Sahimi and co-workers.<sup>137</sup>

**4.1.2. Serial/Parallel Models.** Some important considerations in this section deal with the application of thermodynamic gradients. We recall that self-diffusion and tracer diffusion, which are at the heart of this section, occur both in systems at equilibrium (i.e., without any thermodynamic gradient) and in nonequilibrium systems (i.e., with thermodynamic gradients). Therefore, while some important derivations below involve thermodynamic gradients, they allow describing

situations that correspond to self-diffusion or tracer diffusion where no such driving forces are applied. Many attempts have been made to establish simple models of diffusion in porous media based on its analogy with electrical transport in resistance networks. In what follows, we review the four models that can be established based on this analogy: resistance in series, resistance in parallel, Maxwell's equation, and the effective medium theory. All these models rely on simple transport equations in which a net flow is induced by a thermodynamic (or electrical gradient)  $\Delta\chi$ . However, thanks to the linear response theory, predictions from transport models are also relevant to diffusion at equilibrium (i.e., with no net flow) since the limit of a vanishing driving force  $\Delta\chi \rightarrow 0$  can be taken.

Let us consider a network of domains in which a fluid is transported according to different transport coefficients. The derivation below is done for the collective diffusivity  $D_0$ , i.e., the permeance  $K \sim D_0$  but the self-diffusivity  $D_s$  will be readily obtained by considering the limit for an infinitely diluted medium where  $D_s \sim D_0$ . The collective diffusivity in each domain type  $\alpha$  is  $D_0^\alpha$  and the system is subjected to a chemical potential gradient  $\nabla\mu = \Delta\mu/L$  where  $L$  is the thickness of the sample. Let us first consider that the domains are organized in parallel as depicted in Figure 13(a)—for the sake of simplicity, only two domain types  $\alpha = 1, 2$  are shown but the derivation below can be generalized to any number of domains. The total flux  $J$  across the material having a section area  $A$  is the sum of the fluxes in each domain weighted by its section area  $A_\alpha J \times A = \sum_\alpha J_\alpha \times A_\alpha$ . In the framework of the linear response theory, the flux  $J$  induced by the chemical potential gradient is  $J = -\rho\overline{D}_0\Delta\mu/Lk_B T$  where  $\overline{D}_0$  is the effective permeance of the composite material. As the number of molecules  $N$  in the material is  $N = \rho AL$ ,  $J \times A = -N/L^2 \times \overline{D}_0\Delta\mu/k_B T$ . Similarly, because the domains are subjected to the same driving force  $\Delta\mu$  when set in parallel, the flow in each domain is  $J_\alpha \times A_\alpha = -N_\alpha/L^2 \times D_0^\alpha\Delta\mu/(k_B T)$  where  $N_\alpha$  is the number

of molecules in each domain  $\alpha$ . With these relations, by writing  $J \times A = \sum_{\alpha} J_{\alpha} \times A_{\alpha}$  and taking the limit  $D_s \sim D_0$ , we obtain

$$\overline{D}_s = \sum_{\alpha} x_{\alpha} D_s^{\alpha} \quad (94)$$

where  $x_{\alpha} = \rho_{\alpha}/\rho = N_{\alpha}/N$  is the mole fraction of molecules in the domain type  $\alpha$ . As mentioned above, while this equation was derived for the collective diffusivity, i.e., permeance, it also applies to any other transport coefficient such as the electrical conductivity and the self-diffusivity.

Let us now consider a porous network in which the domains are organized in series as depicted in Figure 13(b). Again, in the framework of the linear response theory, the flow  $J \times A$  induced by the chemical potential gradient is  $J \times A = -\rho A \times \overline{D}_0 \Delta \mu/k_B T$  where  $\overline{D}_0$  is the effective collective diffusivity of the composite material and where  $N = \rho AL$  is the total number of fluid molecules. Similarly, let us define the flow in each domain  $\alpha$  as  $J_{\alpha} \times A = -\rho_{\alpha} A \times \overline{D}_0 \Delta \mu/L_{\alpha} k_B T = -N_{\alpha}/L_{\alpha} \times \overline{D}_0 \Delta \mu/k_B T$  ( $N_{\alpha} = \rho_{\alpha} A L_{\alpha}$  and  $L_{\alpha}$  are the number of molecules and the thickness for this domain  $\alpha$ , respectively). Because of mass conservation upon transport in the composite material, the flow  $J_{\alpha}$  in each domain is equal to the overall flow  $J$ , i.e.,  $J_{\alpha} = J \forall \alpha$ . Moreover, the difference  $\Delta \mu_{\alpha}$  in the thermodynamic variable across the domain  $\alpha$  must be such that  $\Delta \mu_{\alpha} = \sum_{\alpha} \Delta \mu$ . With these conditions, it is straightforward to show that  $J L^2 / N \overline{D}_0 = \sum_{\alpha} J L_{\alpha}^2 / N_{\alpha} D_0^{\alpha}$ . Finally, by noting that  $N_{\alpha} \propto L_{\alpha}$  and taking the limit  $D_s \sim D_0$ , we obtain

$$\frac{1}{\overline{D}_s} = \sum_{\alpha} \frac{x_{\alpha}}{D_s^{\alpha}} \quad (95)$$

where  $x_{\alpha} = \rho_{\alpha}/\rho = N_{\alpha}/N$  is the mole fraction of molecules in the domain type  $\alpha$ .

**4.1.3. Maxwell Model.** The combination rules for domains in series and in parallel rely on a very simplified representation of real systems. A more rigorous treatment of the problem was first derived by Maxwell in an attempt to describe the conductivity of an electrolyte containing conducting spheres at infinite dilution.<sup>35</sup> As shown in the following paragraph, this model can be used to describe the effective diffusivity at constant temperature— $\nabla T = 0$ —of a heterogeneous medium made of spheres having a different self-diffusivity than the medium in which they are included. Let us consider in Figure 13(c, bottom) a medium 1 with a spherical inclusion of radius  $R_0$  made up of medium 1 and small spherical domains of medium 2. The whole system is subjected to a chemical potential gradient  $\nabla \mu_0$  in the far field. Maxwell's model allows modeling this system by replacing the heterogeneous inclusion by an effective medium  $e$  having the same radius  $R_0$  as shown in Figure 13(c, top). In what follows, the subscripts 1 and 2 refer to the main medium and to the small spherical inclusions in the large inclusion, respectively. The subscript  $e$  refers to the large inclusion treated as an effective medium. From a very general viewpoint,  $\nabla \mu_0$  can be replaced by any thermodynamic gradient  $\nabla \chi$  such as a pressure or temperature gradient or an electrical field (so that the treatment below can be seen as a very general solution to such a broad class of complex problems). Because there is no molecule source/sink, the solution  $\mu(\mathbf{r})$  is given by the Laplacian equation  $\Delta \mu = 0$  with the following boundary conditions: (1) chemical potential continuity at  $r = R_0$ , i.e.,  $\mu(r = R^+) = \mu(r = R^-)$ , (2) if  $\rho_1 D_0^1$  and  $\overline{D}_0$  are the conductivity, i.e., the collective diffusivity multiplied

by the fluid density, in the medium 1 and in the effective medium  $e$ , the flux balance from 1 to  $e$  and from  $e$  to 1 at  $r = R_0$  imposes that  $\rho_1 D_0^1 \mathbf{n} \cdot \nabla \mu)_+ = \overline{\rho} \overline{D}_0 \mathbf{n} \cdot \nabla \mu)_-$ , and (3) in the far field, i.e.,  $r \rightarrow \infty$ ,  $\mu(r) \rightarrow \nabla \mu_0 \cdot \mathbf{r}$ . The general solution of this system in a space of dimension  $d = 3$  is

$$\begin{aligned} \mu(\mathbf{r}) &= \nabla \mu_0 \cdot \mathbf{r} - \beta_{e1} \left( \frac{R_0}{r} \right)^3 \nabla \mu_0 \cdot \mathbf{r} \quad (r \geq R_0) \\ \mu(\mathbf{r}) &= \nabla \mu_0 \cdot \mathbf{r} - \beta_{el} \nabla \mu_0 \cdot \mathbf{r} \quad (r \leq R_0) \end{aligned} \quad (96)$$

where  $\beta_{e1} = [\overline{\rho} \overline{D}_0 - \rho_1 D_0^1]/[\overline{\rho} \overline{D}_0 + (d-1)\rho_1 D_0^1]$  with  $\overline{\rho}$  and  $\overline{D}_0$  the effective density and collective diffusivity in the large spherical inclusion.

Let us now treat explicitly the spherical inclusion in Figure 13(c) as made up of medium 1 but with many small spherical inclusions of a radius  $R$ . First, considering a single domain of medium 2 having a radius  $R$ , the solution in the far field  $r > R_0$  can be derived like in the previous treatment:  $\mu(\mathbf{r}) = \nabla \mu_0 \cdot \mathbf{r} - \beta_{21}(R/r)^3 \nabla \mu_0 \cdot \mathbf{r}$  for  $r \geq R_0$ .<sup>147</sup> We now consider the more physical case where there are  $N$  domains of medium 2 in the inclusion. Within the infinite dilution regime, we can assume that all perturbations created by the domains of medium 2 add up in the far field region  $r \gg R_0$ . Since we have  $N$  cavities, the solution is simply obtained by multiplying by  $N$  the last equation:  $\mu(\mathbf{r}) = \nabla \mu_0 \cdot \mathbf{r} - \beta_{21} N (R/r)^3 \nabla \mu_0 \cdot \mathbf{r}$  [the last equality

$$= \nabla \mu_0 \cdot \mathbf{r} - \beta_{21} \nu (R_0/r)^3 \nabla \mu_0 \cdot \mathbf{r}$$

was obtained by introducing the volume fraction of the domains 2 within the spherical inclusion,  $\nu = N(R/R_0)^3$ ]. By comparing this last equation with eq 96, we obtain that  $\beta_{e1} = \nu \beta_{21}$  or equivalently

$$\frac{\overline{\rho} \overline{D}_0 - \rho_1 D_0^1}{\overline{\rho} \overline{D}_0 + (d-1)\rho_1 D_0^1} = \nu \left[ \frac{\rho_2 D_0^2 - \rho_1 D_0^1}{\rho_2 D_0^2 + (d-1)\rho_1 D_0^1} \right] \quad (97)$$

By noting that the conductivity  $\sigma = \rho D_0$ , and using the volume fraction  $\nu = 1 - \phi_{ext}$  where  $\phi_{ext}$  is the porosity of the large spherical inclusion and  $d = 3$ , it is straightforward to check that eq 97 is equivalent to Maxwell's formula given in eq 93 for the effective conductivity of an electrolyte containing spherical particles having a different conductivity than its bulk counterpart. Finally, taking the limit of an infinitely diluted medium, i.e., by replacing the chemical potential gradient  $\nabla \mu$  by  $\nabla \rho/\rho$ , the treatment above leads to the same equation as eq 97 but with the effective collective diffusivity  $\overline{D}_0$  replaced by the effective self-diffusivity  $\overline{D}_s$ .

**4.1.4. Effective Medium Theories.** Generalization of Maxwell's formula given in eq 97 to any heterogeneous medium made of domains  $\alpha = [1, M]$  occupying a volume fraction  $\nu^{\alpha}$  reads

$$\frac{\overline{\rho} \overline{D}_s - \rho_1 D_0^1}{\overline{\rho} \overline{D}_s + (d-1)\rho_1 D_0^1} = \sum_{\alpha=1,M} \nu^{\alpha} \left[ \frac{\rho_{\alpha} D_0^{\alpha} - \rho_1 D_0^1}{\rho_{\alpha} D_0^{\alpha} + (d-1)\rho_1 D_0^1} \right] \quad (98)$$

where we recall that  $d$  is the dimension of the medium. Further development of Maxwell's model was proposed by Bruggeman<sup>148</sup> and Landauer<sup>149</sup> who introduced in eq 98 a self-consistent approximation. As shown in Figure 13(c), Maxwell's formulation relies on the idea that the inclusion acts as a perturbation to the uniform field  $\mu(\mathbf{r})$  applied outside the

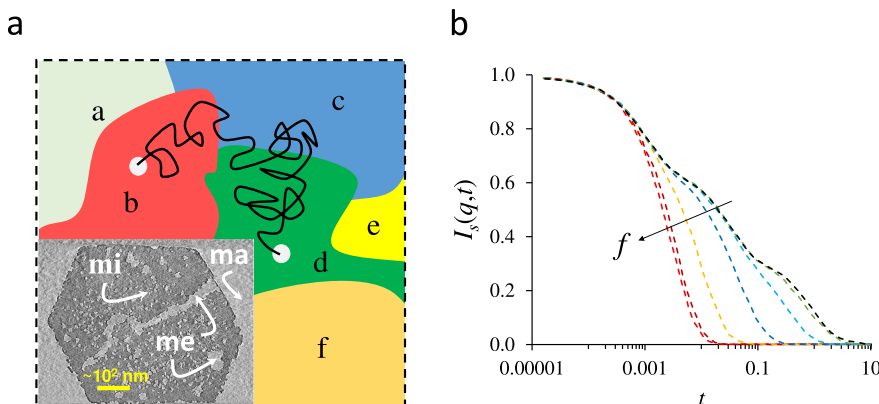


**Figure 14. Self-diffusion in heterogeneous media.** (a) Principle of self-diffusion in heterogeneous media made of different domains—here, 6 domains denoted with different colors and letters a, b, c, d, e, and f. A molecule follows a single trajectory which is made of segments in these different domains  $b \rightarrow c \rightarrow d \rightarrow c \rightarrow d$ . As an example of such domain decomposition, electron tomography data of a hexagonal zeolite crystal are shown in which micropores (“mi”) and mesopores (“me”) domains are shown. Modified with permission from ref 152. Copyright 2010 Wiley-VCH Verlag GmbH & Co. KGaA. Typical self-diffusion in such hierarchical systems include trajectories segments in these micropores and mesopores but also in the macropores (“ma”) which are located outside the zeolite grains. (b) Incoherent scattering function  $I_s(q, t)$  determined for a heterogeneous medium made of 3 domain types (a, b, c) in which molecules display different self-diffusion coefficients:  $D_s^c \sim 33D_s^b \sim 1000D_s^a$ . The different color lines correspond to increasing switching rates  $f$  which vary from 0, 0.1, 1, 10, 100, 1000, 10000. Figure adapted with permission from Roosen-Runge et al.<sup>67</sup> Copyright 2016 AIP Publishing.

inclusion. In the self-consistent scheme, the different perturbations induced by all the domains  $\alpha = [1, M]$  to the homogeneous field average to zero,  $\langle \Delta\mu(\mathbf{r}) \rangle = 0$ . In terms of conductivity, this condition implies that

$$\sum_{\alpha=1,M} v_\alpha \frac{\rho_\alpha D_{0,\alpha} - \bar{\rho} \bar{D}_0}{\rho_\alpha D_{0,\alpha} - (d-1)\bar{\rho} \bar{D}_0} = 0 \quad (99)$$

Interestingly, as shown by Kirkpatrick,<sup>150</sup> this formula can be retrieved by applying the percolation theory to an array of electrical conductors of different resistivities. In the case of heterogeneous materials made of two domain types, eq 99 can be easily solved to predict the diffusivity in porous media from the known diffusivities in the different domains. While the self-consistent approximation to Maxwell’s formula provides a very general framework to discuss diffusion and transport in complex porous media, its application is mostly limited to semi-quantitative prediction as it relies on crude assumptions which neglect issues such as interfacial transport limitations. For an example of the application of Bruggeman’s equation, i.e., eq 99, to self-diffusion in heterogeneous media, the reader is referred to refs 26 and 151.

#### 4.2. Hierarchical and Mesoscopic Approaches

**4.2.1. General Considerations.** Statistical physics is a very robust and general framework to describe the complex problem of diffusion in heterogeneous media such as porous materials. A detailed description of the field of statistical mechanics and its application to diffusion in complex systems is out of the scope of the present context. However, we note that important statistical physics derivations can be found in refs 46, 48 for general aspects and in ref 10 for diffusion in disordered media. In a previous section, the physics of the Intermittent Brownian Motion was introduced to describe the problem of diffusion in a single pore in which the confined fluid subdivides into an adsorbed phase at the pore surface and a bulk-like phase in the pore center. Here, we move to a larger scale by considering molecular diffusion in a heterogeneous medium such as a fluid confined in a disordered porous solid made of different domains. This problem can be treated in a rigorous fashion using theoretical frameworks such

as Langevin and Fokker–Planck equations.<sup>67</sup> As shown below, this formal approach allows predicting the dynamics in such complex media using intermediate functions which are readily obtained using experiments (typically, quasi-elastic and inelastic neutron scattering).

Let us consider the situation depicted in Figure 14(a). A host solid is made of different porous domains—a, b, c, d, e, and f—in which a molecule diffuses. The molecule diffusion is illustrated using the trajectory shown as the black line between a set of initial and final positions corresponding to the gray circles. In order to provide a concrete analogy, Figure 14(a) shows electron tomography data of a zeolite crystal in which one distinguishes the microporous domains (“mi”), the corresponding porosity is invisible because the experimental resolution is larger than the corresponding pore size), the mesoporous domains (“me”), and macroporous domains (“ma”), located outside the zeolite crystal). In Section 3.2.2, we have already introduced the self-correlation function  $G_s(\mathbf{r}, t)$  defined in eq 61. This function describes the probability that a molecule diffuses by a quantity  $\mathbf{r}$  over a time  $t$ . We have also introduced its spatial Fourier transform  $I_s(\mathbf{q}, t) = \int G_s(\mathbf{r}, t) e^{i\mathbf{q}\cdot\mathbf{r}} d\mathbf{r}$ . As already discussed in Section 3.2.2, in the limit of very slow switching rate between domains, i.e.,  $\tau_C^\alpha \gg (D_s^\alpha q^2)^{-1}$  where  $(D_s^\alpha q^2)^{-1}$  is the time needed to diffuse through a typical domain  $\alpha$  having a size  $q \sim 2\pi/r$  while  $\tau_C^\alpha$  is the typical crossing time estimated as the mean first-passage time, molecule exchange between the different domains is limited. In this limit, the correlation function  $I_s(\mathbf{q}, t)$ , which is dominated by diffusion in the different domains, is given by the sum of all intradomain diffusion contributions,  $I_s(\mathbf{q}, t) = \sum_\alpha x_\alpha \exp(-D_s^\alpha q^2 t)$ .

**4.2.2. Diffusion in Heterogeneous Media.** In order to derive a general framework to analyze diffusion in heterogeneous media, Roosen-Runge et al.<sup>67</sup> used a path integral approach in which the self-correlation function  $G_s(\mathbf{r}, t)$  is written by considering every possible path that leads from a point  $\mathbf{r} = 0$  to a point  $\mathbf{r}$  over a time  $t$ . In more detail, upon assuming that the trajectory segment within a given domain is independent of that within the previous domain visited,  $G_s(\mathbf{r}, t)$  can be expressed as

$$G_s(\mathbf{r}, t) = \sum_{m=0}^{\infty} \sum_{i_1, \dots, i_m} \int_V d\mathbf{r}_1 \int_0^{\infty} dt_1 P_{i_1}(\mathbf{r}_1, t_1 | \mathbf{0}, \mathbf{0}) \times \\ \int_V d\mathbf{r}_2 \int_{t_1}^{\infty} dt_2 P_{i_2}(\mathbf{r}_2, t_2 | \mathbf{r}_1, t_1) \times \dots \times \\ \int_V d\mathbf{r}_m \int_{t_{m-1}}^{\infty} dt_m P_{i_m}(\mathbf{r}_m, t_m | \mathbf{r}_{m-1}, t_{m-1}) \times Q_{i_{m+1}}(\mathbf{r}, t | \mathbf{r}_m, t_m) \quad (100)$$

In this equation,  $P_{i_m}(\mathbf{r}_m, t_m | \mathbf{r}_{m-1}, t_{m-1})$  denotes the probability that the molecule leaves a domain  $m$  at time  $t_m$  and position  $\mathbf{r}_m$  while initially entering the same domain at time  $t_{m-1}$  and at position  $\mathbf{r}_{m-1}$  (this definition implies that  $\mathbf{r}_{m-1}$  and  $t_{m-1}$  are the position and time at which the molecule leaves the domain  $m-1$  to enter the domain  $m$ ).  $Q_{i_{m+1}}(\mathbf{r}, t | \mathbf{r}_m, t_m)$  is the probability that a molecule is located at a position  $\mathbf{r}$  in a domain  $m+1$  at time  $t$  after entering the same domain at a position  $\mathbf{r}_m$  and time  $t_m$ . The subscripts  $i_m$  and  $i_{m+1}$  in  $P_{i_m}$  and  $Q_{i_{m+1}}$  indicate the domain types corresponding to the  $m^{\text{th}}$  and  $m+1^{\text{th}}$  visited domains, respectively (e.g., type a, b, c, d, e, or f in Figure 14). A few remarks are in order to fully understand the above equation.

- In eq 100, the first discrete sum over  $m$  from 0 to  $\infty$  accounts for the fact that the distance  $\mathbf{r}$  traveled over a time  $t$  can correspond to different sets of  $m$  visited domains before ending up in the domain  $m+1$  (with  $m$  taking any integer number of trajectory segments in different domains). Typically, taken as an example, the individual trajectory shown in Figure 14 corresponds to a traveled path made of  $m+1 = 5$  domain visits: b → c → d → c → d. The term  $m=0$  corresponds to a molecule that diffuses by a distance  $\mathbf{r}$  over a time  $t$  while staying within the same domain. On the other hand, the terms  $m \neq 0$  corresponds to a trajectory over a distance  $\mathbf{r}$  traveling through  $m+1$  different domains (even though the same domain can be visited several times as illustrated in Figure 14).
- For a given  $m$ , there are  $2m$  integrals contributing to  $G_s(\mathbf{r}, t)$  in eq 100; each set of two integrals is of the form  $\int_V d\mathbf{r}_k \int_{t_{k-1}}^{\infty} dt_k P_{i_k}(\mathbf{r}_k, t_k | \mathbf{r}_{k-1}, t_{k-1})$ . Each of these terms accounts for the contribution from the trajectory segment within the  $k^{\text{th}}$  visited domain to the total self-correlation function  $G_s(\mathbf{r}, t)$  (we recall that the subscript  $i_k$  indicates the domain type corresponding to the  $k^{\text{th}}$  visited domain). In more detail, for each term, the probability  $P_{i_k}(\mathbf{r}_k, t_k | \mathbf{r}_{k-1}, t_{k-1})$  that the molecule leaves this domain at the position  $\mathbf{r}_k$  at a time  $t_k$  while entering at the position  $\mathbf{r}_{k-1}$  at a time  $t_{k-1}$  is integrated over the time  $t_k$  (with  $t_k$  going from  $t_{k-1}$  to  $\infty$ ) and over the position  $\mathbf{r}_k$  (with  $\mathbf{r}_k$  taking any possible value over the entire volume of the porous medium).
- The term  $Q_{i_{m+1}}(\mathbf{r}, t | \mathbf{r}_m, t_m)$  accounts for the fact that after entering the last visited domain, i.e., domain  $m+1$ , the particle remains located in this domain and reaches the position  $\mathbf{r}$  at time  $t$ .
- The second discrete sum in eq 100 corresponds to every combination of possible path sequence  $[i_1, \dots, i_k, \dots, i_m]$  for the  $m$  visited domains before ending in the final  $m+1$  domain—where  $i_k$  corresponds to the domain type (a, b, c, d, e, or f in Figure 14)—before ending up in the domain

$m+1$ . The sets of values taken by  $[i_1, \dots, i_k, \dots, i_m]$  are restricted to integers with different consecutive values. As noted by Roosen-Runge et al.,<sup>67</sup> the formalism above only relies on the assumption that trajectory segments within one domain are uncorrelated with that in the previous/next domains. The heterogeneous dynamics is all included in the values taken by the passage positions and times, i.e.,  $\mathbf{r}_m$  and  $t_m$ , and in the domain connectivity which is accounted for in the values taken by the functions  $P_{i_k}$  (two unconnected domain types  $i_k$  and  $i_{k+1}$  will not contribute to  $G_s(\mathbf{r}, t)$  as no trajectory segment within a domain of type  $i_k$  can lead to the border of a domain of type  $i_{k+1}$ ).

Assuming invariance under time and space translation of the different functions  $P_{i_k}$  and  $Q_{i_k}$ , the integral expression in eq 100 can be used to predict the heterogeneous dynamics in such complex environments. In practice, one calculates the following Fourier–Laplace transform which reads

$$\tilde{I}(\mathbf{q}, s) = \int d\mathbf{r} e^{i\mathbf{q}\cdot\mathbf{r}} \int dt e^{-st} G_s(\mathbf{r}, t) \\ = \sum_{m=0}^{\infty} \sum_{i_1, \dots, i_m} \tilde{P}_{i_1}(\mathbf{q}, s) \tilde{P}_{i_2}(\mathbf{q}, s) \dots \tilde{P}_{i_m}(\mathbf{q}, s) \tilde{Q}_{i_{m+1}}(\mathbf{q}, s) \quad (101)$$

with  $\forall k$ :

$$\tilde{P}_{i_k}(\mathbf{q}, s) = \int d\mathbf{r} e^{i\mathbf{q}\cdot\mathbf{r}} \int dt e^{-st} P_{i_k}(\mathbf{r}, t) \\ \tilde{Q}_{i_k}(\mathbf{q}, s) = \int d\mathbf{r} e^{i\mathbf{q}\cdot\mathbf{r}} \int dt e^{-st} Q_{i_k}(\mathbf{r}, t) \quad (102)$$

Let us consider a porous medium made of two domain types *a* and *b*. Typically, in the context of the present review, these two domains can correspond to domains within a porous particle and outside the porous particle or to different porosity types within the same porous particles. As treated in detail in ref 67, for such two domain systems, eq 101 leads to

$$I(q, s) = \sum_{k=0}^{\infty} (\tilde{P}_a \tilde{P}_b)^k \times [c(\tilde{Q}_a + \tilde{P}_a \tilde{Q}_b) + (1 - c)(\tilde{Q}_b + \tilde{P}_b \tilde{Q}_a)] \\ = \frac{c(\tilde{Q}_a + \tilde{P}_a \tilde{Q}_b) + (1 - c)(\tilde{Q}_b + \tilde{P}_b)}{1 - \tilde{P}_a \tilde{P}_b} \quad (103)$$

where  $c = P_a(q, t=0)$  is the initial concentration in domain *a*. Note that we omit in the above equation to explicitly write the function dependence, i.e.,  $P_{a,b} = P_{a,b}(q, s)$ .

To predict the heterogeneous dynamics using the formalism above, one needs to provide simple expressions or determine using molecular simulation the functions  $P_{a,b}(r, t)$  and  $Q_{a,b}(r, t)$ . As far as formal expressions are concerned, a simple treatment consists of assuming that the switching probability  $\psi_{a,b}(t)$ , i.e., the probability that a molecule switches after a time  $t$ , and the diffusion propagator  $g_{a,b}(r, t)$ , i.e., the probability that a molecule diffuses by a distance  $r$  over a time  $t$ , are independent of each other. With these approximations, the probability distributions  $P_{a,b}(r, t)$  are given by the probability that the molecule diffuses by  $r$  over a time  $t$  multiplied by the probability that the molecule switches to a different domain at time  $t$ . Similarly, the function  $Q_{a,b}(r, t)$  is defined as the probability that the molecule diffuses by  $r$  over  $t$  multiplied by the probability that the molecule

remains within the same domain  $\phi_{a,b}(t) = 1 - \int_0^t \psi_{a,b}(t') dt'$ . These choices lead to the following expressions:

$$\begin{aligned} P_{a,b}(r, t) &= \psi_{a,b}(t) g_{a,b}(r, t) \\ Q_{a,b}(r, t) &= \phi_{a,b}(t) g_{a,b}(r, t) \end{aligned} \quad (104)$$

All the complex underlying phenomena involved in the heterogeneous dynamics are included in the functions  $\psi_{a,b}(t)$  and  $g_{a,b}(r, t)$ . In the most general situations, the switching functions  $\psi_{a,b}(t)$  depend on the geometry and structure of the porous medium with some known rigorous mathematical forms in some specific cases.<sup>67</sup> Similarly, the propagator  $g_{a,b}(r, t)$  can take various forms depending on the type of diffusion involved. A reasonable approximation that applies to many situations is to take for  $g_{a,b}(r, t)$  a Gaussian propagator defined in normal diffusion with its Fourier transform given by  $g_{a,b}(q, t) \sim \exp(-D_s^{a,b} q^2 t)$  where  $D_s^{a,b}$  is the self-diffusivity in domains  $a$  and  $b$ , respectively. With these choices, the Fourier–Laplace transforms of eq 104 write

$$\begin{aligned} \tilde{P}_{a,b}(q, s) &= \tilde{\psi}_{a,b}(s + D_s^{a,b} q^2) \\ \tilde{Q}_{a,b}(r, t) &= \tilde{\phi}_{a,b}(s + D_s^{a,b} q^2) = \frac{1 - \tilde{P}_{a,b}(q, s)}{s + D_s^{a,b} q^2} \end{aligned} \quad (105)$$

which, upon using  $\Gamma_{a,b} = D_s^{a,b} q^2$  and insertion into eq 103, leads to

$$\begin{aligned} \tilde{I}(q, s) &= \frac{c}{s + \Gamma_a} + \frac{1 - c}{s + \Gamma_b} \\ &+ (\Gamma_a - \Gamma_b) \frac{\tilde{\psi}_a \tilde{\psi}_b (1 - 2c) + \tilde{\psi}_a c - \tilde{\psi}_b (1 - c)}{(1 - \tilde{\psi}_a \tilde{\psi}_b)(s + \Gamma_a)(s + \Gamma_b)} \end{aligned} \quad (106)$$

In this equation, the third term carries all the dependency on the switching functions  $\tilde{\psi}_{a,b}(q, s)$ . On the other hand, the first two terms can be gathered as  $\tilde{I}_{\text{slow}}(q, s)$  as they correspond to the limit defined above for the slow-switching limit which is independent of the switching distributions:

$$\begin{aligned} I_{\text{slow}}(q, t) &= c \exp(-D_s^a q^2 t) + (1 - c) \exp(-D_s^b q^2 t) \\ S_{\text{slow}}(q, \omega) &= \frac{c}{\pi} \frac{D_s^a q^2}{\omega^2 + D_s^{a2} q^4} + \frac{1 - c}{\pi} \frac{D_s^b q^2}{\omega^2 + D_s^{b2} q^4} \end{aligned} \quad (107)$$

Equation 106 is very powerful as it allows describing the dynamics in complex porous media from simple functions that can be estimated using molecular simulation or for which known analytical solutions exist. This formalism can be extended using a transition matrix approach to more complex media that contain, for instance, more than two domain types.<sup>67</sup> Figure 14 illustrates the scattering function  $I_s(q, t)$  expected for a medium containing three domain types ( $a, b, c$ ) as a function of the switching rate  $f$ . As expected based on the approach described above, for a vanishing switching rate, i.e.,  $f \rightarrow 0$ ,  $I_s(q, t)$  follows the slow-switching limit where  $I_s(q, t)$  is the sum of three independent contributions with characteristic times given by  $(D_s^{a,b,c} q^2)^{-1}$ . In contrast, as the switching rate  $f$  increases, the third term in eq 106 becomes important and a single characteristic time that depends on the switching rate as well as on the switching functions is observed.

**4.2.3. Random Walk.** Random walk approaches constitute a powerful class of techniques that can be used to investigate the self-diffusion of molecules in heterogeneous media such as porous materials. In this context, monitoring of particles using “single particle tracking” experiments has become a powerful tool for diffusion measurements.<sup>153</sup> In fact, as will be discussed below, random walk methods allow one to go beyond the framework of self-diffusion as they can be applied to situations where transport is induced by a thermodynamic gradient (i.e., with a nonzero net flow condition). From a very general viewpoint, diffusion and transport in porous materials, and in any heterogeneous medium in general, can be described using the Fokker–Planck equation.<sup>60,154</sup> More precisely, we start with the Smoluchowski equation which applies to the probability  $P(\mathbf{r}, t)$  to find a molecule at a position  $\mathbf{r}$  at time  $t$ :<sup>46</sup>

$$\frac{\partial P(\mathbf{r}, t)}{\partial t} = \nabla \cdot \left[ D_s \frac{\nabla F(\mathbf{r}, t)}{k_B T} + \nabla(D_s P(\mathbf{r}, t)) \right] \quad (108)$$

This equation is analogous to the advection-diffusion equation introduced in Section 2 which describes the variations in space and time of the concentration in a heterogeneous medium. However, in contrast to the advection-diffusion equation, the Smoluchowski equation refers to the molecule distribution  $P(\mathbf{r}, t)$ , i.e., the propagator, so that it relies on a statistical mechanics approach rather than a deterministic picture of the problem. Interestingly, the Smoluchowski equation encompasses very general situations such as Brownian Dynamics as described by the Langevin equation<sup>46</sup> but it is more general as it does not assume any stochastic dynamics *a priori*. In eq 108, the left-hand side term describes the time evolution of the molecule distribution  $P(\mathbf{r}, t)$ . Such an evolution arises from two contributions described in the right-hand side of eq 108. The first term, i.e.,  $\nabla \cdot D_s \nabla F(\mathbf{r}, t) / k_B T$ , is an advection contribution where the molecule distribution  $P(\mathbf{r}, t)$  is transported through a velocity field  $v \sim \nabla F(\mathbf{r}, t) / k_B T$  (in practice,  $F(\mathbf{r}, t)$  is a free energy gradient that can correspond to any thermodynamic quantity like pressure, temperature, etc.). The second term, i.e.,  $\nabla \cdot \nabla [D_s P(\mathbf{r}, t)]$ , describes Fick’s diffusion where the particle distribution evolves because of fluctuations which are explicitly written as dependent on both time  $t$  and position  $\mathbf{r}$ . Equation 108 is a very general expression that allows describing transport, i.e., diffusion and advection, in heterogeneous media under any flow conditions. In particular, as will be discussed below, the formalism briefly described above gives rise to a number of numerical approaches which include random walk strategies for transport in porous materials with different schemes available (continuous time random walk, time domain random walk, etc.).<sup>155</sup>

The Smoluchowski equation is at the heart of random walk approaches to probe self-diffusion in heterogeneous media under no flow conditions (in the absence of an external force, i.e., no thermodynamic field  $F(\mathbf{r}, t)$  is applied). In that case, eq 108 simplifies to yield the diffusion equation with a heterogeneous diffusion coefficient  $D_s$ :

$$\frac{\partial P(\mathbf{r}, t)}{\partial t} = \nabla \cdot [D_s(\mathbf{r}, t) \nabla P(\mathbf{r}, t)] \quad (109)$$

Equation 109 can be interpreted in terms of the density of an ensemble of independent particles whose trajectories are determined by a stochastic differential equation, the Langevin equation. In the general case where  $D_s(\mathbf{r}, t)$  depends on position and/or time, this interpretation is delicate, and requires a careful

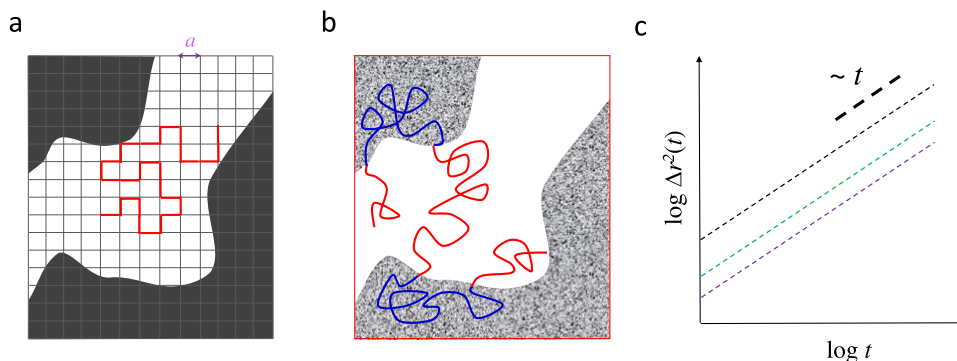


**Figure 15. Random walk models in confined environments.** (a) Random walk on a lattice model mapped onto structural data for a porous material (with dark regions corresponding to nonporous solid domains and white regions corresponding to the porous domains). The red segments correspond to the molecule trajectory as described in this coarse-grained lattice random walk approach. (b) In a constant time random walk (CTRW), a molecule follows an off-lattice trajectory with consists of a succession of trajectory segments within domains of different porosities (gray and white regions in this example). In each domain, the molecule displays a different self-diffusivity  $D_s^\alpha$  so that the distance between two points separated by a constant time step  $\Delta t$  depends on  $D_s^\alpha$  (typically,  $|\Delta r| \sim \sqrt{D_s^\alpha \Delta t}$ ). (c) Regardless of the random walk approach used, the mean square displacement  $\Delta r^2(t)$  scales linearly with time as expected for a molecule obeying Brownian motion.

description of the calculus rule used for integrating the stochastic equation (the so-called Itô–Stratonovich rules discussed in detail in specific textbooks, e.g. ref 154). If one restricts the approach to uniform, time independent  $D_s$ , the equation  $\partial P(\mathbf{r}, t)/\partial t = D_s \nabla^2 P(\mathbf{r}, t)$  is equivalent to the Langevin equation

$$m \frac{d\mathbf{v}}{dt} = -\xi m\mathbf{v} + \delta\mathbf{F}(t) \quad (110)$$

where  $m$  and  $\mathbf{v}$  are the molecule mass and velocity, respectively. In the Langevin equation, which relates to Newton's equation of motion, the left-hand side term is the Brownian molecule acceleration while the right-hand side corresponds to the different forces exerted on the molecule. The contribution  $-\xi\mathbf{v}$  is the average friction term arising upon the motion of the Brownian molecule in the solvent while the contribution  $\delta\mathbf{F}(t)$  is a random, fluctuating force describing the deviation from the average. The random force is zero on average, i.e.,  $\langle \delta F_\alpha(t) \rangle = 0$  with  $\alpha = x, y, z$ . Moreover, because the collisions with the solvent occur on a time scale much shorter than the characteristic time scale corresponding to the change in velocity described in eq 110, the random force  $\delta\mathbf{F}(t)$  must verify that  $\langle \delta F_\alpha(t) \delta F_\beta(t') \rangle = 2\delta F_0 \delta_{\alpha\beta} \delta(t - t')$  where  $\delta F_0$  is the amplitude of the fluctuating force,  $\delta_{\alpha\beta}$  the Kronecker symbol and  $\delta(t - t')$  the Dirac function. With these considerations, the solution of the Langevin equation is known (see ref 46 for more details):

$$\mathbf{v}(t) = \mathbf{v}(0)\exp(-\xi t) + \frac{1}{m} \int_0^t dt' \exp[-\xi(t - t')] \delta\mathbf{F}(t') \quad (111)$$

While  $\langle \mathbf{v}(t) \rangle = 0$  in the absence of external driving force (i.e., thermodynamic field to induce a velocity drift),  $\langle v(t)^2 \rangle$  is nonzero with a value obtained by squaring eq 111:<sup>156</sup>

$$\begin{aligned} \langle v(t)^2 \rangle &= \langle v(0)^2 \rangle \exp(-2\xi t) \\ &+ \frac{1}{m^2} \int_0^t \int_0^t dt' dt'' \exp[-\xi(2t - t' - t'')] \\ &\times \langle \delta\mathbf{F}(t') \delta\mathbf{F}(t'') \rangle \end{aligned} \quad (112)$$

The long time limit,  $t \rightarrow \infty$ , of this equation, i.e.,  $\langle v^2 \rangle \sim 3\delta F_0/m^2\xi$ , must be equal to its value defined via the

equipartition energy theorem,  $\langle v^2 \rangle \sim 3k_B T/m$ . This leads to the important following relationship, which is an expression of the fluctuation–dissipation theorem:  $m\xi k_B T = \delta F_0$ .

To predict the trajectory of Brownian molecules, one can determine the velocity autocorrelation function from eq 111, i.e.,  $\langle v(t)v(t') \rangle = 3k_B T/m \times \exp(-\xi|t - t'|)$ , which can be transformed as described in Section 2.2.2 into

$$\langle |\mathbf{r}(t) - \mathbf{r}(t')|^2 \rangle = \frac{6k_B T}{m\xi} \left( |t - t'| + \frac{1}{\xi} (\exp[-\xi|t - t'|] - 1) \right) \quad (113)$$

This equation shows that the dynamics obeys normal diffusion for times longer than the characteristic time  $\xi^{-1}$ , i.e.,  $t \gg \xi^{-1}$ . In this case, called the “overdamped limit”, the mean square displacement obeys normal diffusion,  $\Delta r^2(t) = 6D_s t$  with a self-diffusion coefficient given by  $D_s = k_B T/m\xi$ , and the evolution of  $P(r, t)$  is described by the Smoluchovski equation.

We have already introduced the concept of random walks when discussing Fickian diffusion at the pore scale in Section 3.1.3. In short, with this model, normal diffusion is probed by considering a molecule, the walker, that jumps from a site to a random neighboring site on a lattice of lattice constant  $a$  within a time  $\delta t$  (Figure 7). The average mean-square displacement of the molecule at a time  $t$  is given by  $\langle r^2(t) \rangle \sim 2dD_s t$  where  $d$  is the dimensionality of the lattice (1D, 2D, etc.) and  $D_s = ka^2$  is the self-diffusivity with  $k$  the hopping rate (all details can be found in Section 3.1.3). The random walk model is very useful in the specific context of diffusion in porous media. While the fundamentals are quite simple and general, different random walk approaches are available to investigate the self-diffusion in porous solids. In what follows, the two following approaches are presented: (1) on-lattice random walk and (2) random walk particle tracking. Other methods such as the correlated random walk theory<sup>157,158</sup> and biased-diffusion calculations for the determination of transport coefficients<sup>159,160</sup> can also be used.

**4.2.3.1. On-Lattice Random Walk.** The most straightforward application of the random walk model to diffusion in porous materials consists of measuring the effective diffusivity. In particular, this method can be used to determine the tortuosity as the diffusivity factor which corresponds to the ratio of the bulk diffusivity to the effective diffusivity within the porous material,

$\tau \sim D_s^0/D_s$ .<sup>161,162</sup> In practice, with this approach, one starts with some structural data in real space of a porous material such as tomography data, transmission electron microscopy data, focused ion beam scanning electron microscopy data, etc. A 2D or 3D lattice is mapped onto such data with each node being assigned a domain type—porous void or solid domain—as shown in Figure 15(a). The effective self-diffusivity  $D_s$  is then determined by simulating the random walk of a molecule onto such a lattice. More in detail, starting from an accessible node chosen randomly, the random walk is simulated by moving the molecule to an adjacent node chosen randomly while incrementing the time by a time step  $\delta t$ . If the chosen node is inaccessible, i.e., belongs to the solid domains, the move is rejected and the molecule remains at the same site until the next move. The effective self-diffusivity  $D_s$  is determined from the slope of the mean-square displacement  $\Delta r^2(t)$  as a function of time  $t$ ,  $D_s = \Delta r^2(t)/6t$  as shown in Figure 15(c). An average over many initial points chosen randomly is needed to obtain data that are representative of the whole porous material, i.e., independent of any particular initial condition. To obtain the tortuosity  $\tau = D_s^0/D_s$ , the effective diffusivity  $D_s$  must be compared to the bulk diffusivity  $D_s^0$  which is equal to  $a^2/6\delta t$  (see Section 3.1.3). The simple method above provides an estimate for the diffusion tortuosity that only accounts for morphological (pore shape) and topological (network connectivity) effects. However, such a geometrical description of a given porous material and its diffusion properties can be completed by including the description of adsorption effects as follows. In a simulation of random walk trajectories in a porous material, when the chosen adjacent node is inaccessible, the move is rejected and a residence time corresponding to a number  $n$  of time step  $\delta$  is added to the current time  $t$ . By increasing the current time  $t$  to  $t + n\delta t$ , adsorption effects can be taken into account. While this approach remains mostly empirical, it is efficient at capturing and disentangling adsorption and geometry effects on the diffusion in complex porous media. As a possible refinement, the effects of adsorption can be captured in a more realistic, i.e., semiquantitative, fashion by choosing the residence time according to the time distribution probability  $\psi_A(t)$  which corresponds to the probability that an adsorption step lasts a time  $t$ .<sup>123,126</sup> (this distribution was defined in the Intermittent Brownian Motion model introduced in Section 3.2.3).

**4.2.3.2. Random Walk Particle Tracking.** The on-lattice random walk approach described above is limited to binary structures made of an accessible (porous voids) and an inaccessible (solid domains) phases. In contrast, it is not suitable for more complex structures where the accessible phase can be made of domains with different diffusion properties. Examples of such heterogeneous media include complex, multiscale porous materials exhibiting domains with different pore sizes. For each domain, the confined fluid will diffuse according to a given self-diffusivity that depends on factors such as pore size and porosity. The random walk particle tracking method (RWPT)<sup>163</sup> is an efficient off-lattice method which allows probing the diffusion in such complex porous solids.<sup>164,165</sup> Like for the on-lattice method described above, such numerical simulations require to have available structural data which can be used to investigate their self-diffusion property according to the random walk model. Such real space data must be of a resolution good enough to allow distinguishing the different diffusing domains. Typically, for hierarchical

porous adsorbents such as mesoporous zeolites shown in Figure 14(a), a segmentation procedure must be performed to assign each pixel to a domain type: microporous, mesoporous, and macroporous domain. When impermeable/inaccessible domains exist such as nonporous patches, an additional domain type must be considered with a corresponding self-diffusivity set to zero. A self-diffusivity value  $D_s^\alpha$  is then assigned to each domain type  $\alpha$ . Such values can be estimated from experimental data available for single-phase materials (zeolite crystal, mesoporous material, etc.) while the diffusivity in macroporous domains can be taken as the value for the bulk phase under the same thermodynamic conditions (pressure, temperature, chemical potential, etc.).

Once the structural data and domain diffusion properties have been set up, a RWPT simulation is carried out as follows. A molecule is placed randomly within the material at a position  $\mathbf{r}$  belonging to a domain type  $\alpha$ . As illustrated in Figure 15(b), the random walk of this molecule is then simulated by moving the molecule by a random vector  $\delta\mathbf{r}$  so that its new position is  $\mathbf{r}' = \mathbf{r} + \delta\mathbf{r}$ . The vector  $\delta\mathbf{r}$  has a random orientation but a norm  $|\delta\mathbf{r}|$  equal to  $\sqrt{6D_s^\alpha\delta t}$  where  $\delta t$  is the time step used to integrate the random walk trajectory. By virtue of the Brownian motion, this definition of the norm  $|\delta\mathbf{r}|$  for the random walk displacement ensures that the self-diffusivity of the particle is equal to  $D_s^\alpha$  if the particle remains in a domain of type  $\alpha$ . Like with any discretized numerical approach, the time step  $\delta t$  must be chosen small enough to ensure that the integration of the random walk trajectory is stable and accurate. If the new position at  $t + \delta t$  belongs to the same domain as the position at time  $t$ , the move is accepted and the time is increased from  $t$  to  $t + \delta t$ . However, if the new position belongs to a different domain, a mass balance condition must be verified to impose that the flow from the domain  $\alpha$  to the domain  $\alpha'$  is equal to the flow from the domain  $\alpha'$  to the domain  $\alpha$ . This condition is very important to impose the ergodicity condition, i.e., the fact that the fraction of time spent by the molecule in domains of type  $\alpha$  is equal to the fraction of molecules occupying these domains. Such a mass balance condition reads<sup>166</sup>

$$p_{\alpha\alpha'}c_\alpha\phi_\alpha D_s^\alpha = p_{\alpha'\alpha}c_{\alpha'}\phi_{\alpha'}D_s^{\alpha'} \quad (114)$$

In this equation,  $c_k$ ,  $\phi_k$  and  $D_s^k$  are the molecule concentration, porosity, and the self-diffusivity in domain  $k$  ( $k = \alpha$  or  $\alpha'$ ).  $p_{\alpha\alpha'}$  is the probability to accept the random move from a position in a domain  $\alpha$  to a position in a domain  $\alpha'$  (and *vice versa* for  $p_{\alpha'\alpha}$ ). The condition given in eq 114 can be understood as follows. The left-hand side describes in a probabilistic fashion the molecular flow from a domain  $\alpha$  to a domain  $\alpha'$ . More in detail, in this contribution,  $c_\alpha\phi_\alpha$  is proportional to the number of molecules in a domain  $\alpha$  so that  $D_s^\alpha c_\alpha\phi_\alpha$  is proportional to the number of molecules attempting to leave the domain per unit of time.  $p_{\alpha\alpha'}$  is the fraction of molecules that eventually succeeds in leaving the domain  $\alpha$  to enter the domain  $\alpha'$  (the same reasoning applies for the right-hand side of the above equation but for the transfer from molecules in a domain  $\alpha'$  to a domain  $\alpha$ ).

With the algorithm above, the dynamics in heterogeneous media can be modeled while properly taking into account the ergodicity principle through the probability to accept or reject at each step the proposed random walk move (whenever it involves switching from one domain to another). In particular, the random walk particle tracking method is very general as it encompasses the first random walk technique described in this

section. Indeed, by considering that solid domains are domains in the RWPT method but with a porosity set to zero, the acceptance probability to have a random walk move leading the molecule from the porosity to the impermeable solid skeleton is zero. In practice, as illustrated in Figures 15(b) and (c), once the rules defined above have been set up, the RWPT simulation is performed and analyzed in a very similar fashion as regular random walk simulations. Like with any random walk approach, the effective self-diffusivity  $D_s$  is determined from the slope of the mean-square displacement  $\Delta r^2(t)$  as a function of time  $t$ ,  $D_s = \Delta r^2/6t$  as shown in Figure 15(c).

**4.2.3.3. Other Random Walk Approaches.** The random walk technique was introduced above in the limited context of diffusion (i.e., in the absence of any advective flow). Here, we intend to describe its generalization to transport situations where both diffusion and advection are at play. Reviews such as ref 155 are available for a general presentation of random walk approaches to diffusion and transport in porous materials. In what follows, we only report some key aspects with a focus on the extension of these techniques to transport with flow conditions.

The particle tracking random walk (PTRW) can be used to treat the general problem of combined diffusive and advective transport. Typically, this is achieved by integrating with a constant time step  $\delta t$  the particle position;  $\mathbf{r}(t)$  at a time  $t$  becomes  $\mathbf{r}(t + \delta t) = \mathbf{r}(t) + \mathbf{v}(\mathbf{r})\delta t + \delta \mathbf{r}$  at a time  $t + \delta t$  where  $\mathbf{v}(\mathbf{r})$  is the local Stokes velocity field while  $\delta \mathbf{r}$  is a vector having a random orientation. While the velocity field  $\mathbf{v}$  can be precalculated using Lattice Boltzmann simulations for instance, the random vector  $\delta \mathbf{r}$  must have a norm governed by the self-diffusion coefficient  $[6D_s\delta t]^{1/2}$  as already discussed above. In heterogeneous materials, the constant time approach used in most random walk approaches can raise important issues, especially when the coexisting diffusion domains have very different associated self-diffusivity coefficients (typically, diffusion will involve either very large displacements in the fast domains or very small displacements in the slow domains). Different strategies are available to overcome such limitations inherent to the constant time approach: namely, the continuous time random walk (CTRW) and the time domain random walk (TDRW). In CTRW, as discussed in ref 155 and references therein, the particle position  $\mathbf{r}(t)$  and time  $t$  are both implemented with position and time increments that depend on the position  $\mathbf{r}$ . Moreover, these increments are coupled through the probability distribution function describing the probability that a molecule at a given position  $\mathbf{r}$  moves by a quantity  $\delta \mathbf{r}$  over a time increment  $\delta t$ . Such a scheme allows transforming both the molecule position and time into continuous variables despite the use of a discrete trajectory integration frame. Such methods can prove to be very powerful to investigate transport and diffusion problems in complex porous media such as hierarchical structures and fractured solids.<sup>167</sup> In particular, owing to their simplicity and versatility, they can be used to model problems such as molecule (solute) dispersion under liquid flow in any porous structure type. In the spirit of the CTRW, albeit different, the TDRW can also be employed to investigate the diffusion and transport of molecules in realistic numerical reconstructions of real porous media. In contrast to CTRW, the TDRW technique assumes—regardless of the particle position  $\mathbf{r}$ —a constant position increment  $|\delta \mathbf{r}|$  and calculates the time increment needed to achieve such a translation.

#### 4.2.3.4. Free Energy and Hierarchical Simulations.

Molecular dynamics is a technique of choice to probe the self-diffusivity of adsorbates in porous media such as nanoporous catalysts. However, in many situations, this technique, which is limited to times of  $\sim 100$  ns up to a few  $\mu$ s depending on the system size, proves to be inefficient at describing self-diffusivity. Such situations are often encountered for bulky molecules in nanoporous materials with very small pores. Even in case of small molecules, probing diffusivity at low temperatures can become a complex task. Let us consider a nanoporous material with a heterogeneity length  $L$ . This length is defined as the typical length which must be explored by the diffusing molecules to obtain data that are representative of the overall macroscopic diffusivity (typically, in the case of zeolites,  $L$  is of the order of the unit cell parameter). In order to efficiently probe diffusivity using molecular dynamics, we can assume that the molecules must diffuse over a distance that is at least twice the length scale  $L$ . The time  $\tau$  required to meet this condition is given by  $\tau \sim 4L^2/D_s$  where  $D_s$  is the self-diffusivity. For a bulky molecule such as cyclohexane, with a diffusivity of the order of  $10^{-12}$  m<sup>2</sup>/s in nanoconfinement,<sup>168</sup>  $\tau \sim 4 \mu$ s, i.e., a value beyond the typical time that can be achieved with molecular dynamics. When regular molecular dynamics does not allow probing diffusivity in nanoporous media, other strategies such as hierarchical simulations are available.<sup>169,170</sup> Such simulations, which consist of determining the diffusivity of an adsorbed molecule using a methodology based on the transition state theory, are very powerful at predicting the slow macroscopic dynamics in complex heterogeneous materials.<sup>171–174</sup> In practice, such molecular simulations rely on a two-step approach. First, one calculates a free energy map to identify all adsorption sites within the host porous solid. Second, using the transition state theory, a kinetic Monte Carlo algorithm or Brownian dynamics simulation is used to determine the macroscopic diffusivity through the motion on this free energy map. Different versions of these hierarchical simulations can be found in the literature. In what follows, we focus mostly on the original version as proposed by Theodorou and co-workers for monatomic<sup>169</sup> and more complex fluids.<sup>170</sup> However, it should be noted that improvements have been proposed in more recent years such as an extension of the transition state theory to adsorbed loadings where collective effects strongly affect the dynamic correction factor  $\kappa$  (see below).<sup>172,175</sup>

In hierarchical simulations, diffusion within the porous material is assumed to occur through uncorrelated jumps from a local free energy minimum  $i$  to another local free energy minimum  $j$ . In more detail, as described in Section 3.1.3, the transition rate  $k_{ij}$  between the two local minima is obtained from their free energies using eq 47

$$k_{ij} = \kappa \frac{k_B T}{2\pi m} \times \frac{\int_{S_{ij}} \exp(-U/k_B T) d\mathbf{r}^2}{\int_{V_i} \exp(-U/k_B T) d\mathbf{r}^3} \quad (115)$$

where  $U$  is the system internal energy and  $m$  the mass of the adsorbed atom. This expression is valid for a monatomic fluid where there is no configurational entropy contribution. For a molecular fluid,  $U$  in the expression above must be replaced by the free energy  $F$  which is probed by considering at a given position  $\mathbf{r}$  the following average over  $N$  configurations  $k$  picked randomly  $F(\mathbf{r}) = -k_B T \ln[\sum_k^N \exp(-U_k/k_B T)/N]$  ( $U_k$  is the internal energy of the  $k^{\text{th}}$  molecular configuration of the fluid molecule).<sup>176</sup> The integral in the numerator in eq 115 is

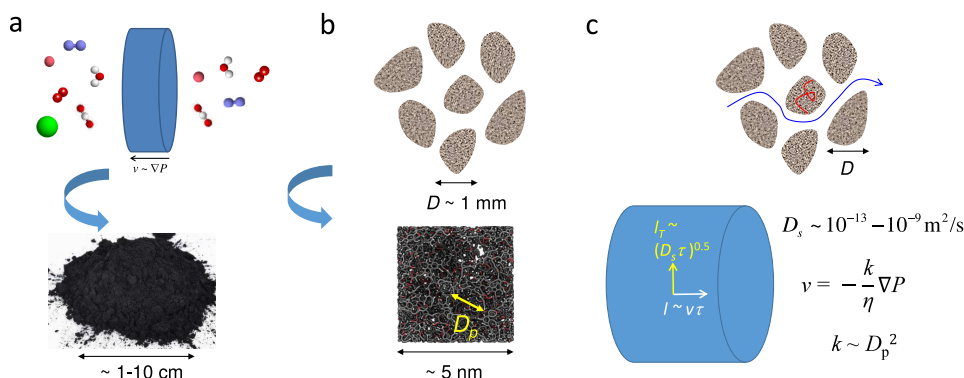


**Figure 16. Transport in nanoporous catalysts.** (a) Schematic representation of gas and liquid transport across a pellet or a column packed with grains of a nanoporous material (blue cylinder). The flow across this system having macroscopic dimensions ( $\sim 1\text{--}10\text{ cm}$ ) is typically induced by a pressure gradient  $\nabla P$  which leads to a flow rate  $v$  proportional to  $-\nabla P$  (in the linear regime). (b) At smaller scales, the pellet or packed column is made up of grains having a size  $D$  of the order of mm or even smaller. Each grain is made of a nanoporous material having very small pores of a size  $D_p$  down to the molecular scale (here, a disordered porous carbon is shown for illustration). We note that  $D$  refers to the grain size in the powder material while  $D_p$  refers to the size of the pores forming the porosity in the grain. (c) Transport in such complex materials, i.e., assemblies of packed grains, involves different flow regimes such as advection and possibly convection in large voids between grains and diffusion and/or advection in the very small porosity within the grains. The competition between advection and diffusion at the smallest porosity scale depends on the self-diffusion coefficient  $D_s$  and the permeability  $k$ . The image of the activated carbon powder is taken from ref 185 (creative commons license).

evaluated at the surface boundary between sites  $i$  and  $j$  while the integral in the denominator is evaluated over the volume around the site  $i$  (typically, a cutoff in energy  $U$  can be used as positions around site  $i$  with strongly repulsive energies do not contribute significantly to the integral in the denominator). The term  $\kappa$  in the above equation is the dynamic correction factor which was already introduced in Section 3.1.3. This factor, which is comprised between 0 and 1, accounts for the fact that only a fraction  $\kappa$  of molecules attempting to jump from site  $i$  to site  $j$  eventually succeeds in doing so. Such a contribution can be estimated using the Bennett–Chandler approach<sup>97</sup> from Molecular Dynamics simulations in which molecules are positioned at the top of the energy barrier with an initial velocity  $v_i(0)$  at time  $t = 0$  selected randomly according to a Maxwell–Boltzmann distribution at temperature  $T$ . With these simulations,  $\kappa$  is determined by counting the number of molecules that ends up in state  $j$  at a time  $t$  later,  $\kappa = \sqrt{2\pi m/k_b T} \langle v_i(0)\theta_k(t) \rangle$  (where  $\theta_k(t) = 1$  if the molecule ends up in site  $j$  and 0 otherwise and  $\langle \dots \rangle$  denotes average over many realizations in the microcanonical NVE ensemble). As discussed by Smit and co-workers,<sup>172,175</sup> the impact of loading, i.e., collective effects, in the determination of  $\kappa$  and therefore in the macroscopic diffusivity in nanoconfinement is an important issue that is usually not accounted for. These authors have proposed an extended version of the transition state theory in which the density dependence of  $\kappa$  is measured to account for such dynamic corrections. In practice, such an extension consists of determining the corrections  $\kappa_{ij}$  for the transition between state  $i$  and  $j$  as a function of loading while taking into account the necessary mass balance condition between these two sites.

As discussed in Section 3.1.3, for a homogeneous medium, i.e., with a constant jump rate  $k$ , the self-diffusivity is readily obtained as  $D_s = ka^2/6$  where  $a$  is the distance between adjacent sites. However, for a heterogeneous medium such as in nanoporous materials where adsorption sites are separated by free energy barriers, the jump rate is not constant and an additional numerical strategy is needed to simulate the molecular dynamics in the underlying free energy landscape. In practice, this is usually achieved using a kinetic Monte Carlo approach as described in detail in refs 169, 173. In this approach, the

probability  $\pi_{ij}(t)$  that a molecule jumps from a site  $i$  to a site  $j$  between the times  $t$  and  $t + dt$  is assumed to follow a Poisson distribution:<sup>177</sup>  $\pi_{ij}(t) = \rho_{ij} \exp(-\rho_{ij}t)dt$ . In this expression,  $\rho_{ij}$  is the transition rate which is given by the jump rate  $k_{ij}$  multiplied by the number of molecules in state  $i$ . As discussed by June et al.,<sup>169</sup> with the underlying Poisson distribution, the average time between two jumps between states  $i$  and  $j$  is  $\tau_{ij} = 1/\rho_{ij}$ . When  $N$  different events, i.e., moves, are possible from a state  $i$ , the Poisson distribution defined above imposes that the overall rate parameter (frequency) is given by  $\rho = \sum_k \rho_k$  where  $\rho_k$  is the rate parameter of the move of type  $k$ . Moreover, the probability that a move  $k'$  occurs first is given by  $P_{k'} = \rho_{k'}/\sum_k \rho_k$ . With these theoretical considerations, the molecular dynamics in the precalculated free energy landscape is simulated as follows. First, considering the overall rate parameter  $\rho$  discussed above, the time interval of the occurrence of the next move is chosen according to the Poisson distribution  $\pi(t) = \rho \exp(-\rho t)$ . In practice, using the technique known as the inverse transform sampling,  $\tau$  is sampled as follows.  $\Pi(t) = \int_0^{t'} \pi(t)dt$  is a cumulative function that describes the probability that a move occurs between a time  $t = 0$  and a time  $t$ . A random number  $e \in [0, 1]$  is chosen such that  $e = \Pi(\tau)$ . In the specific case of a Poisson distribution  $\pi(t)$ , one obtains  $\Pi(t) = 1 - \exp(-\rho t)$  and  $\tau = -\ln(1 - e)/\rho$ .<sup>178</sup> Then, in a second step, a particular move  $k'$  is picked by comparing a random number  $\xi \in [0, 1]$  with the probability  $P = \sum_k P_k$ . Once a given move  $k'$  and a time interval  $\tau$  have been selected, the trajectory of the molecule is updated. As usual, the self-diffusivity is readily obtained from the mean square displacements using the Einstein equation,  $D_s = \lim_{t \rightarrow \infty} \Delta r^2(t)/6t$ .

## 5. GRADIENT-DRIVEN TRANSPORT IN NANOPOROUS MATERIALS

### 5.1. Flow Mechanisms

**5.1.1. Convection, Advection, and Diffusion.** Let us now consider transport phenomena in materials containing nanopores while more complex structures including different

porosity scales will be considered in [Section 6](#). Concerning transport, we here refer to situations where a net fluid flow is induced by a driving force corresponding to a thermodynamic gradient such as a chemical potential, pressure or temperature gradient. In contrast, the diffusion aspects, which were covered in [Sections 3](#) and [4](#), correspond to a no net flow condition. The typical transport experiment considered in the present and subsequent chapters is depicted in [Figure 16\(a\)](#). A pellet or a column packed with grains made up of a nanoporous solid is set in contact with a fluid phase which is then subjected to a pressure gradient. The fluid phase, which flows under the action of the pressure gradient, is either a single component phase or, more generally, a mixture and can exist within the porosity as a gas or a liquid. Provided the pressure gradient  $\nabla P$  is not too large, the fluid response to the driving force is linear so that the flow rate  $v$  is directly proportional to  $\nabla P$ . While transport occurs at the macroscopic scale typically over lengths in the range  $10^{-2} - 10^{-1}$  m, the solid sample at a smaller scale is made of small particles having a size  $D \sim 10^{-6} - 10^{-3}$  m (roughly, for a granular medium, the intergranular spacing is of the same order of magnitude as  $D$ ). In turn, as illustrated in [Figure 16\(b\)](#), these particles are made up of a nanoporous material with pore sizes in the molecular range  $D_p \sim 0.1 - 100$  nm. Generally speaking, as already discussed in [Section 2](#), transport occurs through convection, advection, and/or diffusion.<sup>179</sup> Here, to avoid ambiguity as conventions differ from one scientific community to another, we recall that we refer to the following definitions throughout the present review: (1) convection corresponds to inertial effects (the nonlinear part of the Navier–Stokes equation) and (2) advection corresponds to the transport carried by the flow parallel to the applied driving thermodynamic gradient (linear part of Navier–Stokes equation). For more details, the reader is referred to the corresponding discussion in [Section 2.1](#). From a very general viewpoint, as discussed below, the exact nature of the flow between the different mechanisms above depends on many parameters such as the molecular size of the flowing fluid, the pore size and morphology/topology of the porous network, and the thermodynamic conditions that apply to the system. As an important illustration in the field of membrane and separation science, the flow of water and organic solvents in very narrow pores for reverse osmosis and nanofiltration was found to obey a pore flow regime (i.e., advection) rather than a solution-diffusion regime.<sup>180–184</sup>

Specific situations such as that considered in [Figure 16](#) will be addressed in the next subsection by discussing the influence of pore and particle sizes on transport but also of thermodynamic conditions (corresponding either to fluid in a gas or liquid state). However, generally speaking, regardless of the porous solid and flowing fluid considered, the competition between convection, advection, and diffusion can be assessed using the two following dimensionless numbers: the Reynolds number  $Re$  and the Peclet number  $Pe$ . As discussed in [Section 2.1.1](#),  $Re = \rho v L / \eta$  characterizes the ratio of the convective to the advective contributions in the Navier–Stokes equation given in [eq 1](#) ( $v$  and  $L$  are the flow velocity and characteristic length scale while  $\eta$  and  $\rho$  are the fluid dynamic viscosity and density). For practical situations as illustrated in [Figure 16\(c\)](#), two  $Re$  numbers can be defined as transport involves intragranular [ $L \sim D_p$ ] and intergranular [ $L \sim D$ ] flows. In practice,  $Re$  depends on different parameters, such as the pore/particle size and pressure gradient, which affect the flow rate. However, convection is usually negligible unless large  $D_p$  or  $D$  are considered. In fact, while

intergranular transport can involve a convective contribution (non-negligible  $Re$  because of the large intergranular size  $\sim D$ ), intragranular transport does not include any convective contribution when nanoporous grains are considered ( $Re \ll 1$  because  $D_p \sim 0.1 - 10$  nm). In addition to  $Re$ , the Peclet number is a very useful parameter as it describes the balance between the diffusive and advective contributions to transport in porous materials:  $Pe = vL/D_s$  where  $v$  is the fluid velocity,  $D_s$  the fluid self-diffusion coefficient, and  $L$  the characteristic length scale. Like for  $Re$ , two  $Pe$  numbers can be defined as overall transport involves intragranular [ $L \sim D_p$ ] and intergranular [ $L \sim D$ ] flows. Again, the corresponding  $Pe$  values for a specific problem depend on parameters such as the pressure gradient and particle/pore sizes but, usually, intergranular transport is found to be dominated by the flow, as the velocity is large (large  $Pe$ ). On the other hand, intragranular transport can be advective or diffusive depending on the pore size  $D_p$  and the corresponding self-diffusivity  $D_s$ .

**5.1.2. Gas and Liquid Flows.** In what precedes, the specific conditions to observe convection, advection, and diffusion upon fluid transport in porous media were presented. Using the generic dimensionless numbers  $Re$  and  $Pe$ , the different contributions and flow mechanisms can be predicted as a function of the following fluid, solid, and thermodynamic parameters. The relevant fluid parameters are the viscosity  $\eta$  and density  $\rho$  at the experimental temperature  $T$  while those related to the porous solid are the particle size  $D$ , pore size  $D_p$ , and column/sample size  $L_s$ . As for the thermodynamic conditions, the temperature  $T$  and the pressure gradient  $\nabla P = \Delta P/L_s$  are the key parameters affecting the flow mechanisms. For a given system and thermodynamic conditions, the resulting flow mechanisms will be driven by the fluid self-diffusivity  $D_s$  and flow rate  $v \sim \nabla P$  in the different porosity scales. In what follows, liquid flow is first considered before discussing gas or supercritical fluid flow. This dichotomy fluid/liquid, which can appear as arbitrary at first, is important because of the following. On the one hand, liquids are incompressible or weakly compressible so that the transport parameters  $D_s$ ,  $D_p$ ,  $\eta$ ,  $v$ , etc. at a given temperature can be treated as independent of the average pressure and pressure gradient. In other words, for most practical situations, unless very large pressure drops  $\Delta P$  are used to induce transport, a single relevant flow type will be observed. On the other hand, owing to their non-negligible compressibility, even if other parameters are maintained constant, gas or supercritical fluid flow can pertain to very different mechanisms depending on the density  $\rho$  and, therefore, pressure  $P$ .

**5.1.2.1. Liquids.** Let us consider as an illustrative example the case of a liquid flowing in a complex porous medium as depicted in [Figure 16\(c\)](#). The mean free path  $\lambda \sim 1/\rho\sigma^2$  for a liquid remains nearly constant since  $\rho$  does not vary or only very little with pressure ( $\sigma$  is the molecular diameter of the liquid molecule). In practice, considering typical liquid densities,  $\lambda$  is very small or of the order of magnitude of the pore size  $D_p$ . As a result, as discussed in [Section 2](#), even if the density changes because of compressibility effects when the liquid is subjected to a pressure gradient, the liquid flow remains in the same regime with no change in the underlying transport mechanisms. As discussed in [Section 2.1.1](#), for water at room temperature, the flow in large pores such as in the intergranular pores is advective or convective while the diffusive flow remains negligible. The nature of the flow—being either advective or convective—depends on the pressure drop (or flow rate) imposed as defined in the expression for  $Re$ . In contrast, in small pores such as in the

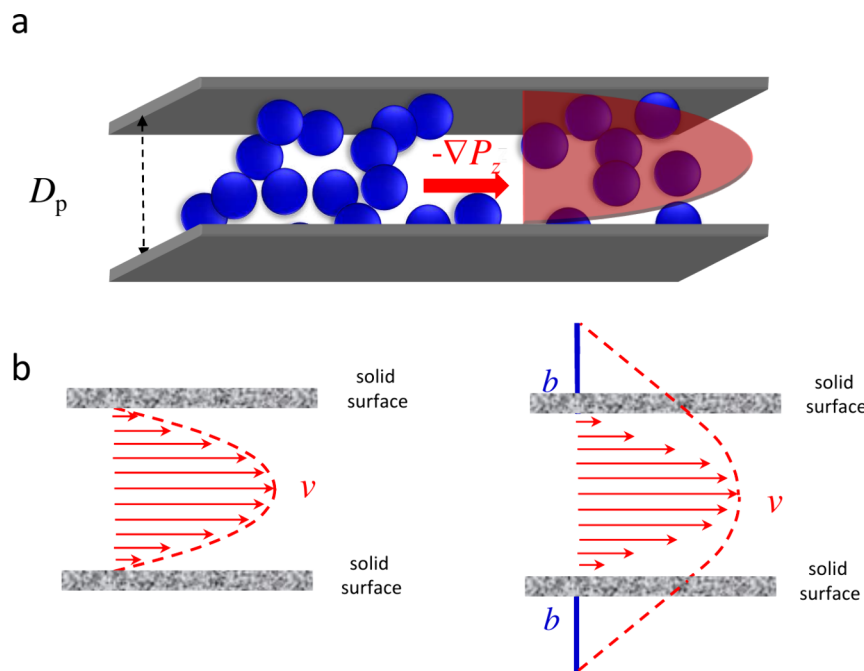


**Figure 17. Poiseuille flow with and without slippage.** (a) Poiseuille flow for fluid molecules (blue spheres) confined in a slit nanopore having a pore size  $D_p$  (gray walls). A parabolic velocity profile (red shaded area) is induced by a pressure gradient  $\nabla P$  parallel to the pore walls.  $x$  and  $z$  are the directions perpendicular and parallel to the pore surface, respectively. (b) Depending on the boundary condition at the pore surface, the velocity parabolic profile  $v_z(x)$  tends to zero at the pore surface—stick or no-slip boundary condition (left panel)—or to a finite value—nonstick or slip boundary condition (right panel). In the latter situation, slippage occurs with a slip velocity  $v_x$  and the corresponding slip length  $b$  is defined as the distance where the extrapolated velocity profile reaches zero:  $-b\partial v_z/\partial x = v_x$ .

intragranular space in Figure 16,  $Re$  is very small so that the liquid flow is either advective or diffusive. On the one hand, the advective flow rate  $v$  is related to the pressure gradient  $\nabla P$  through the permeability  $k$ . As will be discussed further below, the permeability scales with the squared pore size,  $k \sim D_p^2$ . On the other hand, the self-diffusivity decreases with decreasing the pore size  $D_p$  (see Section 2). Therefore, for water at room temperature, when pore sizes are in the range  $D_p \sim 1$ – $100$  nm, the self-diffusivity can vary from  $10^{-13}$  to  $10^{-9}$  m<sup>2</sup>/s (the latter value being close to the bulk diffusivity as no confinement effect is expected for large pores  $D_p \sim 100$  nm). Going back to the situation in Figure 16, the competition between advection and diffusion within the nanoporous particles depends on the flow rate  $v$  and pore size  $D_p$ . To estimate the trade-off between these two mechanisms, it is instructive to consider the typical liquid displacement over a characteristic time  $\tau$ . In the direction parallel to the pressure gradient, advection induced by the pressure gradient  $\nabla P$  in the large porosity displaces the liquid by a distance  $l_T \sim v\tau$  with  $v \sim -k/\eta\nabla P$ . In the direction perpendicular to the pressure gradient, the liquid diffuses by a quantity  $l \sim \sqrt{D_s\tau}$  over the same characteristic time  $\tau$ . The ratio between these two characteristic lengths allows defining the efficiency of a given sample, by imposing that  $l_T = v\tau$  is the sample size. For large  $l_T/l$ , the advective transport is very fast so that diffusion in the nanoporous particles is limited—in other words, most of the flowing liquid does not explore the entire granular particles because it moves across the sample in a very short time. On the other hand, for small  $l_T/l$ , the fluid flow rate in the sample is small and its diffusion through the intragranular space is very efficient.

**5.1.2.2. Gases and Supercritical Fluids.** In contrast to liquids, which are incompressible or weakly compressible, the transport

of gases or supercritical fluids in porous materials is more complex as the density can vary drastically upon changing the applied thermodynamic conditions. Even when constant thermodynamic boundary conditions are applied, the gas flow induced by a pressure gradient implies that the fluid density along the flow varies with the local pressure. Moreover, because of possible adsorption effects, even when low fluid densities/pressures are considered, the fluid density within the porous material can be large. In order to rationalize gas or fluid transport in nanoporous materials, it is instructive to consider the mean free path  $\lambda \sim 1/\rho\sigma^2$  as a function of the applied gas pressure. For gases or supercritical fluids,  $\lambda$  varies drastically depending on the exact pressure conditions considered.  $\lambda$  covers a broad range from values close to the pore size  $D_p$  (“tight gas” conditions) to values very large compared to  $D_p$  (diluted gases). As discussed in Section 2, for a given pore size  $D_p$ , the relevant dimensionless number to describe the change in flow regime with  $\lambda$  is the Knudsen number  $Kn = \lambda/D_p$ .<sup>88</sup> In what follows, the different regimes that can be encountered depending on  $Kn$  are introduced (for a deeper presentation, the reader is also referred to refs 88, 89).

- **Viscous flow,  $Kn < 0.01$ .** In this asymptotic regime, the flow is advective as described using Darcy’s law which will be introduced in Section 5.2.2. The flow is assumed to be laminar so that it only applies to situations corresponding to low  $Re$ .
- **Slip flow,  $Kn \sim [0.01–0.1]$ .** As the Knudsen number increases above 0.01, the gas flows according to a corrected Darcy’s law. Such a correction, known as Klinkenberg effect, will be also discussed in Section 5.2.2. This correction, which leads to faster flow rate compared to that predicted from the regular Darcy’s law,

corresponds to gas slippage at the pore surface because of compressibility effects.

- **Transition flow,  $\text{Kn} \sim [0.1–10]$ .** Transition flow corresponds to a regime where transport occurs both through advection and diffusion. As noted in ref 6, in such conditions, the advective and diffusive fluxes sum up as the two contributions act in parallel in terms of transport. Indeed, while the flow rate associated with advection induces a displacement of the fluid center of mass, diffusion adds up a mean-square displacement to the overall fluid molecular motion. In this transition regime, as the Knudsen number increases, a continuous transition is observed from a pure advective flow toward a pure diffusive flow.
- **Knudsen diffusion,  $\text{Kn} > 10$ .** In this asymptotic regime, the fluid mean free path is much larger than the pore size so that transport occurs through Knudsen diffusion (predominant collisions of the molecules with the pore surface). This regime was discussed at length in Section 2.

## 5.2. Viscous Flow

**5.2.1. Poiseuille Law.** **5.2.1.1. Incompressible Flow.** Let us consider an incompressible liquid confined in a slit pore of width  $D_p$  and length  $L$  as depicted in Figure 17. The liquid flows when subjected to a pressure gradient  $\nabla P$  in the direction  $z$  parallel to the pore surface ( $x$  is the direction normal to the pore surface). Physically, even for pores as small as a few nm in width, the liquid flow in such a configuration is well captured by the Navier–Stokes relation for the momentum conservation given in eq 1.<sup>19,102,186</sup> In the laminar regime, i.e., for small  $\text{Re}$ , the inertial term is negligible,  $\mathbf{v} \cdot \nabla \mathbf{v} \sim 0$  (where  $\mathbf{v}$  is the fluid velocity field), so that the momentum conservation reads<sup>52</sup>

$$\rho \frac{\partial \mathbf{v}}{\partial t} = -\nabla P + \eta \nabla^2 \mathbf{v} \quad (116)$$

where the gravity term  $\mathbf{f}$  was omitted as this contribution is negligible for liquids confined in nanopores. The stationary solution of eq 116 is obtained by imposing  $\partial \mathbf{v} / \partial t = 0$ , which leads to the differential equation  $\nabla P = \eta \nabla^2 \mathbf{v}$ . Considering the symmetry of the configuration shown in Figure 17, the velocity field is parallel to the  $z$  direction with an amplitude that only depends on the position along  $x$ :  $\mathbf{v} = v_z(x) \mathbf{k}_z$  where  $\mathbf{k}_z$  is a unit vector in the  $z$  direction. In practice, the pressure gradient is obtained by imposing a pressure difference  $\Delta P > 0$  over the length of the pore  $L$  so that  $\nabla P = -\Delta P / L$ . A first integration with respect to  $x$  of the latter differential equation leads to  $\partial v_z / \partial x = -x \Delta P / L \eta + C_1$ . The constant  $C_1$  is necessarily equal to zero as the velocity field is symmetrical in  $x = 0$  ( $\partial v_z / \partial x = 0$  for  $x = 0$ ). This allows defining the shear stress  $\sigma_{xz} = -\eta \partial v_z / \partial x$  exerted by a liquid layer located in  $x$  on the adjacent layer in the  $x$  direction,  $\sigma_{xz} = x \Delta P / L$ . This equation shows that the shear stress is maximum at the pore surface  $x = D_p/2$  with a value  $\sigma_{xz}^s = D_p \Delta P / 2L$ .

A second integration with respect to  $x$  of the differential equation above leads to  $v_z(x) = -\Delta P x^2 / 2L\eta + C_2$  where the constant  $C_2$  is obtained by considering the velocity boundary condition at the pore surface. At the macroscopic scale, the boundary condition for a viscous fluid at the solid surface is “no slip”, i.e.,  $v_z(x = D_p/2) = 0$ , so that  $C_2 = \Delta P / 8L\eta \times D_p^2$ . This leads to the following parabolic profile for the velocity field:

$$v_z(x) = \frac{\Delta P D_p^2}{8L\eta} \left[ 1 - \left( \frac{2x}{D_p} \right)^2 \right] \quad (117)$$

The derivation above performed for a cylindrical pore of diameter  $D_p = 2R_p$  leads to the following equation:

$$v_z(r) = \frac{\Delta P R_p^2}{4L\eta} \left[ 1 - \left( \frac{r}{R_p} \right)^2 \right] \quad (118)$$

Regardless of the pore geometry, the flow  $J$  is obtained by multiplying the velocity profile by the fluid density  $\rho$  and integrating over the pore section area (or, equivalently, by multiplying the constant fluid density by the average flow rate  $\bar{v}$ ).

At the microscopic scale, as discussed in ref 187, the velocity boundary condition at the pore surface depends on the fluid wetting properties toward the solid. For perfectly wetting fluids, the strong interactions between the fluid and solid phases impose that the liquid velocity field vanishes at the fixed solid boundary. This situation, which is illustrated in the left panel of Figure 17(b), is described by eq 117. On the other hand, for a partially wetting liquid, the fluid molecules at the pore surface slip so that their velocity  $v_z$  does not vanish as illustrated in the right panel of Figure 17(b). In this case, one defines the so-called slip length  $b$  which corresponds to the distance at which the extrapolated velocity profile reaches zero,  $-b \partial v_z / \partial x = v_z$ . With such a boundary condition for the slit pore geometry  $C_2 = \Delta P D_p^2 / 8L\eta \times [1 + 4b/D_p]$ . In turn, this constant also leads to a parabolic velocity profile but with a shifted boundary condition:

$$v_z(x) = \frac{\Delta P D_p^2}{8L\eta} \left[ 1 + \frac{4b}{D_p} - \left( \frac{2x}{D_p} \right)^2 \right] \quad (119)$$

**5.2.1.2. Compressible Flow.** Regardless of the velocity boundary condition considered, the description above relies on the assumption that the flowing liquid is incompressible. This raises the question of the relevance of the Poiseuille flow to low density fluids such as gases as they are compressible. In this respect, as already discussed in Section 2, the Mach number is a very important dimensionless number defined as the ratio of the flow velocity  $v$  to the sound velocity  $c$ ,  $\text{Ma} = v/c$ . This dimensionless number indicates whether or not the fluid flow can be treated as incompressible. In practice, for  $\text{Ma} < 0.3$ , the flow velocity is smaller than the sound velocity so that the fluid can be regarded as incompressible because the compression wave generated by its displacement does not interfere with the flow. In this case, the derivation provided above for the Poiseuille flow applies even if the flowing fluid is a gaseous phase. In contrast, for  $\text{Ma} > 0.3$ , the fluid compressibility must be taken into account because the compression wave induced by the fluid motion affects the flow. In this case, the derivation provided above no longer applies as the change in the fluid density along the pressure gradient imposed to the flowing fluid leads to a different velocity profile. For a compressible flowing fluid, the molecules slip at the pore surface but it is important to emphasize that such slippage is of different nature as that described for the Poiseuille liquid flow. Indeed, while slippage in the Poiseuille liquid flow occurs from nonwetting surface interactions, it corresponds to a compressibility effect in the case of compressible flows.

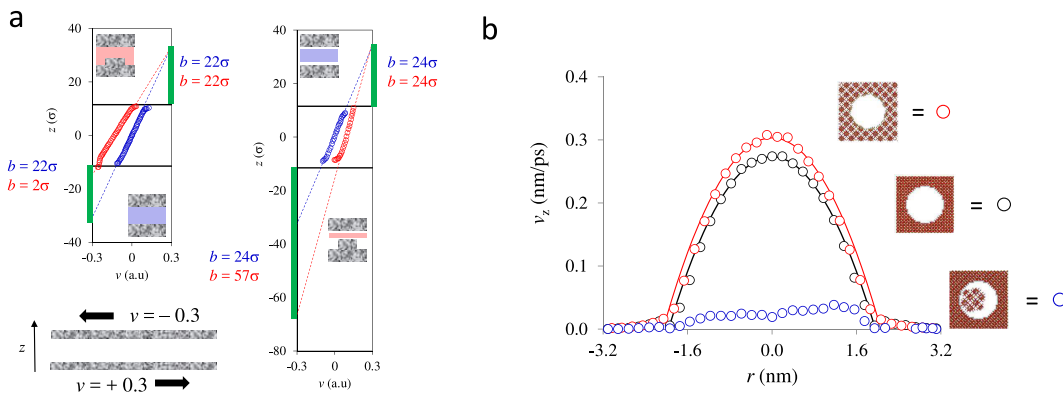


**Figure 18.** Poiseuille flow at molecular surfaces. (a) Velocity profile  $v(z)$  for a wetting Lennard-Jones fluid confined in a slit pore subjected to shear flow. While the upper surface is moved at a constant velocity  $v = -0.3$ , the other surface is moved in the other direction at a constant velocity  $v = +0.3$  (all quantities are reduced with respect to Lennard-Jones units). In the left panel, the velocity profiles for a wetting fluid confined in a slit pore formed by two smooth surfaces (blue data) and in a slit pore formed by a smooth surface and nanopatterned surface (red data) are shown. The slip lengths  $b$  at each wall (upper and lower surfaces) are denoted by the green thick lines and their numerical values are provided. Such slip lengths are determined as the  $z$ -positions at which the extrapolated velocity profiles reach  $v(z) = 0$ . The solid black lines indicate the positions of the upper and lower surfaces. In the right panel, the same data are shown but for a nonwetting fluid. In this case, the confined fluid does not wet the smooth surfaces (as illustrated by the “vacuum layers” between the confined fluid and the surfaces) and the confined fluid does not occupy the troughs at the nanopatterned surface. Adapted with permission from ref 188. Copyright 2003 Springer Nature. (b) Velocity profile for  $\text{N}_2$  confined in a cylindrical silica pore (black circles), a cylindrical silica pore with walls made up of zeolite (red circles) and a cylindrical silica pore containing a zeolite nanoparticle (blue circles). The abscissa  $r$  denotes the radial position with respect to the pore center. In each case, the cylindrical cavity has a diameter  $D_p \sim 4.2$  nm. For the data corresponding to the regular cylindrical pore and the cylindrical pore with walls made up of zeolite, the lines are fits against the Poiseuille flow law. Adapted with permission from ref 189. Copyright 2013 American Chemical Society.

In practice, as discussed in ref 52, the compressible flowing fluid behaves with a slip length  $b$  defined like the slip boundary condition introduced earlier,  $v_z = -b\partial v/\partial x$ . Because of the analogy with the slip length defined in the context of the Poiseuille flow, the flow for a compressible fluid under a pressure gradient  $\Delta P/L$  leads to the same mathematical expression as eq 119. Experimentally, it is observed that the slip length  $b$  scales with the reciprocal of the pressure,  $b = b_0/\bar{P}$  in which  $b_0$  is a constant and  $\bar{P}$  is the average pressure between the upstream and downstream pressures,  $\bar{P} = (P_u + P_d)/2$ . This leads to the following equation for the velocity profile of a compressible flow in a slit pore of a width  $D_p$ :

$$v_z(x) = \frac{\Delta P D_p^2}{8L\eta} \left[ 1 + \frac{4b_0}{D_p \bar{P}} - \left( \frac{2x}{D_p} \right)^2 \right] \quad (120)$$

This equation is an important result for compressible fluids such as gases and supercritical fluids. It is the essence of the Klinkenberg correction which was mentioned for confined gases as an intermediate regime between Knudsen diffusion and viscous flow. While this correction will be discussed in the next section dealing with Darcy's law, a few remarks are in order here. On the one hand, for large  $\bar{P}$ , the slip correction  $\sim b_0/\bar{P}$  becomes negligible and eq 120 is equivalent to Poiseuille flow with no-slip condition. This result is an expected asymptotic regime as fluids become incompressible in the limit of large pressures. On the other hand, for small  $\bar{P}$ , the slip correction known as the Klinkenberg correction in the context of compressible flows, becomes very important as it scales as  $\sim 1/\bar{P}$ .

**5.2.1.3. Structured, Patterned Surfaces.** Most real materials exhibit rough surfaces which depart from the smooth, i.e., structureless, pore wall assumption used to derive the Poiseuille's law above. Surface roughness can refer either to atomistic surfaces or patterned surfaces such as crenelated walls with troughs as shown in Figure 18(a). In the context of the

present work, surface roughness also includes situations illustrated in Figure 18(b) with mesoporous materials ( $D_p \sim 2\text{--}50$  nm) made of microporous walls ( $D_p \leq 2$  nm). These different situations raise the question of surface roughness and, more generally, of the role played by surface disorder on viscous flow in porous materials. In the case of patterned surfaces, this question was addressed using molecular simulation by Cottin-Bizonne et al., who considered the hydrodynamics of a fluid confined in smooth and rough nanopores.<sup>188</sup> More specifically, as shown in Figure 18(a), the flowing properties of the confined fluid were probed by imposing a shear stress. To do so, the lower and upper walls of the slit nanopore were moved at a constant positive and negative velocity, respectively (parallel Couette flow geometry). This numerical setup allows determining the liquid flow but also the hydrodynamic boundary conditions at each pore surface by monitoring the fluid velocity profile.

As shown in Figure 18(a), the authors in ref 188 found different behaviors depending on the wetting properties of the confined fluid with respect to the solid phase. For smooth pore surfaces, the fluid response in terms of velocity profile conforms the classical picture provided by Poiseuille's law. The velocity boundary condition at the pore surface depends on the strength of the fluid/wall interactions with a slip length  $b$  that increases upon decreasing the wetting of the fluid phase. Typically,  $\sigma$  being the fluid molecule size,  $b$  varies from  $22\sigma$  to  $24\sigma$  as the thermodynamic condition switches from wetting to partial dewetting (in the latter case, as schematically illustrated in the right panel of Figure 18(a), a gas phase forms between the solid surface and the confined liquid). In the case of the patterned surfaces, the situation is more complex as the fluid flow properties drastically depend on the wetting scenario. Under wetting conditions, the fluid occupies the whole porosity as it also wets the troughs formed by the patterned surface. As expected, the velocity boundary condition, i.e., slip length at the smooth pore surface, is identical to that obtained for the regular pore with two smooth surfaces ( $b = 22\sigma$ ). However, at the rough

surface, under wetting conditions, the disorder drastically suppresses the slippage as  $b = 2\sigma$ . This result is due to the fact that, when the whole porosity is filled by the liquid, the troughs hinders transport by imposing a boundary condition which slows down the liquid flow in the pore center. Under partial dewetting conditions, an opposite trend is observed. At the smooth pore surface, like under wetting conditions, the slip length is identical to that observed for the regular smooth slit pore ( $b = 24\sigma$ ). However, at the rough surface, because the liquid does not wet the troughs under dewetting conditions, the velocity boundary condition corresponds to a very large slip length  $b = 57\sigma$ . This result can be rationalized by noting that the gas layer formed under partial dewetting reduces drastically the friction at the solid surface. The results above are important as they show, in agreement with available experimental data, that the liquid/solid friction in flowing liquids can be either increased or decreased depending on the surface wetting properties by tuning surface disorder.

As another important illustration of the effect of surface roughness on liquid flow in porous materials, Figure 18(b) shows the parabolic profiles obtained for liquid N<sub>2</sub> in cylindrical silica mesopores.<sup>189</sup> Several porous materials are considered as they pertain to different physical situations encountered in real applications (in all cases, the cylindrical mesopore has a diameter  $D_p = 4.2$  nm). First, as a reference system, a single cylindrical mesopore with dense, impermeable walls is carved out of an amorphous silica block. The silica surface is modeled in a realistic fashion by saturating all O dangling bonds with H atoms in order to form silanol groups. Second, the same silica pore is obstructed by adding into its mesoporosity a supported zeolite nanoparticle having a diameter of about 2 nm. Such a zeolite nanoparticle was prepared from a faujasite zeolite crystal having a silicon to aluminum ratio Si/Al = 15 (the compensating cation is Na<sup>+</sup>). Third, a cylindrical mesopore of a diameter  $D_p = 4.2$  nm was carved out of a faujasite zeolite crystal (in order to compare the different samples, the starting faujasite material is identical to that used to prepare the second system). These three realistic materials allow probing the effect of surface disorder and patterning on liquid flow under conditions relevant to practical applications in catalysis, filtration, etc. In practice, using such atomistic structures, the flow and collective dynamics of the confined liquid is simulated by inducing transport through an external force  $f$  acting on each molecule. This force is an equivalent description of a chemical potential gradient  $f = -\nabla\mu$  or, correspondingly, a pressure gradient for an incompressible liquid (since the Gibbs–Duhem relation states that  $\rho d\mu = dP$ ). Using such non equilibrium Molecular Dynamics simulations, the velocity profile  $v(r)$  can be determined in the course of simulation runs [Figure 18(b)]. As expected, the velocity profile for the single silica mesopore obeys Poiseuille's law. In particular, the velocity profile shown for this system in Figure 18(b) is quantitatively described by a parabolic function as predicted with Poiseuille's law (the fitted viscosity was found to be in reasonable agreement with the experimental value). As expected, as a result of the strong fluid/wall interactions, the velocity of the molecules at the pore surface in the single mesopore is zero (no-slip boundary condition). The velocity profile for the cylindrical mesopore with porous walls also obeys Poiseuille's law. However, compared to the mesopore with impermeable walls, the flow for the model with porous walls is larger due to the fluid molecule transfer between the wall porosity and the mesopore. More precisely, molecules at the mesopore surface have a nonzero velocity which contributes to

enhance the flow within the mesopore. The corresponding slip length,  $b \sim 0.2\text{--}0.4$  nm, is about the size of the fluid molecule ( $\sigma_{N_2} \sim 0.36$  nm). Considering that N<sub>2</sub> fully wets the silica surface, such a slip length induced by the surface microporosity is fully consistent with the results by Cottin-Bizonne et al. reported above.<sup>188</sup> Indeed, in the case of wetting fluids, the slip length at the rough surface was found to be of the order of the trough depth. In the case of the porous wall made of zeolite, the typical pore size is about 0.8 nm—a value which is indeed roughly similar to the observed slip length. While such a slip length seems very small at first, it leads to a large flow enhancement because the flux corresponds to the fluid average velocity multiplied by the pore cross-section area and the fluid density (typically, the slip length observed in Figure 18(b) leads to a 20% flow increase with respect to the no-slip condition). As for the third model shown in Figure 18(b), the velocity profile shows that the nanoparticle insertion into the single mesopore drastically reduces the overall fluid flow as it obstructs the porosity.

**5.2.2. Darcy's Law and Its Extensions.** *5.2.2.1. Darcy's Law.* In the previous section, the constitutive equations for Poiseuille flow, with or without surface slippage, were obtained for pores of a simple geometry (planar or cylindrical pore). The use of a well-defined geometry is required to write a rigorous flow boundary condition—typically the fluid velocity at the pore surface. However, when dealing with most real man-made or natural porous media, the porosity does not consist of pores of a simple geometry. Yet, under the same assumptions as those used to derive the Poiseuille's law—namely the linear response regime, the fluid incompressibility and the pure advective nature of the flow—it is possible to extend its applicability to any porous material. This is the essence of Darcy's law which can be seen as a linear response model of an incompressible liquid submitted to a pressure gradient.<sup>89,179</sup> More specifically, Darcy's law states that the average flow rate  $\bar{v}$  in a given porous material is directly proportional to the pressure gradient inducing transport with a proportionality constant that depends on the fluid viscosity  $\eta$  and the material permeability  $k$ :

$$\bar{v} = -\frac{k}{\eta} \nabla P \quad (121)$$

From this equation, the flow  $J = \rho\bar{v}$  is readily obtained by multiplying the average flow velocity  $\bar{v}$  by the fluid density  $\rho$  (with the latter being constant since the fluid is assumed to be incompressible). In general,  $k$  depends on the pore size but also the pore shape. However, in the case of simple geometries such as for planar and cylindrical pores, the permeability  $k$  must be consistent with the flow predicted using Poiseuille flow. Typically, by averaging over the pore section area the velocity profile determined in eqs 117 and 118, we obtain  $\bar{v} = \Delta P D_p^2 / 12 L \eta$  for the planar geometry and  $\bar{v} = \Delta P D_p^2 / 32 L \eta = \Delta P R_p^2 / 8 L \eta$  for the cylindrical geometry. This implies that the permeability is  $k = D_p^2 / 12$  and  $k = R_p^2 / 8$  for the slit and cylindrical pores, respectively.

Equation 121 can be easily generalized to a disordered porous medium with pores of a distorted shape that are strongly connected. In practice, let us consider a porous solid having a porosity  $\phi$  (defined from the free volume available to the flowing fluid) and pores with a nonregular shape and a tortuosity  $\tau$ . As discussed in Section 4, the tortuosity is defined as the average in-pore fluid flow path divided by the pore length. For a disordered

porous solid, with strongly interconnected pores, the tortuosity is defined as the average path  $\langle L \rangle$  followed by the fluid molecules divided by the sample height  $h$ . Such a tortuosity implies that the physical pressure drop  $\Delta P$  imposed across the sample does not exert a physical pressure gradient  $\nabla P = \Delta P/h$  but  $\nabla P = \Delta P/\tau h$  because the corresponding force applies to a physical length  $\langle L \rangle = \tau h$  instead of  $h$ . As for the flux,  $J = \bar{\rho} \bar{v}$ , it is obtained by multiplying the effective fluid density  $\bar{\rho} = \phi \rho$  (where  $\rho$  is the physical fluid density and  $\phi$  the porosity) by the mean flow rate  $\bar{v}$ . With these considerations, the flux in a given porous material can be defined as

$$J = -\frac{\rho \phi k}{\eta} \frac{\Delta P}{\tau h} \quad (122)$$

In the spirit of this last equation, the Kozeny equation is a generalized Darcy expression which was derived for an assembly of tubes of any arbitrary shape. Such a relation expresses the permeability  $k$  as<sup>35,89</sup>

$$k = \frac{\phi^3}{c_0 s^2} \quad (123)$$

where  $\phi$  is the solid porosity,  $c_0$  is a numerical factor that depends on the shape of the tube section, and  $s$  is the pore surface area per unit of volume. As discussed in ref 35,  $c = 2$  for a circular pore section,  $c = 5/3$  for a regular triangular pore section, and  $c = 1.78$  for a regular square section. In fact, for real isotropic porous materials,  $c$  is an adjustable parameter but  $c = 5$  is often found to work well. In particular, this latter value is found to apply to the specific case of packed beds of solid particles. For such systems, the Kozeny–Carman relation reads<sup>89</sup>

$$k = \frac{1}{5s^2} \times \frac{\phi^3}{1 - \phi^2} \approx \frac{D^2}{180} \times \frac{\phi^3}{1 - \phi^2} \quad (124)$$

where the second equation applies to spherical particles of a diameter  $D$  for which the surface area per unit of volume is  $s = 6/D$  (so that  $5s^2 = 180/D^2$ ).

When using Darcy's equation, regardless of the pore morphological and topological disorders, it is often assumed that the two physical constants in the proportionality factor in eq 121 are decoupled. In more detail, while  $\eta$  only depends on the fluid nature and temperature,  $k$  is assumed to be an intrinsic material parameter (i.e., a fluid independent quantity). This assumption is of practical use to engineering approaches as it allows predicting the permeability  $k$  from a simple in-laboratory transport experiment. However, from a more physical standpoint, there is no fundamental reason to expect the permeability  $k$  to be fluid independent. In fact, as explained above, eq 121 is a simple linear response theory in which the fluid flow rate is assumed to scale with the pressure gradient inducing transport. As will be shown in Section 5.2.3, the viscous approximation breakdown for small pores at the nm scale leads to effective permeabilities that are no longer fluid independent even though the linear response assumption still holds.<sup>53</sup>

**5.2.2.2. Klinkenberg Effect.** As discussed earlier, the Darcy equation—which can be seen as a generalization of Poiseuille flow to any porous medium—relies on the hypothesis that the liquid sticks to the pore surface (no slip boundary condition). However, as discussed in the section devoted to Poiseuille flow, compressibility effects such as with low density gases lead to slippage at the pore surface. Such slippage effects, inherent to compressible systems, are referred to in the context of Darcy's

equation as Klinkenberg correction. Such slippage only manifests itself in pores of a diameter  $D_p$  close to the gas mean free path  $\lambda$  and leads to the following corrected permeability

$$k_c = k_\infty \left( 1 + 8a \frac{\lambda}{D_p} \right) \quad (125)$$

where  $k_\infty$  is the permeability obtained for the liquid phase, i.e., under no-slip condition, while  $a$  is a proportionality factor close to 1 in practice. Because the mean free path scales with the reciprocal of the gas pressure,  $\lambda \sim P^{-1}$ , the latter equation can be recast as

$$k_c = k_\infty \left( 1 + \frac{b}{P} \right) \quad (126)$$

where  $b$  is a constant that depends on the pore size but also the nature of the solid/gas combination. As discussed in Section 5.1.2, the Knudsen number  $\text{Kn} = \lambda/D_p$  is the appropriate dimensionless number to determine whether or not the Klinkenberg correction should be applied.

**5.2.2.3. Darcy–Forchheimer Law.** The advective nature of the fluid flow is an important assumption at the root of Darcy's equation. As for the linear response hypothesis between the pressure gradient and the flow rate, it only applies to low Reynolds number—typically,  $\text{Re} < 10$ . For larger  $\text{Re}$ , such an approximation breaks down and higher order terms in the driving force/flow rate relationship must be included:

$$-\nabla P \approx av + bv^2 + O(v^3) \quad (127)$$

In this equation, known as Forchheimer equation,  $O(v^3)$  encompasses all higher order terms which are assumed to be negligible. Physically, eq 126 describes the fact that the flow resistance becomes non linear as the flow becomes turbulent. In order to account for such effects, using eq 126, a corrected Darcy equation—the so-called Darcy–Forchheimer law—can be proposed

$$-\frac{k}{\eta} \nabla P = v(1 + a'v) = v(1 + a''\text{Re}) \quad (128)$$

where the second equality is obtained by noting that  $\text{Re} = \rho v D_p / \eta$ . As expected, for low  $\text{Re}$ , the second order correction becomes negligible and one recovers the conventional Darcy equation.

**5.2.3. Beyond Viscous Flows.** **5.2.3.1. De Gennes Narrowing.** As discussed in Section 2.2.2, the permeability  $k$  that characterizes the viscous flow of a confined fluid induced by a pressure gradient  $\nabla P$  is strictly equivalent to the collective diffusivity  $D_0$ . More precisely, by writing the flow response of an incompressible liquid to a chemical potential gradient  $\nabla \mu$ , it is straightforward to show that the permeance  $K = k/\eta = D_0/\rho k_B T$ . From a fundamental viewpoint, in contrast to the self-diffusivity, which can be described using simple models such as a free volume theory or a surface diffusion model (see Section 4), modeling the collective diffusivity  $D_0$  and, therefore, the permeance  $K$  of a confined fluid proves to be a complex task. This is due to the fact that, as shown in eq 32, the time autocorrelation function of the fluid center of mass velocity, which defines the collective diffusivity in the Green–Kubo formalism, involves cross-terms between different molecules (in contrast to the self-diffusivity that only involves time correlations of the velocity of individual molecules). Such cross-correlations reflect the molecular interactions within the

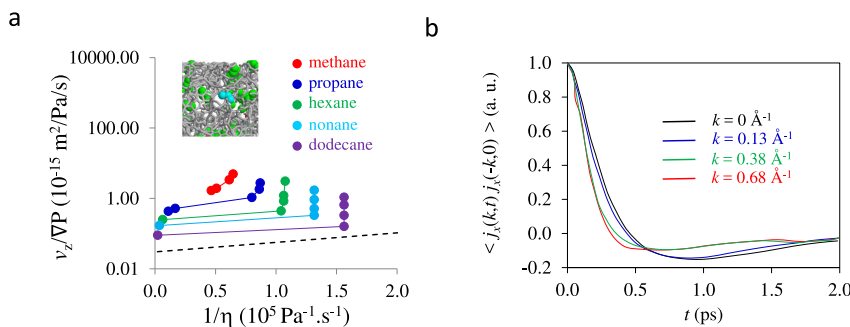


**Figure 19. Permeability and viscous flow in nanopores.** (a) Flow rate normalized to the pressure gradient,  $v_z/\nabla P$ , as a function of the dynamic viscosity  $\eta$  for different alkanes in a disordered nanoporous carbon: methane (red circles), propane (blue circles), hexane (green circles), nonane (cyan circles), and dodecane (purple circles). The dashed line corresponds to Darcy's law as predicted from the typical pore size  $\sim 1$  nm. The inset shows a typical molecular configuration for propane in a disordered porous carbon (the blue and green spheres are the  $\text{CH}_x$  groups of propane while the gray segments are bonds between carbon atoms in the host material). (b) Time autocorrelation function of the transverse current for methane dodecane. Each color corresponds to a given  $k$ -value:  $k = 0, 0.13, 0.38$ , and  $0.68 \text{ \AA}^{-1}$ . These transverse current autocorrelation functions do not follow the expected exponential decay for a simple viscous fluid. Adapted with permission from ref 74. Copyright 2015 Macmillan Publishers Limited under Creative Commons Attribution 4.0 International License (<http://creativecommons.org/licenses/by/4.0/>).

flowing liquid and are, therefore, crucial to calculate the permeance  $K$ . In the case of ultraconfined liquids or in the limit of very low loadings, such cross-correlations are often found to be negligible so that the collective diffusivity can be approximated by the self-diffusivity,  $D_s \sim D_0$ .<sup>74</sup> In this particular situation, the collective diffusivity can be modeled in a simple fashion using the different techniques cited above to describe and predict the self-diffusivity. However, in most practical situations, this approximation does not hold and modeling the collective diffusivity or, equivalently, the permeance remains often empirical.

In fact, besides the Green–Kubo formalism which offers a robust framework to describe the collective diffusivity from measurements such as coherent neutron scattering, there is only one model that allows predicting in a simple way the collective diffusivity: De Gennes narrowing.<sup>190</sup> This model, which was derived to describe the wave-vector  $q$  dependence of neutron scattering in liquids, relates the collective diffusivity of the fluid to the structure factor  $S(q)$  that characterizes its structural ordering.<sup>191</sup> Recently, it was shown that the concept of De Gennes narrowing is a robust formalism to describe the flow of fluids in nanoporous materials.<sup>78</sup> In detail, De Gennes narrowing model constitutes more than a predictive tool for the collective diffusivity in flowing liquids as it describes the wave-vector dependence of the collective diffusion,  $D_0(q)$ , i.e., the collective dynamical response of the fluid to a density fluctuation over a length  $l \sim 1/q$ . To introduce the concept of De Gennes narrowing, let us consider a confined liquid whose local density at a time  $t$  is given by the distribution  $\rho(\mathbf{r}, t)$  (see Chapter 12 in ref 46). The free energy per unit of volume  $\mathcal{F}$ , which only depends on the distribution of molecules, i.e., being a time independent quantity, is a functional form defined as  $\mathcal{F}[\rho(\mathbf{r})]$ . The local chemical potential  $\mu(\mathbf{r})$  can be defined as the derivative of the local free energy with respect to the local density, i.e.,  $\mu(\mathbf{r}) = \delta\mathcal{F}/\delta\rho(\mathbf{r})$  where  $\delta$  denotes the functional derivative. Locally, the mass conservation imposes that  $\partial\rho(\mathbf{r}, t)/\partial t + \nabla \cdot \mathbf{J}(\mathbf{r}, t) = 0$  where the flux  $\mathbf{J}$  is given by the following linear response relation  $\mathbf{J}(\mathbf{r}, t) = -\alpha\nabla\mu(\mathbf{r}, t)$ . With these considerations, mass conservation leads to the following relationship:

$$\frac{\partial\rho(\mathbf{r}, t)}{\partial t} = \alpha\nabla^2 \frac{\delta\mathcal{F}(\mathbf{r}, t)}{\delta\rho(\mathbf{r}, t)} \quad (129)$$

By describing the free energy functional and density distribution using Fourier components, the above equation can be solved in Fourier space as

$$\frac{\partial\rho(\mathbf{q}, t)}{\partial t} = -\alpha q^2 \frac{\delta\mathcal{F}(\mathbf{q}, t)}{\delta\rho(\mathbf{q}, t)} \quad (130)$$

The Fourier transform of the free energy can be written as a sum of uncoupled modes with a quadratic dependence,  $\mathcal{F}(\mathbf{q}, t) = \sum_q \frac{1}{2} A(\mathbf{q}) \rho(\mathbf{q}, t)^2$ . In more detail, this expression assumes that, locally, the free energy profile is composed of harmonic oscillators in the local density  $\rho(\mathbf{q}, t)$ . Inserting this free energy expression into eq 129 leads to the following differential equation,  $\partial\rho(\mathbf{q}, t)/\partial t = -\alpha q^2 A(\mathbf{q}) \rho(\mathbf{q}, t)$  for all  $\mathbf{q}$ , which admits the following solution:

$$\rho(\mathbf{q}, t) = \rho(\mathbf{q}, 0) \exp[-D_0(\mathbf{q})q^2 t] \quad (131)$$

where  $D_0(\mathbf{q}) = \alpha A(\mathbf{q})$  is the wave-vector dependent collective diffusivity. As a result of the energy equipartition theorem, each thermodynamically accessible mode  $\mathbf{q}$  involves a free energy contribution  $\sim k_B T$ , i.e.,  $A(\mathbf{q})\rho(\mathbf{q})^2 \sim k_B T$ , which can be rewritten as

$$S(\mathbf{q}) = \langle \rho(\mathbf{q})\rho(-\mathbf{q}) \rangle = \frac{k_B T}{A(\mathbf{q})} \quad (132)$$

where  $S(\mathbf{q}) = \langle \rho(\mathbf{q})\rho(-\mathbf{q}) \rangle$  is the structure factor and  $\langle \dots \rangle$  denotes ensemble average. Combining eq 132 with  $D_0(\mathbf{q}) = \alpha A(\mathbf{q})$  leads to

$$D_0(\mathbf{q}) = \frac{\alpha k_B T}{S(\mathbf{q})} \quad (133)$$

This is the essence of De Gennes narrowing which can be interpreted as follows. Density fluctuations over a characteristic length  $\sim 1/q$  are frequent [large  $S(q)$ ] if the corresponding free energy cost is low [small  $A(q)$ ]. In turn, because such fluctuations are thermodynamically favorable, the relaxation toward equilibrium is slow [ $D_0(q)$  small]. On the other hand, unfavorable density fluctuations over a characteristic length  $\sim 1/q$  [small  $A(q)$ ] involve a large free energy cost so that they relax rapidly toward equilibrium, i.e.,  $D_0(q)$  is large.

A more refined treatment allows introducing collective interactions. As discussed in ref 192, at infinite dilution, the

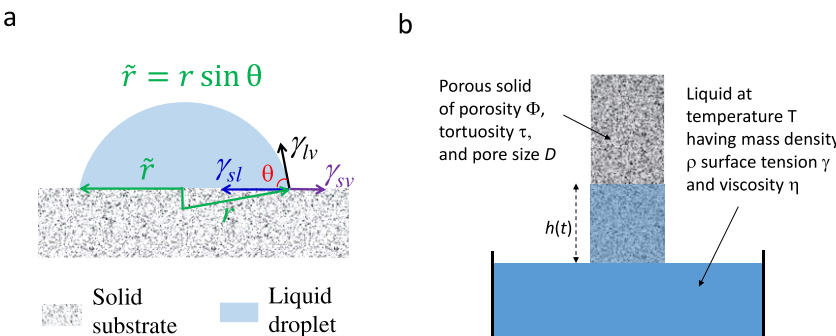


**Figure 20. Imbibition in nanoporous materials.** (a) Schematic representation of a liquid droplet of radius  $r$  at the surface of a solid substrate. The angle  $\theta$  formed by the droplet with the substrate depends on the liquid–vapor ( $\gamma_{lv}$ ), solid–liquid ( $\gamma_{sl}$ ), and solid–vapor ( $\gamma_{sv}$ ) surface tensions via Young equation. (b) A porous solid (gray, stone-like aspect) with pores of a diameter  $D$  is immersed partially into a wetting fluid (blue) at a temperature  $T$ . The porous solid has a porosity  $\phi$  and tortuosity  $\tau$  while the fluid has a density  $\rho$ , surface tension  $\gamma$  and a viscosity  $\eta$ . Owing to the capillary force, which overbalances the friction force, the fluid rises in the porosity of the porous solid with an imbibed height at a time  $t$  that is proportional to the square-root of time,  $h(t) \sim \sqrt{t}$ .

constant  $\alpha \sim D_s/k_B T$  is proportional to the self-diffusivity as collective effects are negligible. However, in finite dilution conditions, the constant  $\alpha$  can be replaced by  $D_s H(q)/k_B T$  where  $H(q)$  are the corrections that need to be taken into account because of collective interactions. This leads to a modified De Gennes narrowing expression:

$$D_0(q) = \frac{D_s \times H(q)}{S(q)} \quad (134)$$

In the case of bulk molecular liquids or colloidal suspensions, De Gennes narrowing is often invoked to provide a rational description of  $q$ -dependent neutron scattering data.<sup>192,193</sup> In particular, several attempts have been made over the years to provide a microscopic picture of De Gennes narrowing effects.<sup>194,195</sup> In contrast, less attention has been devoted to the use of De Gennes narrowing in the specific context of fluids confined in porous media. In this respect, it is interesting to note that Nygård et al. have shown that dense confined fluids possess a wave-vector dependent collective diffusion consistent with De Gennes narrowing. Moreover, in contrast to their bulk counterpart, the bulk structure factor and de Gennes narrowing in confinement were found to be anisotropic.<sup>196</sup> In the case of a nanoconfined fluid, the fluid collective dynamics was shown to be accurately described through De Gennes narrowing.<sup>78</sup>

**5.2.3.2. Deviations from Viscous Flow.** Coming back to Darcy's law given in eq 121, as already stated, it is usually assumed that the permeability  $k$  is an intrinsic property of the host porous material and  $\eta$  equals the bulk value (i.e., interfacial effects are neglected). However, when dealing with nanoporous materials, many experimental and theoretical works report important failure of this hypothesis at the heart of Darcy's approach. As an illustration, Figure 19 shows molecular simulation data of the flow observed for different alkanes—methane, propane, hexane, nonane, and dodecane—in the disordered porosity of a host nanoporous carbon.<sup>74</sup> These data show the flow rate normalized to the pressure gradient,  $v_z/\nabla P$ , as a function of the fluid viscosity  $\eta$  for different alkanes at various densities. At constant temperature, for the different pressure gradients considered in this study, the confined alkanes were found to flow with a flux obeying the linear response regime, i.e.,  $J \sim -K\nabla P$ . As expected from the fluctuation–dissipation theorem, the proportionality factor  $K$ , known as the permeance, was found to be consistent with the collective diffusivity  $D_0 = K\rho k_B T$  measured using the same confined liquid but under

equilibrium (i.e., no flow condition). However, in contrast to the expected Darcy behavior, the permeability  $k$  depends on the flowing molecule as well as on its fluid density as shown in Figure 19.

For reasons that will become clearer below, the non-Darcy behavior observed in Figure 19 has its roots in the strong adsorption and confinement effects in nanoporous solids. Such effects inherent to fluids confined within nanosized cavities lead to a breakdown of the viscous flow hypothesis by introducing memory effects into the time autocorrelation of the fluid velocity. To identify the origin of this breakdown of viscous flow, it is instructive to probe the transverse component of the fluid momentum fluctuations in Fourier space<sup>46</sup>

$$j_x(k_z, t) = \sum_l m v_x^{(l)}(t) \exp[-ik_z z^{(l)}(t)] \quad (135)$$

where  $x$  and  $z$  are two orthogonal directions and  $m$  is the fluid molecule mass. The sum runs over all molecules  $l$  of the fluid. As discussed in ref 46, for a bulk viscous fluid, the correlation time for momentum must be consistent with the momentum conservation law,  $\rho \partial \mathbf{v} / \partial t = -\nabla P + \eta \nabla^2 \mathbf{v}$ . Solving this equation in Fourier space and in a direction  $x$  normal to the fluid flow (component  $\nabla P_x = 0$ ) leads to the following differential equation,  $\partial j_x(\mathbf{k}, t) / \partial t = -\eta k^2 / \rho j_x(\mathbf{k}, t)$ . In turn, this equation implies that the time correlation function of the momentum Fourier components is of the form:  $\langle j_x(\mathbf{k}, t) j_x(-\mathbf{k}, 0) \rangle \sim \exp(-\eta k^2 / \rho t)$  (where  $\langle \dots \rangle$  denotes statistical ensemble average). For a fluid confined inside a porous solid, the momentum conservation relation in the laminar flow regime, which leads to Darcy's equation, reads

$$\rho \frac{\partial \mathbf{v}}{\partial t} = -\nabla P + \eta \nabla^2 \mathbf{v} - \xi \rho \mathbf{v} \quad (136)$$

where  $\xi$  is the friction parameter at the solid/fluid interface. Solving this equation in the Fourier space and in a direction  $x$  normal to the flow leads to the differential equation  $\partial j_x(\mathbf{k}, t) / \partial t = -(\eta / \rho) / k^2 + \xi j_x(\mathbf{k}, t)$  which admits the following solution:

$$\langle j_x(\mathbf{k}, t) j_x(-\mathbf{k}, 0) \rangle \approx \exp \left[ - \left( \frac{\eta}{\rho} k^2 + \xi \right) t \right] \quad (137)$$

As shown in Figure 19, it was found that the transverse momentum fluctuations of the confined fluids in the disordered nanoporous solid do not follow the behavior expected from eq

137. This demonstrates that the viscous flow approximation at the root of Darcy's equation does not hold in such extreme confinements. This suggests that memory effects such as Mori-Zwanzig functions defined in generalized hydrodynamics should be included (see Chapter 9 in ref 48).

From a fundamental viewpoint, the breakdown of the viscous flow approximation can be rationalized as follows.<sup>16</sup> The use of the continuum conservation law in eq 136 implicitly assumes that there is a time scale separation between the molecular relaxation time  $\tau_R$  of the fluid molecules and the fluid momentum transfer time  $\tau$ . On the one hand, the relaxation time within the fluid is given by the characteristic decay time in the stress tensor since  $\eta = 1/Vk_B T \int \sigma_{\alpha\beta}(t)\sigma_{\alpha\beta}(0)dt$  with  $\alpha, \beta = x, y, z$ . In practice,  $\tau_R$  depends on the nature of the fluid but also on thermodynamic conditions such as temperature and density, but it is typically of the order of  $10^{-12}$  s. On the other hand, the characteristic time for momentum transfer is given by the decay time of the correlation function defined in eq 137:  $\langle j_x(k, t)j_x(-k, 0) \rangle \sim \exp[-t/\tau]$  with  $\tau = [(\eta k^2 + \xi)/\rho]^{-1}$ . In the hydrodynamic limit, the time scale separation, which is inherent to viscous flows, is valid since  $k \rightarrow 0$ , i.e.,  $\tau_R \ll \tau$ . However, for a nanoconfined fluid, momentum transfers occur with characteristic wave vectors  $k \sim 1/L$  where  $L$  is typically of the order of the pore size  $\sim 1$  nm. As shown in ref 16, for such ultraconfined fluids,  $\tau_R \sim \tau$  and the time scale separation leading to the viscous flow description is no longer valid.

### 5.3. Adsorption/Desorption Kinetics

**5.3.1. Liquid Imbibition.** We now consider non stationary problems such as imbibition at a temperature  $T$  of a liquid having a density  $\rho$ , a surface tension  $\gamma_{lv}$  and a viscosity  $\eta$  into a porous solid having a porosity  $\phi$ , a tortuosity  $\tau$  and an average pore radius  $R_p$  (Figure 20). When the porous solid is brought to contact with the liquid, imbibition occurs due to capillary forces.<sup>13,197,198</sup> Let us first assume that the porous solid can be described as an assembly of cylindrical pores having a pore radius  $R_p$ . In order to determine the height  $h(t)$  of the liquid that has penetrated the solid at a time  $t$ , one has to solve the following equation of motion

$$\frac{d(mv)}{dt} = -mg + 2\pi R_p \gamma_{lv} \cos \theta - 8\pi \eta h v \quad (138)$$

where  $m$  is the mass of fluid inside the porous material,  $\theta$  is the contact angle that is characteristic of the liquid/solid couple, and  $v$  is the imbibition velocity. The left-hand side term in the above equation is the rate of change of the momentum of the liquid contained in the pore. The first term on the right-hand side is the gravity term which limits imbibition while the second term is the capillary term (i.e., the driving force for imbibition). As shown in Figure 20(a), the contact angle  $\theta$  depends on the liquid/vapor, liquid/solid and gas/solid surface tensions through Young equation. The last term in the above equation is the viscous (friction) term which is described using Poiseuille–Hagen flow. By noting that the mass  $m = \rho\pi R_p^2 h$  is related to the height  $h$ , the above equation can be rewritten as

$$\rho \frac{d(hv)}{dt} = -\rho gh + \frac{2\gamma_{lv} \cos \theta}{R_p} - \frac{8\eta hv}{R_p^2} \quad (139)$$

This equation can be obtained starting from Poiseuille law for the flow rate  $v$  induced by a pressure gradient  $\nabla P$ ,  $v = -k/\eta \nabla P$  where  $k$  is the permeability. For a cylindrical pore of radius  $R_p$  the latter is  $k = R_p^2/8$  so that Poiseuille equation can be

rewritten as  $v = -R^2/(8\eta) \nabla P$ . Considering that  $\nabla P = \Delta P/h$  for an imbibition height  $h$ , the latter expression can be inverted to arrive at  $\Delta P = -8\eta hv/R^2$ . By noting that the viscous force  $F_v$  acting on the fluid corresponds to the pressure difference multiplied by the pore cross-section area, we can write  $F_v = \Delta P \times \pi R^2 = -8\pi\eta hv$  which is identical to the expression used in eq 138. Equation 139 was derived for a cylindrical pore having a regular, straight section. Extension of eq 139 to a cylindrical pore having a tortuous shape can be done by introducing the tortuosity  $\tau$  in the permeability  $k = R_p^2/8\tau$  where the permeability for a regular cylindrical geometry is recovered for  $\tau = 1$ .<sup>199</sup> Using this definition, the tortuosity describes the fact that the friction force (between the liquid and the porous material) is proportional to the physical length of the pore and not its height. We note that this tortuosity differs from another common definition via the diffusion factor (in the latter, the tortuosity is defined as the ratio of the bulk diffusivity to the diffusivity of the confined liquid taken under the same thermodynamic conditions). After introducing the tortuosity  $\tau$ , eq 139 simply reads

$$\rho \frac{d(hv)}{dt} = -\rho gh + \frac{2\gamma_{lv} \cos \theta}{R_p} - \frac{8\eta\tau hv}{R_p^2} \quad (140)$$

The inertial term  $\rho d(hv)/dt$  only manifests itself in the short-time range.<sup>200</sup> After a rapid transient regime, liquid imbibition becomes stationary and inertia becomes negligible so that eq 140 can be recast as

$$-\rho gh + \frac{2\gamma_{lv} \cos \theta}{R_p} - \frac{8\eta\tau hv}{R_p^2} = 0 \quad (141)$$

For liquid imbibition in a horizontal setup, the gravity term is to be discarded and one arrives at the simple, known solution for eq 141

$$h(t) = \sqrt{\frac{R\gamma_{lv} \cos \theta \times t}{2\eta\tau}} \quad (142)$$

where we used that  $v = \dot{h}$  and  $\int 2h\dot{h}dt = h^2$  (the dot in these notations indicate time derivative). The same derivation can be extended in case the liquid slips at the solid surface as done in ref 201. In case gravity cannot be neglected (vertical experiment), eq 140 can be recast as

$$\dot{h} = \frac{a}{h} - b \quad (143)$$

with  $a = 2\gamma_{lv} \cos \theta R_p / 8\eta\tau$  and  $b = \rho g R_p^2 / 8\eta\tau$ . The solution of eq 143 is obtained by noting that it can be expressed as  $dt/dh = h/(a - bh)$  which leads to the solution:  $t(h) = -a/b^2 \times \ln(1 - bh/a) - h/b$ . Equation 143 can also be solved using Lambert function [ $x = W(x) \exp W(x)$ ] to obtain directly  $h(t)$ .<sup>202</sup> However, for practical purposes, experimental data can be fitted to estimate  $a$  and  $b$  from which  $\tau$  can be inferred since  $a = 2\gamma_{lv} \cos \theta R_p / 8\eta\tau$  and  $b = \rho g R_p^2 / 8\eta\tau$ . Moreover, usually, one measures the mass uptake  $m(t)$  rather than the liquid height  $h(t)$ . However, these two values can be linked in a straightforward way since  $m(t) = \rho A \phi h(t)$  where  $\phi$  is the solid porosity (assumed to be constant throughout the sample),  $A$  the cross-section area of the solid face through which imbibition occurs, and  $\rho$  the liquid density.

**5.3.2. Mass Uptake: Surface, Internal, and External Resistances.** Let us now consider adsorption kinetics which

corresponds to the filling of a porous solid by a fluid phase having a density  $\rho$ . Initially, the solid porosity is either empty or filled with the fluid but at a lower density. In what follows, we present a simple yet representative picture of sorption kinetics into porous solids. For a deeper discussion of the problems at play, the reader is referred to the book by Kärger, Ruthven and Theodorou.<sup>6</sup> From a very general viewpoint, looking at the schematic picture given in Figure 16(b), the dynamical process leading to adsorption involves three mechanisms: transport within the bulk external phase, transport across the interface between the porous solid and external phase, and transport within the porous solid. Identifying the relative importance of these underlying dynamics is a key problem as it allows one to determine the overall adsorption kinetics and the limiting rate. In particular, we emphasize here that the observed mass transfer for a given fluid/material couple results from a competition between the driving force that induces the motion within the material and any resistances arising from surface barriers at the interface or from internal and external diffusion limitations.

From this general viewpoint, the overall resulting transfer occurs by involving subsequent steps in series of the three mechanisms above (transport within the solid porosity, transport through the external phase and transfer across the interface). In the different subsections below, we consider asymptotic limits where one or two of these mechanisms constitute the limiting step. This is for instance the essence of the Linear Driving Force model, where one assumes that external diffusion and in-pore diffusion are very rapid so that surface transfer is the limiting step.<sup>203,204</sup> With these assumptions, the fluid density in the gas phase and within the pores are predicted to be homogeneous and the interface is the bottleneck for gas transfer. Describing how the different regimes combine when an asymptotic limit cannot be taken is a central question in this field. In that context, the effective medium approaches such as those presented in Section 4 are very important. In these strategies, one considers a far field chemical potential gradient (which corresponds to a concentration or pressure gradient applied at the macroscopic level) and then solves the problem of combining external and in-pore diffusion. From a formal viewpoint, the problem can also be solved by using the work by Roosen-Runge et al. which was presented in Section 4.2.2. Finally, engineering-based approaches such as the random walk models described in Section 4.3.2 also offer a relevant numerical strategy. With this approach, one performs numerical simulations of a random walker on domains distributed on a lattice (each domain can be a pore, a wall, or the external phase). The approach is rendered stochastic to include surface transfer limitations by adding mass balance conditions across domains (this is the adsorption isotherm that can be used to ensure that at equilibrium random walkers are distributed according to the free energy landscape) and a probability to overcome the free energy barrier at interfaces.

From a general standpoint, predicting the overall transport in multiscale porous materials combining surface transfer with external and internal transport is a complex issue as the three dynamical mechanisms depend on temperature, fluid density in the external and confined phases, etc. Also, for given thermodynamic conditions, the impact of each dynamical step depends on the partition distribution between the bulk fluid, fluid at the solid/fluid interface, and confined fluid. Typically, for a large bulk crystal, i.e., having a small surface to volume ratio, adsorption kinetics will be mostly governed by the diffusion within the solid phase. On the other hand, the adsorption

kinetics for a very finely divided porous solid (grains at the  $\sim$  nm scale) can be largely controlled by surface barriers.<sup>205–207</sup>

On top of this intrinsic complexity, the situation can be very puzzling depending on the physical chemistry phenomena occurring at the solid external surface and within its porosity. Typically, while physical adsorption is always exothermal, chemisorption and/or chemical reactions within the porosity of the host solid can be either exothermal or endothermal. Moreover, in the latter situation, the existence of different species, which can convert from and into each other, raises the question of additional transport driving forces arising from local concentration gradients. In any case, the existence of exothermal or endothermal processes makes the general solution of adsorption kinetics very complex. Because a general presentation of this problem is beyond the scope of this review, we invite those interested in more details to read reference documents such as Chapter 6 of ref 6. In what follows, we provide the main elements by considering the following situation. We assume that the time scale for heat dissipation within the porous solid and adsorbed phase is short compared to that involved in adsorption kinetics so that the problem can be assumed to be isothermal. Moreover, by restricting the problem to low loadings and small concentration changes inducing sorption kinetics, the diffusivity can be assumed to be constant (i.e., no loading dependence of the transport coefficients). In the rest of this subsection, we present in the following order: diffusion at and across the interface between the porous solid and the fluid external phase, diffusion within the host porous solid, and diffusion in the external fluid phase. The coupling between these different mechanisms can be also treated formally with different possible combinations (namely, combination of surface diffusion and in-pore diffusion or combination of in-pore diffusion and diffusion in the external phase). For the sake of clarity, we do not treat these coupled regimes in what follows as specialized documents are available on the topic. However, the specific example of combined surface and in pore diffusion is discussed in Section 5.3.3 where available molecular simulation techniques to probe transport mechanisms and diffusion barriers are presented.

**5.3.2.1. Transfer at the Interface.** In what follows,  $\rho$  denotes the fluid density or concentration in the bulk external phase while  $n$  refers to the density (concentration) of the adsorbed phase in the porous solid. Initially, the porous solid is filled with an adsorbed phase having a density  $n_0$  in equilibrium with the external fluid at a density  $\rho_0$ . At a time  $t = 0$ , the density in the external fluid is increased (or decreased) from  $\rho_0$  to  $\rho$ . Such a density change is induced by a chemical potential change,  $\Delta\mu$ . Fick's first law, which was introduced in Section 2, allows writing

$$\frac{dn}{dt} = \frac{\rho k_s}{k_B T} \frac{\Delta\mu}{a} \approx \rho k_s \frac{\Delta\rho}{a} \quad (144)$$

where the last expression was obtained by considering the low density regime where  $\mu \sim k_B T \ln \rho$ . In the equation above,  $k_s$  is the mass transfer coefficient—related to the surface diffusivity—while  $a$  is the thickness of the interface across which diffusion occurs. Typically,  $a$  depends on the nature of the surface diffusion process which can be of thermodynamic or geometrical nature. On the one hand, diffusion at the solid external surface can be limited by the so-called fluid external film resistance, i.e., the diffusion of adsorbing molecules through the laminar flow surrounding the solid particles. In this case,  $a$  is simply the volume to surface ratio of the solid particles with  $a = l$  for platelet particles of a width  $2l$  and  $a = R_p/3$  for a spherical particle of

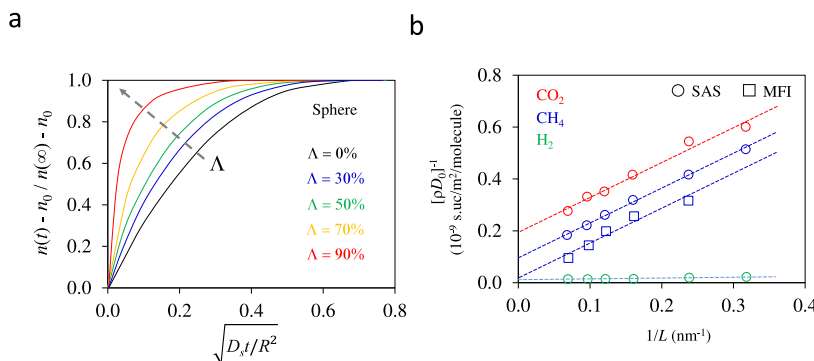


**Figure 21. Mass uptake and surface resistance.** (a) Theoretical mass uptake showing the change in the adsorbed density  $n(t)$  as a function of time normalized to the change in the adsorbed density reached at equilibrium ( $t \rightarrow \infty$ ). These data are predicted by solving for different  $\Lambda$  the diffusion equation for a porous particle having a spherical geometry. The parameter  $\Lambda$  corresponds to the concentration change in the bulk fluid between the initial and final states (see text). Adapted with permission from ref 6. Copyright 2012 Wiley-VCH. (b) Effective collective diffusivity  $D_0$  (proportional to the permeance  $K$ ) as a function of the membrane thickness  $L$  for gas transport across a zeolite membrane. The data show molecular simulation results for different zeolites (circles for SAS and squares for MFI) and gases (red for carbon dioxide, blue for methane, and green for hydrogen). The surface resistance to transport is obtained from such data (see text). The density is given in molecules/unit cell (uc). Adapted with permission from ref 27. Copyright 2018 Royal Society of Chemistry.

radius  $R_p$ . On the other hand, if diffusion is limited by geometrical constraints such as pore partial or complete obstruction,  $a \sim \delta$  where  $\delta$  is the width over which these defects are present at the solid external surface.

Generally speaking, surface diffusion can involve diffusion limitations because of external fluid resistance and geometrical resistance. Because these two resistances act in series, the corresponding mass transfer coefficients,  $k_f$  and  $k_g$ , should be combined into an effective mass transfer coefficient  $\bar{k}_s$ :

$$\frac{1}{\bar{k}_s} = \frac{1}{k_f} + \frac{1}{k_g} \quad (145)$$

This equation was derived in Section 4 when considering the effective diffusivity in composite materials with domains aligned in series with respect to the flow direction. Henry's regime is a special situation where eq 144 can be simplified.<sup>208</sup> In this regime, valid in the limit of very small  $\rho$ , the density of the adsorbed phase is proportional to its bulk counterpart, i.e.,  $n = K_H \rho$  where  $K_H$  is the so-called Henry constant. Using this relationship into eq 144, we obtain  $dn/dt = k_s/K_H \times \Delta n/a$ . If we use the initial conditions  $\rho = 0$  for  $t \leq 0$ , this differential equation leads to the following solution:

$$n(t) = K_H \rho \left( 1 - \exp \left[ -\frac{k_s t}{a} \right] \right) \quad (146)$$

**5.3.2.2. In-Pore Diffusion.** In-pore diffusion, often termed as intraparticle diffusion, corresponds to the diffusion of the adsorbed molecules within the porosity of the host solid. The solution of the diffusion equation leads to different equations depending on the geometry of the porous solid particle. For spherical particles, the diffusion equation can be written in spherical coordinates as

$$\frac{\partial n}{\partial t} = \frac{1}{r^2} \frac{\partial}{\partial r} \left( r^2 D_T \frac{\partial n}{\partial r} \right) \approx D_s \left( \frac{\partial^2 n}{\partial r^2} + \frac{2}{r} \frac{\partial n}{\partial r} \right) \quad (147)$$

where  $D_T = D_0 (\partial \ln f / \partial \ln \rho)_T$  is the transport diffusivity as introduced in eq 36. In the second equality, the self-diffusivity was assumed to be constant upon changing the density  $n$ . The latter is in general valid in the infinite dilution limit where, as discussed in Section 2.2.2, the Darken factor  $(\partial \ln f / \partial \ln \rho)_T = 1$

is constant and  $D_0 = D_s$ . As a result, upon transient sorption kinetics,  $D_T = D_0 = D_s$  does not depend on the location  $r$  within the porosity and can therefore be taken out of the differential equation. Starting from a configuration filled with an adsorbed phase  $n_0$  in equilibrium with the bulk fluid at a density  $\rho_0$ , a sudden change from  $\rho_0$  to  $\rho$  at a time  $t = 0$  induces a change in the adsorbed density  $n(t)$  described by eq 147. In many cases, the sorption starts from  $\rho_0 \sim 0$  in which case the infinite dilution limit on the right-hand side of eq 147 is justified. Using constant  $D_s$ , the solution can be obtained as<sup>209</sup>

$$\frac{n(t) - n_0}{n(\infty) - n_0} = 1 - \frac{6}{\pi^2} \sum_{m=1}^{\infty} \frac{1}{m^2} \exp \left[ -\frac{m^2 \pi^2 D_s t}{R^2} \right] \quad (148)$$

where  $R$  is the radius of the spherical particle and  $n(\infty)$  is the solution at equilibrium ( $t \rightarrow \infty$ ). We recall that this solution is only valid for solid particles having a spherical shape. In the short time limit  $t \rightarrow 0$ , eq 148 leads to the solution  $n(t) - n_0 \sim [n(\infty) - n_0] \times 6\sqrt{D_s t / \pi R^2}$  with a typical dependence in  $t^{1/2}$  as expected for diffusion. In contrast, in the long time limit  $t \rightarrow \infty$ , eq 148 can be approximated by keeping only the leading term  $m = 1$  in the series. This leads to  $n(t) - n_0 \sim [n(\infty) - n_0] \times (1 - 6/\pi^2 \exp[-\pi^2 D_s t / R^2])$  where the exponentially decaying term describes the fact that the adsorption kinetics slows down as the system reaches asymptotically equilibrium (leading to a vanishing driving force  $\Delta n$  for adsorption).

In the above derivation, it was assumed that the concentration  $\rho$  in the external phase remains constant. In practice, if the porous solid has a large adsorption capacity, this implies that the volume of the external phase has to be large enough to verify this condition of constant external density. However, as discussed in ref 6, if this condition is not verified, the general solution of eq 147 is given by

$$\frac{n(t) - n_0}{n(\infty) - n_0} = 1 - 6 \sum_{m=1}^{\infty} \frac{\exp[-D_s p_m^2 t / R^2]}{9\Lambda/(1-\Lambda) + (1-\Lambda)p_m^2} \quad (149)$$

where  $\Lambda = (\rho - \rho_\infty)/(\rho - \rho_0)$  and  $\rho$  is the density imposed in the bulk fluid at  $t = 0$  while  $\rho_\infty$  is the residual bulk density when

the adsorption process is complete. In practice, in the previous solution where the bulk density was assumed to remain constant,  $\Lambda = 0$ . In fact,  $\Lambda$  can be seen as the fraction of fluid molecules added upon the density change during adsorption in the porous solid when equilibrium is approached. As for the constants  $p_m$ , they correspond to the nonzero solutions of the equation  $\tan p_m = 3p_m/[3 + (1/\Lambda - 1)p_m^2]$ . Figure 21(a) shows the result of eq 149 for different values of  $\Lambda$ . As expected, the short and long time results show the expected asymptotic solutions with  $\sim t^{1/2}$  for  $t \rightarrow 0$  and  $\exp(-t)$  for  $t \rightarrow \infty$ .

**5.3.2.3. External Diffusion.** If the diffusion is limited by the diffusion in the external fluid phase, a different mass balance equation must be considered. In this context, we stress that external diffusion includes diffusion in the system's macro-porosity—in fact, external diffusion refers to all molecules that can be treated as equivalent to those in the bulk external phase (therefore, this definition applies to any molecules located in regions where the contribution from surface adsorption is negligible). Instead of eq 147, the overall mass conservation for the adsorbed and external phases reads

$$\epsilon_p \frac{\partial \rho}{\partial t} = \epsilon_p D_s^0 \left[ \frac{\partial \rho^2}{\partial r^2} + \frac{2}{r} \frac{\partial \rho}{\partial r} \right] - (1 - \epsilon_p) \frac{\partial n}{\partial t} \quad (150)$$

where  $D_s^0$  is the self-diffusivity of the external phase (which is assumed to be density independent).  $\epsilon_p$  is the external porosity which is proportional to the volume accessible to the external phase. The last term in eq 150 is a sink term that describes the loss of molecules in the fluid due to mass uptake by the solid. For a system in the low density region, i.e., in the Henry regime, the adsorbed density is  $n = K_H \rho$  where  $K_H$  is the Henry constant. Using this relationship, eq 150 can be recast as

$$\frac{\partial \rho}{\partial t} = \frac{\epsilon_p D_s^0}{\epsilon_p + (1 - \epsilon_p)K} \left( \frac{\partial \rho^2}{\partial r^2} + \frac{2}{r} \frac{\partial \rho}{\partial r} \right) \quad (151)$$

Such an equation leads to the same expression as in eq 148 but with the self-diffusivity of the confined phase,  $D_s$ , replaced by an effective bulk diffusivity,  $\overline{D}_p^0 = \epsilon_p / [\epsilon_p + (1 - \epsilon_p)K_H]$ . Because of the equivalence between eqs 147 and 151, the analytical solution given in eq 148 remains valid but  $D_s/R^2$  must be replaced by  $\overline{D}_p^0/R_p^2$ .

**5.3.3. Transport Barriers.** Like with experimental set-ups, there are different molecular simulation strategies that can be undertaken to identify barriers in transport of confined fluids. In experiments, possible surface barriers can be probed either under stationary flow conditions or under transient kinetic regimes. In more detail, while transport barriers in sorption kinetics are probed using fluid uptake measurements as described in the previous section, those involved in stationary regimes will manifest themselves in experiments at equilibrium such as pulsed-field gradient NMR or neutron scattering (at the mesoscopic  $\sim \mu\text{m}$  length scale for the former and at the  $\sim \text{nm}$  scale for the latter). Similarly, in molecular simulation, transport barriers will be identified under different conditions but always at the microscopic level because of the intrinsic molecular scale involved in these approaches. As will be discussed in this section, such techniques include at equilibrium<sup>210–212</sup> and nonequilibrium<sup>27,213,214</sup> molecular dynamics simulations but also Monte Carlo<sup>215</sup> and free energy<sup>216</sup> approaches. Finally, while this is not treated here for the sake of simplicity, we also emphasize that some authors have investigated the problem of thermal effects

on adsorption/desorption.<sup>217–218</sup> In what follows, molecular simulation strategies that can be used to probe surface barriers in stationary regimes are first considered before treating transient regimes. The end of this subsection is devoted to the important problem of activated transport where surface barriers lead to phenomena over time scales beyond those accessible with molecular simulation. Other molecular simulation aspects that will not be covered below include the investigation of geometrical surface effects in biomimetic systems<sup>219</sup> and sub- or superadditive effects when considering pore array systems.<sup>220</sup> Only a few representative works have been selected rather than a complete overview of the molecular simulation literature available on the topic and we acknowledge that other significant contributions have been reported on phenomena involving surface barriers in transport of nanoconfined fluids.

**5.3.3.1. Transport Barrier in Stationary Flow.** Using molecular simulation approaches, Bhatia and co-workers have considered in detail the surface barriers involved in the transport of fluids through various porous media including carbon nanotube<sup>214,221</sup> and zeolite<sup>27</sup> membranes. In their study on  $\text{CO}_2$  and  $\text{CH}_4$  transport across a zeolite membrane, these authors investigated in depth the existence of surface barriers for various zeolite structures and temperatures.<sup>27</sup> The strategy consists of simulating the stationary flow across a zeolite membrane of thickness  $L$  as induced by a chemical potential gradient  $\nabla \mu$  at constant temperature  $T$ . In practice, as already discussed earlier, the chemical potential gradient is simulated by applying to each molecule the corresponding force,  $f = -\nabla \mu$ . In the framework of Onsager theory of transport, provided the driving force remains small (typically  $\Delta \mu < k_B T$ ), the flux should be proportional to the force inducing transport,  $J = -\rho D_0/k_B T \times \nabla \mu$ , where  $D_0$  is the collective diffusivity and  $\rho$  is the density of the confined fluid (we recall that  $K = D_0/\rho k_B T$  is the permeance as defined in flow experiments). For an infinite zeolite crystal, such molecular simulations allow determining the intrinsic collective diffusivity  $D_0$  which can be compared to its experimental part obtained using coherent neutron scattering. However, for a system with an interface as considered in ref 27, because the surface barrier—if any—acts in series with respect to transport within the zeolite membrane, one expects the effective collective diffusivity,  $\overline{D}_0$ , to obey the following combination rule (see derivation in Section 4)

$$\frac{L}{\rho \overline{D}_0} = \frac{L}{\rho A D_0} + R_s \quad (152)$$

where  $L$  is the membrane thickness and  $A$  the membrane section area through which fluid transport occurs.  $R_s$  is the surface resistance barrier which subdivides into an entrance surface resistance and an exit surface resistance,  $R_s = R_{in} + R_{out}$  (these two resistances add up because they are in series). Using the simple formalism above, by probing the effective collective diffusivity as a function of the membrane thickness, Dutta and Bhatia determined the surface resistance for different gases, temperatures, etc. In more detail, by rewriting eq 152 as  $(\rho \overline{D}_0)^{-1} = (\rho D_0)^{-1} + AR_s/L$ , the surface resistance  $R_s$  can be readily obtained from the data shown in Figure 21(b). As expected, significant differences can be observed between different gases/zeolites with small gases such as  $\text{H}_2$  being unlikely prone to surface barriers at room temperature owing to its small size and weak molecular interactions.

**5.3.3.2. Transport Barrier in Transient Regime.** In the previous example, a stationary flow was considered as would be

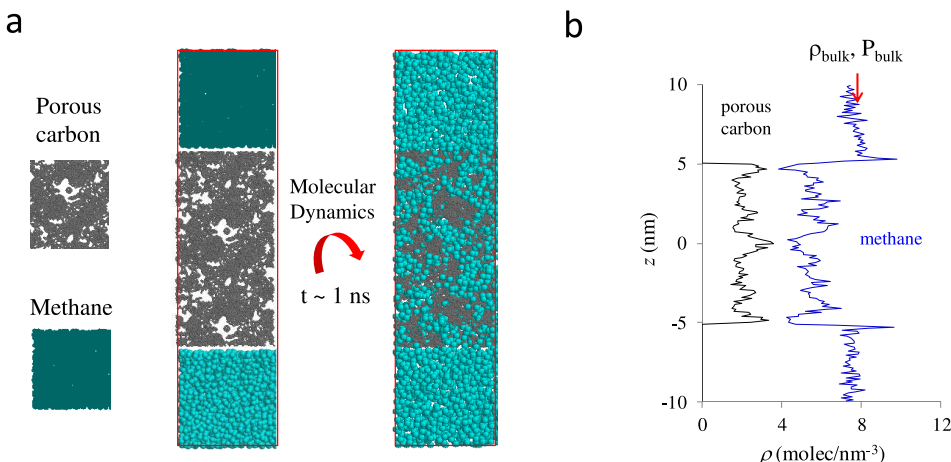


**Figure 22. Mass transfer.** (a) Mass transfer techniques can be used to investigate the adsorption kinetics while accounting for inaccessibility issues (i.e., the fact that part of the porosity might be closed and, therefore, inaccessible to an external fluid phase). In practice, a reservoir of fluid molecules at an initial pressure  $P_0$  and temperature  $T$  is set in contact with a porous solid. A molecular dynamics simulation is then performed such that the fluid molecules diffuse through the fluid/solid interface to fill the porosity—except for porous regions inaccessible to the fluid phase on a time scale corresponding to the typical simulation run ( $1\text{ ns}-1\mu\text{s}$ ). (b) By monitoring the fluid density profile within the porous solid, one can measure the mass uptake  $N(t)$  as a function of time  $t$  (which is obtained by integrating the fluid density profile between boundaries corresponding to the external surfaces of the host porous solid). Eventually, in the long time limit, the adsorbed amount at equilibrium is readily obtained by plotting  $N(t \rightarrow \infty)$  as a function of the final pressure  $P_{\text{bulk}}$  reached in the fluid reservoir (the latter can be determined from the density  $\rho_{\text{bulk}}$  using the bulk equation of state at the temperature  $T$ ).

involved in chromatography experiments for instance. However, in many relevant experimental situations, probing transport barriers involved in adsorption kinetics is very important. A rather straightforward molecular simulation method, which can be easily implemented, is illustrated in Figure 22(a) (see refs 210, 212, 222 for examples where this technique was successfully applied). To determine the fluid adsorption kinetics in a given porous solid (here, a disordered porous carbon), one prepares a porous solid film of a given thickness  $L$  in contact with two fluid reservoirs under given thermodynamic conditions  $T$ ,  $P_0$  (the fluid density is  $\rho_0$ ). First, in the framework of molecular dynamics simulations at constant  $T$ , reflective boundary conditions between the fluid reservoirs and the porous solid are used so that the fluid molecules cannot invade the solid porosity. At a time  $t = 0$ , these boundary conditions are removed so that the fluid invades the porosity—because Molecular Dynamics simulations at constant temperature  $T$  are used, the temperature in the bulk and confined fluids remain constant at all times. On the other hand, the pressure  $P(t)$  in the bulk fluid decreases with time as the number of molecules  $N(t)$  within the porosity increases. By monitoring the density profile in the porous solid as shown in Figure 22(b),  $N(t)$  as a function of  $t$  can be determined. This allows probing the adsorption kinetics under conditions similar to experimental situations. Indeed, in many cases, the experimental sorption kinetics is determined using finite reservoir conditions by measuring the decrease in the bulk external pressure (or molecule concentration for liquid phase adsorption). In particular, for such final reservoir conditions, as shown in ref 6, the solution of the diffusion equation with or without surface transport barriers is known so that adsorption kinetics data can be used to quantitatively assess the different transport mechanisms at play.

As an important consistency check, in the long time regime, the value of  $N(t \rightarrow \infty)$  as a function of the residual pressure in the reservoir  $P(t \rightarrow \infty)$  must fall onto the adsorption isotherm  $N(P)$  (which can be determined using standard molecular simulations such as Monte Carlo simulations in the Grand

Canonical ensemble). In addition to providing useful information regarding the adsorption kinetics for a given fluid/solid system, the simulation strategy described above has another important merit. It allows one to probe accessibility issues which can be severe and lead to much lower fluid concentrations within the porous solid compared to those obtained using methods that ignore such limitations. Indeed, as shown in ref 223, in case of complex disordered porous materials, many pores can be accessible through very narrow necks. In practice, depending on the time scale probed in experiments, these cavities can be considered inaccessible. In that sense, the simple simulation method proposed above allows accounting for such inaccessibility issues. However, when using this method for such purpose, it should be kept in mind that only barriers inaccessible on very short time scales are probed, i.e., the typical time scale accessible to molecular simulation, roughly  $1\text{ ns}-1\mu\text{s}$ . In the context of the transition state theory described in Section 3, if a molecular dynamics simulation is performed over a time  $t_{\text{run}}$  at a temperature  $T$ , this means that only cavities accessible through a free energy barrier  $\Delta F^*$  such that  $t_{\text{run}} > \tau_0 \exp[\Delta F^*/k_B T]$  will be visited on average (we recall that  $\tau_0$  is the characteristic molecular time of the order of  $10^{-12}\text{ s}$ ). This is an important limitation of the method proposed above when probing pore inaccessibility issues in porous solids. In the next subsection, we address this problem by considering free energy techniques which are specifically designed to treat the complex problem of such free energy barriers.

**5.3.3.3. Activated Transport.** The molecular simulation methods proposed above implicitly assume that transport limitations induced by surface barriers occur over time scales shorter than those probed (typically,  $1\text{ ns}-1\mu\text{s}$  with molecular dynamics). While this constraint is often verified for many examples of fluid transport across porous membranes, there is a number of situations where this criterion is not met. In what follows, we provide an example of such complex time scale issues taken from ref<sup>216</sup>. While the situation below might appear as a specific situation at first, it pertains to the general physics of fluid

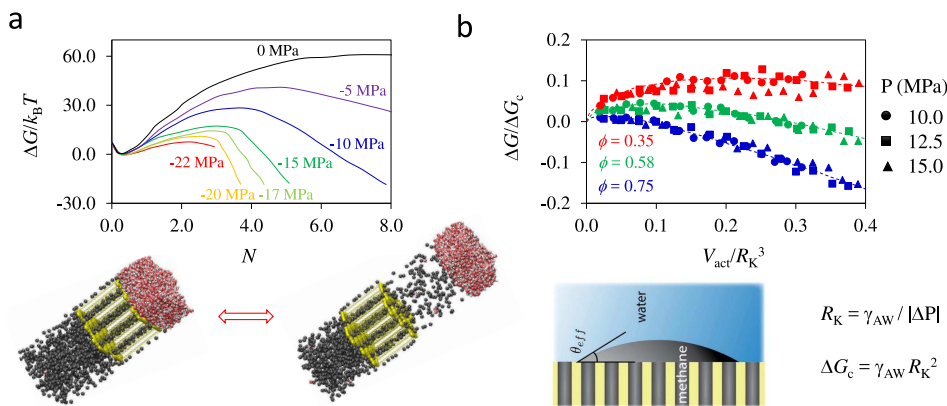


**Figure 23. Activated desorption kinetics.** (a) Free energy  $\Delta G/k_B T$  as determined using molecular simulation combined with umbrella sampling as a function of the amount of methane  $N$  extracted per unit of surface area. These data are obtained for different pressure differences  $\Delta P$  as indicated in the graph. The free energy is shifted with respect to its value  $N \sim 0$  when most methane is trapped within the porous material. The initial ( $N \sim 0$ , before desorption) and final ( $N \gg 0$ , after desorption) states are illustrated in the typical molecular configurations provided below the graph. The porous carbon hosting initially the methane molecules is a nanoporous membrane made up of carbon nanotubes having a pore radius  $r \sim 0.59$  nm and separated from each other by a pore spacing  $D_p \sim 1.7$  nm. (b) Free energy  $\Delta G$  for the methane nucleus formed at the surface of the carbon nanotube membrane covered by water as a function of its volume  $V_{act}$ . The free energy  $\Delta G$  is normalized to the value  $\Delta G_c = \gamma_{AW} R_K^2$  while the volume  $V_{act}$  is normalized by  $R_K^3$  ( $R_K$  is the Kelvin radius  $R_K = \gamma_{AW}/|\Delta P|$ ). These data were obtained by minimizing the surface energy for several pressure differences as indicated in the graph ( $\Delta P = 10, 12.5$ , and  $15$  MPa which correspond to different symbols). The different colors correspond to different membrane porosities  $\phi$ , i.e., pore spacings as indicated in the graph. For a given porosity, all data corresponding to various pressure drops collapse onto a single curve. The dashed lines denote the free energy predicted for a spherical cap geometry with an effective contact angle  $\theta_{eff}$ . The geometry of the contact angle formed by the methane spherical cap (gray phase) at the interface between the carbon nanotube membrane (yellow) and water (blue) is schematically shown below the graph. Adapted with permission from ref 216. Copyright 2016 Macmillan Publishers Limited under Creative Commons Attribution 4.0 International License (<http://creativecommons.org/licenses/by/4.0/>).

immiscibility in confined environments which is relevant to both basic and applied sciences. Moreover, it should be emphasized that the general strategy below, which relies on free energy techniques such as umbrella sampling, can be applied to any transport situation where a non negligible free energy barrier leads to activated transport. As shown in ref 216, such activated transport can lead to very intriguing phenomena which span several orders of magnitude in time and length scales.

Let us consider a porous membrane—made of an array of carbon nanotubes for the sake of simplicity—filled with methane at a given temperature  $T$  and pressure  $P$  as shown at the bottom of Figure 23(a). On the left side of the membrane, a piston is pressurizing a methane bulk reservoir in contact with confined methane to maintain the pressure  $P_\uparrow$  and therefore the chemical potential constant in the system. On the right side of the system, the membrane is fully wetted by water which is maintained at constant pressure through a second piston at a pressure  $P_\downarrow$ . At equilibrium, when the two pressures are equal, i.e.,  $P_\uparrow = P_\downarrow$ , the confined fluid is at rest. Because of the very low solubility of methane in water, the former remains confined within the porous membrane while water remains outside the membrane. Using Molecular Dynamics simulations at constant temperature, methane desorption induced by a pressure drop was simulated by lowering  $P_\downarrow$  to a value inferior to  $P_\uparrow$ . Even for large pressure drops, the amount of desorbed methane as a function of time was found to remain constant for a long time before extraction. Moreover, by repeating the same simulation from different initial configurations, the retention time  $\tau_{act}$  prior to extraction was found to be non reproducible. However, on average,  $\tau_{act}$  was found to scale as  $\tau_{act} \sim \exp(v^* \Delta P/k_B T)$  where  $v^* \sim 1.2 \text{ nm}^3$  is a characteristic molecular volume. This scaling relation suggests that methane desorption through the wet external surface corresponds to an activated process. Even for large pressure drops,  $\Delta P = P_\uparrow - P_\downarrow \sim 10\text{--}25 \text{ MPa}$ ,  $\tau_{act}$  is of the

order of 1–100 ns. Clearly, this time scale falls in the range of Molecular Dynamics simulation times routinely available. As discussed above, this raises the question of the relevance of short Molecular Dynamics runs to probe such activated processes.

For such activated transport, being either relevant to adsorption or desorption, free energy techniques such as umbrella sampling offer a mean to probe transport mechanisms at play even though they involve time scales beyond the microscopic and mesoscopic times. In practice, such simulations consist of biasing the simulation algorithm to force the system to explore large free energy regions of the phase space (for details, the reader is referred to specialized textbooks such as ref 43). Figure 23(a) shows the free energy  $\Delta G/k_B T$  as a function of the amount of desorbed methane  $N$  for different pressure drops  $\Delta P$ . As expected, for  $\Delta P = 0$ , the stable solution corresponds to  $N = 0$  (no desorbed methane). In contrast, for large  $\Delta P$ , the stable solution corresponds to  $N \neq 0$  as the strong driving force leads to methane desorption. By probing different surface areas, pore diameters, etc., it was shown that the free energy barrier involved in the activated desorption process illustrated in Figure 23(a) corresponds to the free energy cost of replacing the initial membrane/water interface [left configuration at the bottom of Figure 23(a)] by a membrane/methane interface and methane/water interfaces [right configuration at the bottom of Figure 23(a)]. Using a mesoscopic model, it was shown that the critical nucleus, which allows triggering the desorption of methane through the wet external surface, corresponds to the hemispherical cap shown in Figure 23(b). As expected in the classical nucleation theory, which allows describing activated processes, this nucleus shape was obtained by minimizing the surface energy at constant volume. The free energy  $\Delta G$  of the methane nucleus is shown in Figure 23(b) as a function of its volume  $V_{act}$  for different membrane porosities  $\phi$  and pressures drops  $\Delta P$ . For each system, the solution corresponds to a hemispherical cap of

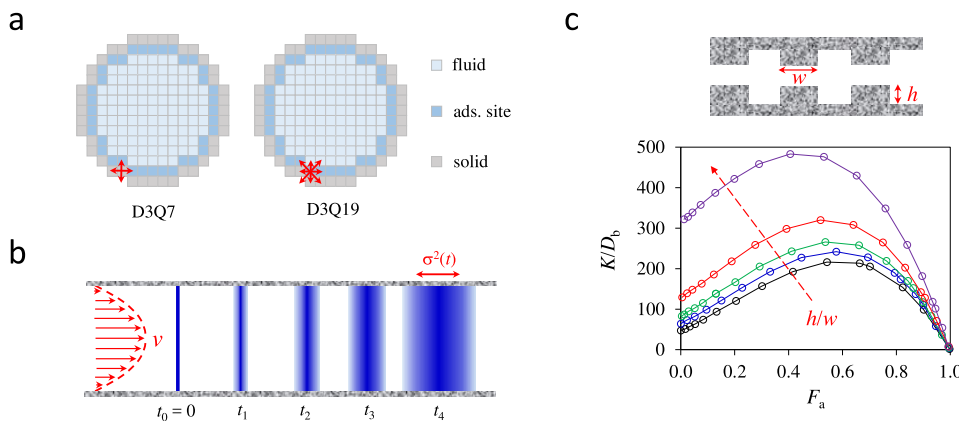


**Figure 24. Lattice Boltzmann method.** (a) Grid mapping onto a cylindrical pore in Lattice Boltzmann calculations. The gray sites are solid domains which are not accessible to the fluid while the blue sites are accessible to the fluid. For the latter, the dark blue sites are adsorption sites as they are located in the vicinity of the solid surface while the light blue sites are nonadsorption sites (bulk-like, i.e., free fluid). Adapted from ref 227. In Lattice Boltzmann simulations, different choices can be made to discretize the velocities as indicated by the codes “D3Q7” and “D3Q19” (see text). (b) Taylor dispersion for adsorbing particles dispersed in a liquid flowing into a cylindrical pore. As expected, the liquid flow obeys a parabolic (i.e., Poiseuille) velocity profile  $v$  with a velocity maximum at the pore center. The concentration profile of adsorbing particles are indicated by the blue color code (with a concentration that increases from light blue to dark blue). At time  $t_0 = 0$ , an infinitely narrow concentration profile of adsorbing particles is injected into the pore center. At a time  $t$  later, the concentration profile broadens with a variance  $\sigma^2(t)$  that scales linearly with time. Adapted from ref 228. (c) Dispersion coefficient,  $K = \lim_{t \rightarrow \infty} \sigma^2(t)/2t$ , normalized to the bulk self-diffusivity of the adsorbing particles,  $D_b$ , as a function of the fraction of adsorbed molecules  $F_a$ . These data are obtained for a slit pore having patterned surfaces as shown in the subfigure above the graph. The pattern corresponds to a crenelated pore and the data shown in the graph are obtained for different aspect ratios  $h/w = 0, 1, 2, 4, 10$ . Adapted with permission from ref 229. Copyright 2015 Royal Society of Chemistry.

methane at the pore surface as illustrated in the bottom panel of Figure 23(b). The effective contact angle of this critical nucleus,  $\theta_{\text{eff}}$ , is close to the solution provided by the Cassie–Baxter equation (this model describes the contact angle on the porous surface as a linear combination of the contact angles on the different regions, i.e., porous and non porous surfaces). As a confirmation that this model rigorously captures the physics of the activated desorption observed in the molecular simulations, the contact angle  $\theta_{\text{eff}}$  was found to lead to free energies that are consistent with those determined using the complete numerical calculations as shown in Figure 23(b).

## 6. GRADIENT-DRIVEN TRANSPORT IN POROUS NETWORKS

### 6.1. Coarse-Grained Models

**6.1.1. Lattice Boltzmann Method.** *6.1.1.1. Boltzmann Equation.* While Onsager theory of transport provides a macroscopic framework to describe transport in porous media, it does not rely on a microscopic description of the underlying dynamics. In contrast, statistical physics provides a set of descriptions—typically based on the Langevin, Boltzmann, and Fokker–Planck equations—which adopt a microscopic point of view by relying on the probability density  $f(\mathbf{r}, \mathbf{v}, t)$ . Accordingly,  $f(\mathbf{r}, \mathbf{v}, t)d\mathbf{r}d\mathbf{v}^3$  is the probability that, at a time  $t$ , a molecule is located in a small volume element  $d\mathbf{r}^3$  around  $\mathbf{r}$  with a velocity in an element  $d\mathbf{v}^3$  around  $\mathbf{v}$ . In the following, we focus on the Boltzmann equation, which was the first equation in which the dynamics of dilute gas molecules was described using the distribution function  $f(\mathbf{r}, \mathbf{v}, t)$  long before the derivation of the Fokker–Planck equation. The Boltzmann equation relates the density distribution current  $\partial f / \partial t$  to the forces exerted on the fluid as well as to the collisions between the fluid molecules<sup>154</sup>

$$\left( \frac{\partial}{\partial t} + \mathbf{v} \cdot \nabla + \frac{\mathbf{F}(\mathbf{r}, t)}{m} \nabla_{\mathbf{v}} \right) f(\mathbf{r}, \mathbf{v}, t) = \left( \frac{\partial f}{\partial t} \right)_{\text{coll}} \quad (153)$$

where  $\nabla$  and  $\nabla_{\mathbf{v}}$  are the gradient operators with respect to position and velocity, and the second and third terms on the left-hand side refer to the diffusive and force contributions, i.e.,  $\mathbf{F}(\mathbf{r}, t)$  is the force acting on the fluid at position  $\mathbf{r}$  and time  $t$ . The right-hand side term in eq 153 corresponds to the change in the distribution function  $f$  because of collisions between fluid molecules. The complexity of the Boltzmann equation, which can be shown to be equivalent to the Fokker–Planck equation, lies in the collision operator  $(\partial f / \partial t)_{\text{coll}}$ . Rigorously speaking, this operator can be expressed using the scattering cross section  $\sigma(\mathbf{v}_1, \mathbf{v}_2 | \mathbf{v}'_1, \mathbf{v}'_2)$  of two molecules colliding at a position  $\mathbf{r}$  with velocities  $\mathbf{v}_1$  and  $\mathbf{v}_2$  before the collision and  $\mathbf{v}'_1$  and  $\mathbf{v}'_2$  after the collision

$$\left( \frac{\partial f}{\partial t} \right)_{\text{coll}} = \int d\mathbf{v}_1 \int d\Theta d\mathbf{v}_2 - \mathbf{v}_1 | \sigma(\mathbf{v}_1, \mathbf{v}_2 | \mathbf{v}'_1, \mathbf{v}'_2) \times [f(\mathbf{r}, \mathbf{v}'_2, t)f(\mathbf{r}, \mathbf{v}'_1, t) - f(\mathbf{r}, \mathbf{v}_2, t)f(\mathbf{r}, \mathbf{v}_1, t)] \quad (154)$$

where  $\Theta$  is the angle formed by the two vectors  $\mathbf{v}'_2 - \mathbf{v}'_1$  and  $\mathbf{v}_2 - \mathbf{v}_1$ . The two integrals in eq 154 denote that all initial velocities  $\mathbf{v}_1$  and  $\mathbf{v}_2$  (given through the angle  $\Theta$ ) must be considered. For a system at local equilibrium,  $(\partial f / \partial t)_{\text{coll}} = 0$ , the distribution function must follow the Maxwell–Boltzmann distribution  $f^{\text{eq}}$

$$f(\mathbf{r}, \mathbf{v}, t)^{\text{eq}} = \frac{\rho}{(2\pi v_T^2)^{d/2}} \exp \left[ -\frac{(\mathbf{v} - \mathbf{u})^2}{2v_T^2} \right] \quad (155)$$

where  $d = 1, 2, 3$  is the dimension of space,  $\rho$  the fluid density,  $\mathbf{u}$  the local fluid velocity and  $v_T = \sqrt{k_B T / m}$  the thermal velocity.

**6.1.1.2. Discretized Boltzmann Equation.** Despite its complexity, the Boltzmann equation can be transformed into a robust and efficient numerical method to describe the transport of fluids in different environments of arbitrary geometry.<sup>224</sup> This technique, which is known as the Lattice Boltzmann method (LBM), relies on a discretized version of the Boltzmann

equation given in eq 153.<sup>225</sup> In more detail, with this technique, both the space position  $\mathbf{r}$  and velocity  $\mathbf{v}$  are discretized. Spatial discretization is achieved by treating the fluid and solid on a lattice so that  $\mathbf{r}$  can only take values corresponding to lattice nodes. As for the velocities, only a set of velocity vectors are treated by considering different propagation directions of the fluid onto the grid.<sup>226</sup> As illustrated in Figure 24(a), the convention  $D_n Q_m$  is a convenient meshing classification which contains all needed information on the space and velocity discretization scheme adopted. On the one hand, the value  $n$  indicates the space dimension so that  $n = 1, 2$ , or  $3$ . On the other hand,  $m$  indicates the number of propagation directions considered. There are only a few values that  $m$  can take for a given  $n$ . For instance, when  $n = 2$ , the smallest possible value is  $m = 5$  (4 nearest neighbor directions and the direction  $\mathbf{v} = 0$  for which the fluid density distribution does not propagate) while the second-smallest value is  $m = 9$ . In the  $D_n Q_m$  convention, these two discretization schemes are referred to as D2QS and D2Q9. For  $n = 3$ , available discretization schemes are D3Q7, D3Q15, D3Q19, etc. For a given space dimension  $n$ , the accuracy of the Lattice Boltzmann method strongly depends on the discretization scheme adopted. A trade-off between a large value of  $m$  leading to high accuracy and a reasonable computational time is usually sought for. Discretization allows replacing the probability distribution  $f(\mathbf{r}, \mathbf{v}, t)$  by its discretized version  $f_i(\mathbf{r}, t)$  where  $i$  corresponds to a propagation velocity  $\mathbf{c}_i$  so that  $i \in [0, m]$  and  $\mathbf{r}$  only takes values corresponding to node positions on the lattice. With this discretized probability distribution, the Boltzmann equation defined in eq 153 can be recast as

$$f_i(\mathbf{r} + \mathbf{c}_i \Delta t, t + \Delta t) = f_i(\mathbf{r}, t) + F_i(\mathbf{r}) + \Omega_i \quad (156)$$

where  $F_i$  corresponds to the external force acting on the fluid at the node position  $\mathbf{r}$  while  $\Omega_i$  is the collision operator introduced above.

As mentioned earlier, generally speaking, the collision operator  $\Omega_i$  is of a complex form. However, it is possible to make some simplifications to render eq 156 feasible and efficient. In the Lattice Boltzmann method, one typically approximates the nonlinear collision operator by the linear BGK operator that makes the local distribution function  $f_i(\mathbf{r}, t)$  relax toward its equilibrium value  $f_i^{\text{eq}}(\mathbf{r}, t)$  over a characteristic time  $\tau$ :<sup>226</sup>

$$\Omega_i = -\frac{1}{\tau}[f_i(\mathbf{r}, t) - f_i^{\text{eq}}(\mathbf{r}, t)] \quad (157)$$

The BGK operator is the simplest collision operator that respects the fundamental conservation laws of mass, momentum, and total and internal energy. For small Mach numbers, upon introducing the sound velocity  $c_s$ , the discrete equilibrium distribution can be written as a power series in  $c_i/c_s$ :  $f_i^{\text{eq}} = w_i \rho [1 + 1/c_s^2 \times \mathbf{c}_i \cdot \mathbf{u} + 1/2c_s^4 \times (\mathbf{c}_i \cdot \mathbf{u})^2 - u^2/c_s^2]$  ( $w_i$  is a coefficient that accounts for the weight of the propagation direction  $i$  in a given lattice geometry). In the Lattice Boltzmann method, the evolution of the probability distribution  $f_i$  is determined using eqs 156 and 157 which allow determining key quantities at each site  $\mathbf{r}$  such as the mass density  $\rho = \sum f_i$ , momentum density  $\rho \mathbf{u} = \sum c_i f_i$  and momentum-flux tensor  $\Pi_{\alpha\beta} = \sum c_{i\alpha} c_{i\beta} f_i$ . For more detailed information on the Lattice Boltzmann method, the reader is referred to the text book by Krüger et al.<sup>226</sup> The Lattice Boltzmann method is receiving increasing attention owing to its broad applicability to fluid flow

in porous media or in the vicinity of solid particles. As a very classical example, Figure 24(b) illustrates the solution obtained using the Lattice Boltzmann method to the problem of Taylor dispersion.<sup>228</sup> Let us consider a regular slit or cylindrical pore in which a liquid (solvent) is subjected to a pressure gradient. As discussed earlier, the solution of this simple problem corresponds to Poiseuille flow where the liquid velocity profile is parabolic with a maximum value in the pore center. At a time  $t = 0$ , solute particles are injected in the pore at a position  $x = 0$  with a concentration profile given by a delta function,  $c(x) = c_0 \delta(x - x')$  ( $x$  is the direction parallel to the pressure gradient inducing the liquid flow). The solution of this problem, known as Taylor dispersion, is given by a concentration peak being transported at a velocity equal to the average liquid velocity while its variance  $\sigma^2(t)$  increases linearly with time  $t$ .

**6.1.1.3. Adsorption and Moment Propagation Scheme.** The Lattice Boltzmann method has been extended to account for adsorption effects. For the sake of clarity, we here only present the key elements of the formal treatment of adsorption/desorption phenomena into the Lattice Boltzmann method (for more details, readers are referred to ref 230). Such an extension to include adsorption effects relies on the moment propagation technique as developed by Lowe and Frenkel.<sup>231,232</sup> In this method, as discussed in ref 230, the probability density  $P(\mathbf{r}, t)$  at node position  $\mathbf{r}$  and time  $t$  is propagated to/from adjacent lattice nodes while being modified by adsorption/desorption. The time evolution for  $P^*(\mathbf{r}, t)$ , defined in absence of any adsorption effects, obeys the following equation (streaming step in the Lattice Boltzmann method):<sup>226</sup>

$$P^*(\mathbf{r}, t + \Delta t) = \sum_i [P(\mathbf{r} - \mathbf{c}_i \Delta t, t) p_i(\mathbf{r} - \mathbf{c}_i \Delta t, t)] \\ + P(\mathbf{r}, t) \left[ 1 - \sum_i p_i(\mathbf{r}, t) \right] \quad (158)$$

where the sum runs over all velocity propagation directions  $i$  that lead to site  $\mathbf{r}$  and  $p_i(\mathbf{r}, t)$  is the probability that the fluid particle leaves site  $\mathbf{r}$  along the velocity propagation direction  $i$  at time  $t$ . Physically, eq 158 describes that the quantity  $P$  in  $\mathbf{r}$  at time  $t + \Delta t$  is given by the sum of two terms: (1) The value of  $P$  in site  $\mathbf{r} - \mathbf{c}_i \Delta t$  at time  $t$  multiplied by the probability that fluid particles leave site  $\mathbf{r} - \mathbf{c}_i \Delta t$  in the direction of site  $\mathbf{r}$  (first term), (2) The value of  $P$  minus the fraction of fluid particles that leave this site (second term).

In order to account for adsorption and desorption, one introduces the probability density  $P_{\text{ads}}$  associated with the adsorbed particles ( $P_{\text{ads}}$  is only nonzero for sites in the vicinity of the solid surface). The evolution of the quantity  $P_{\text{ads}}$  is given by

$$P_{\text{ads}}(\mathbf{r}, t + \Delta t) = P(\mathbf{r}, t) p_a - P_{\text{ads}}(\mathbf{r}, t) p_d \quad (159)$$

where  $p_a$  and  $p_d$  are linked to the probability that fluid molecules get adsorbed and desorbed, respectively. The probability density  $P$  associated with free (i.e., not adsorbed) fluid molecules then obeys the following evolution equation

$$P(\mathbf{r}, t + \Delta t) = P^*(\mathbf{r}, t) + P_{\text{ads}}(\mathbf{r}, t) p_d - P(\mathbf{r}, t) p_a \quad (160)$$

where the second term accounts for the adsorbed particles that get desorbed while the third term accounts for free molecules that get adsorbed.

The method above was used in different works to simulate the dynamics of fluids in porous materials in the presence of adsorption/desorption effects.<sup>229,230</sup> As an illustration, Figure

**24(c)** shows the dispersion coefficient,  $K = \lim_{t \rightarrow \infty} \sigma^2(t)/2t$ , as a function of the fraction of adsorbed molecules  $F_a$  in patterned slit pores [ $\sigma^2(t)$  is the time-dependent variance of the molecule distribution function as indicated in Figure 24(c)]. Such an effective diffusivity displays an optimum in  $F_a$  as the dispersion—which reflects the variance of the molecule distribution—is maximal when the fluid molecules subdivide into free molecules being transported by the advective flow and adsorbed molecules sticking to the surface (in contrast, for  $F_a=0$  or 1, all molecules are either transported with the advective flow or adsorbed at the pore surface). As expected, for a given adsorbed molecule fraction  $F_a$ , the dispersion increases with increasing the pore surface area through an increase in the aspect ratio  $h/w$  of the patterned surface.<sup>229</sup>

**6.1.2. Dynamic Monte Carlo.** Dynamic or kinetic Monte Carlo methods (DMC) extend the classical Monte Carlo methods for equilibrium systems to non equilibrium problems such as chemical reactions and diffusion. They are based on the time  $\tau$  between jumps in the system phase space which corresponds to a hopping rate  $k \sim \langle \tau \rangle^{-1}$ , where the brackets denote the expectation value. This time can be the chemical reaction rate or the typical adsorption/desorption time of a molecule on a surface. The time between successive transitions  $\tau$  is distributed exponentially around its mean according to  $P(\tau) \sim e^{-k\tau}$ . The latter is a direct result from a discrete-time Markov jump process.<sup>233,234</sup>

The basic idea behind Dynamic Monte Carlo schemes is as follows. A particle is randomly selected and the trial reaction is chosen in a random manner from all possible reaction sites (Random Selection Method, RSM). The reaction will occur with a probability proportional to  $k$  which is determined using another random number. For each attempted jump, the time is incremented which corresponds to some unit of real time,  $t/N$ , where  $N$  is the number of MC molecules. In so doing, processes corresponding to surface diffusion, adsorption/desorption or chemical reaction can be implemented straightforwardly. The drawback of this method, however, is that if the transition probabilities  $1/k$  are small, there will be many unsuccessful transition attempts for each update of the system configuration. In the case of surface diffusion, for instance, many unsuccessful jump attempts will occur for every successful jump.<sup>235</sup>

A more common approach, which significantly improves the efficiency of Dynamic Monte Carlo approaches, is to construct a list of all possible jumps,  $W_{\alpha\beta}$ , from the current configuration  $\alpha$  to another configuration  $\beta$ . A success probability weighted by the cumulative transition probability for the change  $\alpha \rightarrow \alpha'$  to take place is associated with each possible jump in this First Reaction Method (FRM):  $f_{\alpha\alpha'} = k_{\alpha\alpha'}/\sum_\beta k_{\alpha\beta}$ . The new time  $t'$  is then selected according to  $t' = t + \Delta t$  with

$$\Delta t = -\frac{1}{\sum_\beta k_{\alpha\beta}} \ln r \quad (161)$$

where  $r$  is a uniform random number taken in the interval  $]0, 1]$ . After each update  $\Delta t$ , the transition  $\alpha \rightarrow \alpha'$  is selected with a probability  $f_{\alpha\alpha'}$  and the reaction list is updated. This approach ensures that each iteration of the simulation results in a change in the configuration. Although the FRM and RSM yield the same results for a given model, the computational effort differs drastically depending on the system. A detailed introduction to the formal connection with the master equation and variations of the presented algorithm are given in ref 236.

A central point in the DMC methods lies in the fact that the time scale for the evolution of the simulated system is exact if the rates are correct and the underlying reaction is Markovian.<sup>237</sup> Note that the Markovian assumption implies that reactions are uncorrelated—a strong assumption for many systems. The main disadvantage with DMC is that all possible rates  $k_{\alpha\beta}$  and configurational changes or reactions have to be known in advance. Common ways to obtain  $k_{\alpha\beta}$  from theoretical considerations are quantum chemical calculations or atomistic simulations. Yet, due to the exponential scaling of the hopping probability,  $\exp(-kt)$ , small errors can lead to enormous uncertainties. Thus, for most practical applications, the rates are determined experimentally from adsorption/desorption isotherms or diffusion measurements.

If reaction paths and rates are well-known, DMC can provide insights into simple and binary diffusion in strongly heterogeneous media<sup>238–241</sup> or reaction mechanisms in porous materials.<sup>242</sup> Today, DMC algorithms are incorporated into many open source codes as well as commercial software packages.<sup>243</sup> Algorithmic development allows one to treat increasingly complex problems with DMC.<sup>244,245</sup> However, structural confinement can significantly influence reaction kinetics,<sup>246</sup> making quantitative predictions using DMC highly sensitive to the detailed input parameters. Summarizing, the main advantage of the DMC method is that, if we assume a simple problem where for every state there is one fast pathway, the simulation time step  $\Delta t$  scales with the free energy barrier (i.e., inversely with the rate  $k$ ) associated with this path. For rare events, this enables capturing simulation times of minutes to hours at room temperature. On the other hand, DMC is usually not exact as it requires the full rate list for all possible pathways in the system under study.<sup>247</sup>

**6.1.3. Dynamic Mean-Field DFT.** In the Dynamic Mean-Field Density Functional Theory (Dynamic Mean-Field DFT in short), one considers a lattice model of a fluid confined in a porous material interacting via nearest neighbor interactions only. The configurational energy is given by

$$U = -\frac{\epsilon}{2} \sum_i \sum_{j=i+a} n_i n_j + \sum_i n_i \phi_i \quad (162)$$

where  $\epsilon$  is the nearest neighbor interaction strength,  $n_i$  is the occupancy (0 or 1) of the lattice site at position  $i$ , and  $a$  denotes the vector to the nearest neighbors. The second term denotes the interaction of each lattice site  $i$  with the external potential  $\phi_i$ , which typically corresponds to the interaction between the fluid particles and the pore wall or other solid particles. Within the lattice gas framework, the self-diffusion constant  $D_s$  of a tracer molecule can be obtained by following its Kawasaki dynamics. Such a dynamical evolution is obtained by performing mass-conserving moves to neighboring sites in contact with a heat bath according to a Metropolis criterion.<sup>248</sup> The latter approach is therefore somehow similar to the Dynamic Monte Carlo simulations discussed in the previous section, but without taking into account properly the energy barrier between two successive states.<sup>235</sup> This yields the advantage that, for a homogeneous lattice gas,  $D_s$  can be obtained analytically.<sup>249</sup> Kawasaki dynamics simulations have been applied for example to the phase separation of confined fluid mixtures<sup>250,251</sup> and the relaxation dynamics of capillary condensation/evaporation.<sup>252–254</sup>

A significant reduction in the computational cost of the model outlined above can be achieved using a mean-field approx-

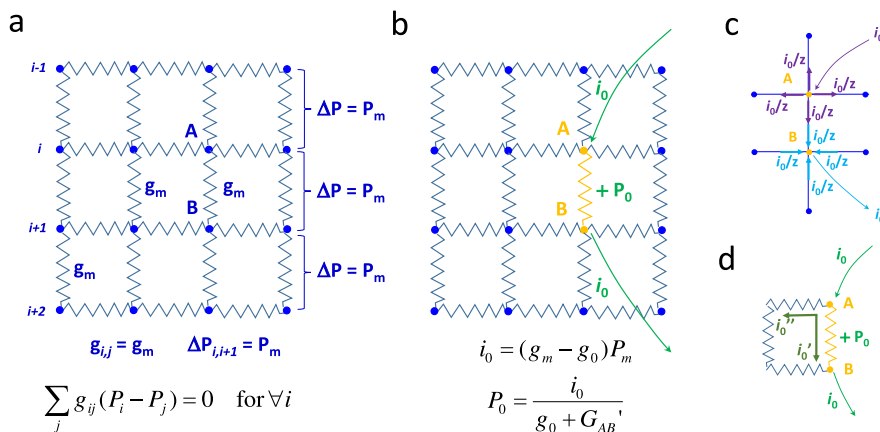


**Figure 25. Pore network model.** (a) Network model as defined in the Kirkpatrick percolation theory of electrical transport in resistor networks. Here, by analogy with the Kirkpatrick model, a 3D network of fluid conducting domains—pores—are subjected to a pressure drop  $\Delta P = P_m$  (the domain length is assumed to be equal to unity). In the equivalent network, which allows determining the effective transport properties such as the effective pore conductance  $g_m$ , the stationary solution is given by the fluid mass conservation at each node  $i$ ,  $\sum_j g_{ij} (P_i - P_j) = 0$ . (b) In order to solve the problem stated in (a), a perturbation is induced by varying the conductance of the domain between nodes A and B. Such a perturbation induces a variation of  $+P_0$  in the local pressure difference  $\Delta P$  as well as an additional fluid current  $i_0$  between nodes A and B. (c) and (d):  $i_0$  can be measured by noticing that the extra-current is injected in the domain network at node A and removed at node B.

imation. Within this assumption, one minimizes the following Helmholtz free energy:

$$F = k_B T \sum_i [\rho_i \ln \rho_i + (1 - \rho_i) \ln(1 - \rho_i)] - \frac{\epsilon}{2} \sum_i \sum_{j=i+a} \rho_i \rho_j + \sum_i \rho_i \phi_i \quad (163)$$

The first term in eq 163 represents the system entropy, the second term the interaction energy between the nearest neighbors and the last term stems from the external field  $\phi$  (corresponding to the interaction of the fluid with wall particles). In the standard mean-field approach, eq 163 is minimized with respect to the mean density at lattice site  $i$  under the constraint

$$\frac{\partial F}{\partial \rho_i} - \mu = 0 \quad (164)$$

where  $\mu$  is the chemical potential acting as a Lagrange multiplier in order to fix the total number of molecules  $N \sim \sum_i \rho_i$ . Combination of eqs 163 and 164 results in a set of coupled equations that can be solved numerically. The basic idea of a dynamic mean-field theory is to follow the time evolution of the local density<sup>255,256</sup>

$$\frac{\partial \rho_i}{\partial t} = - \sum_j J_{ij}(t) \quad (165)$$

where  $J_{ij}(t)$  is the net flux from site  $i$  to its neighboring site  $j$  at time  $t$ . Within the mean-field approximation,  $J_{ij} = w_{ij} \rho_i (1 - \rho_j) - w_{ji} \rho_j (1 - \rho_i)$  where the transition probabilities  $w_{ij}$  can be obtained using Kawasaki dynamics according to a Metropolis scheme

$$w_{ij} = w_0 \exp(-\Delta E_{ij}) \quad (166)$$

In the latter equation,  $\Delta E_{ij}$  is the energy difference between lattice sites  $i$  and  $j$  and the prefactor  $w_0$  essentially takes care of relating the chemical potential difference between neighboring sites to their difference in local densities. Due to the use of the underlying mean-field approach, correlation effects in collective

transport—which we treated in detail in Section 3—are necessarily described in an approximated fashion. With these limitations, dynamic mean-field DFT has been applied to study the dynamics of capillary condensation/evaporation of simple fluids and mixtures in porous materials.<sup>257–260</sup> Finally, we note that lattice-free dynamic DFT methods have been developed earlier to study the relaxation dynamics of fluids<sup>261,262</sup> and hydrodynamic interactions can be incorporated on a continuum level, see e.g. refs<sup>263–265</sup> and ref<sup>266</sup> for a review.

## 6.2. Network Models

**6.2.1. Pore Network Models.** Pore network models are a class of systems in which the transport properties of a given porous structure are solved on a lattice.<sup>267,268</sup> In this approach, the porous medium of a dimension  $d = 1, 2$ , or  $3$  is described as an assembly of pores connected by channels. Each pore is located on a lattice node while the connecting channels correspond to segments between nodes. Upon applying external driving forces (gradients) at the scale of the whole lattice, the resulting transport properties are obtained by solving the corresponding conservation equations (i.e., the flux of conserved quantities must be the same at the entrance and exit of the lattice). Pore entrance/exit effects are assumed to be negligible so that transport corresponds to fluxes through the nodes. The volume, particle and heat flux through each node are typically assumed to be in the linear regime, i.e., directly proportional to the local gradient. Despite this fundamental linear response assumption, owing to the complexity of the node/channel distributions, the overall transport response to the external macroscopic gradients can be non linear.

Let us consider a porous medium filled with a fluid subjected to different gradients. As a very general example, we consider that pressure  $\nabla P$ , temperature  $\nabla T$ , and chemical potential  $\nabla \mu$  gradients are applied, but note that other driving forces could be applied (in fact, in many practical situations, only one driving force is used which greatly simplifies the problem). By virtue of Onsager theory of transport, the transport properties of this system can be described using a matrix solution in which the flux of each conjugated variable of a given thermodynamic gradient is given by<sup>80</sup>

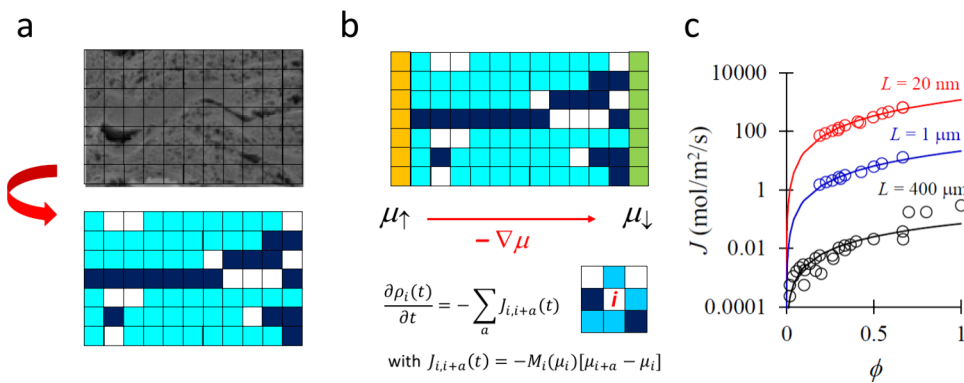


**Figure 26. Upscaling strategy using a lattice model.** (a) A lattice model is mapped onto experimental structural data such as tomography or FIB-SEM data.  $L$  is defined as the size of the porous solid over which the fluid flow is considered as a response to a thermodynamic gradient. Each domain type  $i$  is assigned: (1) an adsorption isotherm  $\rho_i(\mu)$  where  $\rho$  and  $\mu$  are the fluid density and chemical potential, respectively, and (2) a transport relation  $J = -M_i(\mu)\nabla\mu$  where  $J$  is the flux and  $M_i$  the transport coefficient associated with the driving force  $\nabla\mu$ . For each domain type, these two sets of data can be determined from molecular simulation and/or from available experimental data. In the situation depicted here, three domain types are considered: white, cyan and blue. (b) Once the lattice model has been defined, transport is simulated at large scale by placing the lattice between two boundary conditions: the chemical potentials upstream and downstream are constant and equal to  $\mu_\uparrow$  and  $\mu_\downarrow$ , respectively. Because of local mass conservation, the change in the local density at site  $i$  is simply given by the sum of the incoming and outgoing fluxes from/toward neighboring sites. (c) Flux  $J$  as a function of porosity  $\phi$  for an assembly of domains with different porosity scales. The red and blue data are for lattice systems with different lengths indicated in the graph. The black data, which are for a system having a much larger size ( $400 \mu\text{m}$ ), were determined by upscaling the data for the lattice with  $1 \mu\text{m}$ . In all cases, the upstream and downstream chemical potentials were set to values corresponding to pressures of 11 and 10 bar (the temperature is 423 K). The lines are fits against Archie's law,  $J \sim \phi^\alpha$ . Adapted with permission from ref 161. Copyright 2015 American Physical Society.

$$\begin{pmatrix} J_E \\ J_N \\ J_V \end{pmatrix} = - \begin{pmatrix} L_{EE} & L_{EN} & L_{EV} \\ L_{NE} & L_{NN} & L_{NV} \\ L_{VE} & L_{VN} & L_{VV} \end{pmatrix} \begin{pmatrix} \nabla T \\ \nabla \mu \\ \nabla P \end{pmatrix} \quad (167)$$

where  $J_E$ ,  $J_N$  and  $J_V$  are the energy, molecule, and volume fluxes. The values  $L_{\alpha\beta}$  with  $\alpha, \beta = E, N, V$  are the transport coefficients which characterize the system flux in a quantity  $\alpha$  to a gradient in the variable  $\beta$ . To illustrate how the pore network model can be solved to determine the coefficients  $L_{\alpha\beta}$ , we discuss below an ideal case which consists of a filled porous medium submitted to a pressure gradient. This example is identical to the well-known problem of electrical transport in resistance networks as treated in detail by Kirkpatrick.<sup>150</sup>

Let us consider the pore network model depicted in Figure 25(a). Each node  $i$  corresponds to a pore which is connected to its neighbors  $j$  through segments  $ij$  corresponding to channels. The whole lattice is subjected to a pressure gradient  $\Delta P/L$  where  $L$  is the physical size of the connection between two pores (in total, the pressure drop across the lattice is  $n\Delta P$  where  $n$  is the number of nodes in the direction of the pressure-induced flow). Upon introducing the permeance  $g_{ij} = K_{VV}(i \rightarrow j)$  of a channel  $ij$  and the pressures  $P_i$  and  $P_j$  in pores  $i$  and  $j$ , the transport properties of the porous medium mimicked using this pore network model can be determined by solving the following conservation equation at each lattice node  $i$

$$\sum_j g_{ij}(P_i - P_j) = 0 \quad \forall i \quad (168)$$

where the sum runs over all nearest neighbors  $j$  of the pore  $i$ . To solve this problem, one introduces the equivalent network where each segment has the same conductance  $g_m$  and each node  $i$  is at a pressure  $P_i = P_\downarrow + P_m \times k(i)$  where  $P_\downarrow$  is the downstream pressure at the entrance of the network and  $k(i)$  is the position of the pore  $i$  among the  $n$  layers along the flow, i.e.,  $k(i) \in [1, n]$  (as shown in Figure 25(a)), the pressure difference between two subsequent layers is  $\Delta P = P_m$ . Let us now consider a small

perturbation to this equivalent network which is introduced by modifying the initial permeance  $g_m$  of the segment A-B to a value  $g_{AB} = g_0 \neq g_m$ . Replacing  $g_m$  by  $g_0$  fails to satisfy the conservation condition given in eq 168 and, as shown in Figure 25(b), an extra-current  $i_0$  must be introduced in A and removed in B so that mass conservation is recovered with

$$i_0 = (g_m - g_0)P_m \quad (169)$$

The generation of this extra-current requires a shift in the local pressure drop by a quantity  $\Delta P_{AB} = P_0$ . In order to determine the shift  $P_0$ , one can use the equivalent system shown in Figure 25(d) where the blue segments replace all the initial network connecting A and B except the segment AB itself. Mass conservation implies that the extra-current  $i_0$  is the sum of the current running directly along A and B and the current running along the network in the absence of the segment AB:  $i_0 = i'_0 + i''_0$ . Upon introducing the total conductance  $G'_{AB}$  from A to B without including the conductance  $g_0$  through the segment A-B, the latter current conservation relation leads to

$$P_0 = i_0 / (g_0 + G'_{AB}) \quad (170)$$

Let us now introduce the total conductance  $G_{AB} = G'_{AB} + g_m$  from A to B, which includes conduction through the domain A-B as well as through any other path connecting A and B. As illustrated in Figure 25(c), if  $z$  is the network connectivity ( $z = 6$  for a cubic network), each current  $i_0$  splits into a contribution  $i_0/z$  from each segment. The total current along the segment A-B is therefore  $2i_0/z$  (note that we recover the simple case  $i_{AB} = i_0$  for a 1D system). This implies that  $G_{AB} = z/2g_m$  and  $G'_{AB} = (z/2 - 1)g_m$  since  $G_{AB} = G'_{AB} + g_m$ . Combining these relations with eqs 169 and 170 leads to

$$P_0 = \frac{P_m(g_m - g_0)}{g_0 + (z/2 - 1)g_m} \quad (171)$$

If we assume a continuous distribution  $f(g)$  of  $g_{ij}$ , the average value  $\langle P_0 \rangle$  must be equal to zero because the homogeneous model is the macroscopic solution by definition. This implies

$$\int \frac{g_m - g}{g + (z/2 - 1)g_m} f(g) dg = 0 \quad (172)$$

Similarly, using a discretized version where there are  $M$  different (conducting) porous domains, one obtains

$$\sum_{\alpha=1}^M v_\alpha \frac{k_\alpha - k_e}{k_\alpha + (z/2 - 1)k_e} = 0 \quad (173)$$

where  $k_\alpha$  is the conductance of a domain type  $\alpha$  while  $k_e$  is the effective conductance that is the solution of the equivalent problem.  $v_\alpha$  are the volume fractions occupied by each phase  $\alpha$ . Interestingly, by defining the conductance as the density  $\rho$  multiplied by the transport coefficient  $D$ , eq 173 is strictly equivalent to eq 99 obtained using the effective medium theory presented in Section 4. While eq 172 and its discretized version eq 173 are refined effective medium descriptions of transport in porous networks, it is an important remark to note that they are not exact results.

**6.2.2. Other Lattice Models.** The mesoscopic methods proposed above allow one to gain insights into molecular transport at the porous network scale. However, a robust strategy in which nanoscale adsorption and transport phenomena are coupled is still lacking in the literature. Such approaches would allow accounting for complex adsorption (film formation, in-pore relocation, irreversible capillary condensation, etc.) and transport mechanisms (surface diffusion, slippage effects, viscous flow approximation breakdown, activated transport, etc.) that are usually omitted in conventional techniques or included only in an effective way. As an illustration of possible developments, in what follows, we present the simple multiscale model that has been proposed by Botan et al. to describe adsorption and transport in heterogeneous porous materials.<sup>161</sup> This lattice model allows upscaling molecular simulation of adsorption and transport in porous materials at larger length and time scales. In particular, this bottom-up technique accounts for changes in adsorption and transport upon varying pore size, pressure, temperature, etc., so that it does not require to assume *a priori* any adsorption or flow regime. In practice, this approach accounts for any adsorption effects and possible changes in the confined fluid state upon transport by relating at each time step  $t$  the local density  $\rho(r)$  and chemical potential  $\mu(r)$ .

Figure 26 schematically presents the multiscale strategy developed in ref 161. First, 2D or 3D structural data as obtained for a real porous solid using tomography or microscopy experiments are used to map a lattice model. Let us introduce the size  $L$  of the porous solid over which the fluid flows as a response to a thermodynamic gradient (in Figure 26, we consider as an example the fluid flow induced by a chemical potential gradient). Using well-known segmentation techniques, each node of the lattice model can be assigned a porosity domain type (in this context, a type corresponds to a given pore size and/or surface chemistry, etc.). In this context, we define a domain type here as a solid region where the porosity scale is homogeneous so that the physical properties of the fluid in this domain are equal in all points belonging to this domain. As illustrated in ref 161, this domain can be made up of microporous, mesoporous, or macroporous regions (and even nonporous regions if domains impermeable to the fluid are to be considered). For each domain type  $m$ , molecular simulation or

available experimental data are used to provide the two following constitutive equations: (1)  $\rho_m = \rho_m(\mu)$  and  $J_m(\mu) = -M_m(\mu)\nabla\mu$ . The first equation is a thermodynamic relation, known as adsorption isotherm, which relates the confined fluid density for a given domain type  $m$  to the local chemical potential  $\mu$ . The second equation is a linear response relationship that relates the local flux in a given porous domain of type  $m$  to the local gradient in the chemical potential  $\nabla\mu$  (which can be related e.g. to pressure or density gradients) via the transport coefficient  $M$ . Once this mapping has been achieved, as shown in Figure 26(b), the lattice model is set in contact with an upstream and a downstream reservoir imposing chemical potentials equal to  $\mu_\uparrow$  and  $\mu_\downarrow$ , respectively. Transport is then predicted at the porous network scale as a function of the fluid thermodynamic state and driving force imposed across the sample as follows. At each lattice node  $i$ , the following mass conservation equation must be fulfilled

$$\frac{\partial \rho_i}{\partial t} = \sum_j J_{i \rightarrow j}(t) = \sum_j M_{ij} \left( \frac{\mu_j - \mu_i}{l} \right) \quad (174)$$

where  $\mu_i$  and  $\rho_i$  are the local chemical potential and density at site  $i$ , respectively, while  $l$  is the distance between two nearest neighbor sites. The sum runs over all nearest neighbor sites  $j$  with  $J_{i \rightarrow j}$  the flux between site  $i$  and  $j$  (which can be positive or negative depending on the sign of the local chemical potential difference  $\mu_j - \mu_i$ ). In this equation, the local flux between two neighboring sites  $i$  and  $j$  is proportional to the local transport coefficient  $M_{ij}$  which is defined as  $M_{ij} = 2M_{ii}(\mu_i)M_{jj}(\mu_j)/[M_{ii}(\mu_i) + M_{jj}(\mu_j)]$  to ensure local mass conservation at each node. As can be seen from eq 174, local adsorption and transport effects at each node are taken into account as (1) the local chemical potential is directly related to the local density and (2) the transport coefficient depends on the local chemical potential. As shown in Figure 26(c), the approach above was capable to recover physical situations such as the known regime of Archie's law in which the flux varies as a power law of the porosity,  $J \sim \Phi^\alpha$ , (with  $\alpha$  an exponent usually comprised between 1.8 and 2).<sup>141,142</sup> An interesting feature of such lattice models is that they can be upscaled in an iterative fashion to reach the macroscopic scale while transferring at each step all adsorption/transport information from the smaller length scale. This is illustrated in Figure 26(c) where the flux versus porosity relationship is shown for different lattice models and sizes (with sizes ranging from 20 nm to 400  $\mu\text{m}$ ).

## 7. DISCUSSION AND PERSPECTIVES

In this review, we have addressed the complex issue of diffusion and transport of molecules in nanoporous materials under various conditions. By considering phenomena occurring either at the molecular or mesoscopic scales, we have discussed the appropriate simulation techniques to tackle questions relevant to each level of description. While this review focuses on small molecules in prototypical nanoporous materials (e.g., zeolites, active carbons, metal organic frameworks, mesoporous oxides), we believe it applies to a very large number of molecule families. Yet, we acknowledge that the behavior of more complicated molecules can display additional complexity. In any case, for the sake of clarity and concision, we have omitted several important topics relevant to this review on adsorption and transport in nanoporous materials such as transport of multicomponent mixtures and transport in electrical fields (and all electrokinetic effects in general). As for mixture systems, considering that such

aspects have been covered in depth in several already available reviews, we feel that a detailed treatment of the transport of multicomponent mixtures was beyond the scope of our review. As for transport in electrical fields, the dynamics of charged species in nanoconfined solvents is of primary interest for the broad range of domains and applications mentioned in our introduction. However, despite being a very interesting aspect of transport in nanoporous materials, we feel that transport in electrical fields is also beyond the scope of our review to be addressed in a reasonable fashion. Moreover, outstanding reviews on adsorption and transport of charges in uncharged and charged nanopores are already available.<sup>16,269–271</sup> In particular, all electrokinetic effects encompassing electrophoresis, diffusion/osmosis, ionic conductivity in nanoconfined geometries and near solid surfaces are the topic of very specific transport mechanisms that involve long-range electrostatic effects.

In what follows, we briefly discuss a nonexhaustive list of perspectives which have been identified. While such additional topics go beyond the scope of this review, they are needed to tackle important challenges relevant to energy and environment applications. In particular, important efforts are currently devoted to conceiving and developing bioinspired systems which allow reaching efficiency and targets only achieved by nature. Of utmost importance, different axes of development include central problems such as desalination and energy conversion,<sup>272,273</sup> CO<sub>2</sub> separation/capture<sup>274</sup> and the removal of pollutants including novel classes of molecules such as PFAS.<sup>275</sup>

### 7.1. Chemomechanical Effects

More and more reports are available in the literature on transport phenomena in nanoporous environments in which the dynamics of confined fluids couples with mechanical effects. In particular, when complex nanoporous solids such as hybrid porous materials (e.g., metal-organic frameworks) or disordered materials relevant to soft matter (polymers, cellulose, etc.) are considered, novel mechanical phenomena occur which include swelling or breathing effects as well as reorganization of the host material.<sup>276,277</sup> While the interplay between these effects and the thermodynamics of confined fluids has received significant attention,<sup>278</sup> their impact in terms of fluid transport remains to be fully understood. In this context, we note that recent studies have considered transport in polymer membranes with nanometric pores.<sup>180–184</sup> From a formal viewpoint, available approaches have been already proposed to address these effects,<sup>279</sup> but more research is needed to fully unravel how such coupling proceeds. Similarly, many interesting phenomena relevant to such chemo-mechanical effects are also reported for fluids in complex media relevant to biophysics (e.g., molecular and ion transport in biological membranes) and natural materials (e.g., wood, concrete).<sup>280–284</sup>

### 7.2. Separation and Phase Transition at the Nanoscale

The large majority of theoretical studies on fluid transport in nanoporous materials deals with pure fluids. However, many practical situations involve mixtures, which lead to strong competitive adsorption effects with sometimes very large selectivities (defined as the ratio of mole fractions in confinement with respect to the same ratio in the bulk system).<sup>285</sup> In particular, oversolubility refers to large solubility enhancements observed when a solute is set in contact with a solvent nanoconfined within a nanoporous material.<sup>208,286,287</sup> While such thermodynamic effects are at the heart of physical

processes relying on nanoporous materials, they remain to be better understood. Of particular relevance to the present review, phase separation in nanoporous materials is also observed when mixtures made up of fluids with different physical interactions are involved. From a fundamental viewpoint, such nanoscale separation is an important field as it raises important questions. In particular, while thermodynamic frameworks are available to describe such segregation effects, their impact on fluid transport at a large scale remains to be fully explored. In this context, while more specific in nature, the case of conformers and enantiomers separation is an important issue for both basic and applied research.<sup>288</sup>

### 7.3. Solid/Fluid Coupling at Interfaces

There is now a large body of research unravelling the impact of the solid dynamics of the host porous medium on the transport of fluids at their surface. This includes the impact of lattice vibrations on the diffusion or permeability of the nanoconfined fluid.<sup>289</sup> Other interesting situations correspond to the coupling between a mechanical solicitation imposed to the host solid and the fluid dynamical response. In this context, Marbach et al. have recently developed a theoretical framework for studying the impact of fluctuations of the confining surfaces on diffusion. These authors found that diffusion can be enhanced or suppressed depending on the fluctuations.<sup>279</sup> Recent work has also highlighted the impact of pore compliance on the structure and dynamics of the confined liquid water, revealing that the water density profiles depend on the pore elastic properties, which in turn can drastically enhance transport.<sup>290</sup> Other couplings between the host solid and confined fluid includes interesting effects such as the concept of quantum friction.<sup>24</sup> With this concept, electronic relaxation within the solid phase set in contact with the vicinal fluid phase leads to novel phenomena in the fluid thermodynamic and transport properties. Owing to the quantum mechanics nature of the solid response, new formalisms need to be developed to rationalize and predict this physical coupling at the frontier between solid-state and liquid-state physics.<sup>291</sup>

### 7.4. Upscaling Transport under Reactive or Phase-Transition Conditions

Both stationary and transport conditions in nanoporous materials involve a large variety of thermodynamic states.<sup>34</sup> This includes phase transition such as gas/liquid coexistence but also separation mechanisms with coexisting states as described above. These heterogeneous systems can be described using mesoscopic approaches including Lattice Boltzmann simulations or computational fluid dynamics tools. However, understanding the microscopic mechanisms at play in these coexisting states remain an important challenge with many questions left unexplained. In particular, as briefly discussed in this review, interfacial transport in the sense of fluid dynamics at the interfaces between different thermodynamic phases involves large free energy barriers with complex underlying dynamics. While different in spirit, reactive transport also falls in the category of complex molecular mechanisms with a strong impact on macroscopic transport and overall process efficiency. Like for transport in systems involving phase transition, taking into account the “reactivity” of the system (evolution of interfaces upon phase transitions or transformation of molecular species into others upon chemical reactions) is a major challenge that needs to be addressed as it corresponds to a large number of practical situations involving nanoporous materials.

## AUTHOR INFORMATION

### Corresponding Author

Benoit Coasne – Univ. Grenoble Alpes, CNRS, LIPhy, 38000 Grenoble, France;  [orcid.org/0000-0002-3933-9744](https://orcid.org/0000-0002-3933-9744); Email: [benoit.coasne@univ-grenoble-alpes.fr](mailto:benoit.coasne@univ-grenoble-alpes.fr)

### Authors

Alexander Schlaich – Univ. Grenoble Alpes, CNRS, LIPhy, 38000 Grenoble, France; Stuttgart Center for Simulation Science and Institute for Computational Physics, University of Stuttgart, 70569 Stuttgart, Germany; Institute for Atomistic Modeling of Materials in Aqueous Media, Hamburg University of Technology, 21073 Hamburg, Germany;  [orcid.org/0000-0002-4250-363X](https://orcid.org/0000-0002-4250-363X)

Jean-Louis Barrat – Univ. Grenoble Alpes, CNRS, LIPhy, 38000 Grenoble, France;  [orcid.org/0000-0002-4220-2933](https://orcid.org/0000-0002-4220-2933)

Complete contact information is available at:

<https://pubs.acs.org/10.1021/acs.chemrev.4c00406>

### Author Contributions

CRedit: Alexander Schlaich conceptualization, formal analysis, investigation, validation, writing - original draft, writing - review & editing; Jean-Louis Barrat conceptualization, investigation, validation, writing - review & editing; Benoit Coasne conceptualization, data curation, investigation, supervision, validation, writing - original draft, writing - review & editing.

### Notes

The authors declare no competing financial interest.

### Biographies

Alexander Schlaich studied physics at the University of Stuttgart and received his PhD in 2017 from Freie Universität Berlin on water effects on the interaction and friction between polar surfaces. After postdoctoral assignments in Grenoble and Stuttgart he received a fellowship to set up an independent junior research group within the Cluster of Excellence “Data-Integrated Simulation Science” in Stuttgart in 2021. Since 2024, he is a full professor at Hamburg University of Technology. In his research, Alexander Schlaich combines different simulation and theoretical approaches to bridge the description of nanoporous functional matter from the fundamentals at the atomistic scale to engineering applications.

Jean-Louis Barrat received a doctorate from the University of Paris in 1987, working on statistical physics of liquids and phase transitions. He worked as a postdoctoral researcher in Munich and Santa Barbara. After being a CNRS researcher at the ENS in Lyon, he joined in 1994 the University of Lyon, where he created a research group on modeling in materials science. In 2011, he joined the University of Grenoble where he created the statistical physics group within the Interdisciplinary Physics Lab. His research focuses on statistical physics, condensed matter and materials physics.

Benoit Coasne obtained his PhD in Physics on capillary condensation in nanoporous materials (Paris, 2003). After a postdoc in Raleigh, NC, USA (2003–2005), Benoit Coasne was appointed CNRS researcher in Montpellier (2005) and promoted CNRS Research Director (2015). During a 3 year visiting stay, he was leading a fundamental research group on multiscale modeling of adsorption and transport in the CNRS/MIT lab at MIT in Boston (2012/15). He is currently affiliated CNRS Research Director in the Interdisciplinary Physics Lab in Grenoble, France. He is also Permanent Affiliate of the Theory Group at the Institute Laue Langevin in Grenoble. Benoit Coasne’s research

consists of studying by means of statistical mechanics and molecular simulation tools the thermodynamics and dynamics of fluids confined in nanoporous media.

## ACKNOWLEDGMENTS

The authors acknowledge financial support from EUROKIN which is a consortium of academic and industrial members ([www.eurokin.org](http://www.eurokin.org)). We are also grateful to the French Agence Nationale de la Recherche for funding (Project TAMTAM ANR-15-CE08-0008-01 and Project TWIST ANR-17-CE08-0003). A.S. also acknowledges funding from the DFG under Germany’s Excellence Strategy – EXC 2075-390740016 and SFBs 1313/2-327154368 and 1333/2-358283783, and support by the Stuttgart Center for Simulation Science (SimTech). We wish to thank Sophie Marbach for useful comments and discussions. A preprint version of this review is available on arXiv.<sup>292</sup>

## REFERENCES

- (1) Thommes, M.; Kaneko, K.; Neimark, A. V.; Olivier, J. P.; Rodriguez-Reinoso, F.; Rouquerol, J.; Sing, K. S. Physisorption of Gases, with Special Reference to the Evaluation of Surface Area and Pore Size Distribution (IUPAC Technical Report). *Pure Appl. Chem.* **2015**, *87*, 1051–1069.
- (2) Weitkamp, J., Puppe, L., Eds. *Catalysis and Zeolites*; Springer: Berlin, 1999.
- (3) Schüth, F.; Sing, K. S. W.; Weitkamp, J. *Handbook of Porous Solids*; Wiley-VCH, 2002.
- (4) Voort, P. V. D.; Leus, K.; Canck, E. D. *Introduction to Porous Materials*; Wiley: Hoboken, NJ, 2019.
- (5) Davis, M. E. Ordered Porous Materials for Emerging Applications. *Nature* **2002**, *417*, 813–821.
- (6) Kärger, J.; Ruthven, D. M.; Theodorou, D. N. *Diffusion in Nanoporous Materials*; John Wiley & Sons, 2012.
- (7) Bhatia, S. K.; Bonilla, M. R.; Nicholson, D. Molecular Transport in Nanopores: A Theoretical Perspective. *Phys. Chem. Chem. Phys.* **2011**, *13*, 15350–15383.
- (8) Coasne, B. Multiscale Adsorption and Transport in Hierarchical Porous Materials. *New J. Chem.* **2016**, *40*, 4078–4094.
- (9) Smit, B.; Maesen, T. L. M. Molecular Simulations of Zeolites: Adsorption, Diffusion, and Shape Selectivity. *Chem. Rev.* **2008**, *108*, 4125–4184.
- (10) Bouchaud, J.-P.; Georges, A. Anomalous Diffusion in Disordered Media: Statistical Mechanisms, Models and Physical Applications. *Phys. Rep.* **1990**, *195*, 127–293.
- (11) Kärger, J.; Ruthven, M. Diffusion in Nanoporous Materials: Fundamental Principles, Insights and Challenges. *New J. Chem.* **2016**, *40*, 4027–4048.
- (12) Schneider, D.; Mehlhorn, D.; Zeigermann, P.; Kärger, J.; Valiullin, R. Transport Properties of Hierarchical Micro–Mesoporous Materials. *Chem. Soc. Rev.* **2016**, *45*, 3439–3467.
- (13) Huber, P. Soft Matter in Hard Confinement: Phase Transition Thermodynamics, Structure, Texture, Diffusion and Flow in Nanoporous Media. *J. Phys.: Condens. Matter* **2015**, *27*, 103102.
- (14) Kärger, J. Transport Phenomena in Nanoporous Materials. *ChemPhysChem* **2015**, *16*, 24–51.
- (15) Bukowski, B. C.; Keil, F. J.; Ravikovich, P. I.; Sastre, G.; Snurr, R. Q.; Coppens, M.-O. Connecting Theory and Simulation with Experiment for the Study of Diffusion in Nanoporous Solids. *Adsorption* **2021**, *27*, 683–760.
- (16) Bocquet, L.; Charlaix, E. Nanofluidics, from Bulk to Interfaces. *Chem. Soc. Rev.* **2010**, *39*, 1073–1095.
- (17) Faucher, S.; Aluru, N.; Bazant, M. Z.; Blankschtein, D.; Brozena, A. H.; Cumings, J.; Pedro de Souza, J.; Elimelech, M.; Epsztein, R.; Fourkas, J. T.; et al. Critical Knowledge Gaps in Mass Transport through Single-Digit Nanopores: A Review and Perspective. *J. Phys. Chem. C* **2019**, *123*, 21309–21326.

- (18) Aluru, N. R.; Aydin, F.; Bazant, M. Z.; Blankschtein, D.; Brozena, A. H.; de Souza, J. P.; Elimelech, M.; Faucher, S.; Fourkas, J. T.; Koman, V. B.; et al. Fluids and electrolytes under confinement in single-digit nanopores. *Chem. Rev.* **2023**, *123*, 2737–2831.
- (19) Kavokine, N.; Netz, R. R.; Bocquet, L. Fluids at the Nanoscale: From Continuum to Subcontinuum Transport. *Annu. Rev. Fluid Mech.* **2021**, *53*, 377–410.
- (20) Bocquet, L. Nanofluidics Coming of Age. *Nat. Mater.* **2020**, *19*, 254–256.
- (21) Kärger, J.; Valiullin, R. Mass Transfer in Mesoporous Materials: The Benefit of Microscopic Diffusion Measurement. *Chem. Soc. Rev.* **2013**, *42*, 4172–4197.
- (22) Joseph, S.; Aluru, N. R. Why Are Carbon Nanotubes Fast Transporters of Water? *Nano Lett.* **2008**, *8*, 452–458.
- (23) Suk, M. E.; Aluru, N. R. Water Transport through Ultrathin Graphene. *J. Phys. Chem. Lett.* **2010**, *1*, 1590–1594.
- (24) Kavokine, N.; Bocquet, M.-L.; Bocquet, L. Fluctuation-Induced Quantum Friction in Nanoscale Water Flows. *Nature* **2022**, *602*, 84–90.
- (25) Schlaich, A.; Jin, D.; Bocquet, L.; Coasne, B. Electronic Screening Using a Virtual Thomas–Fermi Fluid for Predicting Wetting and Phase Transitions of Ionic Liquids at Metal Surfaces. *Nat. Mater.* **2022**, *21*, 237–245.
- (26) Galarneau, A.; Guenneau, F.; Gedeon, A.; Mereib, D.; Rodriguez, J.; Fajula, F.; Coasne, B. Probing Interconnectivity in Hierarchical Microporous/Mesoporous Materials Using Adsorption and Nuclear Magnetic Resonance Diffusion. *J. Phys. Chem. C* **2016**, *120*, 1562–1569.
- (27) Dutta, R. C.; Bhatia, S. K. Interfacial Barriers to Gas Transport in Zeolites: Distinguishing Internal and External Resistances. *Phys. Chem. Chem. Phys.* **2018**, *20*, 26386–26395.
- (28) Dutta, S.; Galarneau, A.; Minoux, D.; Aquino, C.; Dath, J. P.; Guenneau, F.; Coasne, B. Molecular Diffusion in Hierarchical Zeolites with Ordered Mesoporosity: Pulsed Field Gradient Nuclear Magnetic Resonance Combined with Thermodynamic Modeling. *J. Phys. Chem. C* **2023**, *127*, 1548–1559.
- (29) Thommes, M. Physical Adsorption Characterization of Nanoporous Materials. *Chemie Ingenieur Technik* **2010**, *82*, 1059–1073.
- (30) Auerbach, S. M.; Carrado, K. A.; Dutta, P. K. *Handbook of Zeolite Science and Technology*; CRC Press: Boca Raton, FL, 2003.
- (31) Coppens, M.-O. A Nature-Inspired Approach to Reactor and Catalysis Engineering. *Current Opinion in Chemical Engineering* **2012**, *1*, 281–289.
- (32) Sahimi, M.; Gavalas, G. R.; Tsotsis, T. T. Statistical and Continuum Models of Fluid-Solid Reactions in Porous Media. *Chem. Eng. Sci.* **1990**, *45*, 1443–1502.
- (33) Gheorghiu, S.; Coppens, M.-O. Optimal Bimodal Pore Networks for Heterogeneous Catalysis. *AIChE J.* **2004**, *50*, 812–820.
- (34) Coasne, B.; Galarneau, A.; Pelleng, R. J. M.; Di Renzo, F. Adsorption, Intrusion and Freezing in Porous Silica: The View from the Nanoscale. *Chem. Soc. Rev.* **2013**, *42*, 4141–4171.
- (35) Torquato, S. *Random Heterogeneous Materials: Microstructure and Macroscopic Properties*; Springer Science & Business Media, 2005.
- (36) Hansen, N.; Keil, F. J. Multiscale Modeling of Reaction and Diffusion in Zeolites: From the Molecular Level to the Reactor. *Soft Mater.* **2012**, *10*, 179–201.
- (37) Santiso, E. E.; Gubbins, K. E. Multi-Scale Molecular Modeling of Chemical Reactivity. *Mol. Simul.* **2004**, *30*, 699–748.
- (38) Xie, C.; Yan, D.; Chen, W.; Zou, Y.; Chen, R.; Zang, S.; Wang, Y.; Yao, X.; Wang, S. Insight into the Design of Defect Electrocatalysts: From Electronic Structure to Adsorption Energy. *Mater. Today* **2019**, *31*, 47–68.
- (39) Li, B.; Gao, W.; Jiang, Q. Electronic and Geometric Determinants of Adsorption: Fundamentals and Applications. *J. Phys. Energy* **2021**, *3*, 022001.
- (40) Keil, F. J. Molecular Modelling for Reactor Design. *Annu. Rev. Chem. Biomol. Eng.* **2018**, *9*, 201–227.
- (41) Detmann, B. Modeling Chemical Reactions in Porous Media: A Review. *Continuum Mech. Thermodyn.* **2021**, *33*, 2279–2300.
- (42) Ladd, A. J.; Szmyczak, P. Reactive Flows in Porous Media: Challenges in Theoretical and Numerical Methods. *Annu. Rev. Chem. Biomol. Eng.* **2021**, *12*, 543–571.
- (43) Frenkel, D.; Smit, B. *Understanding Molecular Simulation: From Algorithms to Applications*; Academic Press, 2001.
- (44) Allen, M. P.; Tildesley, D. J. *Computer Simulation of Liquids*, 2nd ed.; Oxford University Press: Oxford, U.K., 2017.
- (45) Balbuena, P.; Seminario, J. M. *Molecular Dynamics: From Classical to Quantum Methods*; Elsevier, 1999.
- (46) Barrat, J.-L.; Hansen, J.-P. *Basic Concepts for Simple and Complex Liquids*; Cambridge University Press, 2003.
- (47) Chaikin, P. M.; Lubensky, T. C. *Principles of Condensed Matter Physics*; 1995, DOI: [10.1017/CBO9780511813467](https://doi.org/10.1017/CBO9780511813467).
- (48) Hansen, J.-P.; McDonald, I. R. *Theory of Simple Liquids: With Applications to Soft Matter*; Academic Press, 2013.
- (49) McQuarrie, D. A. *Statistical Mechanics*; University Science Books: Sausalito, CA, 2000.
- (50) Gubbins, K. E.; Liu, Y.-C.; Moore, J. D.; Palmer, J. C. The Role of Molecular Modeling in Confined Systems: Impact and Prospects. *Phys. Chem. Chem. Phys.* **2011**, *13*, 58–85.
- (51) Landau, L. D.; Lifshitz, E. M. *Fluid Mechanics: Landau and Lifshitz: Course of Theoretical Physics*; Elsevier, 2013.
- (52) Bird, R. B.; Stewart, W. E.; Lightfoot, E. N. *Transport Phenomena*, 2nd ed.; John Wiley & Sons, 2002.
- (53) O’Sullivan, C.; Arson, C.; Coasne, B. A Perspective on Darcy’s Law across the Scales: From Physical Foundations to Particulate Mechanics. *Journal of Engineering Mechanics* **2022**, *148*, 04022064.
- (54) Civan, F. *Porous Media Transport Phenomena*; John Wiley & Sons, 2011.
- (55) Rhodes, M. *Introduction to Particle Technology*; Wiley, 1989.
- (56) Let us consider the Poiseuille flow in a slit pore induced by a pressure gradient  $\nabla P$  corresponding to a pressure drop  $\Delta P = 100 \text{ bar} = 10^7 \text{ Pa}$  over a length  $L = 0.01 \text{ m}$ . For such a viscous flow, as described later in this review, the average fluid flow velocity follows as  $u = D_p^2 \Delta P / (32 L \eta)$ . Using  $\eta = 1 \text{ mPa s}$  for water at room temperature, this yields  $Re = \rho u D_p / \eta \sim 10^{-4}$  for  $D_p = 100 \text{ nm}$ .
- (57) For a fluid, the sound velocity  $c$  is given by the Newton–Laplace equation which involves the stiffness coefficient  $K_s$  (i.e., the bulk elastic modulus for fluids) and the mass density  $\rho$ ,  $c = \sqrt{K_s / \rho}$ . In the case of an ideal gas at a given pressure  $P$ ,  $K_s = \gamma_a P$  so that  $c = \sqrt{\gamma_a P / \rho}$  where  $\gamma_a = C_p / C_v$ , the adiabatic index, is equal to the ratio of the heat capacities at constant pressure and constant volume ( $\gamma_a = 1.4$  for a diatomic ideal gas such as  $\text{N}_2$ ). Using the ideal gas law,  $P = \rho / MRT$  where  $M$  is the molar mass,  $R$  the ideal gas constant, and  $T$  the temperature, we obtain  $c = \sqrt{\gamma RT / M} \sim 350 \text{ m/s}$  for  $\text{N}_2$  at room temperature.
- (58) de Groot, S. R.; Mazur, P. *Non-Equilibrium Thermodynamics*; North-Holland and Publishing Company, 1962.
- (59) Callen, H. B. *Thermodynamics and an Introduction to Thermo-statistics*; Wiley, 1985.
- (60) Pottier, N. *Nonequilibrium Statistical Physics: Linear Irreversible Processes*; Oxford University Press, 2010.
- (61) Let us consider a thermodynamic system subdivided into two subsystems 1 and 2. For each conserved quantity  $X$  such as the energy  $E$  or number of molecules  $N$ , the sum of their contribution in each subsystem is constant, i.e.,  $X_1 + X_2 = 0$ , which implies that  $\partial X_1 = -\partial X_2$ . Moreover, the equilibrium condition is given by the entropy maximization principle, i.e.,  $\partial S / \partial X_1 = \partial S_1 / \partial X_1 - \partial S_2 / \partial X_1 = 0$  which leads to  $F_1 = F_2$  since  $\partial S / \partial X = F$ .
- (62) Kärger, J.; Valiullin, R.; Brandani, S.; Caro, J.; Chmelik, C.; Chmelka, B. F.; Coppens, M.-O.; Farooq, S.; Freude, D.; Jobic, H.; et al. Diffusion in nanoporous materials with special consideration of the measurement of determining parameters (IUPAC Technical Report). *Pure Appl. Chem.* **2025**, *97*, 1–89.
- (63) Klafter, J.; Zumofen, G. Probability Distributions for Continuous-Time Random Walks with Long Tails. *J. Phys. Chem.* **1994**, *98*, 7366–7370.

- (64) Klafter, J.; Sokolov, I. M. *First Steps in Random Walks: From Tools to Applications*; OUP Oxford, 2011.
- (65) Hahn, K.; Kärger, J. Molecular Dynamics Simulation of Single-File Systems. *J. Phys. Chem.* **1996**, *100*, 316–326.
- (66) Chen, Q.; Moore, J. D.; Liu, Y.-C.; Roussel, T. J.; Wang, Q.; Wu, T.; Gubbins, K. E. Transition from Single-File to Fickian Diffusion for Binary Mixtures in Single-Walled Carbon Nanotubes. *J. Chem. Phys.* **2010**, *133*, 094501.
- (67) Roosen-Runge, F.; Bicout, D. J.; Barrat, J.-L. Analytical Correlation Functions for Motion through Diffusivity Landscapes. *J. Chem. Phys.* **2016**, *144*, 204109.
- (68) We here provide a formal proof of eq (20) which follows the derivation proposed by Hansen and McDonald.<sup>48</sup> The displacement of a particle over a time  $t$  can be written as  $\mathbf{r}(t) - \mathbf{r}(0) = \int_0^t \mathbf{v}(t') dt'$ . Upon taking the square and averaging the latter expression, the mean square displacement over a time  $t$  can be expressed as  $\langle |\mathbf{r}(t) - \mathbf{r}(0)|^2 \rangle = \left\langle \int_0^t \mathbf{v}(t') dt' \cdot \int_0^t \mathbf{v}(t'') dt'' \right\rangle$ . Using the symmetry properties upon time reversal and invariance with respect to time translation of the velocity autocorrelation function, the latter equation can be recast as  $\langle |\mathbf{r}(t) - \mathbf{r}(0)|^2 \rangle = 2 \int_0^t dt' \int_0^{t'} dt'' \langle \mathbf{v}(t') \cdot \mathbf{v}(t'') \rangle = 2 \int_0^t dt' \int_0^{t'} dt'' \langle \mathbf{v}(t') \cdot \mathbf{v}(0) \rangle$ . This equation can be simplified using the variable change  $t''$  to  $s = t' - t''$  and an integration by parts with respect to  $t'$ :  $\langle |\mathbf{r}(t) - \mathbf{r}(0)|^2 \rangle = 2 \int_0^t dt' \int_0^t dt'' \langle \mathbf{v}(t') \cdot \mathbf{v}(t'') \rangle = 2t \int_0^t \left(1 - \frac{s}{t}\right) \langle \mathbf{v}(s) \cdot \mathbf{v}(0) \rangle ds$ . By comparing the latter to the definition of the self-diffusivity  $D_s$  in a system of a dimension  $d$  according to Eq. 18,  $D_s = \lim_{t \rightarrow \infty} \frac{\langle |\mathbf{r}(t) - \mathbf{r}(0)|^2 \rangle}{2dt}$ , we arrive at Eq. 20.
- (69) Let  $G(f)$  and  $H(f)$  be the Fourier transform of two functions  $g(t)$  and  $h(t)$  in the time domain. The convolution theorem states that  $G(f)H(f) = \int_{-\infty}^{\infty} g(\tau)h(t - \tau)d\tau$ . For real functions  $g$  and  $h$ , we can use that  $H(-f) = H^*(f)$ , where the \* denotes the complex conjugate. This allows to write the correlation theorem,  $G(f)H^*(f) = \int_{-\infty}^{\infty} g(\tau + t)h(\tau)d\tau$ , which after backwards Fourier transform yields the correlation between  $g$  and  $h$ . If  $g$  and  $h$  are discrete and finite ( $t_{\max} < \infty$ ) observables defined only for  $t \geq 0$  as in Eq. 20, one can make use of the cyclic property of the discrete time Fourier transform and average  $g(\tau + t)h(\tau)$  efficiently over all initial times  $\tau$  using the Fast Fourier Transform (FFT),  $\langle g(\tau + t)h(\tau) \rangle_t = \frac{1}{N_r(t)} \text{iFFT} \left( \text{FFT}(g) \cdot \left[ \text{FFT}(h) \right]^* \right)$  where the normalizing factor  $N_r(t)$  counts the number of samples (i.e., the number of initial times  $\tau$ ) that are considered in the data series for each lag time  $t$ . For the special case of an autocorrelation function,  $g = h$ , one obtains  $G(f) \cdot G^*(f) = |G(f)|^2$ . Also note, that because of the cyclic property of the FFT one usually adds zeros to the signal for  $-t_{\max} < t < 0$  (zero padding). The advantage of employing the FFT for correlation functions is the scaling of  $O(N \log N)$  as compared to  $O(N^2)$  for a direct calculation.
- (70) Arfken, G. B.; Weber, H. J. *Mathematical Methods for Physicists*, 6th ed.; Academic Press: Boston, 2005.
- (71) Yoshida, H.; Mizuno, H.; Kinjo, T.; Washizu, H.; Barrat, J.-L. Molecular Dynamics Simulation of Electrokinetic Flow of an Aqueous Electrolyte Solution in Nanochannels. *J. Chem. Phys.* **2014**, *140*, 214701.
- (72) Maginn, E. J.; Bell, A. T.; Theodorou, D. N. Transport Diffusivity of Methane in Silicalite from Equilibrium and Nonequilibrium Simulations. *J. Phys. Chem.* **1993**, *97*, 4173–4181.
- (73) Zwanzig, R. Time-Correlation Functions and Transport Coefficients in Statistical Mechanics. *Annu. Rev. Phys. Chem.* **1965**, *16*, 67–102.
- (74) Falk, K.; Coasne, B.; Pellenq, R.; Ulm, F.-J.; Bocquet, L. Subcontinuum Mass Transport of Condensed Hydrocarbons in Nanoporous Media. *Nat. Commun.* **2015**, *6*, 6949.
- (75) Alfazazi, U.; Bedeaux, D.; Kjelstrup, S.; Moura, M.; Ebadi, M.; Mostaghimi, P.; McClure, J. E.; Armstrong, R. T. Interpreting Pore-Scale Fluctuations: Predicting Transport Coefficients in Multiphase Flow through Porous Media Using the Green–Kubo Formulation—An Experimental Investigation. *Phys. Fluids* **2024**, *36*, 1070–6631.
- (76) Bedeaux, D.; Kjelstrup, S. Fluctuation-Dissipation Theorems for Multiphase Flow in Porous Media. *Entropy* **2022**, *24*, 46.
- (77) Galteland, O.; Rauter, M. T.; Bratvold, M. S.; Trinh, T.; Bedeaux, D.; Kjelstrup, S. Local Thermodynamic Description of Isothermal Single-Phase Flow in Porous Media. *Transport in Porous Media* **2022**, *145*, 153–173.
- (78) Kellouai, W.; Barrat, J.-L.; Judeinstein, P.; Plazanet, M.; Coasne, B. On De Gennes Narrowing of Fluids Confined at the Molecular Scale in Nanoporous Materials. *J. Chem. Phys.* **2024**, *160*, 024113.
- (79) Mackay, E. K. R.; Marbach, S.; Sprinkle, B.; Thorneycroft, A. L. The Countoscope: Measuring Self and Collective Dynamics without Trajectories. *Physical Review X* **2024**, *14*, 041016.
- (80) Yoshida, H.; Mizuno, H.; Kinjo, T.; Washizu, H.; Barrat, J.-L. Generic Transport Coefficients of a Confined Electrolyte Solution. *Phys. Rev. E* **2014**, *90*, 052113.
- (81) Koros, W. J.; Ma, Y. H.; Shimidzu, T. Terminology for Membranes and Membrane Processes (IUPAC Recommendations 1996). *Pure Appl. Chem.* **1996**, *68*, 1479–1489.
- (82) Henry's law can be derived as follows by starting from the equality of the fugacity  $f$  (or, equivalently, the gas chemical potential  $\mu$ ) in the gas phase and in the liquid phase:  $f_g = f_l$ . Under the assumption that the gas behaves as an ideal gas,  $f_g = P$ . As for  $f_l$ , we can write  $f_l = \gamma x f_l^0$  where  $\gamma$  is the activity coefficient,  $x$  is the mole fraction of gas molecules in the liquid, and  $f_l^0$  is the fugacity of the liquid phase for a pure fluid, i.e.,  $x = 1$ . Using a polynomial expansion for  $\ln \gamma \sim a_1(1-x) + a_2(1-x)^2 + a_3(1-x)^3 + \dots$ , one recovers the two important asymptotic limits: (a)  $\ln \gamma = 0$  for  $x = 1$  as expected for a pure liquid for which  $\gamma \sim 1$  and (b)  $\ln \gamma \sim \text{constant}$  for  $x \ll 1$ . As a result, for  $x \ll 1$ , and noting that  $\rho \sim x$ , one obtains Henry's law with  $K_H \sim [f_l^0]^{-1}$  as a good approximation that describes the fugacity equality between the gas and liquid phases. In practice, the simple scaling between gas concentration and pressure in Henry's law holds provided that the gas partial pressure remains low enough and that the host solid or liquid does not chemically react with the solubilized gas.
- (83) Henry, W.; Banks, J., III Experiments on the Quantity of Gases Absorbed by Water, at Different Temperatures, and under Different Pressures. *Philosophical Transactions of the Royal Society of London* **1997**, *93*, 29–274.
- (84) Borah, B. J.; Maiti, P. K.; Chakravarty, C.; Yashonath, S. Transport in Nanoporous Zeolites: Relationships between Sorbate Size, Entropy, and Diffusivity. *J. Chem. Phys.* **2012**, *136*, 174510.
- (85) Gruener, S.; Huber, P. Knudsen Diffusion in Silicon Nanochannels. *Phys. Rev. Lett.* **2008**, *100*, 064502.
- (86) Let us consider a single fluid molecule diffusing through a medium containing a density  $\rho$  of frozen objects with which the molecule can collide. Introducing the cross-section area for collision  $s \sim \pi\sigma^2$ , the mean free path can be written as  $\lambda \sim 1/\rho\pi\sigma^2$ . For a gas, since the objects are other gas molecules, they cannot be considered as immobile so that the relative velocity of the gas molecules must be taken into account which leads to a slightly different expression:  $\lambda \sim 1/\sqrt{2}\rho\pi\sigma^2$ . Assuming that the gas can be treated as ideal, i.e.,  $\rho = P/k_B T$ , leads to:  $\lambda = k_B T / \sqrt{2} P \pi \sigma^2$ .
- (87) Tortuosity will be introduced later in detail—here, it should be simply considered as the ratio of the pore physical length to the pore height.
- (88) Ziarani, A. S.; Aguilera, R. Knudsen's Permeability Correction for Tight Porous Media. *Transp. Porous Med.* **2012**, *91*, 239–260.

- (89) Bear, J. *Modeling Phenomena of Flow and Transport in Porous Media; Theory and Applications of Transport in Porous Media*; Springer International Publishing, 2018.
- (90) Arya, G.; Chang, H.-C.; Maginn, E. J. Molecular Simulations of Knudsen Wall-Slip: Effect of Wall Morphology. *Mol. Simul.* **2003**, *29*, 697–709.
- (91) Thol, M.; Rutkai, G.; Köster, A.; Lustig, R.; Span, R.; Vrabec, J. Equation of State for the Lennard-Jones Fluid. *J. Phys. Chem. Ref. Data* **2016**, *45*, 023101.
- (92) Hirschfelder, J. O.; Curtiss, C. F.; Bird, R. B. *Molecular Theory of Gases and Liquids*; Wiley, 1954.
- (93) Kramers, H. A. Brownian Motion in a Field of Force and the Diffusion Model of Chemical Reactions. *Physica* **1940**, *7*, 284–304.
- (94) Hänggi, P.; Talkner, P.; Borkovec, M. Reaction-Rate Theory: Fifty Years after Kramers. *Rev. Mod. Phys.* **1990**, *62*, 251–341.
- (95) Camp, J. S.; Sholl, D. S. Transition State Theory Methods To Measure Diffusion in Flexible Nanoporous Materials: Application to a Porous Organic Cage Crystal. *J. Phys. Chem. C* **2016**, *120*, 1110–1120.
- (96) Voter, A. F.; Doll, J. D. Transition State Theory Description of Surface Self-diffusion: Comparison with Classical Trajectory Results. *J. Chem. Phys.* **1984**, *80*, 5832–5838.
- (97) Chandler, D. Statistical Mechanics of Isomerization Dynamics in Liquids and the Transition State Approximation. *J. Chem. Phys.* **1978**, *68*, 2959–2970.
- (98) Reed, D. A.; Ehrlich, G. Surface Diffusion, Atomic Jump Rates and Thermodynamics. *Surf. Sci.* **1981**, *102*, 588–609.
- (99) Hill, T. L. *An Introduction to Statistical Thermodynamics*; Courier Corporation, 1986.
- (100) Zaafouri, Z.; Bauer, D.; Batôt, G.; Nieto-Draghi, C.; Coasne, B. Cooperative Effects Dominating the Thermodynamics and Kinetics of Surfactant Adsorption in Porous Media: From Lateral Interactions to Surface Aggregation. *J. Phys. Chem. B* **2020**, *124*, 10841–10849.
- (101) Langmuir, I. The Adsorption of Gases on Plane Surface of Glass, Mica and Platinum. *J. Am. Chem. Soc.* **1918**, *40*, 1361–1403.
- (102) Gravelle, S.; Holm, C.; Schlaich, A. Transport of Thin Water Films: From Thermally Activated Random Walks to Hydrodynamics. *J. Chem. Phys.* **2022**, *157*, 104702.
- (103) Skouidas, A. I.; Sholl, D. S. Transport Diffusivities of CH<sub>4</sub>, CF<sub>4</sub>, He, Ne, Ar, Xe, and SF<sub>6</sub> in Silicalite from Atomistic Simulations. *J. Phys. Chem. B* **2002**, *106*, 5058–5067.
- (104) Skouidas, A. I.; Sholl, D. S. Molecular Dynamics Simulations of Self-Diffusivities, Corrected Diffusivities, and Transport Diffusivities of Light Gases in Four Silica Zeolites To Assess Influences of Pore Shape and Connectivity. *J. Phys. Chem. A* **2003**, *107*, 10132–10141.
- (105) Chempath, S.; Krishna, R.; Snurr, R. Q. Nonequilibrium Molecular Dynamics Simulations of Diffusion of Binary Mixtures Containing Short N-Alkanes in Faujasite. *J. Phys. Chem. B* **2004**, *108*, 13481–13491.
- (106) Krishna, R.; Paschek, D.; Baur, R. Modeling the Occupancy Dependence of Diffusivities in Zeolites. *Microporous Mesoporous Mater.* **2004**, *76*, 233–246.
- (107) Evans, R.; Tarazona, P. Theory of Condensation in Narrow Capillaries. *Phys. Rev. Lett.* **1984**, *52*, 557–560.
- (108) Evans, R.; Marconi, U. M. B.; Tarazona, P. Fluids in Narrow Pores: Adsorption, Capillary Condensation, and Critical Points. *J. Chem. Phys.* **1986**, *84*, 2376–2399.
- (109) Evans, R.; Bettolo Marconi, U. M.; Tarazona, P. Capillary Condensation and Adsorption in Cylindrical and Slit-like Pores. *Journal of the Chemical Society, Faraday Transactions 2: Molecular and Chemical Physics* **1986**, *82*, 1763–1787.
- (110) Nakanishi, H.; Fisher, M. E. Multicriticality of Wetting, Prewetting, and Surface Transitions. *Phys. Rev. Lett.* **1982**, *49*, 1565–1568.
- (111) Nakanishi, H.; Fisher, M. E. Critical Point Shifts in Films. *J. Chem. Phys.* **1983**, *78*, 3279–3293.
- (112) Dillmann, O.; Janke, W.; Müller, M.; Binder, K. A Monte Carlo Test of the Fisher–Nakanishi–Scaling Theory for the Capillary Condensation Critical Point. *J. Chem. Phys.* **2001**, *114*, 5853–5862.
- (113) Binder, K.; Landau, D.; Müller, M. Monte Carlo Studies of Wetting, Interface Localization and Capillary Condensation. *J. Stat. Phys.* **2003**, *110*, 1411–1514.
- (114) Thommes, M.; Findenegg, G. H. Pore Condensation and Critical-Point Shift of a Fluid in Controlled-Pore Glass. *Langmuir* **1994**, *10*, 4270–4277.
- (115) Morishige, K.; Shikimi, M. Adsorption Hysteresis and Pore Critical Temperature in a Single Cylindrical Pore. *J. Chem. Phys.* **1998**, *108*, 7821–7824.
- (116) Schlaich, A.; Coasne, B. Dispersion Truncation Affects the Phase Behavior of Bulk and Confined Fluids: Coexistence, Adsorption, and Criticality. *J. Chem. Phys.* **2019**, *150*, 154104.
- (117) Coasne, B.; Gubbins, K. E.; Pellenq, R. J.-M. Temperature Effect on Adsorption/Desorption Isotherms for a Simple Fluid Confined within Various Nanopores. *Adsorption* **2005**, *11*, 289–294.
- (118) Ferreira de Souza, N.; Picard, C.; Franco, L. F. M.; Coasne. Thermal Conductivity of a Fluid-Filled Nanoporous Material: Underlying Molecular Mechanisms and the Rattle Effect. *J. Phys. Chem. B* **2024**, *128*, 2516–2567.
- (119) Kasap, S., Capper, P., Eds. *Springer Handbook of Electronic and Photonic Materials*, 2nd ed.; Springer International Publishing, 2017.
- (120) Ashcroft, N. W.; Mermin, N. D. *Solid State Physics*; Holt, Rinehart and Winston, 1976.
- (121) Zeigermann, P.; Naumov, S.; Mascotto, S.; Kärger, J.; Smarsly, B. M.; Valiullin, R. Diffusion in Hierarchical Mesoporous Materials: Applicability and Generalization of the Fast-Exchange Diffusion Model. *Langmuir* **2012**, *28*, 3621–3632.
- (122) Levitz, P. Random Flights in Confining Interfacial Systems. *J. Phys.: Condens. Matter* **2005**, *17*, S4059.
- (123) Levitz, P.; Bonnaud, P. A.; Cazade, P.-A.; Pellenq, R. J.-M.; Coasne, B. Molecular Intermittent Dynamics of Interfacial Water: Probing Adsorption and Bulk Confinement. *Soft Matter* **2013**, *9*, 8654–8663.
- (124) A formal derivation of this relationship is as follows.  $L(t) \sim \int_0^T I(\tau)I(t+\tau)d\tau$  so that  $L'(t) \sim \int_0^T I(\tau)I'(t+\tau)d\tau \sim \int_0^T I(\tau-t)I'(\tau)d\tau$  where the last equality is obtained by using the invariance of the function  $L'(t)$  upon time shift, i.e.,  $A(\tau)B(t+\tau) = A(\tau-t)B(\tau)$ . Starting from the last expression, we derive a second time to obtain  $L''(t) \sim -\int_0^T I'(\tau-t)I'(\tau)d\tau \sim -\int_0^T I'(\tau)I'(\tau+t)d\tau$ .
- (125) Here, we use that  $\psi_A(t)$  and  $\psi_B(t) = 0$  for  $t < 0$  so that  $\tilde{\psi}_A(\omega) = \int_{-\infty}^{\infty} \psi_A(t) \exp(i\omega t)dt = \int_0^{\infty} \psi_A(t) \exp(i\omega t)dt$  and  $\tilde{\psi}_B(\omega) = \int_{-\infty}^{\infty} \psi_B(t) \exp(i\omega t)dt = \int_0^{\infty} \psi_B(t) \exp(i\omega t)dt$ . As a result, upon calculating  $\tilde{L}''(\omega) \sim -2 + \int_0^{\infty} \psi_A(t) \exp(i\omega t)dt + \int_{-\infty}^0 \psi_A(-t) \exp(i\omega t)dt + \dots \sim -2 + \text{Re}[2 \times \tilde{\psi}(\omega) + \dots]$ .
- (126) Bousige, C.; Levitz, P.; Coasne, B. Bridging Scales in Disordered Porous Media by Mapping Molecular Dynamics onto Intermittent Brownian Motion. *Nat. Commun.* **2021**, *12*, 1043.
- (127) Kärger, J.; Pfeifer, H.; Vartapetian, R. S.; Voloshchuk, A. M. Molecular Self-Diffusion in Active Carbons. *Pure Appl. Chem.* **1989**, *61*, 1875–1880.
- (128) Brandani, S.; Ruthven, D. M.; Kärger, J. Concentration Dependence of Self-Diffusivity of Methanol in NaX Zeolite Crystals. *Zeolites* **1995**, *15*, 494–495.
- (129) Coasne, B.; Jain, S. K.; Gubbins, K. E. Adsorption, Structure and Dynamics of Fluids in Ordered and Disordered Models of Porous Carbons. *Mol. Phys.* **2006**, *104*, 3491–3499.
- (130) Bhatia, S. K.; Nicholson, D. Modeling Mixture Transport at the Nanoscale: Departure from Existing Paradigms. *Phys. Rev. Lett.* **2008**, *100*, 236103.
- (131) Chemmi, H.; Petit, D.; Levitz, P.; Denoyel, R.; Galarneau, A.; Korb, J.-P. Noninvasive Experimental Evidence of the Linear Pore Size Dependence of Water Diffusion in Nanoconfinement. *J. Phys. Chem. Lett.* **2016**, *7*, 393–398.

- (132) Bhatia, S. K.; Nicholson, D. Hydrodynamic Origin of Diffusion in Nanopores. *Phys. Rev. Lett.* **2003**, *90*, 016105.
- (133) This simple treatment is important as it allows capturing the overall effect of fluid density and pressure on the effective diffusivity in nanopores in the low pressure range (see Figure 9). The above treatment can be recovered easily from the simple scaling behavior derived earlier  $\overline{D}_s = \sum_{\alpha=1,2} x_\alpha D_s^\alpha$  with  $\alpha = 1$  and  $\alpha = 2$  for the adsorbed phase, respectively. Within the approximation  $\rho_g \sim 0$ , such a linear combination rule leads to  $\overline{D}_s \sim D_s^1$  since the fraction of molecules is  $x_g \sim \rho_g \sim 0$ . In other words, at temperatures low enough, molecular diffusion through the gas phase can be neglected so that, independently of the diffusion combination rules considered, diffusion only occurs through the adsorbed phase with a diffusion coefficient equal to the surface diffusion.
- (134) Obliger, A.; Pellenq, R.; Ulm, F.-J.; Coasne, B. Free Volume Theory of Hydrocarbon Mixture Transport in Nanoporous Materials. *J. Phys. Chem. Lett.* **2016**, *7*, 3712–3717.
- (135) Cohen, M. H.; Turnbull, D. Molecular Transport in Liquids and Glasses. *J. Chem. Phys.* **1959**, *31*, 1164–1169.
- (136) Kärger, J.; Pfeifer, H.; Rauscher, M.; Walter, A. Self-Diffusion of n-Paraffins in NaX Zeolite. *Journal of the Chemical Society, Faraday Transactions 1: Physical Chemistry in Condensed Phases* **1980**, *76*, 717–737.
- (137) Ghanbarian, B.; Hunt, A. G.; Ewing, R. P.; Sahimi, M. Tortuosity in Porous Media: A Critical Review. *Soil Science Society of America Journal* **2013**, *77*, 1461–1477.
- (138) Sobieski, W.; Lipiński, S. *The Analysis of the Relations between Porosity and Tortuosity in Granular Beds*; Technical Sciences/University of Warmia and Mazury in Olsztyn 2017, Vol. 20(1).
- (139) Weissberg, H. L. Effective Diffusion Coefficient in Porous Media. *J. Appl. Phys.* **1963**, *34*, 2636–2639.
- (140) Kolitcheff, S.; Jolimaitre, E.; Hugon, A.; Verstraete, J.; Carrette, P.-L.; Tayakout-Fayolle, M. Tortuosity of Mesoporous Alumina Catalyst Supports: Influence of the Pore Network Organization. *Microporous Mesoporous Mater.* **2017**, *248*, 91–98.
- (141) Archie, G. E. others The Electrical Resistivity Log as an Aid in Determining Some Reservoir Characteristics. *Transactions of the AIME* **1942**, *146*, 54–62.
- (142) Glover, P. A. Generalized Archie's Law for n-Phases. *EGU General Assembly Conference Abstracts*; 2010; p 2518.
- (143) Markel, V. A. Introduction to the Maxwell Garnett Approximation: Tutorial. *J. Opt. Soc. Am. A, JOSAA* **2016**, *33*, 1244–1256.
- (144) Barrande, M.; Bouchet, R.; Denoyel, R. Tortuosity of Porous Particles. *Anal. Chem.* **2007**, *79*, 9115–9121.
- (145) Landauer, R. The Electrical Resistance of Binary Metallic Mixtures. *J. Appl. Phys.* **1952**, *23*, 779–784.
- (146) Duda, A.; Koza, Z.; Matyka, M. Hydraulic Tortuosity in Arbitrary Porous Media Flow. *Phys. Rev. E* **2011**, *84*, 036319.
- (147) When deriving this equation, the far field solution for  $r > R_0$  applies *a fortiori* to  $r > R$  since  $R_0 \gg R$ .
- (148) Bruggeman, D. a. G. Berechnung verschiedener physikalischer Konstanten von heterogenen Substanzen. I. Dielektrizitätskonstanten und Leitfähigkeiten der Mischkörper aus isotropen Substanzen. *Annalen der Physik* **1935**, *416*, 636–664.
- (149) Landauer, R. *Electrical Conductivity in Inhomogeneous Media*; American Institute of Physics Conference Series. 1978; pp 2–45.
- (150) Kirkpatrick, S. Percolation and Conduction. *Rev. Mod. Phys.* **1973**, *45*, 574–588.
- (151) Bonilla, M. R.; Valiullin, R.; Kärger, J.; Bhatia, S. K. Understanding Adsorption and Transport of Light Gases in Hierarchical Materials Using Molecular Simulation and Effective Medium Theory. *J. Phys. Chem. C* **2014**, *118*, 14355–14370.
- (152) de Jong, K. P.; Zečević, J.; Friedrich, H.; de Jongh, P. E.; Bulut, M.; van Donk, S.; Kenmogne, R.; Finiels, A.; Hulea, V.; Fajula, F. Zeolite Y Crystals with Trimodal Porosity as Ideal Hydrocracking Catalysts. *Angew. Chem., Int. Ed.* **2010**, *49*, 10074–10078.
- (153) Maris, J. J. E.; Fu, D.; Meirer, F.; Weckhuysen, B. M. Single-Molecule Observation of Diffusion and Catalysis in Nanoporous Solids. *Adsorption* **2021**, *27*, 423–452.
- (154) Risken, H.; Frank, T. *The Fokker-Planck Equation: Methods of Solution and Applications*, 2nd ed.; Springer Series in Synergetics; Springer-Verlag: Berlin, 1996.
- (155) Noettinger, B.; Roubinet, D.; Russian, A.; Le Borgne, T.; Delay, F.; Dentz, M.; de Dreuzy, J.-R.; Gouze, P. Random Walk Methods for Modeling Hydrodynamic Transport in Porous and Fractured Media from Pore to Reservoir Scale. *Transp Porous Med.* **2016**, *115*, 345–385.
- (156) To obtain this equation, we notice that the cross terms  $\langle \mathbf{v}(0) \times \int_0^t dt' \exp[-\xi(t-t')] \delta \mathbf{F}(t') \rangle$  are equal to zero because the velocity at time  $t = 0$  only depends on the force exerted at times  $t < 0$  and therefore not on the force exerted at times  $t \geq 0$ .
- (157) Bhatia, S. K. Stochastic Theory of Transport in Inhomogeneous Media. *Chem. Eng. Sci.* **1986**, *41*, 1311–1324.
- (158) Bonilla, M. R.; Bhatia, S. K. Multicomponent Effective Medium—Correlated Random Walk Theory for the Diffusion of Fluid Mixtures through Porous Media. *Langmuir* **2012**, *28*, 517–533.
- (159) Schwartz, L. M.; Banavar, J. R. Transport Properties of Disordered Continuum Systems. *Phys. Rev. B* **1989**, *39*, 11965–11970.
- (160) Epicoco, P.; Coasne, B.; Gioia, A.; Papet, P.; Cabodi, I.; Gaubil, M. Mesoscopic Monte Carlo Simulations of Microstructure and Conductivity of ZrO<sub>2</sub>–Glass Composites. *Acta Mater.* **2013**, *61*, 5018–5025.
- (161) Boțan, A.; Ulm, F.-J.; Pellenq, R. J.-M.; Coasne, B. Bottom-up Model of Adsorption and Transport in Multiscale Porous Media. *Phys. Rev. E* **2015**, *91*, 032133.
- (162) Han, M.; Youssef, S.; Rosenberg, E.; Fleury, M.; Levitz, P. Deviation from Archie's Law in Partially Saturated Porous Media: Wetting Film versus Disconnectedness of the Conducting Phase. *Phys. Rev. E* **2009**, *79*, 031127.
- (163) Salles, J.; Thovert, J.-F.; Delannay, R.; Prevors, L.; Auriault, J.-L.; Adler, P. M. Taylor Dispersion in Porous Media. Determination of the Dispersion Tensor. *Physics of Fluids A: Fluid Dynamics* **1993**, *5*, 2348–2376.
- (164) Hlushkou, D.; Bruns, S.; Höltzel, A.; Tallarek, U. From Pore Scale to Column Scale Dispersion in Capillary Silica Monoliths. *Anal. Chem.* **2010**, *82*, 7150–7159.
- (165) Tallarek, U.; Hlushkou, D.; Rybka, J.; Höltzel, A. Multiscale Simulation of Diffusion in Porous Media: From Interfacial Dynamics to Hierarchical Porosity. *J. Phys. Chem. C* **2019**, *123*, 15099–15112.
- (166) Hlushkou, D.; Bruns, S.; Seidel-Morgenstern, A.; Tallarek, U. Morphology–Transport Relationships for Silica Monoliths: From Physical Reconstruction to Pore-Scale Simulations. *J. Sep. Sci.* **2011**, *34*, 2026–2037.
- (167) Yang, X.-R.; Wang, Y. Ubiquity of Anomalous Transport in Porous Media: Numerical Evidence, Continuous Time Random Walk Modelling, and Hydrodynamic Interpretation. *Sci. Rep.* **2019**, *9*, 4601.
- (168) Mehlhorn, D.; Inayat, A.; Schwieger, W.; Valiullin, R.; Kärger, J. Probing Mass Transfer in Mesoporous Faujasite-Type Zeolite Nano-sheet Assemblies. *ChemPhysChem* **2014**, *15*, 1681–1686.
- (169) June, R. L.; Bell, A. T.; Theodorou, D. N. Transition-State Studies of Xenon and Sulfur Hexafluoride Diffusion in Silicalite. *J. Phys. Chem.* **1991**, *95*, 8866–8878.
- (170) Maginn, E. J.; Bell, A. T.; Theodorou, D. N. Dynamics of Long N-Alkanes in Silicalite: A Hierarchical Simulation Approach. *J. Phys. Chem.* **1996**, *100*, 7155–7173.
- (171) Schüring, A.; Auerbach, S. M.; Fritzsch, S.; Haberlandt, R. On Entropic Barriers for Diffusion in Zeolites: A Molecular Dynamics Study. *J. Chem. Phys.* **2002**, *116*, 10890–10894.
- (172) Dubbeldam, D.; Beerdsen, E.; Vlugt, T. J. H.; Smit, B. Molecular Simulation of Loading-Dependent Diffusion in Nanoporous Materials Using Extended Dynamically Corrected Transition State Theory. *J. Chem. Phys.* **2005**, *122*, 224712.
- (173) Abouelnasr, M. K. F.; Smit, B. Diffusion in Confinement: Kinetic Simulations of Self- and Collective Diffusion Behavior of Adsorbed Gases. *Phys. Chem. Chem. Phys.* **2012**, *14*, 11600–11609.

- (174) Bai, P.; Haldoupis, E.; Dauenhauer, P. J.; Tsapatsis, M.; Siepmann, J. I. Understanding Diffusion in Hierarchical Zeolites with House-of-Cards Nanosheets. *ACS Nano* **2016**, *10*, 7612–7618.
- (175) Beerdse, E.; Dubbeldam, D.; Smit, B. Understanding Diffusion in Nanoporous Materials. *Phys. Rev. Lett.* **2006**, *96*, 044501.
- (176) Kim, J.; Abouelnasr, M.; Lin, L.-C.; Smit, B. Large-Scale Screening of Zeolite Structures for CO<sub>2</sub>Membrane Separations. *J. Am. Chem. Soc.* **2013**, *135*, 7545–7552.
- (177) This condition is equivalent to assuming that two subsequent jumps are uncorrelated as usually assumed in any random walk approach.
- (178) In more detail,  $\pi(t) = \rho \exp(-\rho t)$  leads to  $\Pi(t) = \int_0^t \pi(t') dt' = [-\exp(-\rho t')]_0^t = 1 - \exp(-\rho t)$ . In turn, the condition  $\epsilon = \Pi(\tau)$  leads to  $\tau = -\ln(1 - \epsilon)/\rho$ .
- (179) Ho, C. K., Webb, S. W., Eds. *Gas Transport in Porous Media; Theory and Applications of Transport in Porous Media*; Springer: Netherlands, 2006.
- (180) Heiranian, M.; Fan, H.; Wang, L.; Lu, X.; Elimelech, M. Mechanisms and Models for Water Transport in Reverse Osmosis Membranes: History, Critical Assessment, and Recent Developments. *Chem. Soc. Rev.* **2023**, *52*, 8455–8480.
- (181) Wang, L.; He, J.; Heiranian, M.; Fan, H.; Song, L.; Li, Y.; Elimelech, M. Water Transport in Reverse Osmosis Membranes Is Governed by Pore Flow, Not a Solution-Diffusion Mechanism. *Science Advances* **2023**, *9*, No. eadf8488.
- (182) Fan, H.; He, J.; Heiranian, M.; Pan, W.; Li, Y.; Elimelech, M. The Physical Basis for Solvent Flow in Organic Solvent Nanofiltration. *Science Advances* **2024**, *10*, No. eado4332.
- (183) He, J.; Fan, H.; Elimelech, M.; Li, Y. Molecular Simulations of Organic Solvent Transport in Dense Polymer Membranes: Solution-diffusion or Pore-Flow Mechanism? *J. Membr. Sci.* **2024**, *708*, 123055.
- (184) Fan, H.; Heiranian, M.; Elimelech, M. The Solution-Diffusion Model for Water Transport in Reverse Osmosis: What Went Wrong? *Desalination* **2024**, *580*, 117575.
- (185) Wikimedia Commons, Activated Carbon. [https://commons.wikimedia.org/wiki/File:Activated\\_Carbon.jpg](https://commons.wikimedia.org/wiki/File:Activated_Carbon.jpg), 2006 (accessed May 27, 2024).
- (186) Schlaich, A.; Kappler, J.; Netz, R. R. Hydration Friction in Nanoconfinement: From Bulk via Interfacial to Dry Friction. *Nano Lett.* **2017**, *17*, 5969–5976.
- (187) Barrat, J.-L.; Bocquet, L. Large Slip Effect at a Nonwetting Fluid-Solid Interface. *Phys. Rev. Lett.* **1999**, *82*, 4671–4674.
- (188) Cottin-Bizonne, C.; Barrat, J.-L.; Bocquet, L.; Charlaix, E. Low-Friction Flows of Liquid at Nanopatterned Interfaces. *Nat. Mater.* **2003**, *2*, 237–240.
- (189) Coasne, B.; Galarneau, A.; Gerardin, C.; Fajula, F.; Villemot, F. Molecular Simulation of Adsorption and Transport in Hierarchical Porous Materials. *Langmuir* **2013**, *29*, 7864–7875.
- (190) De Gennes, P. G. Liquid Dynamics and Inelastic Scattering of Neutrons. *Physica* **1959**, *25*, 825–839.
- (191) Hohenberg, P. C.; Halperin, B. I. Theory of Dynamic Critical Phenomena. *Rev. Mod. Phys.* **1977**, *49*, 435–479.
- (192) Poulos, A. S.; Constantin, D.; Davidson, P.; Pansu, B.; Freyssingues, É.; Madsen, A.; Chanéac, C. Communications: Short-Range Dynamics of a Nematic Liquid-Crystalline Phase. *J. Chem. Phys.* **2010**, *132*, 091101.
- (193) Alba-Simionescu, C.; Toelle, A.; Morineau, D.; Farago, B.; Coddens, G. “de Gennes” Narrowing in Supercooled Molecular Liquids: Evidence for Center-of-Mass Dominated Slow Dynamics. *arXiv* 2001, *cond-mat/0103599*, accessed 2024/10/10, DOI: 10.48550/arXiv.cond-mat/0103599.
- (194) Kleban, P. Toward a Microscopic Basis for the de Gennes Narrowing. *J. Stat. Phys.* **1974**, *11*, 317–322.
- (195) Wu, B.; Iwashita, T.; Egami, T. Atomic Dynamics in Simple Liquid: De Gennes Narrowing Revisited. *Phys. Rev. Lett.* **2018**, *120*, 135502.
- (196) Nygård, K.; Buitenhuis, J.; Kagias, M.; Jefimovs, K.; Zontone, F.; Chushkin, Y. Anisotropic de Gennes Narrowing in Confined Fluids. *Phys. Rev. Lett.* **2016**, *116*, 167801.
- (197) Gruener, S.; Huber, P. Spontaneous Imbibition Dynamics of an \$n\$-Alkane in Nanopores: Evidence of Meniscus Freezing and Monolayer Sticking. *Phys. Rev. Lett.* **2009**, *103*, 174501.
- (198) Gruener, S.; Sadjadi, Z.; Hermes, H. E.; Kityk, A. V.; Knorr, K.; Egelhaaf, S. U.; Rieger, H.; Huber, P. Anomalous Front Broadening during Spontaneous Imbibition in a Matrix with Elongated Pores. *Proc. Natl. Acad. Sci. U. S. A.* **2012**, *109*, 10245–10250.
- (199) Tsunazawa, Y.; Yokoyama, T.; Nishiyama, N. An Experimental Study on the Rate and Mechanism of Capillary Rise in Sandstone. *Prog. in Earth and Planet. Sci.* **2016**, *3*, 8.
- (200) Quéré, D. Inertial Capillarity. *Europhys. Lett.* **1997**, *39*, 533–538.
- (201) Joly, L. Capillary Filling with Giant Liquid/Solid Slip: Dynamics of Water Uptake by Carbon Nanotubes. *J. Chem. Phys.* **2011**, *135*, 214705.
- (202) Fries, N.; Dreyer, M. An Analytic Solution of Capillary Rise Restrained by Gravity. *J. Colloid Interface Sci.* **2008**, *320*, 259–263.
- (203) Sircar, S.; Hufton, J. Why Does the Linear Driving Force Model for Adsorption Kinetics Work? *Adsorption* **2000**, *6*, 137–147.
- (204) Brandani, S. Exact Equivalence at Cyclic Steady State between Isothermal Diffusion and Linear Driving Force Models for Linear Adsorption Systems. *Adsorption* **2021**, *27*, 171–180.
- (205) Remi, J. C. S.; Lauerer, A.; Chmelik, C.; Vandendaal, I.; Terryn, H.; Baron, G. V.; Denayer, J. F. M.; Kärger, J. The Role of Crystal Diversity in Understanding Mass Transfer in Nanoporous Materials. *Nat. Mater.* **2016**, *15*, 401–406.
- (206) Fasano, M.; Humplík, T.; Bevilacqua, A.; Tsapatsis, M.; Chiavazzo, E.; Wang, E. N.; Asinari, P. Interplay between Hydrophilicity and Surface Barriers on Water Transport in Zeolite Membranes. *Nat. Commun.* **2016**, *7*, 12762.
- (207) Gulín-González, J.; Schüring, A.; Fritzsche, S.; Kärger, J.; Vasenkov, S. The Influence of the Desorption Barrier on the Transport of Molecules through the External Surface of Nanoporous Crystals. *Chem. Phys. Lett.* **2006**, *430*, 60–66.
- (208) Coasne, B.; Farrusseng, D. Gas Oversolvability in Nanoconfined Liquids: Review and Perspectives for Adsorbent Design. *Microporous Mesoporous Mater.* **2019**, *288*, 109561.
- (209) Jaeger, J. C.; Carslaw, H. S. *Conduction of Heat in Solids*; Clarendon, 1959.
- (210) Combariza, A. F.; Sastre, G. Influence of Zeolite Surface in the Sorption of Methane from Molecular Dynamics. *J. Phys. Chem. C* **2011**, *115*, 13751–13758.
- (211) Crabtree, J. C.; Molinari, M.; Parker, S. C.; Purton, J. A. Simulation of the Adsorption and Transport of CO<sub>2</sub> on Faujasite Surfaces. *J. Phys. Chem. C* **2013**, *117*, 21778–21787.
- (212) Sastre, G.; Kärger, J.; Ruthven, D. M. Molecular Dynamics Study of Diffusion and Surface Permeation of Benzene in Silicalite. *J. Phys. Chem. C* **2018**, *122*, 7217–7225.
- (213) Zimmerman, P. M.; Head-Gordon, M.; Bell, A. T. Selection and Validation of Charge and Lennard-Jones Parameters for QM/MM Simulations of Hydrocarbon Interactions with Zeolites. *J. Chem. Theory Comput.* **2011**, *7*, 1695–1703.
- (214) Liu, L.; Nicholson, D.; Bhatia, S. K. Interfacial Resistance and Length-Dependent Transport Diffusivities in Carbon Nanotubes. *J. Phys. Chem. C* **2016**, *120*, 26363–26373.
- (215) Zimmermann, N. E. R.; Balaji, S. P.; Keil, F. J. Surface Barriers of Hydrocarbon Transport Triggered by Ideal Zeolite Structures. *J. Phys. Chem. C* **2012**, *116*, 3677–3683.
- (216) Lee, T.; Bocquet, L.; Coasne, B. Activated Desorption at Heterogeneous Interfaces and Long-Time Kinetics of Hydrocarbon Recovery from Nanoporous Media. *Nat. Commun.* **2016**, *7*, 11890.
- (217) Inzoli, I.; Simon, J. M.; Kjelstrup, S.; Bedeaux, D. Thermal Effects during Adsorption of N-Butane on a Silicalite-1 Membrane: A Non-Equilibrium Molecular Dynamics Study. *J. Colloid Interface Sci.* **2007**, *313*, 563–573.

- (218) Simon, J.-M.; Bellat, J.-P.; Salazar, J. M. Adsorption and Desorption Surface Dynamics of Gaseous Adsorbate on Silicate-1 by Molecular Dynamics Simulation. *Mol. Simul.* **2014**, *40*, 52–57.
- (219) Gravelle, S.; Joly, L.; Detcheverry, F.; Ybert, C.; Cottin-Bizonne, C.; Bocquet, L. Optimizing Water Permeability through the Hourglass Shape of Aquaporins. *Proc. Natl. Acad. Sci. U.S.A.* **2013**, *110*, 16367–16372.
- (220) Gadaleta, A.; Sempere, C.; Gravelle, S.; Siria, A.; Fulcrand, R.; Ybert, C.; Bocquet, L. Sub-Additive Ionic Transport across Arrays of Solid-State Nanopores. *Phys. Fluids* **2014**, *26*, 012005.
- (221) Liu, L.; Nicholson, D.; Bhatia, S. K. Effects of Flange Adsorption Affinity and Membrane Porosity on Interfacial Resistance in Carbon Nanotube Membranes. *ACS Appl. Mater. Interfaces* **2018**, *10*, 34706–34717.
- (222) Falk, K.; Pellenq, R.; Ulm, F. J.; Coasne, B. Effect of Chain Length and Pore Accessibility on Alkane Adsorption in Kerogen. *Energy Fuels* **2015**, *29*, 7889–7896.
- (223) Bousige, C.; Ghimbeu, C. M.; Vix-Guterl, C.; Pomerantz, A. E.; Suleimenova, A.; Vaughan, G.; Garbarino, G.; Feygenson, M.; Wildgruber, C.; Ulm, F.-J.; Pellenq, R. J.-M.; Coasne, B. Realistic Molecular Model of Kerogen's Nanostructure. *Nat. Mater.* **2016**, *15*, 576–582.
- (224) Ladd, A. J. C.; Verberg, R. Lattice-Boltzmann Simulations of Particle-Fluid Suspensions. *J. Stat. Phys.* **2001**, *104*, 1191–1251.
- (225) Verberg, R.; Ladd, A. J. C. Accuracy and Stability of a Lattice-Boltzmann Model with Subgrid Scale Boundary Conditions. *Phys. Rev. E* **2001**, *63*, 016701.
- (226) Krüger, T.; Kusumaatmaja, H.; Kuzmin, A.; Shardt, O.; Silva, G.; Viggen, E. M. *The Lattice Boltzmann Method: Principles and Practice; Graduate Texts in Physics*; Springer International Publishing: Cham, 2017.
- (227) Vanson, J.-M. *Interdépendance Entre Géométrie, Adsorption et Transport Dans Les Matériaux à Porosité Hiérarchique*. PhD Thesis, PSL Research University, Paris, France, 2016.
- (228) Zaafouri, Z. *Modélisation Du Transport Des Surfactants En Milieu Poreux: Influence de l'hétérogénéité Des Grandeur Macroscopiques Sur La Couche Adsorbée*. PhD Thesis, Université Grenoble Alpes, Grenoble, France, 2020.
- (229) Vanson, J.-M.; Coudert, F.-X.; Rotenberg, B.; Levesque, M.; Tardivat, C.; Klotz, M.; Boutin, A. Unexpected Coupling between Flow and Adsorption in Porous Media. *Soft Matter* **2015**, *11*, 6125–6133.
- (230) Levesque, M.; Duvail, M.; Pagonabarraga, I.; Frenkel, D.; Rotenberg, B. Accounting for Adsorption and Desorption in Lattice Boltzmann Simulations. *Phys. Rev. E* **2013**, *88*, 013308.
- (231) Lowe, C. P.; Frenkel, D. The Super Long-Time Decay of Velocity Fluctuations in a Two-Dimensional Fluid. *Physica A: Statistical Mechanics and its Applications* **1995**, *220*, 251–260.
- (232) Lowe, C. P.; Frenkel, D. Do Hydrodynamic Dispersion Coefficients Exist? *Phys. Rev. Lett.* **1996**, *77*, 4552–4555.
- (233) A Markov process is a stochastic model describing a sequence of possible events in which the probability of each future event depends only on the current state. Roughly speaking, this Markov property can be characterized as “memorylessness”. Prominent examples cover random walks, Brownian motion and Markov chain Monte Carlo simulations.
- (234) Gagniuc, P. A. *Markov Chains: From Theory to Implementation and Experimentation*; John Wiley & Sons, 2017.
- (235) Kang, H. C.; Weinberg, W. H. Dynamic Monte Carlo with a Proper Energy Barrier: Surface Diffusion and Two-dimensional Domain Ordering. *J. Chem. Phys.* **1989**, *90*, 2824–2830.
- (236) Jansen, A. P. J. An Introduction to Monte Carlo Simulations of Surface Reactions. *arXiv* 2003, cond-mat/0303028, accessed 2024/10/10, DOI: [10.48550/arXiv.cond-mat/0303028](https://doi.org/10.48550/arXiv.cond-mat/0303028).
- (237) Serebrinsky, S. A. Physical Time Scale in Kinetic Monte Carlo Simulations of Continuous-Time Markov Chains. *Phys. Rev. E* **2011**, *83*, 037701.
- (238) Trout, B. L.; Chakraborty, A. K.; Bell, A. T. Diffusion and Reaction in ZSM-5 Studied by Dynamic Monte Carlo. *Chem. Eng. Sci.* **1997**, *52*, 2265–2276.
- (239) Coppens, M.-O.; Bell, A. T.; Chakraborty, A. K. Dynamic Monte-Carlo and Mean-Field Study of the Effect of Strong Adsorption Sites on Self-Diffusion in Zeolites. *Chem. Eng. Sci.* **1999**, *54*, 3455–3463.
- (240) Paschek, D.; Krishna, R. Diffusion of Binary Mixtures in Zeolites: Kinetic Monte Carlo versus Molecular Dynamics Simulations. *Langmuir* **2001**, *17*, 247–254.
- (241) Liu, X.; Newsome, D.; Coppens, M.-O. Dynamic Monte Carlo Simulations of Binary Self-Diffusion in ZSM-5. *Microporous Mesoporous Mater.* **2009**, *125*, 149–159.
- (242) Schumacher, C.; Gonzalez, J.; Wright, P. A.; Seaton, N. A. Generation of Atomistic Models of Periodic Mesoporous Silica by Kinetic Monte Carlo Simulation of the Synthesis of the Material. *J. Phys. Chem. B* **2006**, *110*, 319–333.
- (243) CARLOS Is a General-Purpose Program, Written in C by J. J. Lukkien, for Simulating Reactions on Surfaces That Can Be Represented by Regular Grids; an Implementation of the First-Reaction Method, the Variable Stepsize Method, and the Random Selection Method. <https://carlos.win.tue.nl/>.
- (244) Rai, V.; Pitsch, H.; Novikov, A. Efficient Dynamic Monte Carlo Algorithm for Time-Dependent Catalytic Surface Chemistry. *Phys. Rev. E* **2006**, *74*, 046707.
- (245) Dybeck, E. C.; Plaisance, C. P.; Neurock, M. Generalized Temporal Acceleration Scheme for Kinetic Monte Carlo Simulations of Surface Catalytic Processes by Scaling the Rates of Fast Reactions. *J. Chem. Theory Comput.* **2017**, *13*, 1525–1538.
- (246) Janda, A.; Vlaisavljevich, B.; Lin, L.-C.; Smit, B.; Bell, A. T. Effects of Zeolite Structural Confinement on Adsorption Thermodynamics and Reaction Kinetics for Monomolecular Cracking and Dehydrogenation of N-Butane. *J. Am. Chem. Soc.* **2016**, *138*, 4739–4756.
- (247) Voter, A. F. Introduction to the Kinetic Monte Carlo Method. *Radiation Effects in Solids*. 2007; pp 1–23.
- (248) Kawasaki, K. *Phase Transitions and Critical Phenomena*; Elsevier, 1972; Vol. 2.
- (249) Godrèche, C.; Luck, J. M. Anomalous Self-Diffusion in the Ferromagnetic Ising Chain with Kawasaki Dynamics. *J. Phys. A: Math. Gen.* **2003**, *36*, 9973–9989.
- (250) Monette, L.; Liu, A. J.; Grest, G. S. Wetting and Domain-Growth Kinetics in Confined Geometries. *Phys. Rev. A* **1992**, *46*, 7664–7679.
- (251) Chakrabarti, A. Kinetics of Domain Growth and Wetting in a Model Porous Medium. *Phys. Rev. Lett.* **1992**, *69*, 1548–1551.
- (252) Luzar, A.; Leung, K. Dynamics of Capillary Evaporation. I. Effect of Morphology of Hydrophobic Surfaces. *J. Chem. Phys.* **2000**, *113*, 5836–5844.
- (253) Woo, H.-J.; Monson, P. A. Phase Behavior and Dynamics of Fluids in Mesoporous Glasses. *Phys. Rev. E* **2003**, *67*, 041207.
- (254) Valiullin, R.; Naumov, S.; Galvosas, P.; Kärger, J.; Woo, H.-J.; Porcheron, F.; Monson, P. A. Exploration of Molecular Dynamics during Transient Sorption of Fluids in Mesoporous Materials. *Nature* **2006**, *443*, 965–968.
- (255) Gouyet, J.-F.; Plapp, M.; Dieterich, W.; Maass, P. Description of Far-from-Equilibrium Processes by Mean-Field Lattice Gas Models. *Adv. Phys.* **2003**, *52*, 523–638.
- (256) Monson, P. A. Mean Field Kinetic Theory for a Lattice Gas Model of Fluids Confined in Porous Materials. *J. Chem. Phys.* **2008**, *128*, 084701.
- (257) Kierlik, E.; Leoni, F.; Rosinberg, M. L.; Tarjus, G. Spontaneous Imbibition in a Slit Pore: A Lattice–Gas Dynamic Mean Field Study. *Mol. Phys.* **2011**, *109*, 1143–1157.
- (258) Leoni, F.; Kierlik, E.; Rosinberg, M. L.; Tarjus, G. Spontaneous Imbibition in Disordered Porous Solids: A Theoretical Study of Helium in Silica Aerogels. *Langmuir* **2011**, *27*, 8160–8170.
- (259) Edison, J. R.; Monson, P. A. Dynamic Mean Field Theory for Lattice Gas Models of Fluid Mixtures Confined in Mesoporous Materials. *Langmuir* **2013**, *29*, 13808–13820.

- (260) Casselman, J. A.; Desouza, A.; Monson, P. A. Modelling the Dynamics of Condensation and Evaporation of Fluids in Three-Dimensional Slit Pores. *Mol. Phys.* **2015**, *113*, 1250–1260.
- (261) Marconi, U. M. B.; Tarazona, P. Dynamic Density Functional Theory of Fluids. *J. Chem. Phys.* **1999**, *110*, 8032–8044.
- (262) Archer, A. J.; Evans, R. Dynamical Density Functional Theory and Its Application to Spinodal Decomposition. *J. Chem. Phys.* **2004**, *121*, 4246–4254.
- (263) Kikkinides, E. S.; Monson, P. A. Dynamic Density Functional Theory with Hydrodynamic Interactions: Theoretical Development and Application in the Study of Phase Separation in Gas-Liquid Systems. *J. Chem. Phys.* **2015**, *142*, 094706.
- (264) Rathi, A.; Kikkinides, E. S.; Ford, D. M.; Monson, P. A. A Comparison of Dynamic Mean Field Theory and Grand Canonical Molecular Dynamics for the Dynamics of Pore Filling and Capillary Condensation of Fluids in Mesopores. *J. Chem. Phys.* **2018**, *149*, 014703.
- (265) Rathi, A.; Kikkinides, E. S.; Ford, D. M.; Monson, P. A. Nonequilibrium Steady States in Fluid Transport through Mesopores: Dynamic Mean Field Theory and Nonequilibrium Molecular Dynamics. *Langmuir* **2019**, *35*, 5702–5710.
- (266) Wu, J.; Li, Z. Density-Functional Theory for Complex Fluids. *Annu. Rev. Phys. Chem.* **2007**, *58*, 85–112.
- (267) Obliger, A.; Jardat, M.; Coelho, D.; Bekri, S.; Rotenberg, B. Pore Network Model of Electrokinetic Transport through Charged Porous Media. *Phys. Rev. E* **2014**, *89*, 043013.
- (268) Gjennestad, M. A.; Vassvik, M.; Kjelstrup, S.; Hansen, A. Stable and Efficient Time Integration of a Dynamic Pore Network Model for Two-Phase Flow in Porous Media. *Front. Phys.* **2018**, *6*, 56.
- (269) Schoch, R. B.; Han, J.; Renaud, P. Transport Phenomena in Nanofluidics. *Rev. Mod. Phys.* **2008**, *80*, 839–883.
- (270) Fedorov, M. V.; Kornyshev, A. A. Ionic Liquids at Electrified Interfaces. *Chem. Rev.* **2014**, *114*, 2978–3036.
- (271) Kondrat, S.; Feng, G.; Bresme, F.; Urbakh, M.; Kornyshev, A. A. Theory and Simulations of Ionic Liquids in Nanoconfinement. *Chem. Rev.* **2023**, *123*, 6668–6715.
- (272) Logan, B. E.; Elimelech, M. Membrane-Based Processes for Sustainable Power Generation Using Water. *Nature* **2012**, *488*, 313–319.
- (273) Werber, J. R.; Osuji, C. O.; Elimelech, M. Materials for Next-Generation Desalination and Water Purification Membranes. *Nat. Rev. Mater.* **2016**, *1*, 16018.
- (274) Reiner, D. *Carbon Capture and Storage*; The Royal Society of Chemistry, 2019.
- (275) Gluge, J.; Scheringer, M.; Cousins, I. T.; DeWitt, J. C.; Goldenman, G.; Herzke, D.; Lohmann, R.; Ng, C. A.; Trier, X.; Wang, Z. An Overview of the Uses of Per- and Polyfluoroalkyl Substances (PFAS). *Environmental Science: Processes & Impacts* **2020**, *22*, 2345–2373.
- (276) Coudert, F.-X. Responsive Metal–Organic Frameworks and Framework Materials: Under Pressure, Taking the Heat, in the Spotlight, with Friends. *Chem. Mater.* **2015**, *27*, 1905–1916.
- (277) Chen, M.; Coasne, B.; Guyer, R.; Derome, D.; Carmeliet, J. Role of Hydrogen Bonding in Hysteresis Observed in Sorption-Induced Swelling of Soft Nanoporous Polymers. *Nat. Commun.* **2018**, *9*, 3507.
- (278) Coussy, O. *Poromechanics*; John Wiley & Sons, 2004.
- (279) Marbach, S.; Dean, D. S.; Bocquet, L. Transport and Dispersion across Wiggling Nanopores. *Nature Phys.* **2018**, *14*, 1108–1113.
- (280) Wei, M.; Liu, Y.; Liu, J.; Elsworth, D.; Zhou, F. Micro-Scale Investigation on Coupling of Gas Diffusion and Mechanical Deformation of Shale. *J. Pet. Sci. Eng.* **2019**, *175*, 961–970.
- (281) Berthonneau, J.; Obliger, A.; Valdenaire, P.-L.; Grauby, O.; Ferry, D.; Chaudanson, D.; Levitz, P.; Kim, J. J.; Ulm, F.-J.; Pellenq, R. J.-M. Mesoscale Structure, Mechanics, and Transport Properties of Source Rocks’ Organic Pore Networks. *Proc. Natl. Acad. Sci. U. S. A.* **2018**, *115*, 12365–12370.
- (282) Hoseini, M.; Bindiganavile, V.; Banthia, N. The Effect of Mechanical Stress on Permeability of Concrete: A Review. *Cement and Concrete Composites* **2009**, *31*, 213–220.
- (283) Zhang, Y.; Wan, X.; Hou, D.; Zhao, T.; Cui, Y. The Effect of Mechanical Load on Transport Property and Pore Structure of Alkali-Activated Slag Concrete. *Construction and Building Materials* **2018**, *189*, 397–408.
- (284) Bai, M.; Elsworth, D. *Coupled Processes in Subsurface Deformation, Flow, and Transport*; American Society of Civil Engineers, 2000, DOI: [10.1061/9780784404607](https://doi.org/10.1061/9780784404607).
- (285) Mitschke, B.; Turberg, M.; List, B. Confinement as a Unifying Element in Selective Catalysis. *Chem.* **2020**, *6*, 2515–2532.
- (286) Ho, L. N.; Clauzier, S.; Schuurman, Y.; Farrusseng, D.; Coasne, B. Gas Uptake in Solvents Confined in Mesopores: Adsorption versus Enhanced Solubility. *J. Phys. Chem. Lett.* **2013**, *4*, 2274–2278.
- (287) Ho, L. N.; Schuurman, Y.; Farrusseng, D.; Coasne, B. Solubility of Gases in Water Confined in Nanoporous Materials: ZSM-5, MCM-41, and MIL-100. *J. Phys. Chem. C* **2015**, *119*, 21547–21554.
- (288) Emmerling, S. T.; Ziegler, F.; Fischer, F. R.; Schoch, R.; Bauer, M.; Plietker, B.; Buchmeiser, M. R.; Lotsch, B. V. Olefin Metathesis in Confinement: Towards Covalent Organic Framework Scaffolds for Increased Macrocyllization Selectivity. *Chemistry – A European Journal* **2022**, *28*, No. e202104108.
- (289) Noh, Y.; Aluru, N. R. Phonon-Fluid Coupling Enhanced Water Desalination in Flexible Two-Dimensional Porous Membranes. *Nano Lett.* **2022**, *22*, 419–425.
- (290) Schlaich, A.; Vandamme, M.; Plazanet, M.; Coasne, B. Bridging Microscopic Dynamics and Hydraulic Permeability in Mechanically-Deformed Nanoporous Materials. *ACS Nano* **2024**, *18*, 26011–26023.
- (291) Coquinot, B.; Bocquet, L.; Kavokine, N. Quantum Feedback at the Solid-Liquid Interface: Flow-Induced Electronic Current and Its Negative Contribution to Friction. *Phys. Rev. X* **2023**, *13*, 011019.
- (292) Schlaich, A.; Barrat, J.-L.; Coasne, B. Theory and Modeling of Transport for Simple Fluids in Nanoporous Materials: From Microscopic to Coarse-Grained Descriptions. *arXiv:2406*, 2024, 03039, DOI: [10.48550/arXiv.2406.03039](https://doi.org/10.48550/arXiv.2406.03039).